UNIVERSITY OF Southampton

University of Southampton Research Repository
ePrints Soton

Copyright © and Moral Rights for this thesis are retained by the author and/or other copyright owners. A copy can be downloaded for personal non-commercial research or study, without prior permission or charge. This thesis cannot be reproduced or quoted extensively from without first obtaining permission in writing from the copyright holder/s. The content must not be changed in any way or sold commercially in any format or medium without the formal permission of the copyright holders.

When referring to this work, full bibliographic details including the author, title, awarding institution and date of the thesis must be given e.g.

AUTHOR (year of submission) "Full thesis title", University of Southampton, name of the University School or Department, PhD Thesis, pagination

http://eprints.soton.ac.uk

University of Southampton

Faculty of Engineering and the Environment
Civil, Maritime and Environmental Engineering and Science

Development and Evaluation of the Hydrodynamic Design of the OWEL Wave Energy Converter

Mark Thomas Leybourne

Thesis for the degree of Engineering Doctorate

June 2013

[This page is intentionally left blank]

UNIVERSITY OF SOUTHAMPTON

ABSTRACT

FACULTY OF ENGINEERING AND THE ENVIRONMENT
Civil, Maritime and Environmental Engineering and Science
Engineering Doctorate

DEVELOPMENT AND EVALUATION OF THE HYDRODYNAMIC DESIGN OF THE OWEL WAVE ENERGY CONVERTER

Mark Thomas Leybourne

The conversion of ocean wave energy has the potential to supply utility magnitudes of electrical generating capacity. It has been predicted that the UK has an annual, practical wave energy resource of 50 TWh which represents 12.5 % of the total electricity consumption. The lack of convergence in the design of wave energy converters, demonstrates that there is not yet a clearly superior concept and so the development of novel technologies is continuing.

OWEL's novel wave energy converter was intended to overcome some limitations of floating OWCs whilst retaining many of the beneficial synergies. The simplicity of the collector, no submerged moving parts and a uni-directional air turbine PTO are all advantages of the technology. A review of the previous development work concluded that little was known about the operating principle of the device and that its hydraulic design was not understood.

Through the extensive small scale, physical modelling of three different device geometries, the conversion process was investigated to increase knowledge and inform the hydrodynamic design. Initial studies considered a simplified duct geometry and found that the suggestions from the previous development phases of the technology were inaccurate and so were discounted. The methodologies developed were used in subsequent testing and provided initial learning on which the future experiments were based. A multi-duct model was tested in a wave basin in order to investigate whether such a configuration would be suitable as a future commercial device. Energy conversion efficiencies exceeding 40 %, proved the potential of the configuration but the testing highlighted the many complexities of the platform that should be addressed before being further developed. A single duct was studied to evaluate and improve the design of a proposed marine demonstrator being developed consecutively with this research in a commercial project. Testing the sensitivity of performance to changes in the geometric design and naval architecture resulted in a configuration that maximised the conversion efficiency.

Various numerical modelling options were considered to create a performance model. CFD was deemed to be the most suitable method to capture all of the relevant flow physics in the conversion process and to provide a useful design tool. A preliminary model was developed to demonstrate the applicability of the method and provide the foundation for further work.

Annual, large scale energy productivity analysis for the optimised device predicted that a 42 m long, single duct would be able to generate 154 MWh/yr at Wave Hub. This was equivalent to a 124 % increase over the original baseline design. Predicted electricity generation for the EMEC site was comparable to the predictions for a competing technology. Although both predictions were relatively low, it was anticipated that these would increase as the designs mature.

[This page is intentionally left blank]

List of Contents

List of Figures

List of Tables

List of Abbreviations

CoG	Centre of Gravity
DECC	Department for Energy and Climate Change
DoF	Degree(s) of Freedom
EMEC	European Marine Energy Centre
EPSRC	Engineering and Physical Sciences Research Council
FFT	Fast Fourier Transform
HMRC	Hydraulics and Maritime Research Centre
ITP	IT Power
LCF	Longitudinal Centre of Floatation
LCOE	Levelised Cost of Electricity
Narec	National Renewable Energy Centre
NWT	Numerical Wave Tank
O&M	Operations and Maintenance
OPEX	Operational Expenditure
OWC	Oscillating Water Column
OWEL	Offshore Wave Energy Limited
PTO	Power Take-Off
RAO	Response Amplitude Oscillator
ROC	Renewable Obligation Certificate
RPM	Revolutions Per Minute
SWL	Still Water Level
SWRDA	South West Regional Development Agency
TSB	Technology Strategy Board
UCC	University College Cork
WEC	Wave Energy Converter
WPA	Water Plane Area

Declaration of Authorship

I, Mark Thomas Leybourne, declare that the thesis entitled '*Development and Evaluation of the Hydrodynamic Design of the OWEL Wave Energy Converter*' and the work presented in the thesis are both my own, and have been generated by me as the result of my own original research. I confirm that:

- this work was done wholly or mainly while in candidature for a research degree at this University;
- where any part of this thesis has previously been submitted for a degree or any other qualification at this University or any other institution, this has been clearly stated;
- where I have consulted the published work of others, this is always clearly attributed;
- where I have quoted from the work of others, the source is always given. With the exception of such quotations, this thesis is entirely my own work;
- I have acknowledged all main sources of help;
- where the thesis is based on work done by myself jointly with others, I have made clear exactly what was done by others and what I have contributed myself;
- parts of this work have been published at international conferences and journals as described in chapter 11 of this thesis.

Signed:

Date: 7th June 2013

Acknowledgements

I am very grateful to my academic supervisors, Dr. William Batten and Prof. AbuBakr Bahaj for their continued guidance and advice throughout this research. I am equally grateful to my industrial supervisor Dr. Ned Minns whose support and enthusiasm has continually encouraged my work.

I would like to thank both IT Power and OWEL for providing the opportunity to conduct research on this device and for part financing this research. I acknowledge EPSRC for providing the additional finances for this research.

I also want to thank Davide, Pascal, Dimitris and Martyn for their sharing of wave energy related problems and solutions in our research group. My fellow EngD cohort; Jon, Kevin and Cath, for whom this has been a constant learning experience.

On a personal level, I wish to thank my friends and colleagues, particularly Jack, Tassos, Ian and Bob, who have been incredibly supportive and patient through the challenging times; the guys of Yellowgroove for always providing a musical distraction from my work.

Finally, I thank my Parents and Family for their love, care and understanding.

[This page is intentionally left blank]

1 Introduction

1.1 Background

In recent decades, the realisation of man's impact on the natural environment has become ever increasingly apparent. The use of fossil fuels as a primary energy source is causing significant and detrimental effects on the gaseous composition of the atmosphere. The Stern Review [Stern (2006)] highlighted the necessity to take immediate action in order to suppress the effects of climate change and avoid the serious socio-economic costs. Stern's main conclusion was that "*The benefits of strong, early action on climate change outweigh the costs*".

A method for reducing the use of fossil fuels is to use alternative, sustainable energy from renewable resources. The IEA (2011) estimated that the 2009 global generation of electricity from renewables was 19.5 %, with 16.2 % from hydro power alone, in comparison to 67.1 % from fossil fuels. In the UK, DECC (2011b) estimated that around only 6.8 % of electricity generation in 2010 was from renewable sources. The UK's target, as set out by the Energy White Paper DTI (2007) however, aimed that 10 % of electricity generation in the UK in 2010 should have been from renewables. The legally binding target of generating 15 % of the UK's energy from renewable resources by 2020 means that around 35 % of electricity generation will need to come from renewables [BWEA (2009)]. The majority of the UK's renewable electricity generating capacity is from large scale hydro plants (around 5 % in 2010 [DECC (2011b)]) however, most of the suitable sites are now currently exploited and little new capacity can be added. The current focus for UK renewable generation is toward both onshore and offshore wind with over 5.5 GW of capacity operational in mid-2011 [RenewableUK (2011a)] and a target of around 38 GW by 2020. However, as the mature renewable energy technologies such as wind and hydro begin to reach their limits of deployment through planning restrictions of sites and resource, other renewable resources, such as ocean wave energy, must be exploited to create a balanced energy mix.

Ocean waves are generated from winds blowing across the sea surface. They occur in all water bodies, however, the best resources are found in the temperate regions of the globe, particularly in deep water, oceanic sites with large fetch lengths. Waves have an energy density many times higher than that of winds or tides and can be often be predicted a number of days in advance therefore making them a useful energy source. Determining a realistic, achievable figure for the global wave energy resource has many difficulties. Thorpe (1999) estimated that the global, annual wave energy resource is around 2,000 TWh, equivalent to approximately 10 % of the

world's electricity demands. A more recent estimate was made by Gunn and Stock-Williams (2012) who predicted that the global wave power resource is 2.11 ± 0.05 TW. By assuming that the Pelamis Wave Energy Converter (WEC) would be the device used to exploit this resource, they showed that approximately 4.6 % of the available power is extractable, equating to ~850 TWh/annum.

The UK has one of the best resources of wave energy in Europe and estimates by DTI (2000) and Winter (1980) predict that along the UK's shores, an annual resource of between 250 TWh/yr and 600 TWh/yr exists. Winter (1980) also estimated that around 7 GW of electricity could realistically be supplied by wave energy converters and more recently, the Carbon Trust (2011) have estimated that the UK has an annual, practical wave resource of 50 TWh. This figure represents 12.5 % of the UK's ~400 TWh/yr electricity consumption [DECC (2011b)]. Capturing ~32 % of this resource would yield the same amount of electricity currently generated from all forms of wind energy, i.e. 15.75 TWh/yr [DECC (2012)]. This demonstrates that wave energy has the potential to usefully contribute to the renewable energy mix as confirmed in the Government's UK Renewable Energy Strategy, [HM Government (2009)].

Although the idea of using ocean waves as a source of power had been first conceived by Girard in 1799 to power saw mills and pumps, the feasibility of large, utility scale deployment of wave energy converters was not investigated until the 1970's when the 1973 oil crisis prompted the world to consider alternative energy sources. The most notable and famous wave energy device from this period was Salter's Duck [Salter (1974)] which is still under development in various guises, [You *et al.* (2012), Lucas *et al.* (2009)]. The large associated economic cost of developing these technologies was soon realised and as oil prices reduced, so did the interest in wave energy and small scale generating plants. Despite this, research continued, albeit at a limited level, and wave energy devices began to regain attention in the late 1990s and increasingly so on into the 2000s. Recent and comprehensive accounts of the history of and progress of wave energy conversion are provided by Cruz (2008) and Falcão (2010). In 2008, Pelamis became the world's first, grid connected, commercial wave energy converter array with three machines deployed off the Portuguese coast. In addition, UK test sites such as those at EMEC and Wave Hub provide excellent opportunities for device developers to test their machines in an ocean environment without the requirements of permissions and infrastructure that would usually be necessary.

The government support for marine renewables is currently being ramped up; in 2011, DECC announced that it had earmarked £20 million of funding for marine energy development. Even

more significantly, the UK government also proposed [DECC (2011a)] to increase support of the Renewable Obligation Certificates (ROCs) to offer 5 ROCs per MWh of electricity generated by wave and tidal devices from 2013 – 2017. This is intended to encourage significant growth in the marine energy industry and help to attract investors to finance the deployment of power generating arrays. A 2012 report by the House of Commons', Energy and Climate Change Committee [ECCC (2012)] suggested that the UK has the potential to become the world leader in marine energy and that it must learn from the mistakes it made in the past with the wind energy industry; a lack of support and financial incentives for wind from the UK government during the 1980s meant that the industry which started out in the UK, grew more rapidly in Denmark where it received the necessary support. As a consequence, Denmark is now the leading country in the wind energy industry. The funding support to be offered by the government is essential if the wave and tidal energy industry is to grow and be successful in the UK. A lack of support could likely see other countries gain a competitive advantage over the UK and develop at a faster rate. The current support through the ROCs scheme will close to new generation capacity in 2017 and will be replaced by a Feed-in Tariff with Contracts for Difference under the new Electricity Market Reform. However, as of the time of writing, the price per unit of electricity supplied, known as the strike price, has not yet been set and so future funding levels are unknown [DECC (2011a)]. A further boost was given to the South West of England in 2012 as the region became the UK's first Marine Energy Park [DECC (2012)], with the advantage of having the Wave Hub, Falmouth Bay and University of Plymouth test facilities.

From the available wave energy resource and government and industry attention, it is apparent that wave energy has the potential to provide a significant contribution the UK electricity supply. An estimate by the Carbon Trust (2011) suggests that there are around 80 companies around the globe currently developing wave energy devices, with 21 of those based in the UK. Despite all of the different concepts being in development and with new ideas still being conceived, there is no apparent convergence in the design. The immature nature of the technology means that, in contrast to stabilised industries like wind, there is not yet a clearly superior concept. It is for this reason that developments in the field of wave energy will continue until one, or a number of devices prove their superiority over other competitors.

Offshore Wave Energy Limited, (OWEL) began developing a new wave energy conversion concept, named OWEL, in 2001. It has novel method of operation and as such, is intended to overcome the some of the disadvantages inherent in other devices and to provide an efficient and economic method for the conversion of wave energy. OWEL is a floating, moored device that uses incident, deep water waves to compress air and drive an air turbine. The schematic in

Figure 1.1 shows the operating principle of the device. As waves enter into the device, the floor which ramps upwards, induces a rise in wave height which causes the wave crests to create a seal with the roof and trap a volume of air ahead of the wave. As the wave progresses along inside the duct it forces the trapped air out of the duct and through a power take-off (PTO) comprising a uni-directional air turbine connected to a generator.

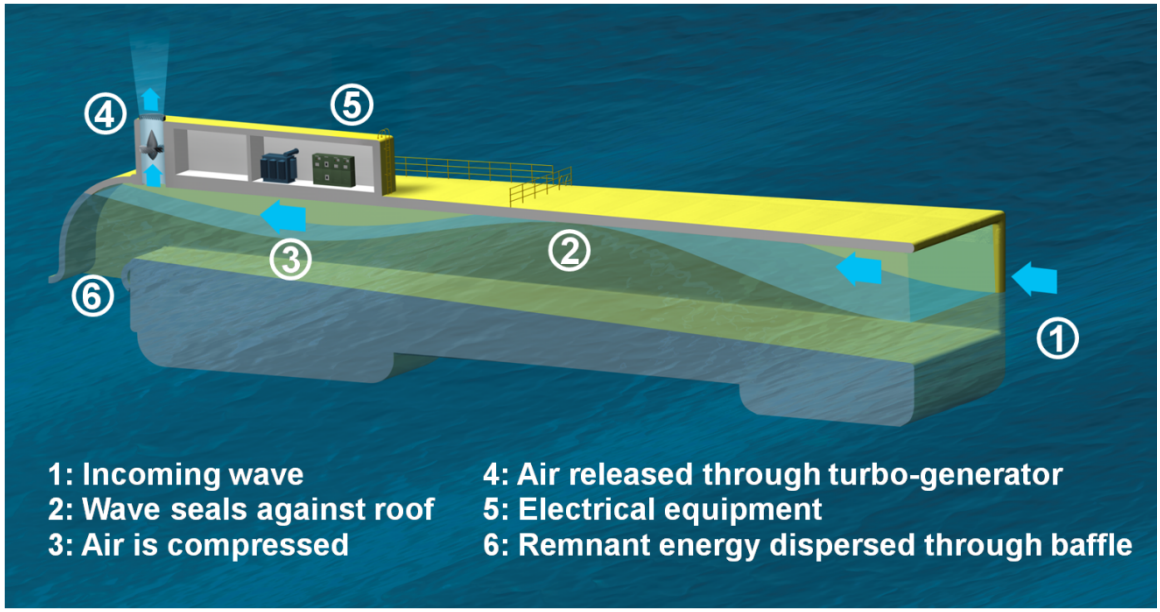

Figure 1.1, A schematic of the OWEL operating principle, provided by Offshore Wave Energy Ltd.

Prior to this research commencing, experimental and numerical investigations had been carried out [Pegrum (2001), Steer (2002), NaREC (2005) & Kemp *et al.* (2005)] to assess the performance and characteristics of the device in order to prove the concept. Results suggested that the concept worked and could have potential to succeed. It was realised however, that a greater, in depth knowledge was required before the concept could be advanced towards the commercial market.

1.2 Project Motivation

The primary motivation for this study was to assist in the development of the OWEL WEC with the intention of advancing the design towards commercial success. It is hoped however, that aspects of this development will also be of use to the broader scientific community. The dissemination of experience and lessons learned over the course of the OWEL projects add to current knowledge base.

This Engineering Doctorate research has been sponsored by IT Power Ltd. (ITP) and the Engineering and Physical Sciences Research Council (EPSRC). In 2005, ITP acquired a majority share of Offshore Wave Energy Ltd and the associated intellectual property of the

device. Although ITP are primarily a renewable energy consultancy, in this instance they have been acting as a device developer with the aim of incubating and commercialising the technology. The timeline in Figure 1.2 shows how the development of OWEL has progressed during the period in which this research has been undertaken. Following a Carbon Trust funded project in 2005, the progression of the development of the device had paused due to a lack of funding. This EngD research commenced in 2007 and was intended by ITP to assist in the development OWEL and advance the design. Shortly afterwards, during 2008, ITP and OWEL were awarded grant funding by the South West Regional Development Agency (SWRDA) to support a project intended to investigate the commercial potential of the OWEL WEC. This project had the primary objective of generating a techno-economic model from a series of physical and numerical modelling. The successful outcomes of the SWRDA project led to further funding being awarded by the Technology Strategy Board (TSB) during 2011. This was £2.5 m of co-finance to support a £5 m project with a consortium of nine companies. The primary aim of this project was to further develop OWEL in order to design, construct and deploy a large scale prototype device at an offshore location, provided the remainder of the 50 % finance could be obtained from private investment.

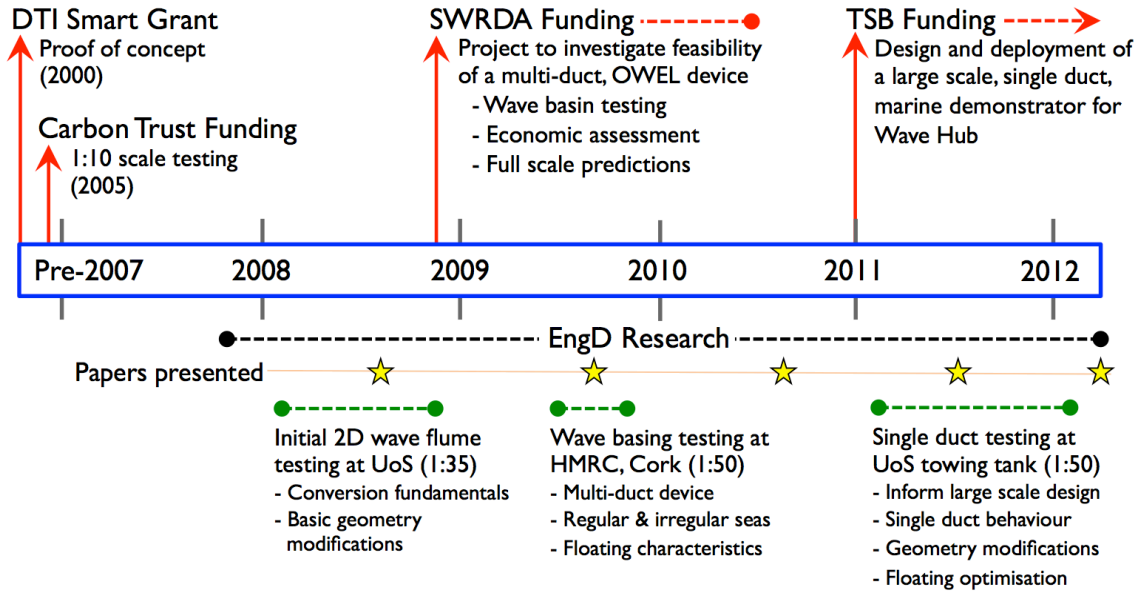

Figure 1.2, Timeline of the OWEL development including, funding awards, commercial projects, experimental testing and publication milestones of academic papers.

At the commencement of this research in 2007, limited data existed to demonstrate the performance capabilities of OWEL. Estimates of the potential for the device to deliver power to the grid were based on simplistic, initial calculations from the proof of concept and early development projects. Further to this, the underlying fundamental operating principles were not fully understood and knowledge of how the device functioned was at an early stage. The motivation for this research was therefore to continue with the development of OWEL, increase

the knowledge base through research and to support the SWRDA and TSB projects that ran in conjunctions with this work.

1.3 Objectives

The aim of this research is to advance the development of the OWEL wave energy converter and increase its potential to be a part of the future wave energy market.
This leads to the hypothesis that:

- Through advancement of the understanding and knowledge of the OWEL wave energy converter, its hydraulic design can be improved to demonstrate a competitive level of power generation.

A review of the previous research and development work into OWEL identified a lack of fundamental knowledge of the energy conversion process. In order for the commercial potential of OWEL to be realised, the operating principle should be understood and the energy yield from the device maximised in order to provide a competitive advantage. Therefore, the objectives of this work are to:

- Study the energy conversion process occurring within the OWEL duct, both visually and with quantitative measurements; in order to provide an understanding of how the device operates.
- Determine the key relationships between the wave characteristics and the conversion performance of the device, so that the geometry of the device can be matched or 'tuned' for a given wave climate.
- Improve the performance by modifying the geometry and floating design based on the learning from the initial investigations.
- Support the on-going commercial development of OWEL and the projects being carried out in parallel to this research. This is in order to inform and improve the design of the commercial prototype and financial implications.
- Commence the development of a suitable theoretical model to predict the power capture and conversion performance that will allow full scale power to be estimated and aid further learning about the conversion process.
- Quantify any improvements in energy conversion performance made as a result of this research.

2 Background to Wave Energy Conversion

2.1 Introduction

This chapter is intended to summarise the relevant background theory that is referred to within this work. This commences with an introduction to the terminology and equations used in describing waves and their properties. Different waveforms, real sea conditions and the transport of wave energy are then all discussed with reference to the conversion of the energy to useful power. The chapter concludes with an overview of the different types of wave energy converters that are currently in development and how the various concepts can be classified. This demonstrates that the technology used in the conversion of wave energy is immature and still developing.

2.2 Waves

Oceanic waves are wind-generated, surface waves which are formed due to the shear force from the wind acting at the water surface, therefore implying that the energy contained within them is a stored form of solar energy. Waves grow in size as more energy is transferred to them by the action of the wind. Their size therefore is determined by the strength of the wind and how long it has acted on the waves. The complex interactions between the winds, waves and bathymetry of the seas leads to waves with differing heights, lengths, periods and directions and a number of statistical models exist to best describe these physical conditions. Within the oceans, waves can be generated from local winds or from distant storms. Local wind seas often appear to have a somewhat erratic and irregular nature with wave crests propagating in different directions. Waves generated by distant storms are known as swell and in comparison to wind seas, are far smoother, with long periods and tend to propagate in a single direction. Swells that are generated in deep water may propagate over long distances with little energy lost. They can therefore be forecast to some degree and contain a high energy density.

The shape and dynamics of a particular waveform are dependent on the conditions in which it is travelling and the parameters of the wave, specifically, the depth and wave steepness. Various wave theories have been developed to describe the different types of waves that can occur. The applicability of the main wave theories are summarised in Figure 2.1, which indicates the range of validity for each theory depending on the steepness of the wave and the depth of the water in which it travels.

The diagram shows that waves conform to two limits;

A "deep water" steepness limit $\frac{\text{Wave Height}}{\text{Wavelength}} = \frac{H}{L} = 0.14$

A breaking limit $\frac{\text{Wave Height}}{\text{Depth}} = \frac{H}{d} = 0.78$

Within these limits wave types range from the simplest, sinusoidal, linear waves to more complex, trochoidal shaped Stokes' waves to shallow water waves, represented by Cnoidal or Stream function theories.

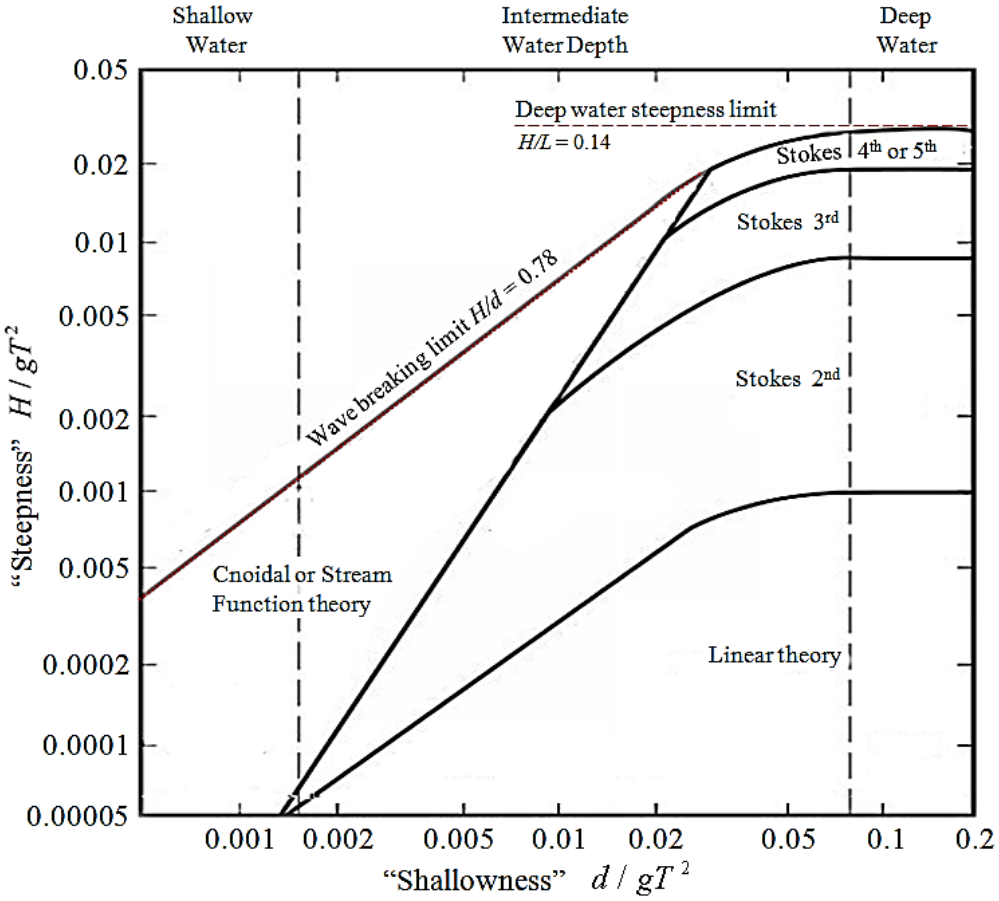

Figure 2.1 The applicability of different wave theories depending on the relative steepness and "shallowness" of the wave, modified from Chakrabarti (1994).

As OWEL will be deployed in "deep water", where the depth is greater than half a wavelength, or "intermediate depth", where the depth is greater than 1/20th of a wavelength, only two of these theories are relevant. In deep water and for small amplitudes where waves are simple sinusoids, conditions can be approximated to be linear. As waves become steeper and possibly shallower, the different orders of Stokes' wave theories become more applicable. To begin, it is pertinent to look at the simplest form of a water wave; an idealised, linear, harmonic wave.

2.3 Linear Wave Theory

The most widely used mathematic description of linear, or regular, waves was suggested by Airy (1845) and is known as linear or first order wave theory. It requires the wave to be small in comparison to its length and is based on ideal fluid flow within a wave of sinusoidal form. The terminology and dimensions of such a wave are shown in Figure 2.2.

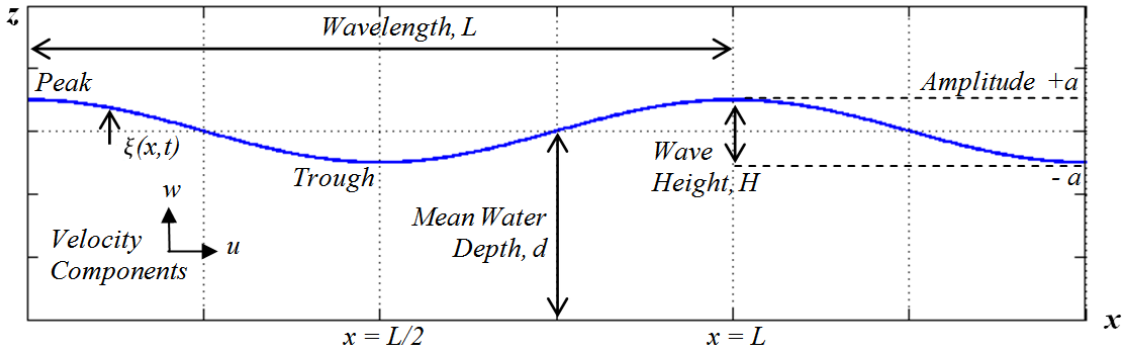

Figure 2.2; An Airy wave with wavelength L [m], height H [m], travelling in a water depth, d [m].

The wave height (H) is the vertical distance from the wave peak to its trough and is equal to twice the wave amplitude (a), so $H = 2a$. The wavelength (L) is the distance between two successive peaks or troughs and the wave period (T) is the time interval between them. The wave steepness is defined as the ratio of a wave's height to its length, (H/L).

For this theory to be valid a number of simplifying assumptions are necessary:

- Surface tension and viscosity are unimportant.
- Flow is incompressible.
- The seabed is impermeable.
- The waves are periodic in space and time.
- Pressure is zero at the free surface (dynamic free surface boundary condition).
- Motion of the free surface is compatible with the motion of the water (kinematic free surface boundary condition).
- Wave amplitude is small in relation to the wavelength.

Although these waves are idealistic, they are a useful starting point when testing wave energy converters; the complexities of a real sea can be excluded and focus can be made on the responses of a system to the input of a single frequency and energy.

2.3.1 Wave Properties

The wavelength is defined as in equation [1] and this relationship is known as the dispersion relation and has to be solved implicitly or using an approximation. The dispersive nature of

waves means that waves of different periods propagate at different velocities, with longer period waves travelling faster than short waves. A graphical output of this equation is provided in Figure 2.3 and shows how wave period and wavelength are related for a range of water depths.

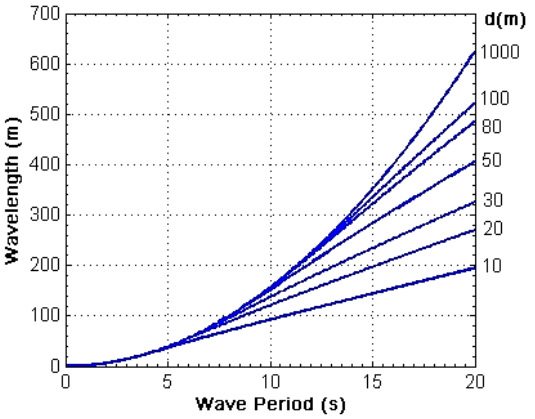

$$L = \frac{gT^2}{2\pi}\tanh\frac{2\pi d}{L} \quad [\mathbf{m}] \qquad [1]$$

Figure 2.3 The dispersion relation is the relationship between wavelength and period for a number of given water depths.

The wave speed or celerity, c, is given by equation [2]. Similarly to [1] this is dependent on the water depth as wave fronts slow in shallow water in a process called "shoaling" as will be discussed in section 2.3.3.

$$c = \sqrt{\frac{gL}{2\pi}\tanh\frac{2\pi d}{L}} \quad [\mathbf{m/s}] \qquad [2]$$

The wave surface profile ξ is defined as

$$\xi = \frac{H}{2}\cos\left(\frac{2\pi x}{L} - \frac{2\pi t}{T}\right) \quad [\mathbf{m}] \qquad [3]$$

For $t = 0$, the profile is a cosine as shown in Figure 2.2.

2.3.2 Deep Water Waves

Waves travelling in water deeper than half their wavelength are classified as deep water waves as the sea bed has little influence upon them. In this instance $d/L < 0.5$ so $\tan(2\pi d/L) \approx 1$ hence equation [1] reduces to equation [4] and the wavelength becomes dependent on wave period alone.

$$L = \frac{gT^2}{2\pi} \quad [\mathbf{m}] \qquad [4]$$

An element of water within an ideal, deep water wave moves in a circular trajectory orbit as shown in Figure 2.4, where its horizontal and vertical velocities are described by equations [5] and [6]. The particle motion decays exponentially with depth below the wave.

Particle velocity *x* direction

$$u = \frac{\pi H}{T}\frac{\cosh\left[2\pi(d+z)/L\right]}{\sinh\left[2\pi d/L\right]}\cos\left(\frac{2\pi x}{L} - \frac{2\pi t}{T}\right) \quad \textbf{[m/s]} \qquad [5]$$

Particle velocity *z* direction

$$w = \frac{\pi H}{T}\frac{\sinh\left[2\pi(d+z)/L\right]}{\sinh\left[2\pi d/L\right]}\sin\left(\frac{2\pi x}{L} - \frac{2\pi t}{T}\right) \quad \textbf{[m/s]} \qquad [6]$$

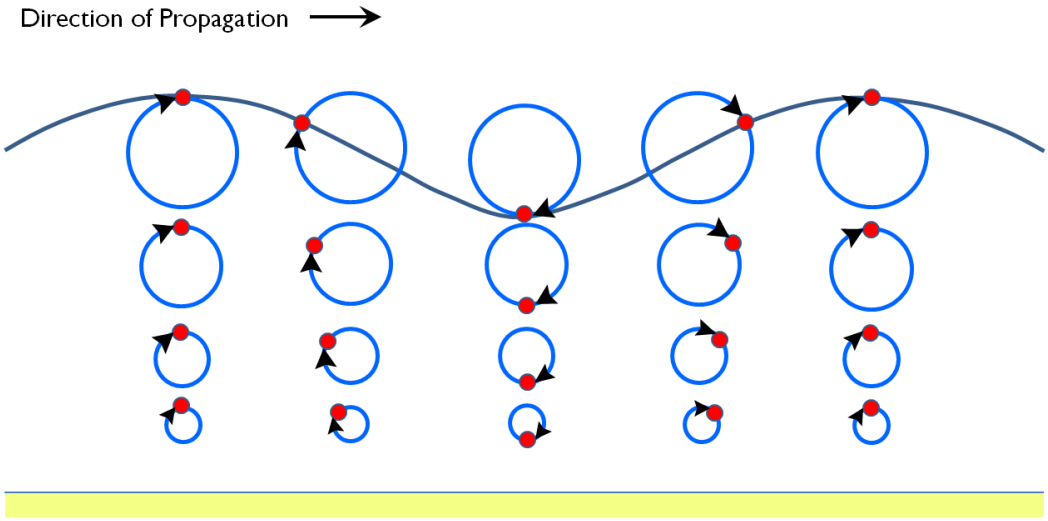

Figure 2.4, The trajectories of water particles within a deep water wave.

2.3.3 Shoaling

The process of shoaling occurs when waves travel from deep water into shallower waters. Interactions with the sea bed cause a series of changes to occur within a wave meaning that;

- Wave orbits become more elliptical.
- Wavelength and celerity decrease, height increases.
- Wave energy is attenuated through friction with sea bed.
- Period remains constant throughout.
- If *H*/*d* becomes greater than 0.78 the wave breaks.
- Refraction occurs so that waves propagate parallel to depth contours.

Waves travelling in water with a depth of less than ½ their wavelength but greater than 1/20th of their wavelength are considered as intermediate depth waves. The motion of the water particles becomes distorted as the water depth decreases and the particles' circular motions become more elliptical as shown in Figure 2.5(a).

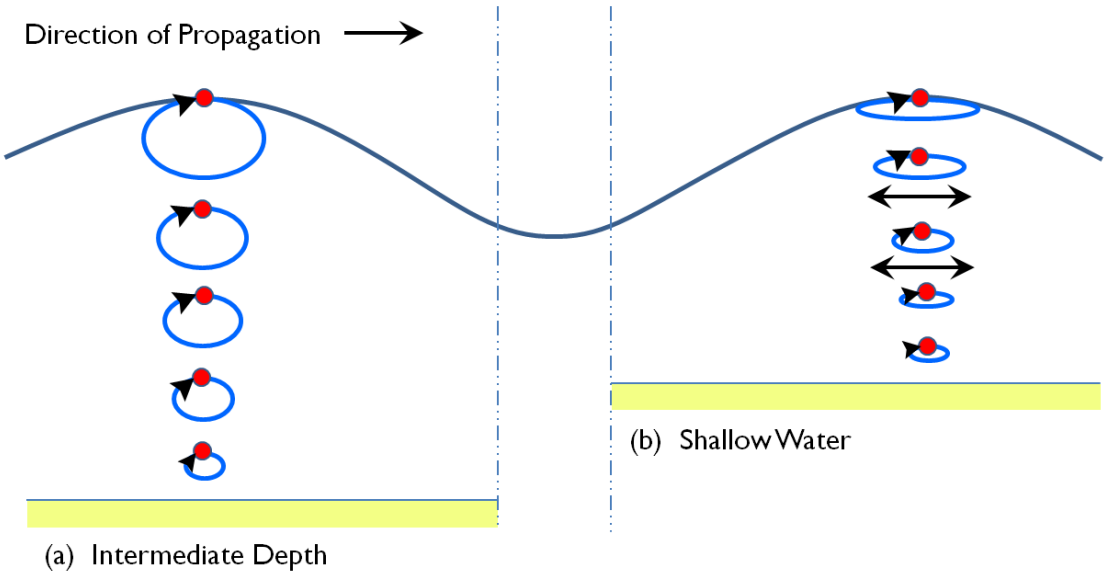

Figure 2.5, The trajectory of water particles in an intermediate depth wave (a) and shallow water wave (b).

In shallower cases where the depth is less than 1/20th of the wavelength waves become shallow water waves and the motion of the water particles become so elliptical that they effectively oscillate back and forth as shown in Figure 2.5(b). As mentioned in section 2.2, other than for small amplitude waves, Linear wave theory becomes unsuitable to model these types of waves and so other theories provide better approximations and their applicability is indicated in Figure 2.1. For shallow water waves the wave celerity of [4] reduces to become a function of depth only.

$$C = \sqrt{gd} \quad \text{[m/s]} \qquad [7]$$

2.4 Stokes' Wave Theory

As shown in the diagram in Figure 2.1, non-linear wave theories become applicable when the *d*/*L* ratio reduces or the steepness increases beyond the ideal limits of the linear theories. These theories are more applicable to conditions in shallower water where the depth reduces and wave steepness increases, or for steep waves associated with storm conditions and so will only be briefly summarised here. The Stokes' wave theories are a further expansion of the linear wave theory and a Stokes' first order wave is analogous to a linear, Airy wave. The equation describing the wave profile of a second order Stokes' wave includes the terms in [3], but with 2nd order expansion terms included as in [8], [see Sorensen (2006)].

$$\xi = \frac{H}{2}\cos\left(\frac{2\pi x}{L} - \frac{2\pi t}{T}\right) + \frac{\pi H^2}{8L}\frac{\cosh kd}{\sinh^3 kd}(2 + \cosh 2kd)\cos 2\left(\frac{2\pi x}{L} - \frac{2\pi t}{T}\right) \quad \text{[m]} \qquad [8]$$

The dispersion relation as described in [1] remains valid for this expansion and so the wavelength remains independent of wave height. The additional terms modify the free surface profile from one of a regular sinusoid to that of a trochoidal form. This leads to waves that appear to be more "peaky" in that their peaks are more pronounced than the flatter troughs and their positive amplitude is greater than that of their negative amplitude. Further expansion leads to Stokes' waves of higher orders, typically up to 5th order and an example of this can be found in the paper by Fenton (1985).

It should be noted that unlike linear waves, the particle orbits of these non-linear waves do not join and so there is a net advance of the particle. This behaviour is known as Stokes drift. Examples of both of these waveform profiles in comparison to linear theory and experimental data, from the free-surface record in a small scale wave tank, are shown in Figure 2.6. From the wave properties of the real wave in Figure 2.6, the wave type can be seen to be a deep water wave but steep and as Figure 2.1 shows a Stokes' 3rd order expansion would best represent this type of wave. Whilst it can be seen in Figure 2.6 that the linear wave profile is dissimilar from that of the others, the Stokes' theory waves both approximate the real condition well.

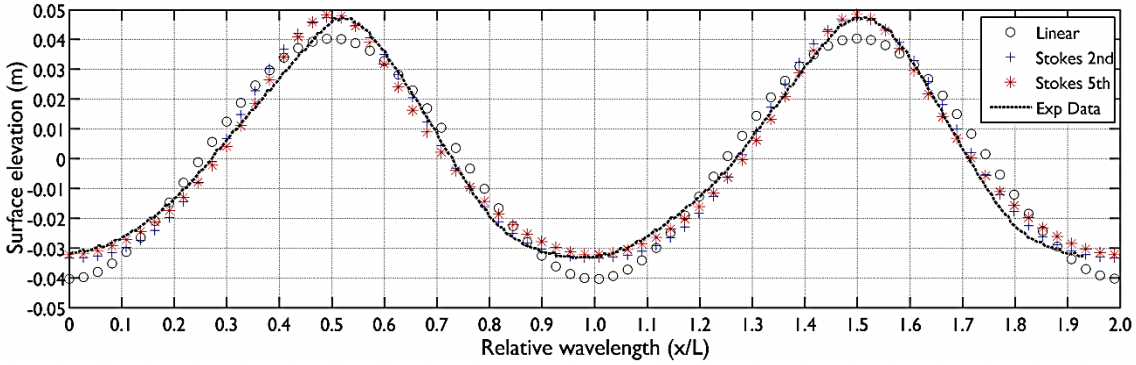

Figure 2.6, A comparison of Stokes' 2nd and 5th Order waveforms with linear theory and a real, deep water, steep waveform. (H = 75mm, T = 0.67s, d = 1.1m, from section 6.5.3)

2.5 Irregular Waves

A real sea can be considered as a random collection of waveforms with differing heights, periods and directions. In reality it is not feasible to accurately replicate the specific conditions of an ocean in a laboratory. Therefore, for simplicity, an irregular sea can be considered as a summation, or superposition, of a number of regular sinusoids of different lengths, heights and phases, but all propagating in the same direction as demonstrated in Figure 2.7.

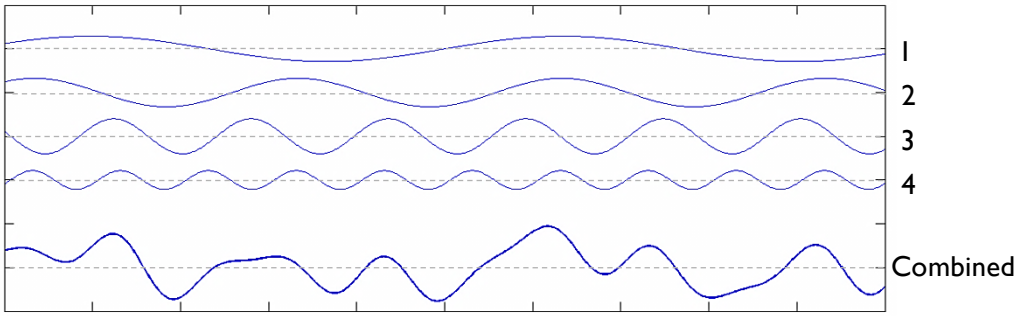

Figure 2.7, An irregular sea can be approximated by the summation of a number of sinusoids with differing wavelength, height and phases.

By definition the pattern of the water surface in an irregular sea does not repeat itself and so an irregular sea cannot be characterised by the composition of its surface profile. However, the total energy of the sea must be a sum of the energy of its constituent sinusoids and so it is convenient to define the intensity of a sea by describing the total energy of the sea as a function of the frequency of each of the component parts. This distribution of energy with respect to wave frequency is known as a wave spectrum and the integral of the energy spectrum is the total energy of the sea.

It is usual to transform the time history of a sea surface to a wave spectrum in the frequency domain by means of a Fast Fourier Transform (FFT) as shown by Figure 2.8 and this process is covered in more detail by Payne (2008). This method can be used to characterise the distribution of spectral energy of any particular irregular wave train. Also shown in Figure 2.8 are the definitions for the two parameters most commonly used when describing the state of a sea; the "significant wave height", H_s and the peak wave period, T_p. H_s is the average height of the 1/3rd highest waves and is roughly the wave height an observer would record when viewing the sea, as psychologically, smaller waves are typically neglected by an observer. T_p is, intuitively, the period at which the wave spectrum peaks. It is common to describe the conditions of the sea over a short period of time using these two parameters and this is known as the sea state.

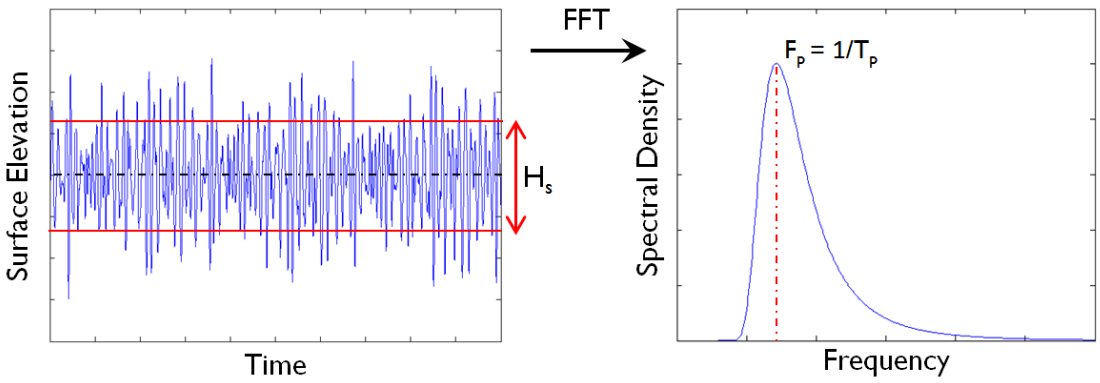

Figure 2.8, Transformation from a time series to a frequency wave spectrum is usually by means of an FFT.

In addition to these two key parameters, a number of other statistical values are commonly measured and used when defining wave spectra. The average zero crossing wave period, T_z, is defined as the measure of the mean time between wave cycles based upon the crossing of the water surface elevation across the still water level (SWL). The energy period, T_e, is wave period value that is used in the calculation of the average wave power in a sea state and is discussed further in section 2.6. Summaries of the many additional definitions, not directly relevant to this work can be found in Holmes (2009) and Venugopal *et al.* (2011).

2.5.1 Classical Wave Spectra

When carrying out investigations with irregular seas, a wave spectrum is commonly chosen by one of two methods; it is either defined from the wave time series data recorded at a specific, real site over a prolonged period of time, or a classic, idealised spectrum is chosen to give a typical sea state using a number of input parameters. In the majority of WEC experimental studies, especially for non-site specific investigations, a classical spectrum is chosen to provide a representative sea state for a range of specified T_p and H_s.

There are three main classical spectral models, typically used in wave energy testing;

- Pierson and Moskowitz (1964) is one of the simplest wave spectra available. It was originally defined by one variable, the wind speed at a given height above sea level but later re-analysed to be defined by the wave period, [Michel (1999)]. This assumes that the wind generating the waves has been blowing steadily for a long time, over a large area so that the waves reach a point of equilibrium with the wind. This is known as a fully developed sea. It is also assumed that, due to the equilibrium, the waves represented in this spectrum have a constant steepness.

- The Bretschneider (1959) spectrum is defined by two variables, T_p and H_s. This is an expansion on the Pierson-Moscovitz spectrum and allows the modification of the spectral shape to those other than a fully developed sea state. The input parameters for this spectrum mean that it is often a popular choice for physical studies as sea states for testing are often defined by their T_p and H_s.

- JONSWAP – (JOint North Sea WAve Project) [Hasselman *et al.* (1973)], has three input parameters, T_p, a peak enhancement factor (γ) and the enhancement shape width (σ). It is simply a Pierson- Moscovitz spectrum multiplied by a shape modifying factor which allows for more control over the spectral shape in comparison to the other two spectra. This was developed from a study of wave data off the western shore of Denmark in order to produce a better spectral model for North Sea, fetch limited sea states which typically have 'peaky' and narrow spectral shapes. It may be the most

adaptable spectrum of the three stated here but often the two shape input parameters may not be known.

The equations for these three classic spectral models are all closely related and by setting specific input parameters they become backward compatible so that for example, a JONSWAP model can reproduce a wave spectrum the same as a Pierson Moskowitz and a Bretschneider; similarly a Bretschnieder can replicate a Pierson Moskowitz spectrum.

In addition to the choice of spectrum chosen, a level of directional spreading may also be specified. Long-crested regular and irregular waves progress with parallel wave fronts and so have no spread. Real seas however, are called short-crested seas and can have a typical spread of up to ±60° in deep water locations but this may reduce for shallower sites due to refraction. The example of short crested seas in Figure 2.9 shows the resultant wave field after the superposition of two regular wave trains propagating in two different directions. Even from such a simple example, it can be seen that the resultant wave pattern has a fairly 'random' appearance and, in reality, a sea may be comprised of many wave components all travelling in different directions. Typically, a spreading function is applied to waves generated in the spectrum to give directionality and the level is chosen by selecting the appropriate coefficients required to represent the desired sea state. In initial phases of investigation, it is likely that long-crested waves will be run and performance later compared with short-crested waves. This will demonstrate the effect directionality has on the device's performance. In more advanced tank testing phases, a specific spreading function representing the sea state of the intended deployment site may be used to gain a more specific understanding.

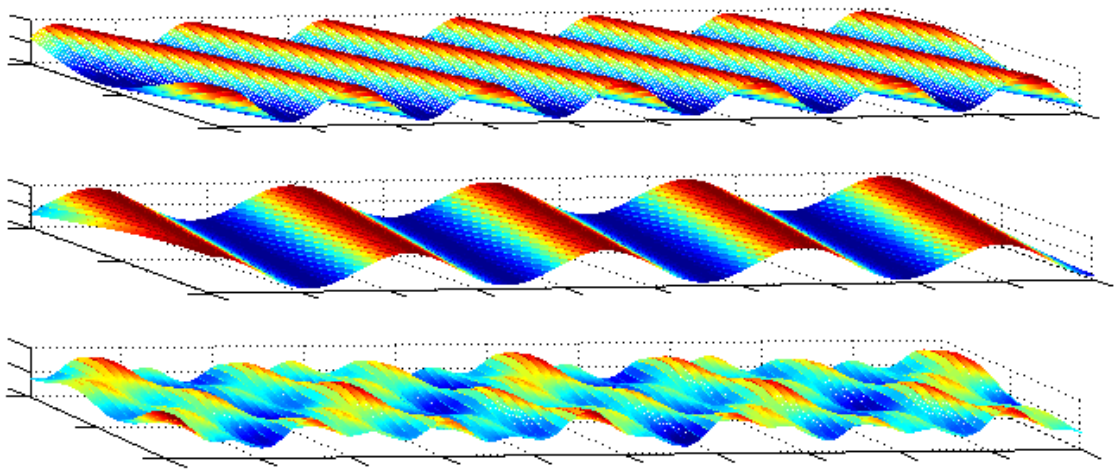

Figure 2.9, The superposition of waveforms with different directions leads to a directional sea that has a far more 'random' appearance.

2.6 Wave Power

The energy content of a water wave is proportional to its height squared and period. This is most usefully described in terms of the energy flux (power) per unit length of wave crest typically expressed in kilowatts per metre of crest width (kW/m). The power available in regular, sinusoidal waves in deep water, defined in Holmes (2009) is

$$P_{mono} = \frac{\rho g^2 H^2 T}{32\pi} \quad (W/m) \qquad [9]$$

Here ρ is the density of water, g is the gravitational acceleration, H is wave height and T is the wave period.

As an irregular sea comprises waves with various wave heights and periods, the power available within them is defined slightly differently to regular waves, however, the power is still proportional to $H^2 T$. The wave power per unit width of wave crest in an irregular sea in deep water is defined by Venugopal *et al.* (2011) as

$$P_{poly} = \frac{\rho g^2 H_s{}^2 T_e}{64\pi} \quad (W/m) \qquad [10]$$

Where H_s is the significant wave height, T_e is the 'energy period' which is the equivalent period of a regular wave train having a wave height equal to H, where $H = H_S/\sqrt{2}$, that contains the same energy as the irregular sea state [Venugopal *et al.* (2011)]. This is a shorter period than T_p but longer than the zero crossing period, T_z. For example, a Bretschneider spectrum, $T_e = 0.86T_p$ and $T_e = 1.2T_z$. For deep water waves, at least 95% of the energy is contained within the upper water column from the surface down to a depth of $L/4$ as the plot in Figure 2.10 shows.

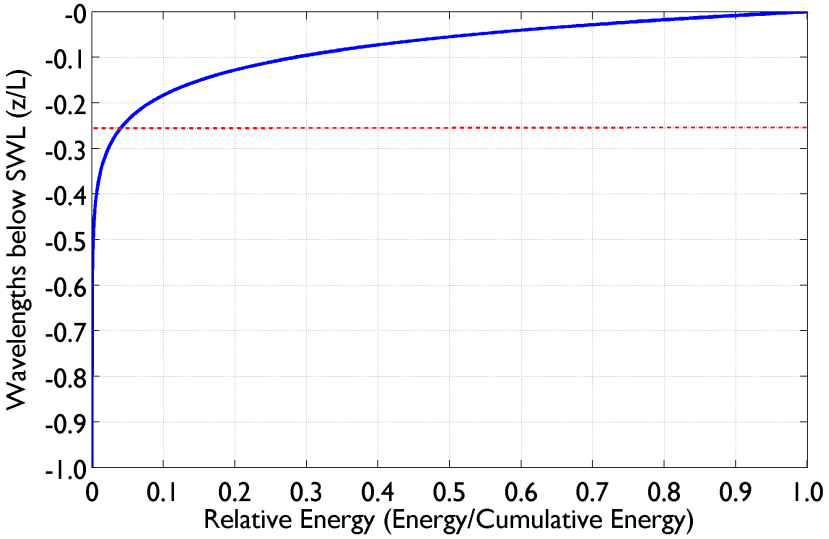

Figure 2.10, Distribution of the kinetic wave energy with respect to depth. Red dashed line shows that at least 95% is within the upper $L/4$ of the water column.

2.7 Types of Wave Energy Converter

Over time, numerous wave energy conversion methods have been suggested and presently many of those are still in active development. As mentioned in section 1.1, unlike the wind energy industry, WEC technology has not yet matured and this is reflected by the variety of machines being trialled. The classical approach to classifying WECs separated devices into three categories; point absorbers, terminators or attenuators, [Thomas (2008)]. This describes the orientation and region in which a device extracts energy from a wave; either a single point, a line orthogonal to the direction of wave propagation or in a line parallel to the wave direction. Myers *et al.* (2010) suggested that this classification approach was not clear and of limited application to the multitude of WECs and presented a much more thorough method. This included the type of energy excitation forces, axis of primary motion, PTO type, fixing method and the type of control implemented. However, a lack of agreement between device developers and researchers has meant that no standard naming convention has been determined and so the terminology used to classify WECs is often fairly interchangeable and descriptive.

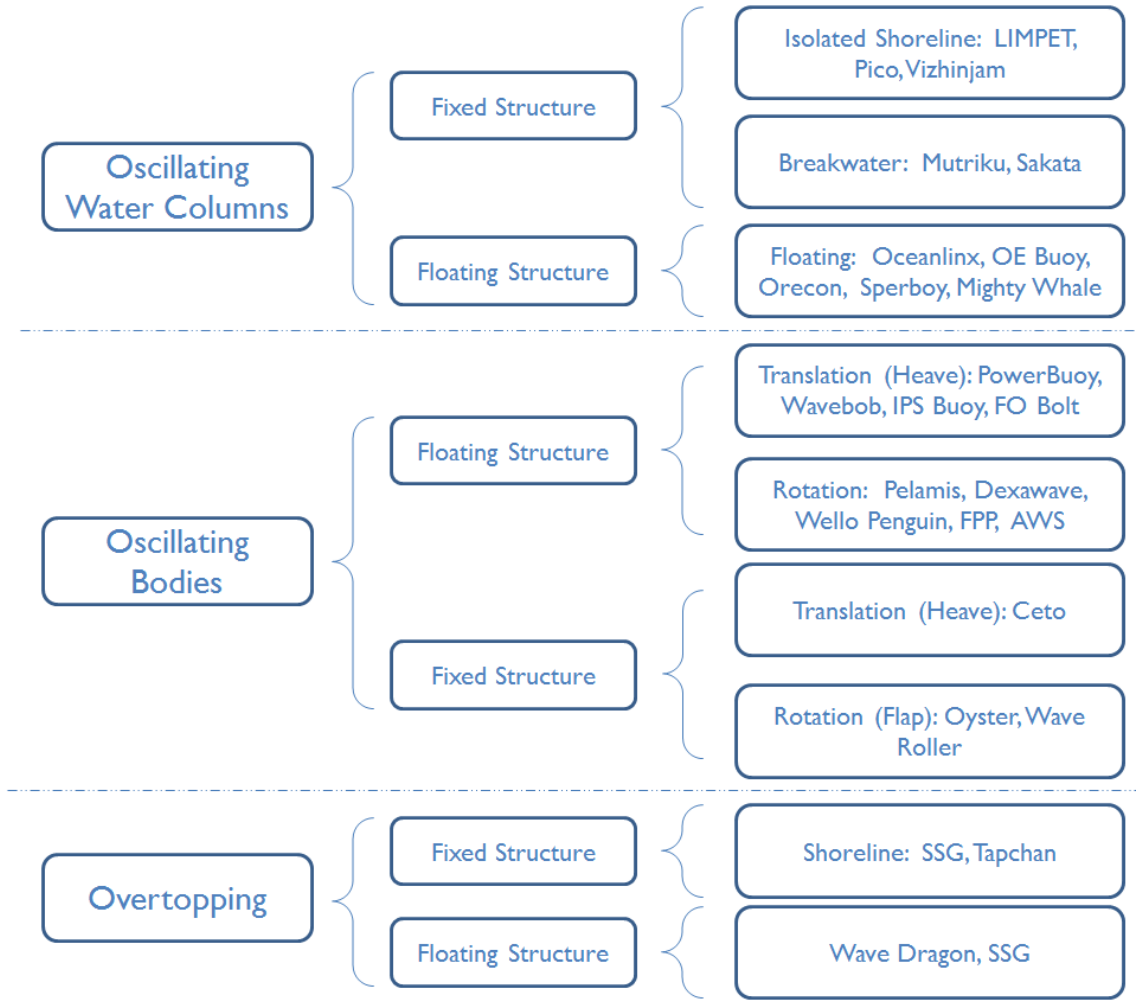

Figure 2.11, The three main categories of wave energy converters with specific examples, modified from Falcão (2010).

A recent summary by Falcão (2010) presents a reasonably complete, general overview of WEC technology and provides examples of each type of device. A modified, updated version of this classification is presented in Figure 2.11, in which the three main groups of WEC type are split depending on whether they are floating or fixed to the seabed and then into their respective sub groups depending on their mode of energy extraction or location. Even this grouping however, has its limitations as it does not allow for any devices with novel energy extraction methods, such as OWEL.

2.8 Additional Background Theory

Further contextual information is provided in Appendix A1 and is included for reference and further reading. This includes a list of the scaling laws used to scale parameters when conducting experiments with models. An introduction to some relevant aspects of naval architecture theory is provided to give context for the work surrounding the later phases of the research when the floating dynamics of the OWEL device were considered. Finally, the various full scale, air power take-off methods that have been implemented on oscillating water column devices are reviewed with reference to their suitability for use on OWEL.

3 Review of Literature

3.1 Introduction

The objectives of this chapter are to provide a context for the reasons of development of the OWEL device and to draw synergies between the research into Oscillating Water Columns (OWCs) and OWEL. As an introduction, the devices that are considered to be direct competitors to OWEL are summarised with their merits and limitations. This demonstrates the potential of OWEL to improve on the disadvantages exhibited by other technologies and the motivation to develop a new device with a novel method of power capture. Subsequently, the previous research into the OWEL WEC is summarised and the approaches taken are critically reviewed. The key conclusions from these previous studies provide a point of reference for the preliminary modelling and hypotheses to test. Of the different WECs in development, OWEL can be most likened to an OWC and therefore the literature reporting investigations into this type of device provide the most use to this research. As this work predominantly focuses on the small scale, physical modelling of OWEL, the techniques and methodologies for the laboratory testing of OWCs are reviewed. Further to this, the implications and limitations of scale modelling are discussed in reference to OWCs. Finally, the options for simulating the air turbine PTO at small scale are discussed with their applicability to OWEL.

3.2 Key Competitors

To establish where OWEL resides within the current cohort of wave energy converter technology, it is prudent to make some suggestion as to the key market competitors. Whilst no wave devices have yet been supplied for a large scale commercial installation, some devices that are identified as direct competitors may in the future become power plants delivering utility scale electricity to the grid. In addition to identifying some of these potential competitors it is also worthwhile to comment upon the merits and limitations of each technology and some of the lessons learnt in their development. This may assist in the development of OWEL by making recommendations to provide a technological advantage.

It is intended that OWEL will be deployed in deep water, with depths of > 50 m where the wave energy resource is greater than shallow water sites, see Folley and Whittaker (2009) for more information. Other devices that are designed to extract power from the deep water wave resource can therefore be considered to be in direct competition with OWEL. Through knowledge of the wave energy industry and recent summaries of the “state of the art” of WECs, 10 devices have been identified and are presented in Table 1, [Waveplam (2009), RenewableUK

(2011b), Krohn *et al.* (2012)]. Whilst this list does not include other 'market leaders' operating in shallower waters, such as Aquamarine's Oyster [Whittaker *et al.* (2007)] or Wavegen's OWC technology [Heath (2012)], these devices should still be considered by OWEL as they will likely take a share of the overall wave energy industry. However, for the purpose of this overview, WECs intended for shallow water or coastal deployment are not discussed.

Table 1, Summary of the direct, technology competitors to OWEL.

Company	Device Name	Type	Most Significant Deployment
Oceanlinx	Green Wave	Floating OWC	Deployed 1:3 scale device in 2010
Ocean Energy	OE Buoy	Floating OWC	Deployed ¼ scale device in 2009-11
Pelamis	P-2	Floating Osc. Body	Two full scale P2s at EMEC in 2012
Wavebob	Wavebob	Floating Osc. Body	Deployed ¼ scale device in 2006-07
OPT	PowerBuoy 150	Floating Osc. Body	Full scale test deployment in 2011
Fred Olsen	BOLT	Floating Osc. Body	Deployed BOLT 2 at Fabtest in 2012
Wello	Penguin	Floating Osc. Body	Full scale machine at EMEC in 2012
AWS	AWS - III	Floating Osc. Body	$1/9^{th}$ scale tested in Loch Ness
Wave Dragon	WD MW	Overtopping	Deployed 1:4.5 scale device in 2003
Floating Power Plant	Poseidon	Floating Osc. Body	37m wide device deployed since 2008

When assessing a WEC it is pertinent to understand which aspects of a device matter. The order of priority will change between the views of each stakeholder however, from the point of the end user, the device needs to be profitable. The economic measure typically used to assess different technologies is the levelised cost of energy (LCOE) which provides a comparable estimate of the cost of electricity. This takes the capital expenditure (CAPEX), operational expenditure (OPEX), depreciation, project life and learning into account to produce long term figures for the cost of energy of a project in £/MWh or equivalent. The CAPEX comprises of the costs of pre-development, device construction, moorings, PTO and the electrical systems infrastructure. The OPEX is made up of costs accrued during the running of the plant such as operation and maintenance (O&M), insurance, sea-bed rent, grid charges and decommissioning costs. Therefore, to increase the commercial prospects of a device, the LCOE should be minimised by maximising the energy yield whilst reducing the CAPEX and OPEX. The Carbon Trust (2011) currently predict an LCOE of between 38-48p/kWh for the first, 10MW offshore wave array. The 10 WECs identified in Table 1 are discussed in sections 3.2.1 to 3.2.9 with reference to these key assessment criteria and the technological limitations of each device.

3.2.1 Oceanlinx

Oceanlinx have been developing a number of different OWC devices with forward facing openings over the past decade [Gareev (2011)]. Their first was a coastal, shallow water machine with supports resting on the seabed and a number of moorings to prevent any movement and is shown in Figure 3.1. Since then they have deployed two different 1:3 scale floating OWCs off the Australian coast [Baghaei (2012)]. A full scale, 1 MW shallow water, static OWC is currently planned with intentions to develop the floating configurations of the technology in the future [Hunter (2011)]. The floating OWC devices have either been a single unit or multiple units combined in a barge and, as is discussed at length subsequently in section 3.4.3, their performance is sensitive to the heave of the device. This is a significant limitation of many floating OWCs as it necessitates the use of taught moorings, heave plates or inertia to counteract the heave inducing forces. In order to oppose a force, an equal opposite force is required which implies an increased device cost due to the additional structural strength needed. OWCs benefit from having no working parts in contact with the sea as these are all housed within the air turbine PTO. This should lead to better reliability and reduce the device costs as the collector geometry is relatively simple. Developing an air turbine that operates efficiently in bi-directional flow has been a challenge for OWCs. To overcome this Oceanlinx have developed their own turbine which is intended to be more efficient than other PTO solutions, see Appendix A2.3. Limited information about the Oceanlinx devices has been publicised making it challenging to make comparisons with other WECs.

Figure 3.1, The Oceanlinx demonstrator with the collector on the right side of the device and turbine exit on the left [Oceanlinx]

3.2.2 OE Buoy

The OE Buoy is another floating OWC but unlike the Oceanlinx OWC, it is a backward bent duct buoy (BBDB) as shown in the schematic in section 3.4.1, Figure 3.14(b). OE Buoy have deployed and extensively tested a ¼ scale device in Galway Bay as shown in Figure 3.2. It had an approximate displacement of 35 tonnes, a beam of 6 m, length of 12 m [Forestier *et al.* (2007)] and had a generator rated at 11 kW [Lavelle and Kofoed (2011)]. The peak wave to mechanical efficiency of the ¼ scale device was reported by Lavelle and Kofoed (2011) to be ~17 % with typical efficiencies of ~7 %. The benefit of a BBDB is that its performance is far less sensitive to heave motions of the device than a sparbuoy type OWC device and so heave reducing methods are not necessary. Nevertheless, the device will require a mooring system that reliably maintains the buoy on station without detrimentally affecting power capture by influencing the motions. A further characteristic of the BBDB is that its optimal length is a quarter of the wavelength [Suzuki *et al.* (2010)] meaning that for most wave climates, the required length of the buoy would be relatively small. As is typical for OWCs, their low number of moving parts and simple geometries means reliability is likely to be good. In comparison to the Oceanlinx OWC the CAPEX of an OE Buoy is likely to be reduced due to the reduction in forces it needs to oppose.

Figure 3.2, Reduced scale OE Buoy device being tested in Galway Bay [Source: Ocean Energy Ltd]

3.2.3 Pelamis

The current Pelamis P2 WEC comprises five floating tubular sections connected by four PTO modules that contain hinges and hydraulic rams to extract energy from the relative motion between the floating sections [Yemm (2008)]. Pressure accumulators are used to 'smooth' the hydraulic power output of the rams before being passed into hydraulic motors to turn the electrical generators. Pelamis have deployed a total of six full scale machines all rated at

750 kW and have had varying degrees of success. The current version of the WEC, as shown in Figure 3.3, has a diameter of 4 m, an overall length of 180 m and a ballasted weight of ~1,300 tonnes [Yemm *et al.* (2012)]. The opposing mechanical stresses induced within these devices are likely to be high. There are a total of 16 hydraulic rams per device, each of which needs adequate sealing from the water. Pelamis intend that all maintenance and repairs will be carried out in a dock which could lead to lengthy downtime particularly if there are no weather windows or the deployment site is far from a dock. The tubes of the WEC have a narrow profile facing the incident waves that hydrodynamically decouple from extreme waves as large crests pass over it thus reducing the forces applied. Its survivability therefore is likely to be better than many devices of a similar rating. Through extensive testing both at sea and at scale, a control strategy has been developed to vary the resistance provided by the PTO in order to act as a tuning mechanism by altering the excitation response. A theoretical paper by Stansell and Pizer (2012) demonstrates the potential capture performance of Pelamis in comparison to Wavebob and OPT. This suggests that, as Pelamis can be theoretically considered as a series of point absorbers inline, it can extract energy over a capture width many times that of a single point absorbing device such as Wavebob and OPT.

Figure 3.3, E.ON's Pelamis P2 device at EMEC, Orkney [Source: Pelamis Wave Power Ltd.]

3.2.4 Wavebob and OPT

Both Wavebob and OPT are very similar in that they are axi-symmetric, self-reacting point absorbers and are both shown in Figure 3.4. Their main differences lie in their PTOs and their self-reactant methods. OPT incorporate direct drive, linear generator PTO technology and a large, horizontal heave plate to provide a reactant force to the buoy's vertical oscillations. Whereas Wavebob utilise a hydraulic PTO and a sparbuoy type design which uses the high inertia of the lower ballasted section to provide the reactant force. A number of small OPT units

have been deployed with their 40 kW device reported to have an average capacity factor of 35 % [Jordan (2008)]. Their first larger scale device, PB150, was deployed off Scotland during 2010. Although not grid connected Stiven (2012) reported that it generated an average of 45 kW i.e. 30 % c.f. The device has a lockable mechanism to prevent opposing motions of the float and spar in storm conditions.

Wavebob's ¼ scale prototype had a diameter of 5.5 m and a mass of 30 tonnes with an additional 100 tonnes of ballast in the submerged, inertial ballast tank [Hartigan (2012)]. It is estimated that a full scale device will be ~14 m in diameter and rated at 300 kW.

Figure 3.4, Wavebob's demonstration device (left) and OPT's PB40 device (right) [Source: Wavebob Ltd. and Ocean Power Technologies]

Both of these devices are limited by point absorber theory and the necessity for accurate control of the float motions to optimise the phase between the buoy displacement and exciting forces [Falnes and Hals (2012)]. Their small size in comparison to many other WECs means that they tend to be the most affordable and this is a likely factor for their progression. Furthermore, the small diameter of the bodies mean that survivability is likely to be good as the forces are reduced and the geometry can hydrodynamically decouple from the wave crests. A disadvantage to this is that their output per unit will be low. This implies that, to achieve an array with a commercial level of power output, many units will be required therefore increasing the O&M costs. A suitable mooring design and WEC spatial arrangement will be required to maximise the power generated over an array and prevent the collision of buoys during storms whilst at the same time allowing the recovery of devices for maintenance.

3.2.5 Fred Olsen

The Fred Olsen BOLT is a point absorber comprising a floating body moored to a seabed attachment for a static point of reference and to provide a reactant force [Bjerke *et al.* (2011)]. A series of mooring lines are directly connected to the PTO system and are wound around drums. As the buoy heaves or surges, the resultant force on the moorings unwinds the drum and a hydraulic pump attached to the drum converts the rotation into pressurised hydraulic fluid. A hydraulic accumulator stores a portion of the energy in order to wind the mooring lines back onto the drums during the trough of the wave cycle. Fred Olsen have deployed two prototypes of the BOLT WEC, the first was a 45 kW device in Norway and more recently they have installed BOLT 2 at the FaB Test site just off the coast in Falmouth, as shown in Figure 3.5 [Hjetland *et al.* (2011)].

Similarly to the other point absorbers mentioned here, the small diameter of the float will reduce loads in extreme conditions. However, if in extreme conditions the float reaches the limit of the allowable mooring line extension it will encounter significant “end-stop” forces. The rewinding of the chain onto the drums will consume a portion of the power generated, thus lowering the overall efficiency and output of an already low output device. High wear on the mooring cables due to continuous movement and use in power generation could lower the reliability and in the event of a breakage both the output power and survivability will reduce. The float itself should be fairly low weight and cost however, when scaling up the device, large gravity anchors will be required or alternatively seabed piling.

Figure 3.5, Fred Olsen's BOLT "Lifesaver"™ device installed at Fab Test, UK [Source: Fred. Olsen Ltd.]

3.2.6 Wello

The Wello Penguin is a 1600 tonne vessel, approximately 30 m in length and 7 m in draft [Krohn *et al.* (2012)]. It resembles the bow of a large cargo ship and is designed to capture rotational energy generated by the movement of its asymmetrically shaped hull. A rotating, vertical axis pendulum within the WEC converts the gyroscopic forces applied through the hull motions into rotational torque used to drive a generator. It also provides energy storage which will help smooth the power output to the grid between waves. During 2012, a full scale, 500 kW prototype device was installed at EMEC and is shown prior to deployment in Figure 3.6. Similarly to SEAREV [Josset *et al.* (2007)], the Penguin benefits from the fact that all of the moving parts and plant machinery are secure within the watertight structure meaning that damage due to wave loading and the environment is unlikely. Its unit cost is likely to be high given the very large mass and ballast for a relatively small device. The forces on the internal plant are also likely to be considerable given the high inertia of the spinning pendulum.

Figure 3.6, Wello Penguin prior to installation at EMEC, UK [Source: Wello Oy]

3.2.7 AWS

The AWS III is the third design attempt by AWS after the previous two highlighted the considerable difficulties associated with the deployment of subsea WECs [Prado *et al.* (2006)]. This new design is based on the old "Coventry Clam" device [Lockett (1985)] and comprises a series of deformable cells around the outside of a torus buoy. As the cells deform they displace the air within them through bi-directional turbines which also generates from the intake stroke as the cells return to their original position. The cells are interconnected by ducting which

allows the exchange of air between cells that are being compressed and those that are expanding, therefore providing the restoring force. During 2010 AWS tested a 1:9 unit on Loch Ness in order to confirm the operating principle, see Figure 3.7. It is intended that a full scale device will have 12 cells, be 60 m in diameter and have a structural mass of 1300 tonnes [AWS Ocean Energy (2012)]. The reliability and operational life of each cell will be dependent on the robustness of the flexible material used. The material will be required to prevent air leakages in the closed system by exhibiting good fatigue properties under a high duty cycle with high loading and within a harsh environment. In addition, the size of each cell is likely to be small in comparison to the volume of an OWC and implying that the airflow will have a low flow rate but at high pressure in order to increase power. This may lead to losses particularly through the air ducting and turbines. There is also the likelihood of high mooring loads on the 60m wide platform.

Figure 3.7, AWS's 1:9 scale device being tested in Loch Ness [Source: AWS Ocean Energy Ltd.]

3.2.8 Wave Dragon

The Wave Dragon is a floating, overtopping type device that has a geometry intended to promote wave overtopping into an elevated reservoir creating a head of water. The water is released back into the sea through a number of low head hydro turbines to generate electricity. A lengthy ¼ scale deployment at Nissum Bredning, shown in Figure 3.8, proved the concept and provided much operational experience albeit in a scale environment. Performance of the ¼ scale device was reported by Kofoed *et al.* (2006) as an average, yearly, wave to-wire efficiency

of ~12 %, in that ~12 % of the energy passing the tips of the reflector arms is converted to electricity. Despite gaining much interest, a project to deploy a large scale device off the Pembroke coast has stalled and recent progress has been limited. Unlike most WECs, its performance is not frequency dependent and is far more reliant upon wave height. An active, variable freeboard system allows control of the trim and vertical position of the platform to be optimised to best match the operational sea state. Numerous "off-the-shelf" low head turbines are intended to improve the redundancy of the system whilst increasing the reliability. Whilst these can be accessed whilst at sea, replacing them or carrying out any major maintenance is unlikely to be done on site. Due to the low head available, the reservoir has to be large in order to generate a useful amount of power. This leads to the WEC being extremely large in both size and mass; a large scale 7 MW device was predicted to have a displacement of 33,000 tonnes and cost between € 20 – 25 m [Sørensen and Friis-Madsen (2010)]. As this shows, whilst the output of the device is predicted to be high, the CAPEX is very large. Even a reduced size device with a rated output of 1.5 MW is estimated to weigh ~7,000 tonnes. The high capital required for this device will make it challenging to attract investors particularly given the associated risks of wave energy and the likelihood of a low return on investment for a number of years.

Figure 3.8, The quarter scale Wave Dragon prototype under test at Nissum Bredning [Source: Wave Dragon ApS.]

3.2.9 Floating Power Plant

Similarly to Wave Dragon, the Floating Power Plant WEC is large moored platform. The forward edge of the platform has a number of dynamically ballasted floats, connected to the device by double acting, hydraulic pistons. The incident wave crests cause these floats to rise and fall, driving the pistons which pump pressurised water to a hydraulic turbine. A novel

feature of this device is that it is a multi-technology platform as there are three wind turbines mounted to its deck. The output of these turbines helps to increase the overall generation to the shared grid connection thus reducing the cost of energy of the device. Floating Power Plant deployed a reduced scale device from 2008–11 comprising 10 floats along the 37 m wide structure, with three 11 kW turbines and a total mass of ~320 tonnes, shown in Figure 3.9 [Kallesøe *et al.* (2009)]. The Floating Power Plant device is likely to suffer from the similar drawbacks owing to its size as the Wave Dragon does; its large span is likely to lead to high mooring and structural forces. This coupled with the inclusion of wind turbines will increase the loading further and incur additional CAPEX. Survivability may also be an issue given the large beam and 'terminator' type of power extraction. The large number of floats and individual PTO units will provide redundancy but also increase the maintenance of the platform. That said increasing the power output of a single platform with a large number of WEC units and wind turbines will maximise the power supplied to the single grid connection. Moreover, the CAPEX of a combined technology platform is likely to be a lot less than the combined cost of deploying the two technologies separately and that the additional generating capacity will compensate for the larger device costs.

Figure 3.9, Floating Power Plant's P37 demonstration device [Source: Floating Power Plant A/S]

3.2.10 Summary

Of the ten devices discussed in this section no technology can be seen the single, ideal solution for WEC design as they all exhibit numerous advantages as well as disadvantages. Extensive development is required on each of these WECs over the coming years to make them economically and commercially viable, renewable energy solutions. It is therefore unlikely that these devices, or any others currently in design, will make significant contributions to the electricity market over the next 5 or so years. This is not to say that they will not be deployed in

arrays, rather that these deployments are likely to only contribute a few MW each. At the current state of the market, electricity utilities are intending to increase their renewable electricity generating capacity as quickly as possible, therefore, more stable technologies such as offshore wind are proving easy solutions. Therefore, for OWEL to have potential to succeed commercially in this energy market, the device should have competitive efficiencies in order to maximise productivity thus lowering the cost of energy. Inherently, by design, the device has many of the benefits of OWCs which should improve the reliability and reduce maintenance. However, the size of the structure, which is dependent on the wave climate of the deployment site, may likely be responsible for the largest proportion of the device CAPEX. Ideally, the characteristics of the device's power curve should demand a smaller structure and provide a high output for the design wave climate to help minimise the CAPEX and LCOE.

3.3 Previous OWEL Work

The following section provides a brief summary of the work that had been carried out on the research and development of the OWEL WEC prior to this EngD commencing. This encompasses two separate projects each with a physical and theoretical modelling work package. See Appendix A1 for a comprehensive review of the previous research carried out by OWEL and ITP.

Both physical and numerical investigations were carried out over the course of the original two development projects, however due to the methodology limitations, issues with the testing and uncertainty in the data, few definitive conclusions could be drawn. Consequently, there was limited information that was of use when informing the preliminary studies for this EngD research. The results from the work carried out in these two projects have been reported internally [Pegrum (2001), Steer (2002), NaREC (2005), OWEL (2005)] but have not been publicised and so are summarised here and in the appendix for the benefit of the reader.

From the thorough review of the previous development work, it was found that little fundamental understanding regarding the method of operation and energy conversion of OWEL was obtained. It was therefore critical for the modelling in this work to explore the underlying energy conversion principles occurring in the device and basic relationships between the device geometry and performance.

3.3.1 Proof of Concept Physical Modelling

The first project was intended to prove the OWEL concept and generate preliminary results to provide initial knowledge and understanding. This project was funded by a DTI Smart award in 2000 and comprised both physical and numerical studies both carried out by QinetiQ.

The physical modelling was carried out in a towing tank with both static and floating, 1:100 scale models in regular wave conditions only. The tests were therefore conducted in simplified, ideal conditions predominantly in order to determine the most beneficial ratios of wavelength to duct length and wave height to duct entry height. The image in Figure 3.10 shows the model under test in the towing tank.

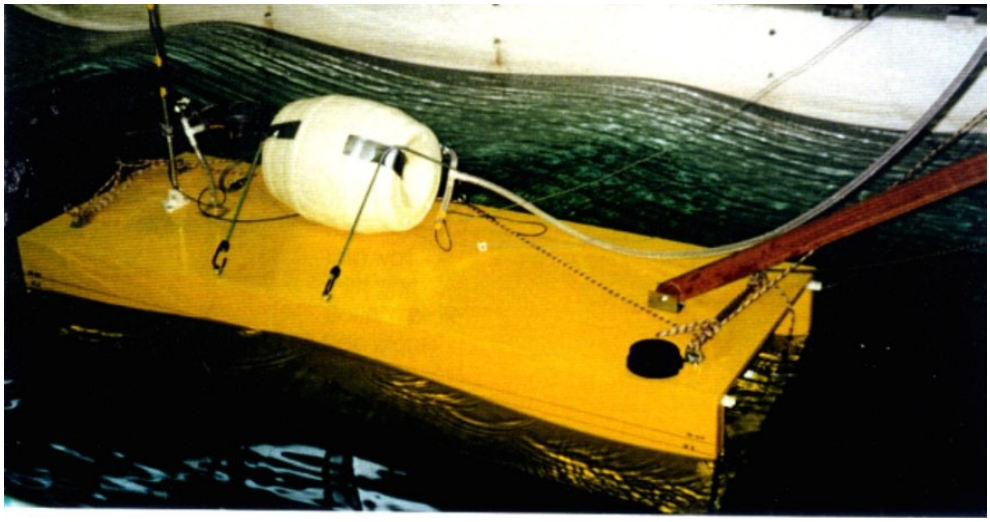

Figure 3.10, Image of the proof of concept physical modelling.

The testing concluded that:

- Implementing a PTO simulator comprising a non-return valve and pressure accumulator was challenging and added a significant degree of uncertainty to the performance results. Alternative PTO methods should be investigated particularly for small scale tests.
- Different duct geometries were trialled and it was found that the geometry could be altered to tune it to the wave climate.
- Results suggested that an optimum freeboard level was achievable to obtain a balance between sealing performance and maximum air flow
- The results from these tests were used to calibrate a theoretical model which was developed in parallel with the physical modelling.

The outcomes of the project formed the basis of the second project which included the testing of a much larger scale device.

3.3.2 Theoretical Modelling

A simple mathematical model was developed alongside the physical testing and was used to model the energy conversion process within a 2D geometry. The model calculated the wave height at the duct entry and the resulting volume of air captured within the duct. It was then assumed that all of the trapped air would be compressed by the wave, causing it to pass out through a non-return valve to a pressure accumulator. It was further assumed that the entirety of the wave energy captured by the duct was converted to pneumatic energy in an isothermal process; both of these assumptions were incorrect and are the likely reason for the large discrepancies between the physical and numerical test results. An overview of the processes modelled is given in the diagram in Figure 3.11.

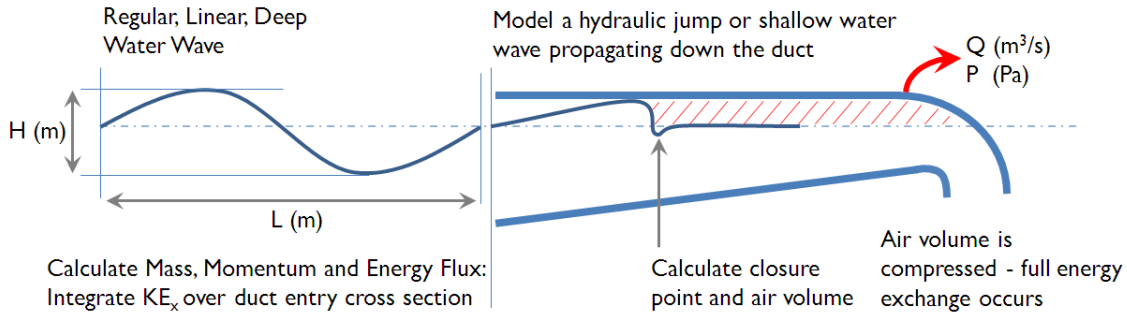

Figure 3.11, An overview of the processes modelled by the mathematical model.

In comparison to the experimental results, the model predicted pressures between 10 % and 100 % greater than those measured. The results from the theoretical investigation are limited and had few conclusions. It was however recommended that;

- the device be operated with a large draught to capture maximum wave energy
- in-depth investigations be carried out into the flow processes involved in wave sealing
- a general improved knowledge be gained before conducting larger scale testing.

Despite these recommendations being made by both components of this phase of testing, no additional investigations were made before proceeding to the much larger scale device a few years later. A successful application by OWEL for funding from the Carbon Trust was based upon the results of this initial proof of concept study.

3.3.3 Intermediate Scale Physical Modelling

A Carbon Trust grant was awarded in 2003 to test a much larger 1:10 scale model both physically and computationally using Computation Fluid Dynamics (CFD).

The model was constructed from steel and was mounted statically in the National Renewable Energy Centre (Narec) wave tank. These tests were very similar in terms of objectives, to the 1:100 study;

- Compare scaled up performance with the previous '1:100' results.
- Geometric optimisation of side wall angle, floor angle, baffle and a remedial modification to the duct entrance.
- Provide data to calibrate and validate theoretical model

The image in Figure 3.12 shows the 1:10 scale model under test in the Narec wave tank.

Figure 3.12, The 1:10 OWEL model under test in the wave tank at Narec in 2003.

Typically most conversion efficiencies reported were less than 30 %. The size of the model tested was too large for the facility and it blocked more than 70 % of the width of the tank. Furthermore, issues with the non-return valve and pressure accumulator brought about uncertainties.

In summary, the results from this testing programme provided little reliable evidence to demonstrate the performance of OWEL and examine the relationships of the parameters that were studied. Furthermore, no realistic conditions were simulated; both the use of irregular sea states and a floating device were neglected.

3.3.4 Preliminary CFD Modelling

Following the physical testing at Narec, the commercial CFD solver ANSYS® CFX 5™ was used in the development of a multiphase, transient model to simulate the tests conducted at Narec and provide scaling predictions.

The model only incorporated the geometry of the duct and not the fluid domain of the wave tank; waves were therefore generated at the boundary located at the duct entrance.

An example of the graphical results generated by the CFD modelling is provided by Figure 3.13.

Figure 3.13, An example of a 1:10 scale CFD simulation showing the water volume fraction of a wave propagating along the duct.

Generation of useful results from the CFD model was hindered by the poor computational resource available and the omission of key physical processes. Limited information exists regarding the CFD testing work package of the project, whether in reports or stored computational data. It is therefore challenging to draw any firm conclusions from it or learn lessons from the methodology

Nevertheless, the CFD model provides the basis for the development of a more thorough model and was identified as having the potential to be used to create the initial stages of a model that takes into account the limitations of the original simulations.

3.4 Physical Modelling of Oscillating Water Columns

3.4.1 Introduction

Of the many wave energy conversion methods that are in existence, the Oscillating Water Column (OWC) is the most studied. Despite this, few full scale devices have been constructed or deployed. The conversion principle is most synonymous with that of the OWEL method and so it is particularly relevant to review their historic development in order to determine similarities and learn from past experience.

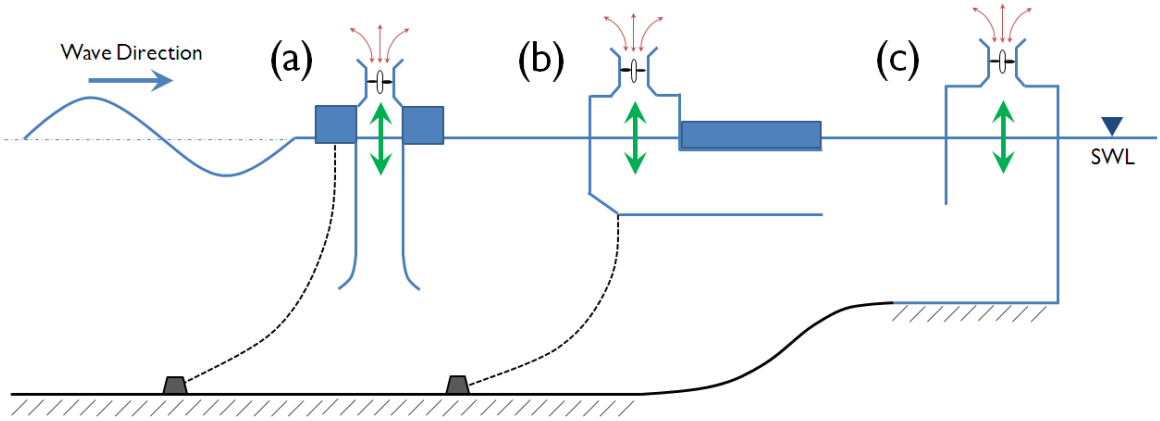

Figure 3.14, Schematic of the three main floating and static OWC types; (a) Floating Spar Buoy OWC, (b) Backward Bent Duct Buoy (BBDB), (c) Shoreline, static, terminator OWC.

This section provides a review of the physical modelling studies of OWCs that have been conducted over the past 40 years. Attention is given to the experimental methodology and conclusions that are relevant in the development of OWEL and how these can be used to inform the physical modelling studies in this EngD. Two categories of OWC are considered; static and floating devices and the schematics of each are shown in Figure 3.14. Static, fixed devices share fewer similarities with OWEL than their floating counterparts and so the focus of this review is biased towards floating OWCs. However, there has been far greater, in-depth research conducted using static models than floating models. The simplicity and practicality of static OWCs has always placed them in favour over floating devices which inherently have far more challenges to overcome to provide reasonable performance. Few academic studies on floating OWCs have been published and any information available is typically limited due to the commercial sensitivity of the investigations.

Whilst the majority of this review is dedicated to the small scale, laboratory testing of OWCs, a topic directly applicable to this research, a number of related lessons can be learnt from full and large scale deployments of these devices. Comment on these instances is made where relevant conclusions can be beneficial to the development of OWEL.

3.4.2 Static Structures

The static, shoreline OWC was first put into practice by Bouchaux-Praceique in France during 1910 and was described by Palme (1920) as a vertical cavity in a cliff face, with an opening below the waterline and an air exit to a turbine. Although this was the first static OWC, there was little research into static devices until the 1980s. In the interim however, much work was carried out on floating buoy OWCs as described in the subsequent section 3.4.3. Static structure OWCs are typically of the terminator configuration as in Figure 3.14(c), with the chamber opening facing the incident waves and the device constructed in a shallow water, shoreline setting. The early static OWCs were often incorporated into rocky shorelines such as those in Norway [Falnes (1992)] and Islay [Whittaker (1997)]. These pioneering devices with their unique challenges, sparked much research enthusiasm for the technology and numerous experimental studies ensued.

The seminal paper reporting on the physical modelling of static OWCs was presented by Maeda *et al.* (1985). This provided some initial, fundamental observations regarding the operating principle and performance characteristics. The first extensive physical studies into OWCs were carried out by Sarmento (1992). This work was primarily aimed at validating the earlier oscillating surface pressure theories provided by Sarmento and Falcão (1985), see section 7.5.2,

which was based on previous models by Evans (1978), Evans (1982). One consequence of studying the physical application of linear theories was that the majority of waves tested were of small amplitude, in comparison to their length, in order to ensure linearity. As the theory developed by Sarmento and Falcão (1978) was able to include non-linear terms to represent non-linear PTO pressure, flow rate relationships, both non-linear and linear PTO simulators were modelled in the experiments, see section 3.6 for further information. The various PTO simulators were calibrated in a wind tunnel in order to check their pressure drop characteristics and to determine the associated coefficients. The wave-to-pneumatic efficiency (η) of these models was determined by an average of the product of the air volume flow rate and pressure drop across the PTO over each wave cycle as defined in equation [11] from Sarmento (1992).

$$\eta = \frac{1}{P_i}\frac{1}{T}\int_0^T q(t)\Delta p(t)dt \qquad [11]$$

η is the wave-to-pneumatic efficiency, P_i is the incident wave power [W], T is the wave period [s], $q(t)$ is the air volume flow rate through the orifice [m^3/s] and $\Delta p(t)$ is the pressure drop across the orifice [Pa].

By measuring the transmitted, incident and reflected wave trains and knowing the pneumatic power developed, an energy balance was calculated for given wave conditions. The remaining energy that could not be accounted for in the transmitted or reflected waves and pneumatic power was attributed to viscous losses from effects such as vortex shedding off the model geometry. This was typically of the order of 5 – 10 % of the incident wave energy and was a likely result of the simple, un-optimised geometry. In the study, two OWC shapes were tested; a symmetric chamber protruding slightly into the water and an asymmetric geometry with a rear wall extending down to the floor of the wave flume. From linear, OWC theory by Evans (1982) the maximum efficiency of the symmetric device is 0.5 whereas the asymmetric device, acting as a terminator, has a theoretical maximum efficiency of 1.0. These values were closely approached by the results and performance data for all the configurations tested agreed relatively well with the simple theory. For these specific examples, this provided good validation for the theory despite the limitations and assumptions imposed.

The first large scale OWC in the UK was proposed and developed by Whittaker (1993) in the late 1980s. During 1987, construction began on a shoreline device on the Scottish island of Islay. Over the two years following the completion of the collector, the power conversion was monitored using an orifice plate arrangement. The plant was fully commissioned in 1991 and featured an early Wells turbine and generator rated at 75 kW. A number of issues with this device were reported [Whittaker *et al.* (1997)] which resulted in significant losses within the system and subsequently, a poor overall power output. To save costs, the column was

constructed within a gully and the back wall was the natural rock face of the cliff. Large hydraulic losses within chamber were reported as a result of the roughness of the natural rock of the back wall. Of the wave energy that was converted to pneumatic energy, the resulting breakdown of the energy and typical associated losses was given as follows:

Power Output (32 %) - electricity delivered to the grid.
Mechanical Losses (23 %) - energy dissipated in flywheel storage.
Swirl Energy (20 %) - rotational component of kinetic energy imparted by the blades on the air.
Residual Kinetic Energy (13 %) - energy in the exiting air flow not converted by the turbine.
Pressure Losses (5 %) - energy loss due to flow separation in regions of high pressure gradient.
Aerofoil Drag (4 %) - the energy required to overcome the drag of the rotating blades.
Electrical Losses (3 %) - energy dissipated as heat and leakage within the electrical system.

Further to these losses, in cases of energetic seas, the proportion of aerodynamic losses significantly increased as the blades of the Wells turbine stalled. This is a typical limitation of the Wells turbine and is discussed in further detail in Appendix A2.3.1. A flow visualisation study by Müller and J.T. Whittaker (1995) investigated a 1:36 scale, Islay OWC geometry using a series of photographic stills to track particle motions. Müller presented a sequence of images across a complete cycle of the OWC to demonstrate the formation of vortices around the lip of the front wall. This showed that at points within the cycle, up to 50 % of the inlet area was 'blocked' by the vortex shed. The vortex interfered with the in and out flow of the column and reduced the effective entry width as well as dissipating kinetic energy within the flow. The experiments also showed other flow features such as uneven chamber filling and internal chamber waves that were detrimental to efficient energy conversion.

A particular limitation of experimental investigations is the modelling of these viscous, turbulent and hydrodynamic losses: the geometry and fluid conform to two different scaling similitudes meaning that one is adhered to but the other neglected. These "scale effects" become more significant as the model size is reduced and so is an important phenomenon to consider when performing scale experiments. Another consequence of this scaling imbalance is that losses scaled up from the small scale experiments under predict those experienced with a full scale device. Effects of scale were reported by Whittaker (1997) from the development of the Islay OWC. It was observed that, when scaling the PTO applied damping from laboratory to full scale, consideration should be given as to the full scale Reynolds number. The turbine for the Islay device was sized using the model scale Reynolds number ($1.5x10^5$) rather than the much larger full scale equivalent (2×10^6). This led to the turbine for the full scale device being incorrectly specified and over damping the column. The issue of scale effects and issues arising

from not maintaining scaling similitude is discussed further in section 3.5. Further to this, Raghunathan *et al.* (1995) reported that non uniform flow and airflow losses into the turbine, significantly reduced the performance of the PTO and so the discrepancies between predicted and measured power were large.

During 1998, the team that pioneered the first UK shoreline OWC began the development of another shoreline device called LIMPET (Land Installed Marine Powered Energy Transformer). This was installed at a site close to the original installation on Islay and was commissioned in 2001. The LIMPET project was supported by significant funding from the DTI, and as a result, comprehensive reports detailing the physical modelling and development of the device are publically available. Whilst the OWEL WEC shares few similarities with the static LIMPET OWC, a number of experimental observations and methodologies are worth noting. It was reported by Whittaker *et al.* (2004) that the electrical output of the device was lower than 60 kW, whereas the plant had been rated at 500 kW, indicating a large discrepancy between the generated production and the anticipated output. This was primarily attributed to a 45 % overestimation of the wave power entering the gully the device was constructed within. This was coupled with the fact that the 500 kW PTO rating was so much higher than the actual output and this led to low capacity factors. The electrical system therefore, typically operated at about 10 – 20 % of its rated power, leading to reduction in efficiency and poor performance [Whittaker *et al.* (2004)]. In hindsight, it would have been better to have rated the plant at a value much closer to that of the realisable power in order to maximise the conversion efficiency. In addition to the over rating of the PTO, the performance of the novel counter rotating Wells turbine design was significantly lower than predicted by theory and model tests [Folley and Whittaker (2005)], see Appendix A2.3.1.

Retrospective small scale physical modelling of the LIMPET OWC was carried out following the commissioning of the device. A series of tank 2D and 3D wave tank testing was carried out with a small, 1:40 scale model [Wavegen (2002)]. These studies were used to determine the causes of the reduced performance of the plant as well as investigating the generic influence of geometric parameters on conversion performance. Geometric optimisation was predominantly carried out within the narrow, 2D flume whilst investigations examining the performance of the model in irregular and directional seas were conducted in the 3D wave basin. A comparison of results between the two facilities proved the validity of using the small wave tank for rapid prototyping however, it was noted that care must be taken to consider the methods and check this validity. This would not be the case for free floating WECs due to the influence of the tank side walls on the floating dynamics. It was found, in the irregular 3D tests, that the directional spread of the sea reduced power capture in all instances but this was not greater than a 15 %

reduction in output. A directional spread of 15° was used and therefore the power capture could reduce for seas with greater directionality. It is likely though, that due to the shallow water deployment of the device, the seas that are encountered are relatively unidirectional due to the effects of shoaling.

The shallow water losses due to the actual seabed bathymetry being different to the assumed profile prior to installation were demonstrated by Whittaker *et al.* (2004). This highlighted the detrimental attenuation of wave power in shallow water, particularly with larger sea states. Observations by Folley and Whittaker (2002) showed that the reduced water depth resulted in water particle motion being predominantly horizontal, leading to a large amount of run up on the front, sloped wall of the chamber. As the water ran back down the wall it interacted with the water exiting the column and restricted its progression, thus limiting the displacement of the outstroke of the column. It was claimed by Whittaker *et al.* (2004) that the retrospective small scale modelling showed that the original laboratory testing had not been at fault in the over prediction of performance.

A number of important conclusions were made from the experiences obtained in the development of the LIMPET device. These included the necessity for accurate scale modelling including the correct bathymetry and surrounding coastline features; a better understanding of the exit losses from the turbine; knowledge of the fluid motion within the chamber that could be detrimental to the resonance of the column; and the need for robust system integration. A further conclusion was that the PTO of a WEC should be carefully rated prior to deployment, based upon realisable and exploitable wave power resource data. This is to ensure that a device operates at powers close to that of the rated power in order for high capacity factors to be achieved and losses in the electrical systems minimised.

3.4.3 Floating Structures

The first ocean deployed OWCs were the floating, navigation light buoys developed for the Japanese market by Masuda from around 1965 onwards [Masuda (1971)]. These early buoys were low rated in power but their simplicity and functionality led to over 1,000 devices being deployed. McCormick provided the first empirically based, theoretical analysis of Masuda's buoy and suggested that peak power conversion occurred at two frequencies corresponding to the natural period of the buoy-water column system and resonant period of the central pipe [McCormick (1974a), McCormick (1974b)]. The first experimental studies of these floating devices was reported in McCormick *et al.* (1975) and was used as to compare and improve the linear theories developed in McCormick (1976). The conclusions from these initial

investigations were of limited applicability however, they did highlight key parameters important in the conversion process within an OWC, such as the system damping and water column length.

The activity and interest in OWCs in Japan was further increased in 1976 as Masuda led the design and deployment of the 80m long, OWC barge, *Kaimei* which initially featured 22, vertical chambers. In later tests the number of chambers was reduced to 8 and these were fitted with a range of turbine PTOs including an early Wells turbine, a McCormick turbine and valve rectified, impulse turbines, see Appendix A1.3, [Charlier and Justus (1993)]. Two separate ocean deployments of *Kaimei* occurred; these concluded that the average wave-to-wire conversion efficiency was ~4 %, with peak performance occurring at wavelengths similar to the barge length [Seymour (1992)]. The low efficiencies were attributed to air chamber losses and excessive heave motions of the barge due to its relatively short length in comparison to the incident wavelength. As the barge was moored in parallel to the predominant wave direction, it is likely that the peak performance coincided with the lowest heave excursion, i.e. where wavelength is the same or less than the device length so that multiple wave crests reduce the floating motions. In addition to the issues of heave, the rudimentary turbines are likely to have had poor aerodynamic efficiencies, although Masuda *et al.* (1987) reported this to be "relatively good", and also the losses associated with the valve, air rectifying arrangements would have been significant.

The particular issue that was experienced with *Kaimei* is common to all floating OWCs with a vertical chamber as the diagram in Figure 3.14(a). It is necessary to ensure that the floating body, heave dynamics of the converter are not in phase with the motion of the water column, otherwise their relative velocities reduce to zero. This can be tackled a number of different ways; the device can be massive, so that it has significant inertia to resist motion; the device can be tension moored; the naval architecture can be optimised by having little reserve buoyancy above the still water line, thus reducing heave response or alternatively damping plates can be attached to provide a drag force to oppose displacement.

Following on from the lessons learnt with the *Kaimei*, Masuda *et al.* (1987) developed an alternative design for a floating OWC that did not require the modifications to the vertical chamber, spar buoy type design; this was named the Backwards Bent Duct Buoy (BBDB). A schematic representation of this design is given in Figure 3.14(b). Unlike terminator type, static OWCs with their forward facing entry or bottom entry, floating spar buoy OWCs the BBDB design has an entry that faces away from the wave direction. Initially, a forward facing design was studied but it was found that the backwards facing entry benefitted power capture by an

average factor of 3 [Masuda *et al.* (1987)]. This also had the effect of reducing the drag of the device, which was a convenient feature as it was originally intended for deployment in areas with high tidal currents. The nature of this design inherently means that the device 'weathervanes' so that the duct opening faces away from the incident waves. Another beneficial feature is that the draft of the hull is small in comparison to that of a spar buoy OWC with the same effective water column length. The operating principle of the BBDB makes use of the wave kinematics and vessel dynamics in addition to the potential head due to the free surface elevation. As the device heaves in a wave crest, the hull rises but, unlike the spar buoy design, it entrains the water column which is 'connected' to the water at a distance ahead of the wave crest. This effective difference in phase in the forcing of the water column means that the vertical motion of the internal water free surface and the vessel heave motion are not synchronous.

The preliminary laboratory studies of the device found that the hydrodynamic performance of the concept was of the order of a factor of 10 better than that of *Kaimei*. As the commercial opportunity viewed by Masuda was the deployment of the BBDB for navigation buoys, as had been done previously, large models were tested in ocean basins and electrical output from them was measured. The devices were then deployed at sea, where they were tested and successfully used as navigation light buoys [Masuda *et al.* (1988), Masuda (1991)]. Further experimental studies were carried out by McCormick and Sheehan (1992) which investigated the behaviour of the device to drift towards the incident waves in certain wave periods. This was attributed to the momentum imparted by the oscillating water column to the bow of the device as the water turns through 90°.

The majority of the early tests with the BBDB were conducted in purely regular waves. Masuda *et al.* (2002) later reported that the pneumatic output of the small scale BBDB model halved when tested in an irregular sea of similar properties to the regular tests. Nevertheless, hydraulic efficiencies of up to 100 % were reported throughout the studies. This is a surprising result but it could have been a result of the motions enhancing and absorbing power from waves beyond its physical capture width. Following on from the initial development of the device concept by Masuda and the Japanese Marine Science and Technology Centre (JAMSTEC), an Irish company called Ocean Energy Limited took on the commercial development of the design, named OE Buoy. Laboratory testing of the device occurred at 1:50 and 1:15 scale before a 1:4 device was constructed and deployed at the benign test site at Galway Bay in Ireland. Forestier *et al.* (2007) provide a discussion on the choice of materials used in the construction in each of the models in order to achieve scale similitudes between them and the large scale device. As the scale of the model is increased the required precision for characteristics such as mass and

buoyancy distribution reduces. Small scale devices, such as the one at 1:50, are extremely sensitive to slight changes in mass and buoyancy arrangement and so care must be taken to ensure that these are recorded and realistic to what is actually achievable at full scale. Forestier *et al.* (2007) also reports on the use of orifice plates as a PTO simulator through all scales of OE Buoy tested and these observations are discussed further in section 3.6. Sheng *et al.* (2010) carried out additional physical investigations on the same 1:50 scale OE Buoy model in a large wave basin. The predominant focus of the work was to study the hydrodynamic characteristics and mooring loads of the small scale model. In the testing, the model was sealed at the open chamber end so that its chamber contained the same volume of water as at rest but that this water could not pass out of or into the device. This modification was intended as a simplifying assumption to make the device more ship-like. It is likely however that this would have significantly impacted on the vessel dynamics due to the internal sloshing of the entrained water. This affect is apparent in the large difference between the observed natural pitch period of the ship-like model (1.05 s) and the scaled down natural pitch period of the large scale device (~5 s).

Physical testing on a two dimensional, BBDB geometry by Suzuki *et al.* (2011) demonstrated the advantageous performance characteristics of the BBDB, such that peak performance occurs at a wavelength to device length ratio of nearly 4. A relatively modest device size is therefore required in order to match a typical design wave for an offshore site of approximately L=100m [Smith *et al.* (2011)]. From the testing by Suzuki *et al.* (2011), a large scale device was designed with a length of 25m and deployed offshore in India. As yet, comparisons between the small scale and large scale devices have not been made as the majority of the work focused on the installed, uni-directional impulse turbine PTO [Prasad *et al.* (2011)]. The hydraulic performance of the device has not been reported in detail, but the results suggest peak values of up to ~60 %. It will be interesting to compare the differences between the two extremes of scale as very few published studies have presented this type of comparison. That said, a recent set of experiments by Imai *et al.* (2011) compared a small scale BBDB model and one of three times the size. The initial small scale model was tested in "2D" and "3D" conditions, meaning wave flumes of different width; 1.03*beam and 6.4*beam. The narrow flume conditions resulted in approximately half of the peak conversion efficiency at ~ 70 %, slightly reduced pitch amplitude and a significantly smaller heave response. As could be expected, due to high blockage, the surge of the model in the narrow flume was greater than for the wide tank. The peak performance of the small model in the wide tank exceeded 100%. This was attributed to "wave diffraction from the corners of the device", however, uni-directional, regular waves are unlikely to contribute such a marked difference in performance. Without further knowledge of the testing methodology it is hard to comment on the definite reasons, however, the larger pitch

and heave response of the model in the wider tank are likely to have been additional contributing factors on the conversion performance. Comparison between static model performance in the two facilities would perhaps have highlighted the key reasons. This result does, however, highlight the need for care when selecting the type of facility for testing wave energy devices, particularly with dynamic, floating models.

A device three times larger than the small model was constructed and tested in the same wave flume facility that was used for the "3D" tests and so the ratio of channel width to model beam became ~2.1 meaning the conditions approached those of the 2D tests. Although this was a relatively small model, a 0.25 m diameter impulse turbine with guide vanes was used as the PTO in conjunction with a small generator attached to a resistive load. Prior to installing the turbine PTO, the device was tested in regular waves with an orifice size scaled from that of the small model. Hydraulic performance of the device was similar to that of the small 2D model with peak performance being of approximately the same magnitude (~70 %) and wave period (L/L_D = 4). Conversion efficiency in shorter waves, below L/L_D = 3, was significantly reduced however, this could have been due to the dissimilar moment of inertia between the different sized models, which was not scaled correctly with the geometry. Nevertheless, over the limited range of wave periods tested the performance was similar enough to suggest that a change in scale by a factor of three did not result in appreciably different efficiency. The subsequent inclusion of the small impulse turbine led to combined total efficiencies (hydraulic-to-electrical) of less than half of the hydraulic efficiency. The authors did state however, that the turbine had not been correctly matched to the device or wave conditions and so the results were preliminary.

Returning to the historic development of wave energy in Japan; despite the favourable performance of the BBDB device, proved by Masuda, JAMSTEC opted for a more conventional OWC arrangement for their successor to the *Kamei*. The large scale, 50 m long, prototype device, called the "*Mighty Whale*" was deployed off the Japanese coast. It featured a forward facing entry, shaped much like the static, shoreline devices. Washio *et al.* (2001) reported that peak hydrodynamic performance of the large scale device occurred at the same scaled period as that of the laboratory model but its magnitude was ~40% lower and consequently the output of the device was far less than anticipated. No discussion as to why the discrepancy between the two results was given and information on the wave tank experiments does not appear to have been published in English. It is therefore challenging to understand why such a large difference existed; it may have been due to incorrect small scale, experimental methodology meaning the similitude between the two OWCs was not the same; alternatively, poor full scale PTO design could have led to vastly over or under damping the column leading to reduction in the efficiency of the OWC; compressibility effects would have had some impact in over predicting

performance at small scale but it is unlikely to account for the whole difference. The full scale, wave-to-wire efficiency of the device peaked at around 15 % for waves with $T = 7$ s but reduced below 10 % for wave periods longer than 8 seconds. A novel feature of the device was that the Wells turbines were connected to two differently rated generators. The selection of the operational generator was electronically controlled in order to select the appropriately rated generator for the shaft power developed by the turbine in different wave conditions. This is beneficial to power production as it reduces the generator losses and increases the capacity factor, as well as providing some system redundancy. The downsides to this feature would be the additional cost of the second generator and the increased complexity of the PTO system with higher risk of failure.

In the UK, the development of floating OWCs has only really focused on one particular device concept: This was a Multi Oscillating Water Column (MOWC) device called Sperboy and was conceived to increase the conversion efficiency bandwidth of a typical OWC. Each of the water columns in the device were contained within tubes of differing length and therefore tuned to different natural periods. At the start of 2001 a 1:5 scale device was installed south of Plymouth Sound to begin sea trials [Johnson *et al.* (2003)]. The Sperboy device was purposefully designed so that it self-limited its power production to avoid over loading the turbine, generator or moorings. This was accomplished by making it relatively free in heave. Although semi-tension moorings were used, the device had little heave in short waves below 3.5 s however, in waves longer than this the heave RAO of the buoy was greater than or equal to 1. Therefore, despite high input wave power, the low conversion efficiency in these waves due to the zero relative difference between internal and external water levels, electrical power output was low. Despite using only a semi-tensioned mooring system rather than a fully tensioned arrangement to restrict heave, and thus incurring higher loads, the device broke all four of its moorings and ran aground shortly after being deployed. Little was concluded from the test, however, the main lesson learned was that the mooring system for these types of devices would require more careful design in future studies.

The subsequent, commercial development of the Sperboy MOWC configuration was undertaken by ORECON who began work on a modified design of the device that featured three differently sized OWC chambers. Similarly to Sperboy, the ORECON design was a floating device with three differently sized columns. The front two vertical chambers had an opening at their base and the larger rear chamber employing a wave focusing back wall and floor so that its opening was directed towards the incident wave field. It is likely that greatest challenge for this device, as had been proven previously with the Kaimei and Sperboy deployments, would have been to control the heave motions in order to maximise the internal free surface displacement.

ORECON chose to counteract heave by designing a fully tensioned mooring [Street (2009)] so that the device would be tautly attached to the seabed and anchors. This approach can be extremely costly in comparison to other mooring methods, simply because of the huge dynamic and buoyant forces it is required to withstand. Despite obtaining significant private investment for the project, ORECON could not deliver the project and the company was eventually dissolved. A significant contributing factor to this demise is very likely to have been the technical logistics associated with the moorings and control of heave. Due to the commercial nature of the project, little development data was ever made publically available and so no specific lessons can be learnt from their shortcomings. Gervelas *et al.* (2011) published some early stage, preliminary work on creating a 1D theoretical model of the device, investigating its performance in irregular seas and comparing the results to experimental models. Whilst this rudimentary, simplified model did produce some results that were comparable to the physical experiments, these were limited to small amplitude, linear conditions with a static, idealised geometry and so would not be applicable for use as a design tool.

Despite all of the issues associated with vertical chamber, floating OWCs and previous failures a company, called Oceanlinx, is maintaining the development of such a device. Their work has spanned nearly a decade of research and has encompassed three large-scale ocean deployments; development of a novel, bi-directional turbine; CFD modelling and a series of physical model testing studies. Unfortunately however, similarly to ORECON, the commercial sensitivity of their work has meant that little detailed information has been publicised. It is apparent from the publically available photographs of their deployed devices [Hunter (2011)], that they have considered different arrangements of their OWC geometry. The initial device design was intended to be a floating structure, deployed in near-shore, shallow water with a 12 point mooring system. Small scale tank testing however, showed this design to have significant heave motion that compromised the OWC's performance. The design was then modified so that it was semi fixed, resting on four legs with a series of pre-tensioned mooring chains to restrict horizontal motions. The device featured two novel components; a bi-directional Dennis-Auld turbine, as an alternative to a Wells type, see Appendix A2.3.1, a parabolic wall behind the chamber in order to focus the wave crests into the device, this however, has not been featured on subsequent designs and so can be assumed to not be beneficial in practice. Following the early full scale device, Oceanlinx deployed two 1:3 scale floating structures: The first of these was a single chamber OWC with a pyramid shaped roof. A turbine was not included on this device and instead, the PTO was represented by a simple orifice plate [Hunter (2011)]. From photographs in Hunter (2011) it can be seen that the associated issues of heave were counteracted by large heave plates, with a total area of the same order as the chamber cross section. The artist's impression graphics provided in Hunter (2011) show a future, single

chamber device based on this 1:3 version, however, the heave plates are replaced by four tension moorings and gravity anchors, suggesting the ineffectiveness of the heave plates. For their second prototype, 1:3 scale device, the focus of the design was switched from a single unit to an array of eight chambers combined in one, large floating structure. This approach is likely to have reduced the motions of the device by making the structure large in comparison to the wavelength, whilst reducing the device £/MW by increasing the electrical output from the multiple units. Of the eight OWC chambers, six were fitted with orifice PTO simulators, one with a Dennis-Auld type turbine and one with a Dresser-Rand, HydroAir™, impulse turbine, see Appendix A2.3.2. Unfortunately though, a storm greater than the 100 year return event occurred, causing the moorings for the device to fail and the structure broke free and sank in shallow water. The photos in Hunter (2011) can be used to estimate the beam of the device which is approximately 9 m, therefore, at full scale each chamber would be ~13.5 m wide. The predicted full scale, rated output is 2.5 MW from 8 chambers which equates to just over 300 kW per OWC and a combined device mass of 2,000 tonnes. This would suggest that the predicted rating would be rather optimistic even by assuming an optimistic wave resource of ~40 kW/m, unless the expected typical wave-to-wire efficiencies were considerably higher than similar devices (20 – 40 % [Babarit *et al.* (2012)]) or that the device would operate at a low capacity factor.

It can be seen from these three examples that the mooring design for floating OWCs is not a trivial task. This is true for any WEC that requires the moorings to provide a large restoring force to oppose motion. To date, few wave energy devices have been deployed for significant periods of time, and even some of those that have, such as Wave Dragon [Tedd *et al.* (2007)], have suffered mooring failures. It is therefore likely that these unfortunate disasters will be witnessed again in the future.

3.5 Effects of Scale

When developing wave energy devices, it is generally regarded best practice [Holmes (2009), Payne (2008), IEA-OES (2003)] to progress with models at an ever increasing scale from small scale, inexpensive, proof of concept models up toward near full scale, development models tested at benign sites. This not only provides a sensible pathway to the deployment of a full scale prototype, it gives crucial information regarding the effects of scale on the device performance. This highlights any issues that are overlooked when choosing the scaling criteria and provides greater confidence in the experimental results.

The concept of scaling similitudes and the theories behind them are presented in Appendix A2.1. It is mentioned that physical phenomena in any given domain, can be scaled by a correctly chosen scaling law. The choice of similitude to follow depends on the dominating effects and forces within the domain. For free surface, hydraulic models, this is typically Froude scaling as the inertial forces are, by far, the greatest. However, by scaling according to the Froude number the scale ratios governing other forces, arising from viscosity, elasticity and surface tension, for example, will not be the same between the small and full scale. The result of this incorrect similitude of forces is a discrepancy between the forces in the reduced scale and real-world scenario and these differences are known as scale effects. Heller (2011) provides a good account of the issues associated with scale effects and notes that, in hydraulic models, there will always be scale effects if the Froude ratio is conserved. The issue therefore, should be whether or not these adverse effects are significant in the scope of the experiments. Furthermore, the dissimilarity between prototype and model scale results will be exacerbated with increasing scale factor due to the growing severity of scale effects.

For the majority of wave energy converters, the key limitation of maintaining Froude similitude is that Reynolds similarity is not met, unless of course the gravitational acceleration or kinematic viscosity of the fluid is altered [Payne (2008)]. This leads to the incorrect scaling of all velocity related effects within the hydrodynamic and pneumatic flows. As Knott and Mackley (1980) showed, viscous losses will occur in smaller waves at the full scale than scaled down Froude conditions, which leads to scale models providing conservative estimations of energy loss. Forestier *et al.* (2007) provides a comparative account of testing the OE Buoy, OWC device at three different scales in conditions from laboratory to sea trials. The examples given demonstrate that as scale is reduced and viscous forces become more significant in comparison to inertial effects, power prediction from small scale models may be slightly pessimistic. Additionally, viscous damping effects on vessel dynamics can be more pronounced at the small scale which can lead to the under prediction of response amplitudes of the prototype. This will particularly be the case for WECs with complex submerged geometries and large wetted surfaces. A further issue of testing at small scales is that, when following Froude, power scales with $X^{3.5}$ as shown in Appendix A2.1.2, Table A2.1. Therefore, modelling a full scale PTO of 500 kW at 1:50 scale implies that the small scale power that could be expected is just greater than 0.5 W. This is a low energy flux and so any losses that are incorrectly modelled in the scaled system may result in drastic variations in the measured power. Consequently, at small scale, very slight changes in power output can equate to large changes in output at full scale.

Scale experiments with wave energy devices such as OWCs and OWEL, where both water and air are working fluids, have the added difficulty in that different forces dominate in the two fluid phases. The air flow within the device and PTO is governed by the viscous forces and so Reynolds similitude is necessary, whereas the water is governed by the inertial forces and so, as is the case with other WECs, maintaining the Froude number is necessary. For an ideal case, parameters associated with water are scaled by Froude and those associated with the air, such as air chamber volume and air ducting, are scaled according to Reynolds. In reality, this is not often practical and, as the inertial forces dominate the overall model dynamics, Froude scaling is used throughout which leads to phenomena within the air flow being neglected and incorrectly represented. A particular issue that has been observed and discussed in many scale experiments and models of OWCs is that of air compressibility and this is the subject of the following paragraphs.

Following purely Froude scaling when testing scale models of OWCs leads to the incorrect modelling of air compressibility as the air volume is dominated by compressive forces acting upon it. The effect of air compressibility on the behaviour of an OWC has been the subject of a number of theoretical studies: A 'mechanical', mathematical OWC model was created by Szumko (1989) and was an extension of the mass-spring-damper model first suggested by Evans (1978). This adapted model included an additional spring term to take account of the compressibility of air within a large scale chamber. It was observed that the simulated compressibility had little effect at the device's resonant period, however, at periods greater than resonance, the hydraulic efficiency was reduced in comparison to the model with no air compressibility. Conversely, for shorter periods, the performance was found to increase. These conclusions corroborated with the findings from another mass-spring-damper type model by Folley and Whittaker (2005). Both Folley and Whittaker (2005) and Szumko (1989), concluded that air compressibility at full scale reduces power capture. It was also concluded that the detrimental effects of compressibility increased with increasing air chamber volume. This result can be explained by the thermodynamic losses that will proportionally increase with an increase in air compressibility effects brought about by a larger chamber volume. In addition to reducing the pneumatic power available at the PTO, air compressibility may also modify system responses at large scale when compared with those at small scale. Short timescale events that may be witnessed as air pressure spikes in results from small scale tests will not occur at large scale. The apparent air flow time history at the PTO will therefore be smoother and not subject to sharp impulses during a conversion cycle.

A further effect of air compressibility at large scale, as noted by Forestier *et al.* (2007) is that the motions of floating OWCs may be modified and that it could alter the phase at which the

forcing due to the air pressure occurs. This cushioning effect within the air chamber would slightly delay the response of the structure to wave forcing in large scale conditions, whereas in small scale models where the compressibility is negligible, the air chamber would be stiffer, resulting in a more rapid response.

In the OWC theory developed by Sarmento and Falcão (1985), it was suggested that to account for air compressibility effects at small scale, the air chamber volume should be scaled with the scale factor squared rather than the scale factor cubed as dictated by Froude similitude. Subsequently, Sarmento (1992) also suggested that if the average chamber height (air volume divided by chamber water area) was less than 0.1 m, the effects of compressibility in that model would be negligible, however this may not be true.

Weber (2007) expands on the alternative scaling methods suggested by Sarmento and Falcão (1985) to provide a hybrid scaling similitude, non-dimensional number, that is the ratio of inertial and compressive forces.

$$\frac{F_{Inertia}}{F_{Compression}} = \frac{\rho U^2 L^2}{p_0 \kappa L^2} \qquad [12]$$

Where ρ is the density of water, U is a characteristic velocity, L is a characteristic length, p_0 is the initial air pressure and κ is the heat capacity ratio, for air under adiabatic conditions $\kappa = 1.4$ Weber (2007) states that in order to maintain this force ratio of F_i/F_c and also comply with Froude similitude, the condition of equation [13] must be satisfied when changing between scales.

$$\frac{\rho g L}{p_0 \kappa} = const. \qquad [13]$$

This is often impractical for scaled physical experiments. However, if the geometry responsible for the hydrodynamics of the device are scaled according to Froude, the geometry above the waterline, on which the air flow is dependent, can be modified to suit equation [13]. As originally suggested by Sarmento and Falcão (1985), by varying the effective chamber height, the magnitude of the compression force can be varied to maintain the Froude similitude as in equation [13]. In the work presented by Weber (2007) a small scale, simple OWC with a variable chamber volume was tested over a range of regular wave conditions. Additional air volume of up to 75 times the original chamber volume was included to show the variation in performance by altering the effective air chamber height whilst maintaining the original hydrodynamic related geometry. The results were compared to a theoretical model based on the approach taken by Evans and Porter (1997). Reasonable agreement of performance was observed for wave periods greater than the resonant period but due to limitations of incorrect

loss modelling in the theory, agreement was poor for short wave periods. Nevertheless, this did demonstrate the reduction in conversion efficiency for an increasing chamber volume. Weber subsequently developed a theoretical model of the shoreline OWC called "*Pico*" and ran the model for two geometries, one at full scale and one at 1:10 scale, over a representative, annual, Irish wave resource. The consequence in not correctly modelling the air compression in the 10^{th} scale model was that the equivalent full scale performance was over predicted by an average of approximately 10 %. The results from this study suggest that the scaling requirements for air compressibility can be satisfied by adjusting the OWC chamber volume with additional chamber volume as included in the experiments by Heath (2007). This however may bring about a number other undesirable aero and thermodynamic effects such as, dynamic pressure loss and vortex shedding due to additional ducting and expansions or contractions. Further to these effects, if additional chamber volume is to be incorporated on a floating model, additional inertia and damping will arise due to the connection of the dynamic model to the stationary additional volume. This may have significant impact on the floating motions and behaviour of the device and its implementation is likely to be unsuitable.

Physical modelling by Wavegen (2002) tested the performance of a small scale, LIMPET OWC geometry with and without additional air volumes. The increase in air volume of the scaled model increased the conversion efficiency for periods close to column resonance by up to 30 %. However, for longer wave periods, the additional volume reduced the efficiency by approximately 10 % in comparison to the Froude scaled model. This relationship, which is similar to that presented by Szumko (1989), was likened to a reduction in applied damping by the PTO simulator. Further to this, changes in the dynamics of the water column were also recorded in that the free surface vertical velocity for both the in and out strokes was greater when the additional volume was included. For the majority of the tests in the study, no additional air volume was included as it was deemed an unnecessary unknown that added complexity and uncertainty to the test results.

From the cases presented here, it can be concluded that air compressibility is a detrimental, physical effect present in OWCs and is therefore likely to be directly applicable to the performance of OWEL at full scale. Testing scaled, physical models of OWEL is also likely to be affected by compressibility, particularly that if it is not modelled correctly, performance predictions are likely to be optimistic and will incur greater errors with increasing scale factor.

3.6 Laboratory Scale Power Take-Off

To convert the energy within the airflow from a WEC such as an OWC or OWEL, into useful, shaft power, a turbine has to be employed. In OWCs the PTO methodology is complicated by the bidirectional airflow into and out of the device, from which energy is extracted through both halves of the cycle. The characteristics of the airflow dynamics in OWEL however, are rather different from that of an OWC. As OWEL utilises the forward moving wave crest to trap and drive the entrained air out of the device, the airflow is predominantly uni-directional as there is no return stroke in the cycle. For this reason, a uni-directional turbine will be required for the full scale OWEL PTO, rather than the bidirectional type turbines that have been conceived for use in OWCs. These types of turbine and their design characteristics are reviewed in appendix A2.3.

To model the complexity of a full scale turbine and generator at reduced scale is generally impractical and costly, although some studies have sought to do this [Imai *et al.* (2011), Jayashankar *et al.* (2009b)]. As discussed previously in section 3.5, the power associated with small scale models (i.e. 1:50) typically reduces towards the order of 1 W meaning that losses, such as friction in bearings of turbines for example, become a significant and dominating feature. Further to the low energy available, maintaining a Reynolds similitude in addition to the requirements of the Froude scaling is not feasible. Ideally, when using physical models to predict the energy productivity of a device, it is better to use as large a scale factor as possible, [Wavegen (2002)]. Typically therefore, full scale PTOs are simulated in small scale physical experiments by some means of flow restriction and a generation of a stagnation pressure drop to represent the energy extraction from a turbine. This impedance provided by the restriction and pressure drop applies damping to the air flow through it. In addition, the pressure drop across the simulator can be used to determine the air flow rate and the pneumatic power available for conversion.

The applied PTO damping, B_A , in conventional units for viscous damping coefficient (Ns.m^{-1}), has been previously defined by Curran *et al.* (1997) for an OWC as

$$B_A = \Delta p_0 \frac{A_C}{V_C} = \Delta p_0 \frac{{A_C}^2}{A_A V_A} \qquad [\text{Ns.m}^{-1}] \qquad [14]$$

Where Δp_0 is the stagnation pressure drop, A_C and A_A are the cross-sectional areas of the water column and turbine duct respectively, and V_C and V_A are the air velocities at the chamber and turbine duct. This however, is more easily applied to OWCs than the internal dynamics of OWEL, particularly if the velocities cannot be determined. A more convenient definition, being

directly applicable to OWEL, is provided by Wavegen (2002) and Tease *et al.* (2007) but is formulated in the unconventional units of Ns.m^{-5}

$$B_A = \frac{\Delta p_0}{Q} \qquad [\text{Ns.m}^{-5}] \qquad [15]$$

As per [14], Δp_0 is the stagnation pressure drop across the PTO and Q is the airflow rate. Regardless of the approach taken to characterising the applied damping of a PTO, as Curran *et al.* (1998) state, the ratio of the pressure drop and air flow rate strongly influence the damping ratio which couples the performance of the device and PTO.

Following Froude similitude the damping of a prototype scale PTO can be shown, through dimensional analysis, to be scaled down by a factor of

$$[N\ s\ m^{-5}] = [MLT^2 \cdot T \cdot L^{-5}] = [X^3 \cdot X^{0.5} \cdot X^{-5}] = X^{-1.5}$$

where X is the scale factor. This was applied by Delauré and Lewis (2003) in the modelling of an idealised 1:36 model of an OWC with a linear damping coefficient of 22,500 Ns.m^{-5} and a full scale equivalent, in a numerical model, of 104 Ns.m^{-5}.

Optimum applied turbine damping to maximise the power conversion and efficiency of an OWC can be found experimentally and an example of such is given in Figure 3.15. The graph, reproduced from work by Tease *et al.* (2007), shows the relationship between PTO damping and pneumatic power for a small scale model of the Mutriku breakwater OWC. The plotted curves show how the power converted by the OWC varies with applied system damping for a range of sea states with increasing incident power. These relationships demonstrate that the performance of an OWC can be sensitive to PTO damping and that the damping of the device should be optimised in order to maximise performance. Similar trends have been observed in other studies of OWCs [Koola *et al.* (1995), Curran *et al.* (1997), Wavegen (2003)] and as Figure 3.15 shows, it is typically better to provide too much damping to prevent a rapid decrease in pneumatic power if the system becomes under-damped. Further to this, setting a high level of damping results in high pressures and low amplitudes of motion, whereas the opposite is true for low PTO damping [Chaplin *et al.* (2012)]. In the case of an OWC, as mentioned in Wavegen (2003), excessive column motion due to under-damping leads to increased turbulent losses and eddy generation at the inlet. It can also be seen in Figure 3.15 that there is no single, unique value of optimum damping but rather a range of values that will lead to maximum power capture. The same is particularly true in the case of random, irregular seas, where an optimum damping selected from flow conditions arising in regular waves does not provide an optimum for all the waves in an individual sea state. In these instances, the PTO damping can be optimised to maximise the overall power capture in the sea state. In addition to maximising efficiency, the

Wavegen (2003) report suggests that the optimum damping should be determined for each geometric configuration of the model to ensure that any variation in power output is a result of changes to the geometry and not exacerbated by un-optimised PTO damping.

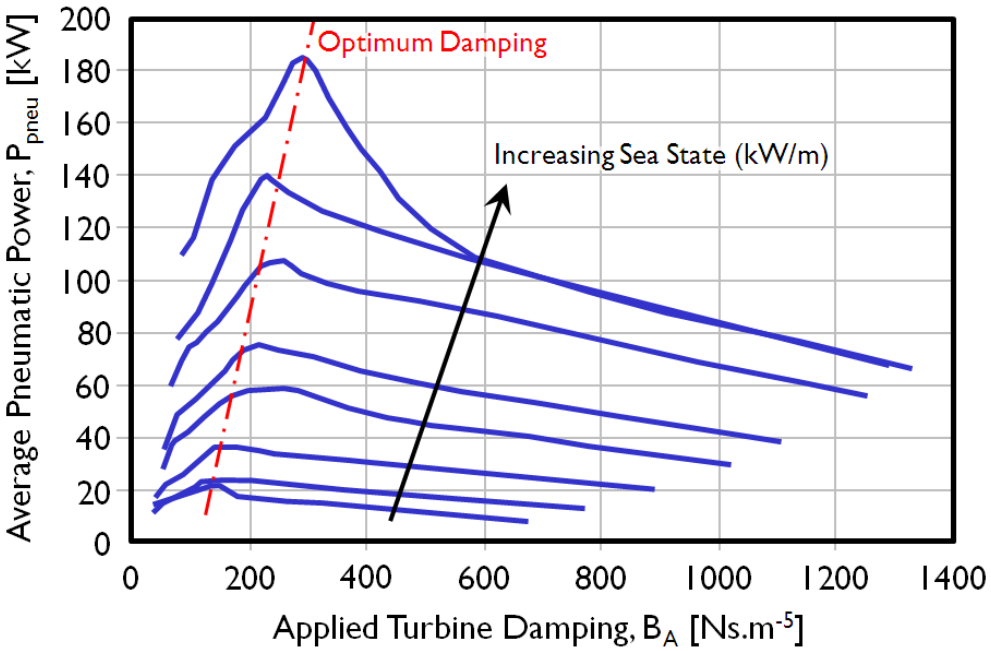

Figure 3.15. The relationship between pneumatic power and applied turbine damping in an OWC. Modified from Tease *et al.* (2007).

A consideration for PTO damping for the OWEL device is that large impedances will result in high pressures being developed within the duct and so could affect the characteristics of the wave sealing within the duct. This phenomenon was observed in the intermediate scale, Narec testing in section 3.3.3 and was deemed as "blowback". This occurred when the high impedance, non-return valve caused pressure to increase ahead of the wave front causing the seal with the duct roof to break and air to escape thus reducing performance.

Simplifying a PTO to a method for simulating the typical characteristics of a full scale system is common place when testing OWCs and WECs utilising air as their working, energy transfer fluid. Whilst Forestier *et al.* (2007) suggest that a simplified PTO should only be used in the preliminary testing stages, many devices have been damped using simple orifice plates even at large scale, ocean deployments [Whittaker (1997), O'Sullivan *et al.* (2010), Baghaei (2010), Camporeale *et al.* (2011)]. This is however, dependent on the scale chosen for the increased scale testing, the objectives of the testing and the budget available as well as consideration of the aforementioned scale effects. A number of different options are available to represent the PTO at small scales and these can be grouped into two main categories depending on whether the method has a linear or non-linear relationship of the pressure drop with the air flow rate. Simulators with a linear, $\Delta p/Q$, relationship are used to model bi-directional, Wells type

turbines. This is a particularly specific case as the majority of other air turbines suitable for WEC applications have a non-linear, $\Delta p/Q$, relationship. Non-linear dampers, such as orifice plates, therefore tend to be commonplace in the physical modelling of OWCs and air WECs. Linear damping methods have been developed for specific OWC applications where modelling Wells turbines with single damping ratios is necessary.

3.6.1 Non-linear Damping - Orifices

Perhaps the simplest method of simulating an air turbine PTO is an orifice within a pipe. Similarly to a Venturi operating on the Bernoulli principle, the escaping air is forced through the orifice and as it does so, the pressure upstream of the orifice increases due to the restriction and the velocity through it increases. The stagnation pressure drops due to the viscous losses associated with flow passing through the restriction. The typical flow characteristics for an orifice are shown by the streamlines drawn in Figure 3.16.

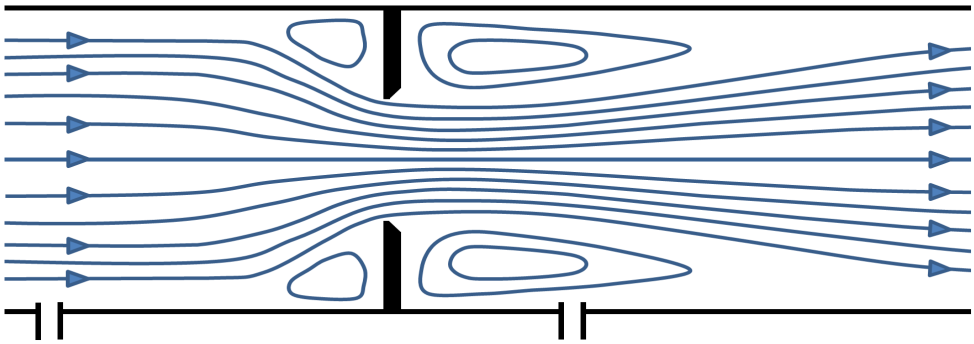

Figure 3.16, Typical airflow streamlines through an orifice plate, including the locations of the pressure measurement points.

Using Bernoulli's equation, the differential pressure drop across the plate can be used to determine the flow rate, Q, through the orifice and for this reason orifices have been used extensively as simple, fluid flow meters [Spencer (1982), Reader-Harris and Sattary (1990)]. Development of international standards for the use of orifice plates as flow meters has been extensive [Spencer (1982)]. The most recent specification is BS 5167-2:2003 provided in British Standards Institution (2003) and defines the relationship between Q and Δp, assuming that the experimental arrangement is as per the details provided in the standard, as equation [16]. The arrangement of the orifice and pressure tappings specified by the British Standard is given in Figure 3.17 along with the labelled symbols.

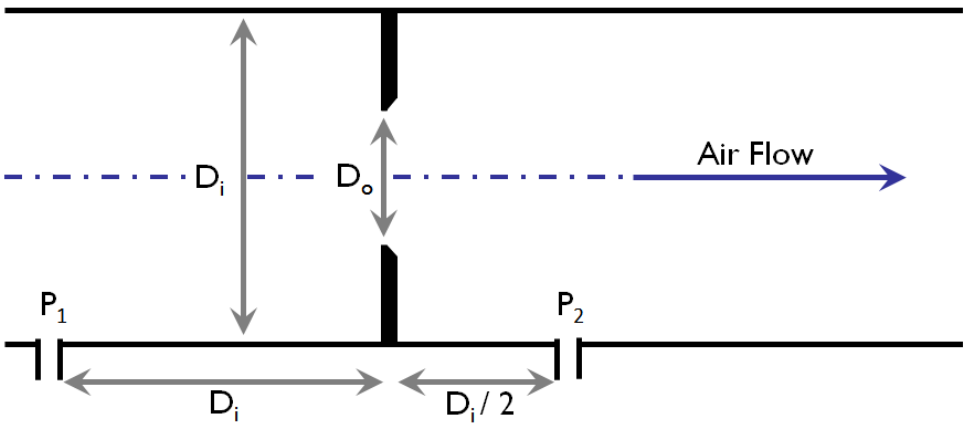

Figure 3.17, Arrangement of an orifice plate flow meter as per BS 5167.

$$Q = \frac{C_D A_2}{\sqrt{1-\beta^4}} \sqrt{\left(\frac{2\Delta p}{\rho}\right)} \qquad [\mathrm{m^3\ s^{-1}}] \qquad [16]$$

where,

$A_2 = \frac{\pi D_O^2}{4}$ area of orifice [m], $\beta = \frac{D_O}{D_i}$ ratio of orifice to pipe diameter, C_D = discharge coefficient, $\Delta p = p_1 - p_2$ = pressure drop across the orifice [Pa] and ρ = air density [kg.m^{-3}]. It follows from equation [16] that $Q \propto \Delta p^{½}$, and this relationship can be readily identified in the example curves in Figure 3.18. The pneumatic power of the flow available at the orifice can be calculated from the product of the pressure differential and the airflow rate, $P_{pneumatic} = \Delta p\, Q$, and is a widely accepted methodology, [Curran *et al.* (1997), Sarmento (1993)]. It should however, be noted that to fully determine the power available to the PTO, the stagnation pressure differential between the internal and external air should be used rather than the static pressure differential. This topic is discussed further, with reference to the methodology for the calculation of conversion efficiency, in section 4.5.

The discharge coefficient can be either approximated from empirical formulae in British Standards Institution (2003) or derived from calibration experiments. The flow measurement methodology outlined in the British Standard is for the particular case of steady flow conditions and no comment is made upon the effect of unsteady or cyclic flow upon the calculation of flow rate. Unsteady flow resulting in the dynamic behaviour of orifice plates can lead to flow rate prediction errors due to the modification of the discharge coefficient. The discharge coefficient is sensitive to the velocity profile upstream of the orifice and the instantaneous velocity changes, as such the non-uniform airflows from the WEC, cause fluctuations in C_D, [Gajan et al. (1992)]. Holmes and Nielsen (2010) however, reported that whilst orifice plates are intended for

steady flow, the author's experience suggests that the method is suited to OWCs and unsteady flow conditions.

Further to the variation in C_D due to generally unsteady flow, Yoon *et al.* (2009) investigated the effects of positioning an orifice close downstream of a 90° elbow with particular attention to the modification of C_D. This arrangement shares similarities with that in the OWEL model whereby flow is ducted from horizontal to vertical flow in the exit pipe. Yoon *et al.* (2009) showed that, for a typical model scale Reynolds number, *Re*, of the order 2 x 10^4, C_D could be reduced, from that calculated in the British Standard, by approximately 3.5 % due to the presence of a 90° bend. This suggests that the unsteady flow effects from the conversion process and airflow ducting could mean conservative results. An improved version of the orifice plate was investigated by Morrison *et al.* (1994) and suggests that a slotted orifice plate provides more stable performance of C_D. With a slotted plate it was found that C_D only varied ±0.25 % over the range of flows tested which is significantly better than the +6 %, -1 % change in C_D with a standard orifice plate. Although this method offers benefits over the standard orifice plate, it is much harder to accurately manufacture and if a series of experiments were undertaken to find an optimum damping value, numerous plates would be required. It would therefore be more suited for use, after an optimum damping is determined.

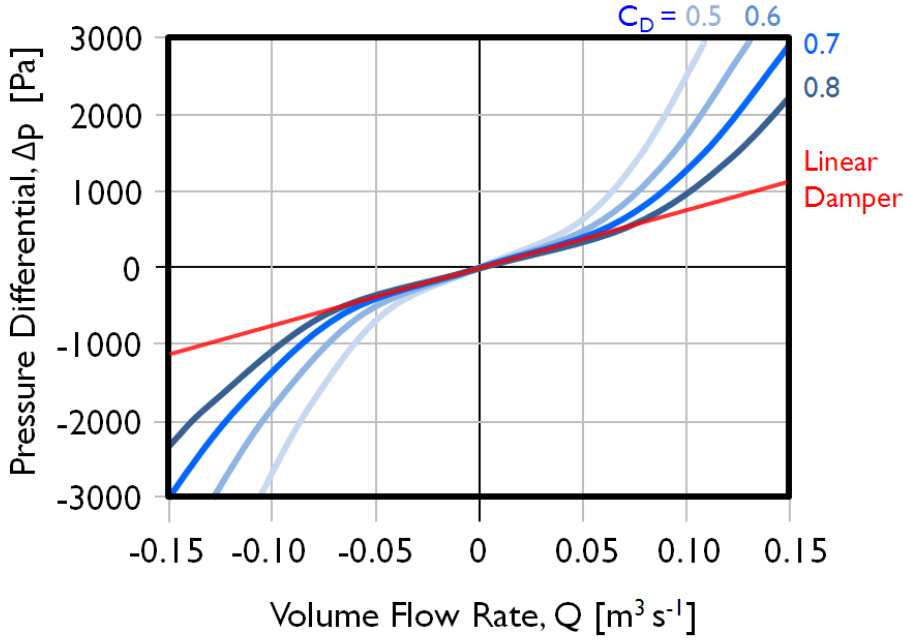

Figure 3.18; Relationship between pressure and air flow rate for different four orifices with varying C_D and a linear damper. Modified from Forestier *et al.* (2007).

Orifice plates are simple, cheap and a well proven technology. The variable damping does not allow a unique value to be applied and so it is not possible to completely isolate the performance from the effects of altering the damping. An alternative is to use a linear damper so that the pressure-flow relationship is linear as in Figure 3.18, and so the damping remains

constant thereby the performance of the device can be assessed as a result of the incident wave characteristics alone. Despite this however, it was found that, during the development of the Limpet OWC, the hydraulic performance of the model was not significantly different when the column was damped with a linear PTO simulator in comparison to an orifice [Wavegen (2003)]. In order to conveniently alter the applied damping, a variable area orifice was used rather than a porous damper, where the porosity would have needed to be changed in order to vary the damping. The orifice was calibrated for each cross sectional area with a method using a water filled, U-tube. In one side of the U-tube, a piston oscillated vertically with a known displacement and velocity. The orifice was fixed within the other side above the water surface so that the displaced water forced air to oscillate through it. The pressure drop across the orifice was measured in order to determine the discharge coefficient. It was used to represent the Wells turbine that would later be installed on the LIMPET device, despite having a non-linear flow relationship.

During the LIMPET physical modelling studies, two power calculation methods were compared in the data analysis; in the first, each positive and negative flow in the oscillatory cycle was identified and the RMS pressure drop calculated [Wavegen (2002)]. With the RMS pressure value, the damping coefficient was determined from the calibration curves and the power was calculated as $(RMS\ \Delta p)^2/Damping$. The second, simpler, method used the RMS pressure drop across the entire time series of the test and a single damping coefficient based on that value. The results from these two methods were compared and the simplified methodology provided values approximately 5% higher than that of the cycle by cycle calculation. For each geometric modification, the optimum damping was determined by repeating the test with a range of orifice sizes. It was found that the model was not particularly sensitive to the damping applied when excited by random seas, as long as the damping was relatively close to optimum. Similarly to other studies [Curran *et al.* (1997), Tease *et al.* (2007), Koola *et al.* (1995)], it was noted that it is typically beneficial to over-damp the column because excessive water motions resulting from under damping lead to higher energy losses from the water flow.

Despite the simplicity of orifice plates, it is often necessary or desired to better replicate the damping characteristics of the full scale PTO. The linear damping from a Wells turbine used in OWC applications is different from that of the orifice characteristics and so a number of methods have been developed to simulate a Wells turbine at model scale.

3.6.2 Linear Damping Methods

Linear damping, PTO simulators often comprise a porous membrane positioned over the air exit of the device to provide a resistance to the escaping air flow. The level of damping is altered by changing the porosity of the damper either through an alteration of the type of material or the thickness of the region. The typical linear flow relationship of these simulators is shown in Figure 3.18 in comparison to the non-linear relationship of various orifice plates.

Sarmento (1992) pioneered the method of using porous materials in his work with OWCs. The simulators were made using layers of 2 – 3 mm thick synthetic material of varying thickness to alter the porosity. These were pre-calibrated in a wind tunnel prior to installation on the model and it was reported that the nonlinearities of the carpet material, PTO simulator were reduced to within 5 % of the linear relationship across the typical range of flows. Using a similar methodology to Sarmento, Lucas *et al.* (2007) also used the synthetic, carpet material but placed over a series of orifices to produce a linear damping relationship. The damping provided by the PTO simulator was varied by altering the area of the orifice that the carpet was covering. This appeared to work relatively well for the small range of pressure drop (0-150 Pa) and flow rates that were tested. It is likely though that the calibration of the carpet and orifice arrangement would have been challenging and the repeatability of varying the damping by a sliding shutter may be questioned. Further to this, Lucas (2011) found that even very small amounts (< 2 mL) of water being splashed onto and absorbed by the material, drastically altered the resistance to the flow through a large increase in damping.

Experiments by Morrison and Greated (1992) were used to develop a numerical model and carry out a particle image velocimetry (PIV) study of the fluid dynamics within the OWC. The PTO in the experiments was simulated by an orifice filled with small tubes to allow air to escape through them. This was intended to lower the Reynolds number in the tubes such that the flow became laminar and so linearise the pressure-flow relationship to better represent a Wells turbine. Comparisons made between the theory and experiment showed that the numerical model significantly under predicted the pressure within the chamber despite closely modelling the free surface displacement and the resonant period of the column. The higher pressure drop observed in the physical tests was attributed to the laminar PTO simulator not achieving laminar flow and so had a non-linear pressure-flow relationship. Chaplin *et al.* (2012) used a series of narrow pipes each filled with many 1.6 mm diameter, steel capillary tubes, 800 mm in length. Similar to the approach taken by Morrison and Greated (1992), the methodology was intended to sufficiently lower the Reynolds number within the capillary tubes to ensure laminar flow within them. By opening and closing off different numbers of the pipes, the damping of the

PTO was varied between 37,000 and 481,000 N.s m^{-5}. Whilst this method could offer a linearised damping, the losses associated with additional air ducting and manifolds could be significant if not quantified. The increased mass and complexity of the simulator in comparison to other methods could also make it unsuitable for floating models. In comparison to the method by Chaplin, Morrison (1995) used a smaller orifice and 3 mm diameter tubes which were 250 mm in length. As a result, these did not reduce the Reynolds number within them sufficiently to ensure linear damping and so the relationship only held for $\Delta p \pm 50$ Pa, therefore restricting the allowable wave amplitude that could be used.

A further alternative for a linear simulator was implemented by Duckers *et al.* (2008) who used spinning, slotted plates to act as an obstruction to the flow out of a small OWC model. The plates were spun at between 2,000-9,000 RPM using a small motor to vary the level of solidity of the plates. This allowed the damping to be continuously altered between ~9,000 – 35,000 N.s.m^{-5} thus simplifying the optimisation procedure for the PTO characteristics. The experimental set up for the simulator was much the same as that for an orifice plate, with the pressure sensors positioned respectively 1D and 0.5D, up and downstream of the disk. Whilst this method offered significant advantages in that the damping could be varied continuously by remote, electronic control, it added a significant degree of complexity to the model set up and calibration. Although not implemented in these experiments, this method could possibly be used to test simple control systems to vary the rotational speed of the disk in order to maintain an optimum value.

Often, the flow – pressure relationship of the type of turbine being modelled can determine the choice of which PTO simulator to use for small scale experimental tests. However, the flow characteristics of a simulated PTO will never completely replicate those of a full scale turbine and as the converted energy from a wave energy device is relatively small when considered with the other energy flows in the system, the exact specification of turbine simulator may be of fairly limited consequence, especially for very small scale experiments.

A mechanical analogue, large scale OWC model developed by Szumko (1989) was used to investigate the effects of linear and non-linear PTO damping in addition to the compressible effects that were discussed previously. In this instance, the non-linear PTO considered was modelled as an orifice which assumed that the turbine PTO could be replicated by the pressure drop characteristics of an orifice and that the turbine was 100% efficient. The results presented showed significant differences in conversion efficiency for cases where linear and non-linear damping was simulated. Typically, a 5 – 10 % reduction in performance was observed with the orifice PTO in comparison to the linear damping. This effect was reduced with increasing wave

period and further reduced when assuming incompressible air. This simple, mathematical model does show that there are likely to be differences in captured power depending on the PTO damping characteristics used however, this was for the particular case of a full scale geometry. No comment was made on the applicability of the model to small scale PTO simulators and whether similar effects could be expected. A comparison between linear and non-linear, orifice PTO simulators was made in the study by Sarmento (1992) and this suggested, albeit with slightly different OWC geometries, that the hydraulic efficiencies of the small scale models were relatively unaffected by the choice of simulator. The comparison made by Forestier *et al.* (2007) between a porous, linear PTO and an orifice plate PTO on a 1:15 scale model of OE Buoy showed that, over a range of sea states, the linear PTO resulted in slightly higher performance than the orifice although, for the longest period conditions, this relationship was reversed. These observations corroborate with the trends predicted by Szumko's theoretical model and therefore it could be that the use of an orifice will result in conservative power output estimations.

3.6.3 Turbines applicable to OWEL

A review of full scale turbines suitable for OWCs was carried out alongside this work and has been included in Appendix A1.3 for reference as it is not of direct consequence to the scale investigations. It was shown in the review that, over the past few decades, a significant amount of research into both Wells and impulse turbines has been undertaken. Progress has been made to improve full scale PTO systems from having a very narrow band of efficient performance to broad range of flows conditions over which the turbine can operate. Modifications to the turbines have led to the optimisation of the static geometries and inclusion of variable geometry features such as pitching blades and guide vanes. Whilst these dynamic configuration changes can greatly increase the performance of a turbine, the implications of a complex mechanical system on the required maintenance have been observed and are detrimental in the interests of reliability and cost.

Results from small scale physical modelling in this work have shown that, in comparison to an OWC, there is little reverse air flow that occurs in the OWEL energy conversion cycle. Therefore, it is likely that, on the full scale device, a bi-directional turbine will not be required. However, from the proven and available technology solutions, a uni-directional turbine for a wave energy application has not been developed and so a bespoke turbine would be required.

Favouring a more "off-the-shelf" type of technology, it is likely that for a prototype OWEL, a bi-directional impulse or appropriately designed reaction turbine could both be well suited. Due to the large range of expected flow conditions, it is likely that an impulse turbine may be better

suited in order to avoid stall conditions with higher flow rates. Furthermore, an impulse turbine would allow for a smaller PTO unit and so have less impact on device motions as it would not raise the CoG and move it aft as much as a larger turbine. However, due to the single uni-directional pulses of air, it is likely that a large amount of stored inertial energy will be required to maintain output between air pulses. This implies that a smaller diameter impulse turbine would be less suited as it would be challenging to incorporate sufficient inertia in a flywheel. From this, the most appropriate turbine would be the Dresser Rand HydroAir as it combines the advantages of a typical impulse turbine with increased performance and a larger diameter to allow for the inclusion of generator and flywheel. An alternative arrangement that could be considered would be to include an accumulator to smooth the air flow pulses from the conversion cycle. This however, will incur losses and require the turbine to operate at relatively low pressure differentials, however if the performance of the turbine benefits significantly from using an accumulator, it may be a viable alternative.

The choice of an impulse turbine would mean that non-linear damping would be applied to the air flow rather than the linear characteristics of a Wells turbine. Depending on how sensitive the OWEL device is to applied damping, this could be detrimental to the overall performance as low flow may be under-damped and conversely, high flow be over-damped. From this review, it is likely that a Wells turbine can be discounted as a full scale PTO option and so simulating linear damping in small scale testing would be of limited worth. Therefore, a simple orifice plate PTO simulator would be sufficient at representing a turbine and would provide insight into the sensitivity of performance to the damping characteristics.

3.7 Summary and Discussion

This chapter has sought to provide a review of; the WEC technologies deemed to be in direct competition with OWEL; the previous development work on the OWEL device; the published research on the development of static and floating oscillating water columns; and the experimental methodologies and considerations when testing WECs with an air power take-off at small scale.

The ten devices were identified as key competitors to OWEL possess both advantageous and limiting characteristics and as such, no single technology can be identified as the superior device. The commercial competitiveness of the wave energy industry means that it is uncommon for performance data to be publically revealed, particularly for large scale devices. It is therefore challenging to make comparative assessments between devices and set targets to judge the commercial potential of OWEL.

The investigations within the previous OWEL development projects had a number of limitations which reduced the validity and reliability of the results. However, their main conclusions suggested that, within the investigations of this research :

- The model geometry for subsequent physical experiments should be based upon the dimensions of the 1:10 scale device.
- Geometric optimisation features such as duct floor and side wall angles should be re-investigated to further investigate their merit and determine the validity of the conclusions from the 1:100 and 1:10 optimisations.
- The key parameters of duct length and freeboard require attention and their relationship between wave input conditions and performance should be investigated.
- From the results of the physical modelling, it was concluded that peak performance occurred when the freeboard of the device was ~2/3^{rds} of the wave amplitude and that the duct length was 1/2 of the incident wavelength.

The novel operating principle of OWEL means that it does not readily fit into any of the conventional classifications of WECs. Of the various types of WEC however, it shares the most synergies with Oscillating Water Columns. Many of the early, large scale, static OWCs suffered from energy losses in the conversion process due to detrimental effects from their geometry, incorrectly rated PTOs, lack of system integration or inefficient and immature turbine design.

The OWEL device was conceived to have many of the benefits of OWCs but was intended to overcome some of the limiting features such as the necessity of a bi-directional turbine.
The advantages of OWCs that are shared by OWEL are that;

- The collector geometry is simple and has no transforming features.
- There are few moving parts and none in direct contact with the water.
- Operating principle is not restricted to a specific water depth.
- The structure could be manufactured from concrete to reduce costs.
- PTO plant is above the waterline allowing good maintenance access.

Further to these advantages, it was thought that, through the use of a uni-directional turbine, the turbine could be better specified to the range of predicted flow conditions thus avoiding the requirement for a bi-directional turbine with its associated disadvantages. OWEL was also considered by the device developer to be scalable to multi-megawatt platforms by combining a number of individual ducts to form a single unit with the potential ability of incorporating wind turbines mounted to the deck.

4 Initial Physical Modelling

4.1 Introduction

The initial investigations of this work were a series of fundamental, physical modelling studies carried out shortly after the commencement of this EngD. These were intended to provide insight into the operation of OWEL through a simplified laboratory scale assessment of the power capture process. A narrow wave flume was the only facility available to conduct testing at the time but the low demand for its use allowed for a lengthy testing period with few time constraints; a fairly rare occurrence in the development of WECs.

As the review of the physical modelling preceding this research showed in section 3.3, the underlying physical principles behind OWEL had not been observed or understood. The experimental studies for the proof of concept and intermediate scale testing however, had suggested that peak performance occurred when;

- The freeboard of the device was ~2/3^{rds} of the wave amplitude,
- The duct length was 1/2 of the incident wavelength.

These tests had been carried out using an unconventional PTO system providing a very high level of damping applied to the airflow and so it was necessary to check these conclusions with a more suitable PTO. Following the review of small scale power take off methods in section 3.6, it was decided to use an orifice plate to represent an air turbine and to provide a way of measuring the available power.

The tests commenced with a series of baseline tests to determine the performance characteristics of the simplified model. The freeboard and trim of the model were altered during these tests and the results demonstrated the potential for performance improvement. This was followed by an investigation of the orifice diameter to optimise the applied damping in order to maximise the power capture. After determining the optimum orifice configuration, the model was extensively tested over many wave conditions to build up a detailed view of its performance characteristics. Following the initial testing with the baseline design, the geometry was altered and retested for five subsequent configurations with the aim of increasing the performance and to better understand the energy conversion process. Internal wave reflections were shown to be necessary for efficient performance and the superior geometry configuration exhibited encouraging power capture trends.

4.2 Objectives

As these tests served as the initial studies in this research, the objectives were focused on the fundamental relationships of the simplified design under idealised conditions.

- Test the main conclusions from previous physical modelling.
- Study the internal fluid behaviour in order to understand the fundamental operating principle and provide initial learning.
- Determine whether a direct turbine PTO could be suitable to replace the proposed valve and pressure vessel energy storage system.
- Find the optimum PTO damping that best benefits power capture.
- Understand the importance of geometric parameters on the conversion process with the possibility of some initial geometry optimisation.
- Generate data and conclusions to inform the subsequent physical modelling studies.

4.3 Wave Flume Facilities

Testing was carried out in a narrow wave flume at the University of Southampton which was 0.7 m deep, 16 m long and 0.42 m wide. The model was rigidly fixed into the flume and was positioned 10 m from the wave maker as indicated by the layout diagram in Figure 4.1. A support structure provided the ability to vary the depth between duct roof and water free surface, known as the freeboard, when required. The model spanned the entire width of the flume and so water was not able to flow around the duct. A 3 m long, passive beach comprised of coarse foam with a gradually reducing permeability was located 2.8 m behind the stern of the duct.

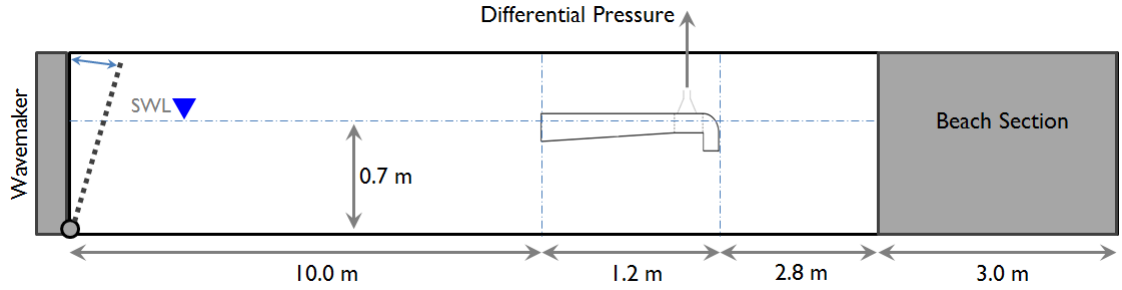

Figure 4.1, A sketch of the arrangement of the model and wave flume with the key dimensions.

A single, base-hinged, paddle wave maker was able to generate a range of regular wave periods and heights well suited to the order of scale tested. The maximum wave height was limited to just over 200 mm which was overly sufficient for this model and water depth. The range of usable wave periods was found to be approximately 0.5 s < T < 2.5 s. The flume was able to generate waves outside of these limits however, their repeatability deteriorated as many of the wave profiles became distorted. This was due to non-linear effects caused by wave steepness but particularly by depth effects from the relatively shallow tank.

An automated system was developed in order to control the flume and carry out extensive batch runs of wave conditions. The program was compiled using TestPoint™ which generated a regular, sinusoidal, wave-maker drive signal for each of the specified wave conditions in a batch. The program then ran the drive signal for a set number of wave periods, typically 20, whilst sampling sensor data at 256 Hz through a 16-bit analogue to digital conversion unit. This system enabled experiments to be run autonomously 24 hours per day which saved time and allowed data analysis to be carried out whilst tests were still being run.

A period of initial testing to assess wave conditions in the flume without a model present revealed that the passive beach was effective at attenuating waves with little reflection from the end of the flume. It was observed that the ability of the beach to absorb waves reduced for waves with increasing wavelength. Through these observations and monitoring of the free surface within the tank using a wave probe following each run, a relationship between the wavelength and settling time following a run was established. This allowed the settling time to be increased for longer period waves and allowed the water to settle before a subsequent run commenced. This ensured that, during the autonomous operation of the tank, the pause after a run would be sufficient to ensure no remnant waves were present in the tank before running the tank. This relationship was modified once testing with the model had commenced; the pause for the settling time was increased to allow longer for the reflected waves from the model to be attenuated after the run. Typically the wait time varied from 3 minutes to approximately 4.5 minutes.

4.4 Model Configurations

The dimensions of the full scale device were supplied by OWEL and were based on proportions similar to the 1:10 model (see Figure 11.2, section 3.3.3). The given figures specified a full scale device with a duct length of 96 m and were reduced by a scale factor of approximately 1:80 for these experiments. A drawing of the model in plan and side views with the key dimensions is shown in Figure 4.2. From this sketch, it can be seen that the characteristic duct length, L_D, was 1.2 m. Unlike a full scale device, the model lacked side wall contractions so that it spanned the entire width of the wave flume. This allowed it to be considered as a simplified 2D representation of a 3D duct, often referred to as a 2.5D model as, having depth, it cannot be truly 2D.

The duct was constructed from 12 mm thick Plexiglas for the walls, floor and roof, 0.5 mm aluminium sheet for the rear back plate baffle and was rigidly supported in the wave flume by an aluminium frame. The exit from the duct into the PTO tube was modelled using a funnel

with a 165 mm diameter entrance, exiting into an exhaust pipe of 63 mm ID which contained the orifice plate PTO simulator. Figure 4.3 shows two images of the model, post construction.

In total, six different model configurations (see sections 4.4.1 - 4.4.6) were tested to evaluate their performance and find the most favourable duct arrangement as well as the effect of geometric features on performance. Each configuration was intended to test a hypothesis conceived through group discussion with the OWEL project members.

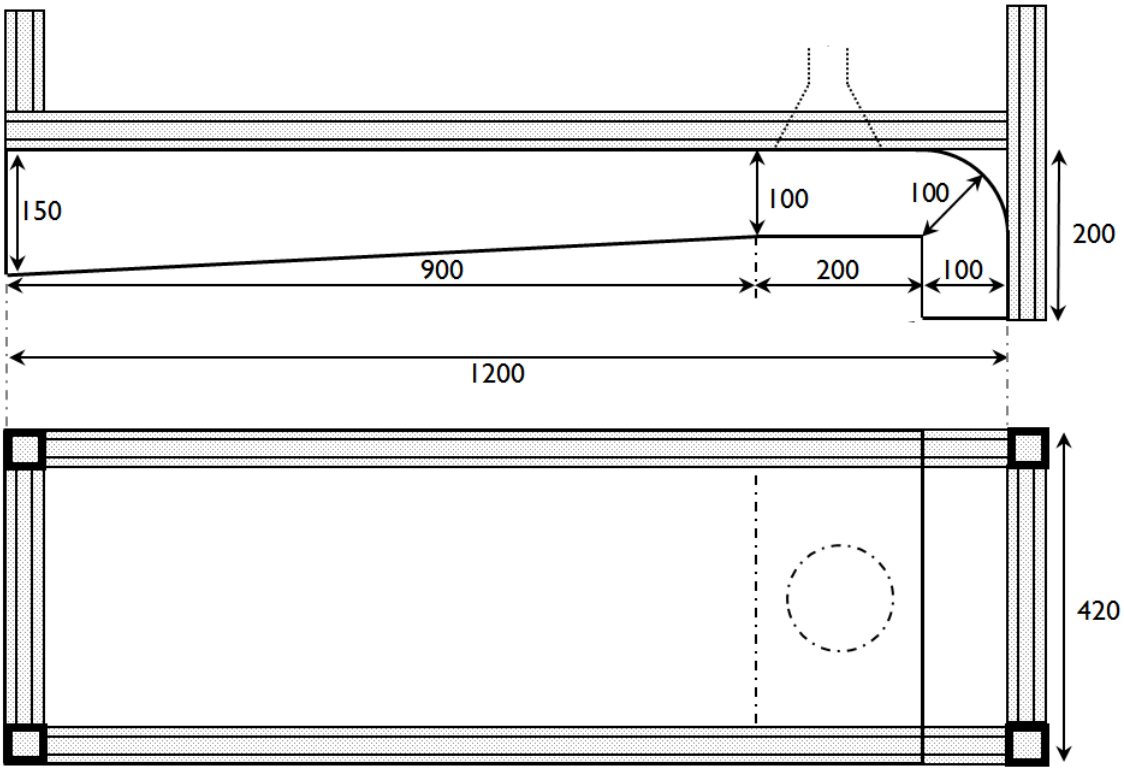

Figure 4.2, Side and plan view drawings of the model including dimensions in mm and showing the surrounding rigid framework.

Figure 4.3, Images of the completed model prior to testing.

4.4.1 Baseline Configuration

This configuration was the standard arrangement of the OWEL duct as defined by the intermediate scale testing at Narec as described in section 3.3.3. The freeboard, distance from the still water level (SWL) to the lower surface of the duct roof, was the same at the bow and stern so that the deck was parallel to the SWL.

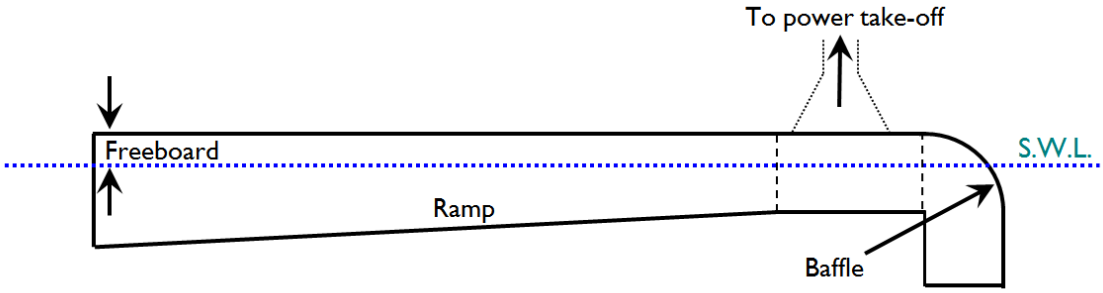

Figure 4.4, Baseline Configuration OWEL Design.

4.4.2 Configuration #1 - Dipped Stern

The freeboard determines if and how a wave crest seals with the duct roof. One suggestion made was to trim the duct bow up so that the stern of the duct had zero freeboard and the base of the PTO just made contact with the SWL. This was intended to allow waves of any height to create a seal with the duct roof at some point along its length. It was also hoped that this would help to attenuate waves as they passed down the duct and so reducing the potential for reflections.

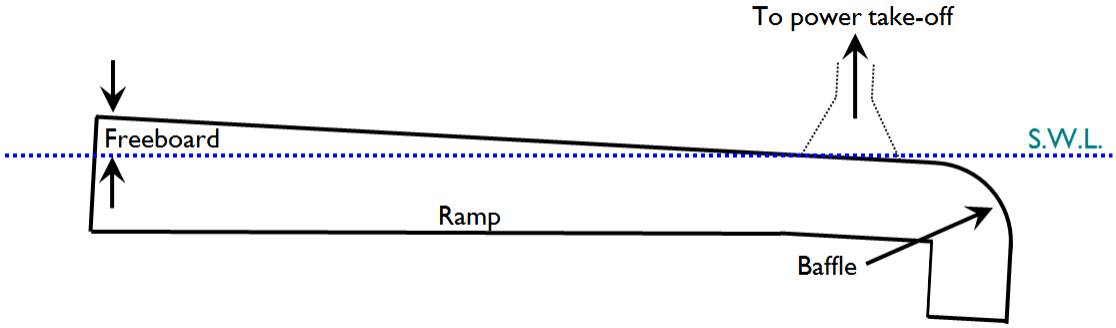

Figure 4.5, Configuration #1 – Dipped Stern.

4.4.3 Configuration #2 - Energy Diffuser

An observation from the initial testing of the baseline configuration was that wave reflections from the baffle could be detrimental to the performance of the device. Consequently, a number of possible wave reflection reducing techniques were conceived. This configuration used a series of coarse foam wedges attached to the baffle in an effort to diffuse remnant wave energy

and so reduce the internal reflections within the duct. This arrangement was tested with the model trimmed as the baseline configuration and subsequently configuration #1.

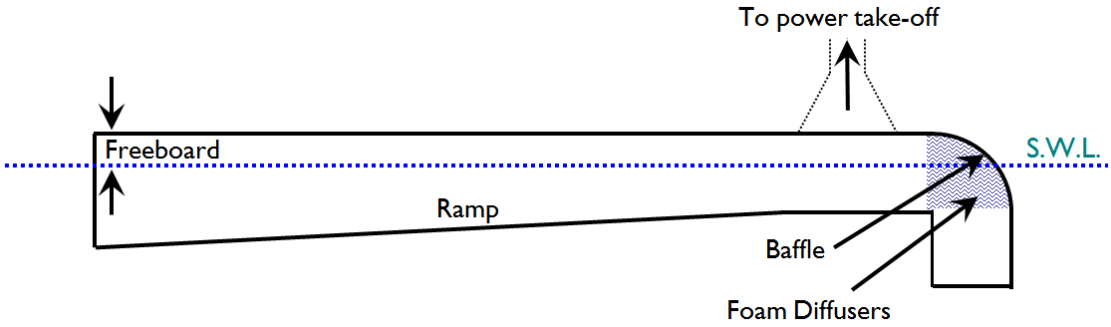

Figure 4.6, Configuration #2 – Baseline with a diffuser.

4.4.4 Configuration #3 - 45° Baffle

This arrangement featured a flat plate baffle, angled at 45° to the roof, as shown during construction in Figure 4.10, rather than the standard curved baffle design. This was also intended to reduce wave reflections by providing less of an abrupt impact surface. During testing, the dipped stern of configuration #1 was found to be beneficial and so was adopted for all other subsequent configurations including this one.

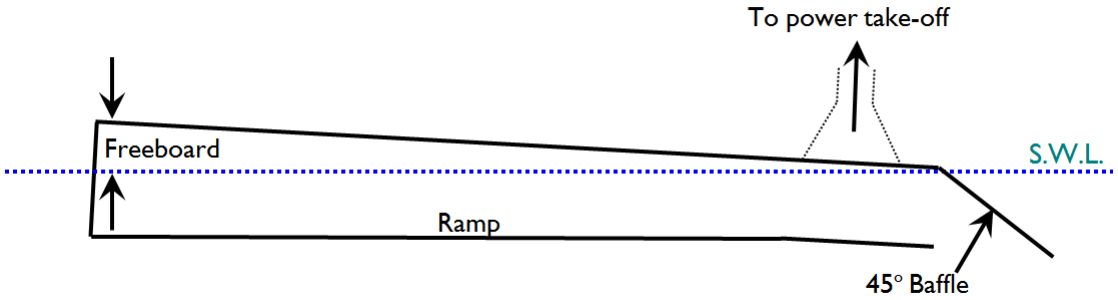

Figure 4.7, Configuration #3 – 45° baffle.

4.4.5 Configuration #4 - No Baffle

This design intended to prevent wave reflections by allowing waves to pass through the duct and exit in the same direction as their propagation. The roof was extended below the water line to provide a barrier to the trapped air and prevent it from exiting out of the baffle rather than the PTO.

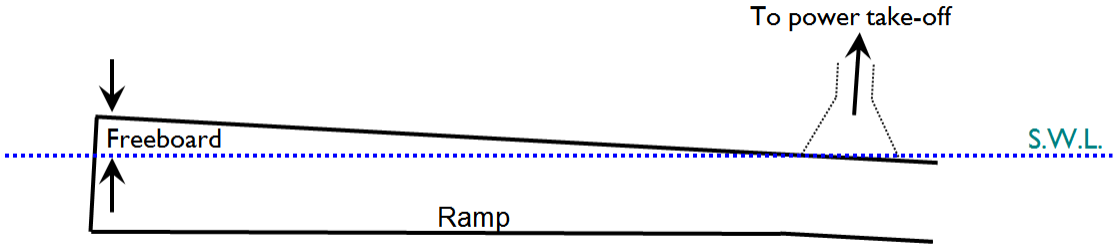

Figure 4.8, Configuration #4 – No baffle.

4.4.6 Configuration #5 - Square Baffle

Conversely to initial observations, it was eventually concluded that the wave reflections were beneficial to the conversion performance and so methods to increase wave reflections were then devised. Configuration #5, shown in Figure 4.11, was similar to configuration #3, but had a vertical baffle plate rather than angled in order to create larger wave reflections. This was also postulated to reduce construction costs at large scale.

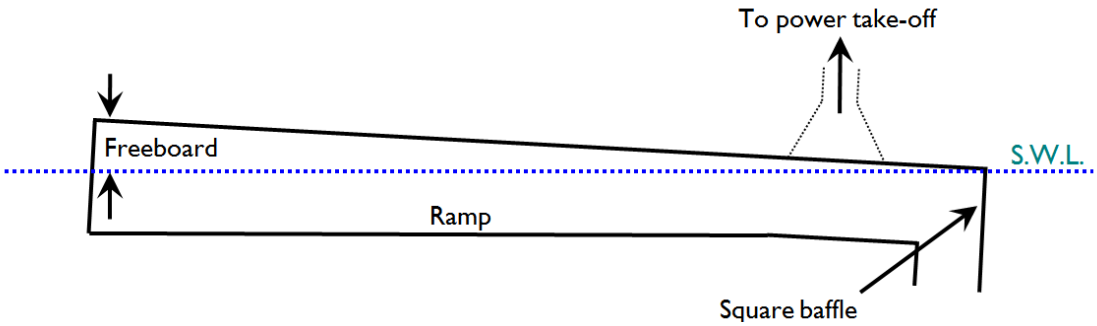

Figure 4.9, A schematic of configuration #5 featuring a square baffle shape.

Figure 4.10, Image of model configuration #3.

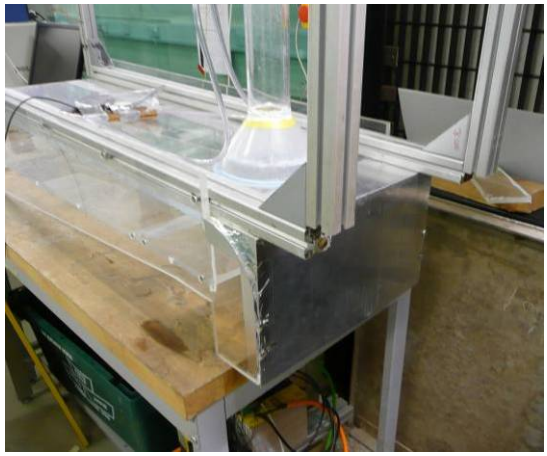

Figure 4.11, Image of model configuration #5.

4.5 Efficiency Calculations and Orifice PTO Simulator

Following the review of model scale power take off options in section 3.6, it was decided to investigate whether a turbine PTO could be used instead of the complex non-return valve arrangement that was used in the preceding physical modelling work as detailed in sections 3.3.1 and 3.3.3. An orifice plate was deemed as a suitable PTO simulator and in addition would provide air flow measurements to estimate the performance of the device.

The orifice arrangement was constructed to BS 5167-2; the British Standard for measuring flow with orifices, [British Standards Institution (2003)]. Figure 3.17 shows a schematic of the setup and summary of the details from the standard. A number of orifice sizes (D_o) were tested and each was cut into a thin, steel plate which was sandwiched and sealed between two brass plates

as shown in Figure 4.29. The orifice was centred in the 63 mm (D_i) Perspex pipe and positioned approximately 420mm downstream of the funnelled exit from the model to reduce the flow instabilities at the orifice. Two 4 mm pressure tappings were positioned either side of the plate, as shown by the sketch in Figure 4.12, and a differential pressure transducer was connected across them to measure the pressure drop across the orifice.

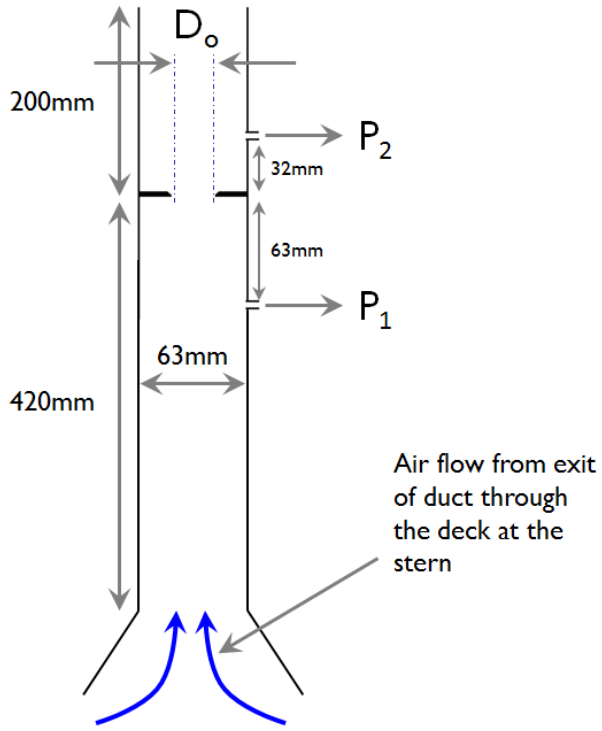

Figure 4.12, Arrangement and dimensions of the orifice assembly.

The discharge coefficient for each orifice used was estimated using the empirical relationship provided by BS 5167-2. A number of sources of error may exist in the calculation of C_D particularly as the relationship is for steady, fully developed flows. The Reynolds number with respect to the pipe diameter is an important parameter in the relationship and so its variability throughout an irregularly pulsating flow will impact the C_D. For the calculation of C_D, the Reynolds number was estimated as ~0.26 x 10^4 for an air flow velocity of 1 m.s^{-1}. Furthermore, the British Standard provides uncertainty values in the calculation of C_D and these are summarised for each of the orifices tested along with their principal values in Table 2. It can therefore be assumed that the estimation of C_D is likely to have an overall error of +/- 1%.

To measure the pressure drop across the orifice a Honeywell 24PCEFA1D differential pressure transducer with a 0.5 psi (~3500 Pa) range was used. The sensor was excited with a constant 10 V DC from a Fylde Instruments FE-492-BBS bridge conditioner.

Table 2, Details of the key parameters of the orifices tested.

β (D_o/D_i)	D_o [m]	A_2 [m²]	C_D	Error C_D [%]
0.20	0.0126	0.000125	0.593	0.66
0.30	0.0189	0.000281	0.609	0.63
0.35	0.0221	0.000382	0.615	0.62
0.40	0.0252	0.000499	0.621	0.60
0.45	0.0284	0.000631	0.627	0.59
0.50	0.0315	0.000779	0.635	0.57
0.60	0.0378	0.001122	0.652	0.54

The signal from the bridge conditioner was then amplified using a Fylde 254GA low-noise amplifier operating at a gain of 500x and sampled at 512 Hz. This transducer was chosen for its low cost and simplicity. The typical repeatability stated was ±0.15 % of the output span; roughly equivalent to ± 6 Pa. A sensitivity analysis was carried out to test the significance of this source of error: In the 0.42 m wide flume, a wave of T = 1.2 s and H = 50 mm has an incident power of 1.15 W. The typical mean differential pressure generated by this wave is around 100 Pa. Table 3 shows the effect of the ± 6 Pa repeatability on the stated efficiency which was calculated by the method explained subsequently in this section.

Table 3; The effect of pressure sensor error on performance.

Average diff. pressure , Δp [Pa]	94	100	106
Air flowrate, Q [m^3s^{-1}]	0.0039	0.0041	0.0042
Air power [W]	0.3706	0.4067	0.4438
Efficiency, η [%]	32.3	35.4	38.6

This shows that, in typical conditions, an error of ± 6 Pa could cause the efficiency to vary by ±3 percentage points. At lower flow rates and pressures, this error will be even more significant, conversely the opposite is true for greater flow.

The manufacturer's typical sensitivity rating for this sensor was given as 70 mV/psi. The calibration test results in Figure 4.13, show that the transducer exhibited a linear response over the range of pressures typically experienced and a good repeatability. The calibration showed the sensitivity coefficient to be 58.5 mV/psi; with an amplifier gain of 500x this equated to approximately 230 Pa/V.

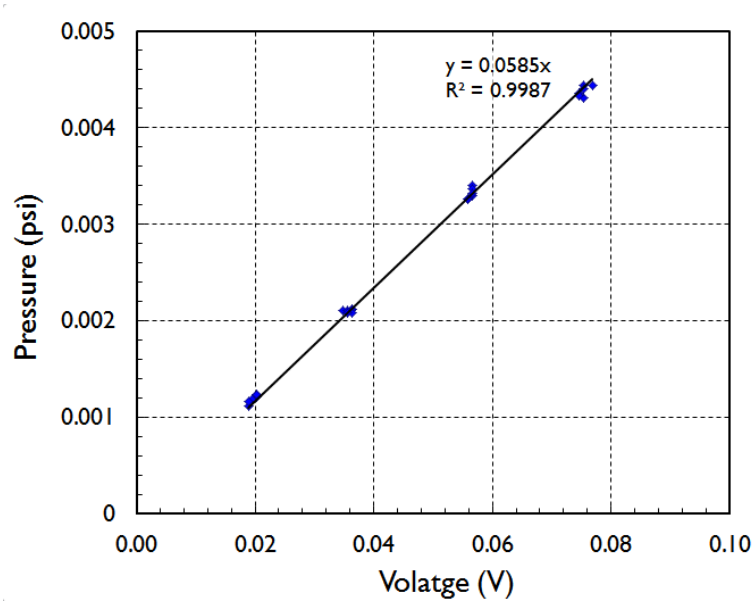

Figure 4.13, Calibration graph for the pressure transducer.

The wave to pneumatic energy conversion efficiency of OWEL has been used as the primary measure of performance and is readily compared between models and configurations.
The wave-to-pneumatic conversion efficiency, η, is calculated from the ratio of the total air power available to the PTO, measured at the orifice, to the incident wave power entering the duct, as in equation [17].

$$\eta = \frac{\overline{P_{air}}}{w.P_{wave}} \qquad [17]$$

Where $\overline{P_{air}}$ is the mean air power, in Watts, measured over the sample time and is defined by equation [18], w is the width of the duct entry in metres and P_{wave} is the incident wave power calculated in terms of Watts per metre width of wave crest, given by equation [9].

$$\overline{P_{air}} = \frac{1}{t_{end} - t_{start}} \int_{t_{start}}^{t_{end}} \Delta p(t)\, Q(t) dt \qquad [18]$$

For each test a range of data over 10 wave periods was taken. t_{start} was the start time of the data range and was typically 4 wave periods after the first wave crest in order to avoid any transients and ramping of the wave input signal, as can been seen in the time series in Figure 4.18. t_{end} is therefore the end time of the data sample, ten periods after t_{start}. $\Delta p(t)$ is the time series of the measured differential pressure across the orifice. $Q(t)$ is the time series of the air flow rate through the orifice, calculated by using the orifice equation in equation [16].

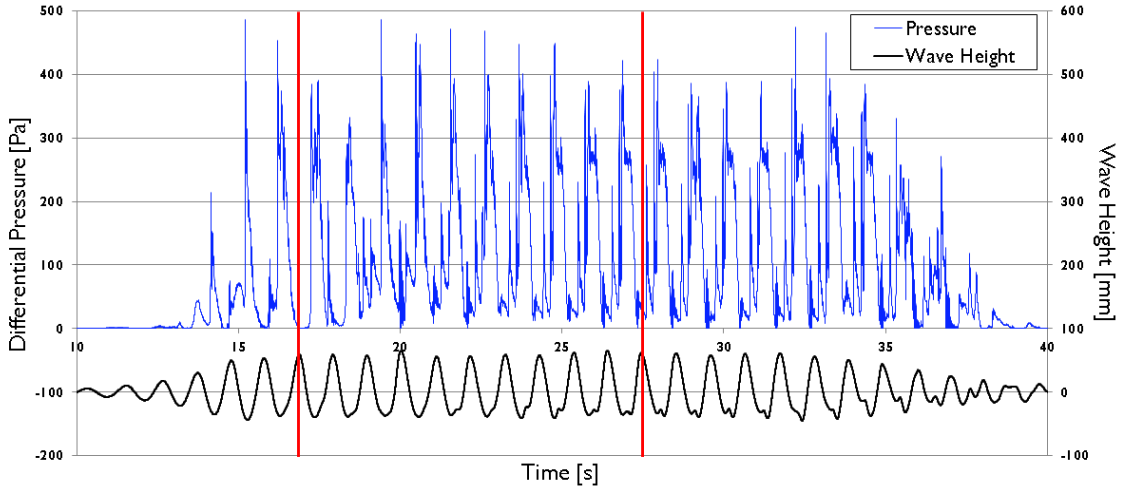

Figure 4.14, Example of the section of the time series used for the performance analysis. (T = 1.08s, H = 72 mm)

It can be seen in equation [18] that the instantaneous power of the air flow is a product of the pressure differential across the orifice and the air flow rate through it. As the only variable in the calculation of the air flow rate is the pressure differential, the time series characteristics are both identical. A comparison between the differential pressure and resulting calculated airflow can be seen for a typical wave case in Figure 4.15

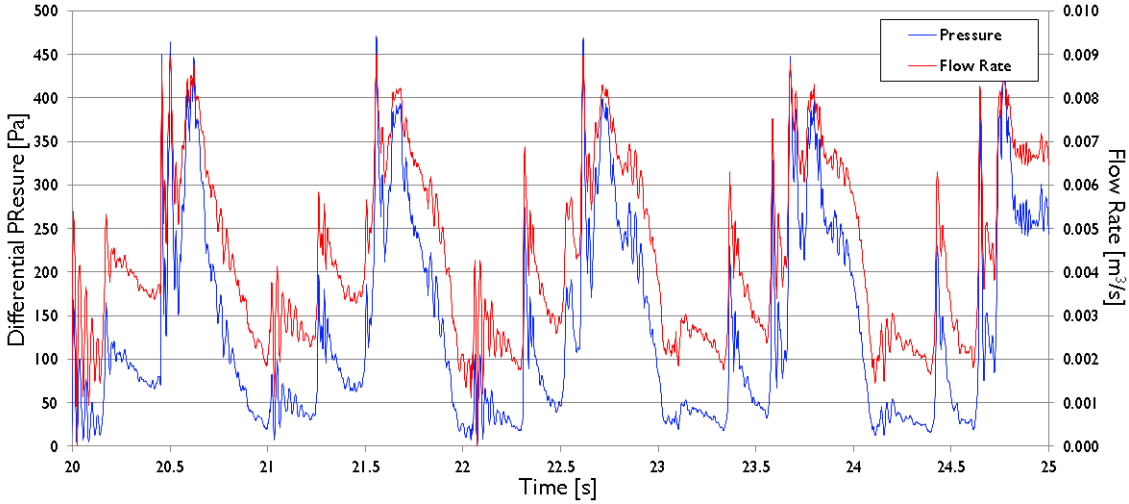

Figure 4.15, A plot of the typical differential pressure across the orifice with the resulting air flow rate calculated from the time series. (T = 1.08s, H = 72 mm)

A slight error is present in the aforementioned methodology for calculating the air power and thus the conversion performance efficiency of the device: This is due to the use of the measured differential pressure across the orifice in equation [18]. Whilst many methodologies [Curran *et al.* (1997), Sarmento (1993)] state that the differential pressure across the orifice should be used, this does not give the total energy available to the PTO for conversion to electricity. The energy in the airflow upstream of the orifice is a combination of dynamic pressure and static pressure.

By measuring the pressure at the wall of the PTO pipe the static pressure of the flow is recorded but the dynamic pressure is neglected. The stagnation pressure of the flow, p_0, is the pressure that would result if the dynamic pressure of the flow, from the air velocity, was converted to a static pressure by reducing the flow speed to zero, and is defined by:

$$p_0 = \frac{1}{2}\rho U^2 + p \qquad [19]$$

where ρ is the density of air, U is the air velocity and p is the static pressure.
The pressure differential used in equation [18] should therefore be the difference between the stagnation pressure within the PTO tube upstream of the orifice and the ambient air pressure, i.e. Δp_0 [Gato & Falcao, (1988)].

The two plots in Figure 4.16 and Figure 4.17 show the variation in static pressure measured at the two pressure tappings; one pipe diameter (D) upstream and half a diameter (D/2) downstream. These results were taken from the experiments reported in chapter 5 and were measured by individual sensors located at each point rather than a single sensor to measure the differential. These plots are presented here to demonstrate that the static pressure measured downstream of the orifice is very close to zero and can be considered to have little effect on the measured pressure differential. This means that the differential pressure measured across the orifice by the single differential pressure sensor is analogous to the differential static pressure between the upstream location and the ambient air pressure.

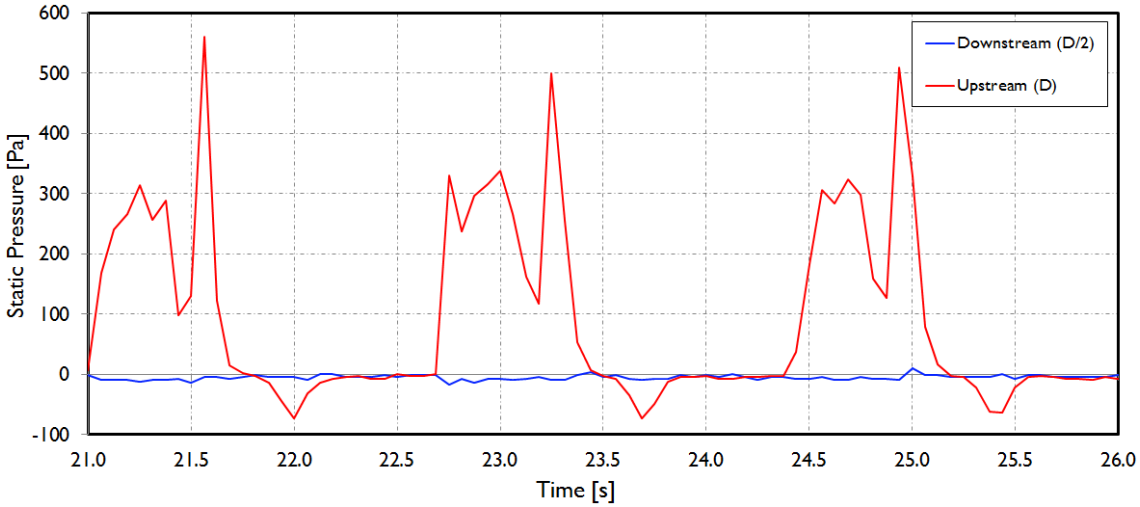

Figure 4.16, An example time series of the static pressure measured one pipe diameter (D) upstream of the orifice and D/2 downstream, for a regular wave with T = 1.7 s, H = 100 mm.

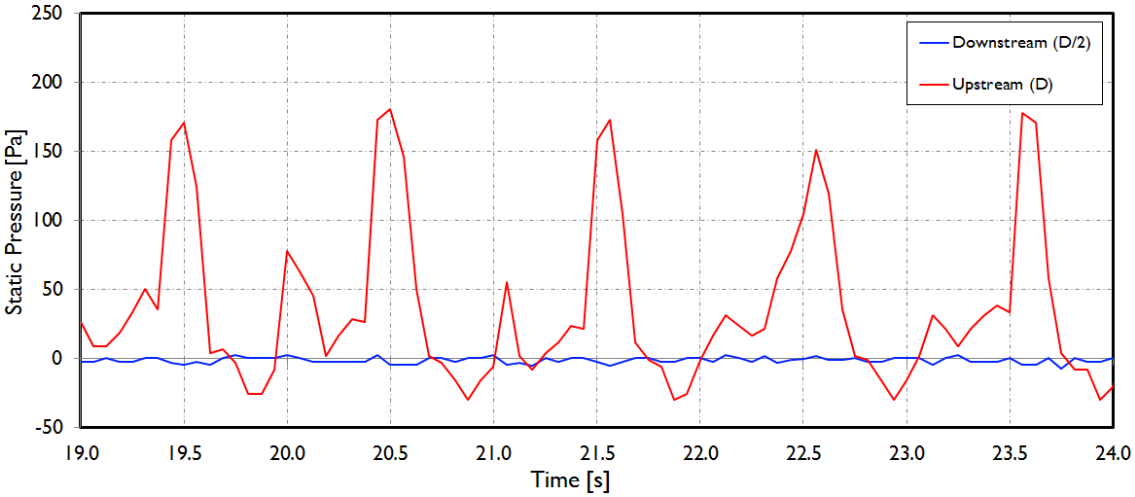

Figure 4.17, An example time series of the static pressure measured one pipe diameter (D) upstream of the orifice and D/2 downstream, for a regular wave with T = 1.0 s, H = 70 mm.

As the downstream pressures measured were equivalent to the ambient air pressure, errors in the calculation are a result of using only the static pressure component at the upstream location and not taking into account the dynamic pressure. Using equation [19], the stagnation pressure within the flow upstream of the orifice can be calculated. Examples of the underestimation errors of the measured pressure used for the performance calculation are provided in Table 4 for the typical, mean pressures and flow rates that were recorded during the experiments. This shows that by using the static pressure alone for the performance calculations may have resulted in a power underestimation of the order of a few percent.

Table 4, Errors in the pressure used in the performance calculations as a result of neglecting the component of dynamic pressure.

p [Pa]	Q [m²]	U [m/s]	p_0 [Pa]	Error p [%]
50	0.001	0.5	50.15	0.3
200	0.006	3.0	205.47	2.74

Regretfully, this error in the calculation of the power and efficiency was realised by the author after the completion of the experiments and data processing in this research and therefore, has not been taken into account in any of the plots or data presented in this thesis. It should therefore be noted by the reader that the efficiencies published in this work may slightly be underestimated.

4.6 Test Conditions

A resistive wave probe was used to measure the water elevation at the test region within the flume. This type of wave probe comprises two thin, parallel metal rods that are part submerged vertically into the water. The rods are energised with a high frequency alternating voltage and the conductance between them is linearly proportional to the depth of immersion and conductivity of the water. A set of Churchill Controls, wave monitors were used to provide the energising signal and voltage amplification output from the wave probe. As the conductivity of the probe and water varies, particularly with temperature (approximately 2 % per °C) [Fryer and Thomas (1975)], it was necessary to calibrate the wave probe twice daily during testing periods. This was done by positioning the probe at three known vertical displacements whilst in still water. The accuracy of these types of wave probes is typically +/- 0.5 mm.

Due to the wave reflections from the model within the flume, it was not possible to accurately measure the wave height at the duct entrance whilst the model was in the water and under test. However, it was decided to 'calibrate' the wave heights in the flume so that the series of test waves were run without the model present in order to measure the wave heights obtained. Figure 4.18 illustrates this issue by comparing two wave probe signals; Figure 4.18(a) shows the wave profile time series for a case without the model in the flume and Figure 4.18(b) is for the same wave case but with the model in the flume with the probe placed ~0.5 m from the duct entrance.

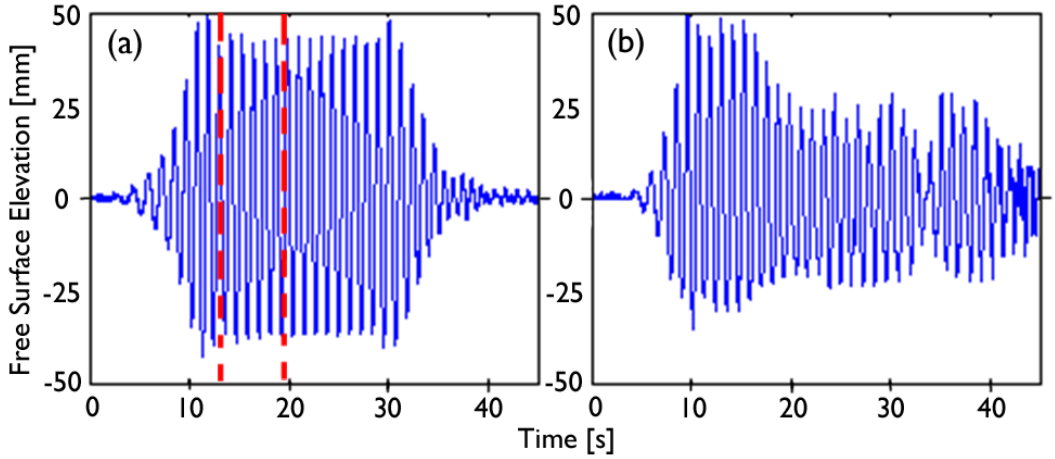

Figure 4.18, An example of water elevation for a test condition with an empty flume (**a**) and with the model in the flume (**b**). The red dashed lines indicate the region used for the average measurement. (T = 1.1 s, H = 80 mm)

The empty wave flume was calibrated a number of times during the course of this testing phase. Due to a small component of wave reflection from the passive beach, the wave height measurements were not solely the incident wave height as they contained a small component of the reflected wave. The reflection coefficient of the beach would have varied depending on the

height and period, with larger and particularly longer waves being absorbed less. Furthermore, the wave paddle did not have active wave absorption meaning that reflected waves from the beach could propagate back to the paddle and reflect off it back towards the beach again. The average height of the incident wave train was therefore sampled over the first five wave cycles after the initial transient wave height peak; the region between the two dashed red lines in Figure 4.18(a).

Initially, 296 wave conditions were calibrated in the wave flume and the results of which are shown in Figure 4.19. Four repeat runs were made using the same set of wave conditions and the surface elevation was measured at the same location as that of the duct entrance. The average height of the four repeats was deemed as the calibrated wave height for each of the input conditions and later used to calculate the conversion performance. In the wave tank calibrations, the average wave height was found to be repeatable with the measured, absolute deviations from the mean wave height over the four runs being approximately +/- 2% of the mean. The error bars in Figure 4.19 show that the repeatability was reduced for wave heights greater than ~100 mm due to increasing "shallowness" of the waves and reduced wave attenuation from the beach. The majority of the tests in the wave flume however, were for $H < 100$ mm and so a wave height error of +/- 2 % was deemed acceptable.

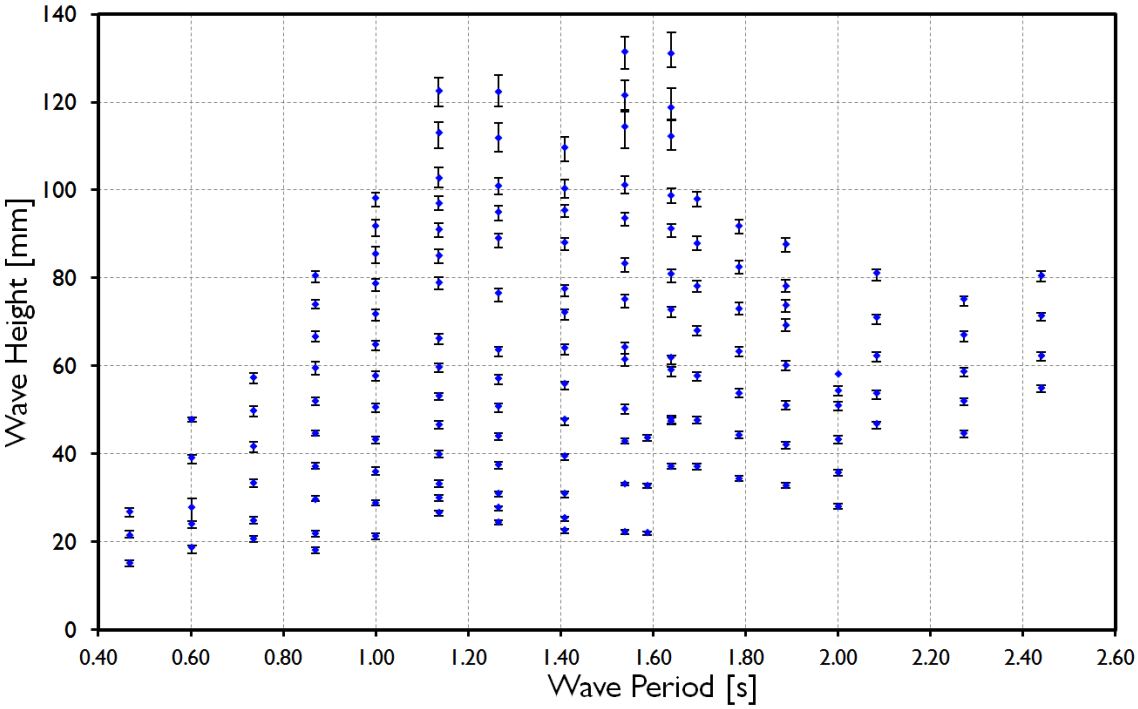

Figure 4.19, An example of the wave height calibration results for the wave flume with the error bars showing the absolute positive and negative deviations from the mean height.

The majority of the model configurations were tested using a sample of 112 test conditions. This provided a high resolution of results to determine the relationship between performance and wave period and height. An additional series of tests with a higher resolution were carried out on the baseline and configuration #1 models. These data sets included 296 test conditions providing a much higher resolution of results which was particularly useful for the initial trials for which the locations of the performance peaks were not known.

The range of wave conditions chosen for the tests was intended to span the typical scaled conditions of a full scale site such as Wave Hub shown in Figure 4.20, derived from data from Halcrow (2006). This diagram shows the annual distribution of available wave energy at the site and indicates that sea states of approximately T_e = 9 s, H_s = 4.25 m have the greatest annual abundance of energy. This design wave, scaled at 1:80, equates to T = 1.0 s, H = 53 mm. As the performance characteristics of the device were largely unknown at the time, the range of periods was extended beyond that of the scaled site conditions. This was intended to determine the conditions at which peak performance occurred and so inform the scaling requirements of the duct to be matched to typical wave sites.

Te (s)	4.59	5.71	6.84	7.96	9.09	10.21	11.34	12.46	13.59	14.71	15.84	Total	
Hs (m)													
0.25	0.00	0.00	0.00	0.00	0.00	0.00	0.00	0.00				0.00	
0.75	0.04	0.14	0.07	0.03	0.02	0.01	0.00	0.00	0.00	0.00		0.31	
1.25	0.02	0.55	0.29	0.13	0.06	0.02	0.01	0.01	0.00	0.00	0.00	1.09	
1.75	0.00	0.27	1.05	0.23	0.09	0.04	0.02	0.01	0.00	0.00	0.00	1.73	
2.25		0.01	1.33	0.60	0.16	0.08	0.03	0.01	0.00	0.00		2.23	
2.75			0.35	1.88	0.26	0.10	0.03	0.01	0.01	0.00		2.64	
3.25			0.03	1.78	0.63	0.12	0.06	0.01	0.01			2.63	
3.75				0.60	1.83	0.15	0.05	0.02	0.00			2.66	
4.25				0.09	2.19	0.30	0.08	0.03				2.69	
4.75				0.01	1.15	1.42	0.05	0.02	0.01			2.66	
5.25					0.26	1.92	0.10	0.02	0.00			2.30	
5.75					0.05	1.49	0.36	0.03				1.93	
6.25					0.01	0.51	0.96	0.02				1.51	
6.75						0.17	1.08	0.07	0.01			1.34	
7.25						0.03	0.62	0.19	0.03			0.88	
7.75							0.31	0.46	0.01			0.77	
8.25							0.03	0.43	0.02			0.48	
8.75							0.01	0.18	0.07			0.26	
9.25							0.01	0.02	0.13			0.16	
9.75									0.17			0.17	
10.25								0.01	0.13			0.14	
10.75									0.03	0.05		0.08	
11.25									0.04	0.02		0.05	
11.75										0.08		0.08	
12.25												0.00	
12.75												0.00	
Total	0.06	0.98	3.11	5.37	6.70	6.37	3.81	1.56	0.68	0.16	0.00	28.82	kW/m

Figure 4.20, Average annual available wave power at Wave Hub indicating a design wave of approximately T_e = 9 s, H_s = 4.25 m.

4.7 Results

A series of frames, A – F, showing the progression of a wave crest within the duct and the resulting differential pressure time series measured across the orifice is shown in Figure 4.21 for a typical wave of T = 2 s H = 60 mm. Each frame shows how the wave seals in the duct and the instantaneous pressure developed as a result of the wave. The average efficiency for this wave with the baseline configuration, as pictured, was 11 % with an average pressure drop of approximately 140 Pa.

An initial spike of high pressure can occur relating to the impulse of the wave first sealing and surging into the duct entrance. Further spikes of pressure can occur during the cycle and are a likely result of waves impacting the geometry and interacting with the exiting reflected wave. Generally a region of lower flow is observed following the initial surge and is attributed to the wave progressing through the duct. Often, the pressure falls below zero between cycles indicating negative flow through the orifice as air is drawn back into the duct by the exiting, reflected wave. This feature of the cycle is neglected in the performance efficiency calculation as, unlike an OWC, the negative return flow is not intended to contribute to the power of the uni-directional air turbine. The intake air flow was typically small in comparison with the exiting air flow and it is likely that the resulting adverse pressure applied across a uni-directional PTO would have little detrimental effect on its performance.

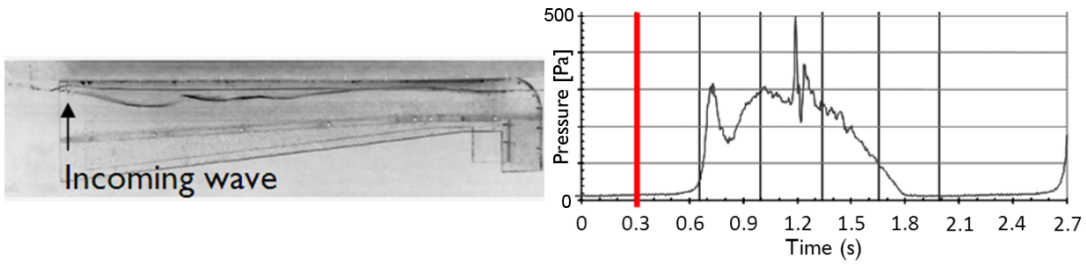

Frame A. Incoming wave prior to first closure – (Time = 0.3 sec)

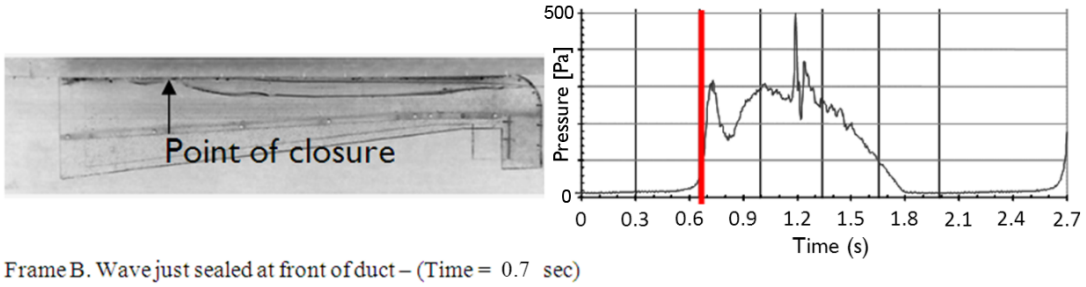

Frame B. Wave just sealed at front of duct – (Time = 0.7 sec)

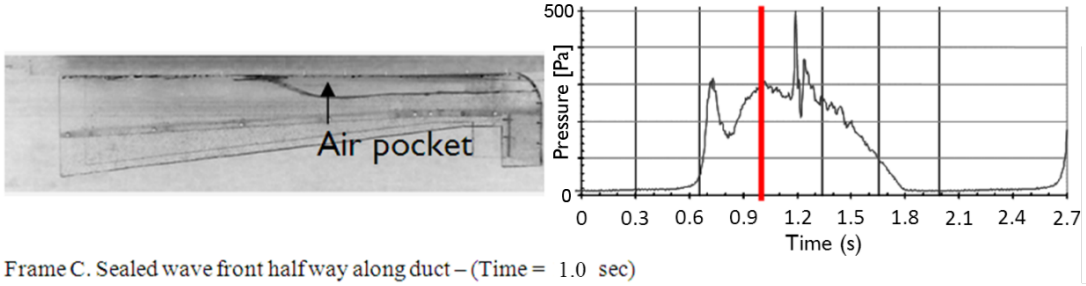

Frame C. Sealed wave front halfway along duct – (Time = 1.0 sec)

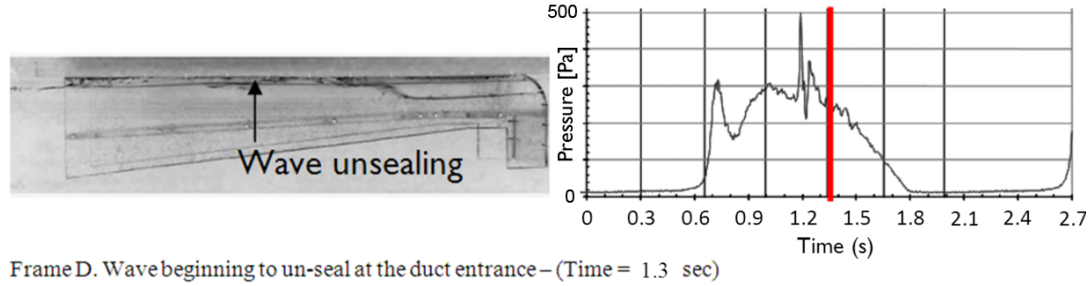

Frame D. Wave beginning to un-seal at the duct entrance – (Time = 1.3 sec)

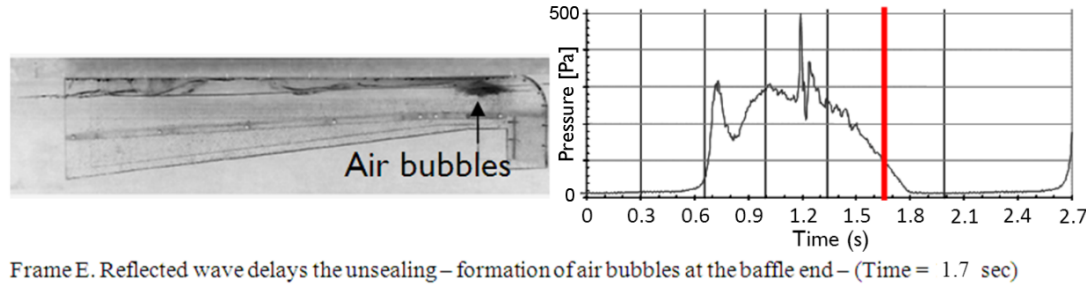

Frame E. Reflected wave delays the unsealing – formation of air bubbles at the baffle end – (Time = 1.7 sec)

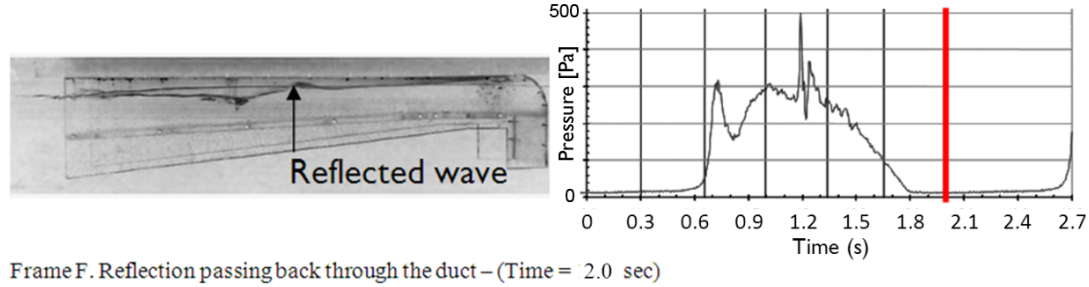

Frame F. Reflection passing back through the duct – (Time = 2.0 sec)

Figure 4.21, Series of 6 frames (A – F) over a wave cycle with corresponding pressure. (T = 2 s, H = 60 mm)

4.7.1 Comparison of Baseline Configuration and Configuration #1

Throughout this work, filled, colour contour plots have been used to show the variation in wave-to-pneumatic conversion efficiency with wave height and wave period. In each plot the colour bar provides a scale for the conversion efficiency and the data points that were used to generate each plot are overlaid onto the plots as black markers. The colour surrounding each marker represents the actual efficiency measured at that point, however the regions in between the markers are interpolated by a function in MATLAB called "*griddata*". This function uses cubic interpolation by the triangulation of data points to fit a 'surface' to the results. A linear interpolation method was also used, however the differences between the plots were minimal. The results were normalised prior to the interpolation in order to improve the fit of the method. The MATLAB function "*contourf*" was then used to generate the fill colours for the plots.

In some instances, this method led to questionable fitting of the coloured contour surface and so, where this has occurred, comment has been made when referencing the plots to state the regions that are likely quirks of the interpolation process. Furthermore, the interpolation across conditions that have not been tested may have meant that some features in the performance have been omitted. Care has been taken to avoid the use of interpolated plots where insufficient performance data were available. Nevertheless, the reader should be aware and cautious of the fact that the regions in between the data points are interpolated and do not represent recorded data, only predicted characteristics.

To aid straightforward comparison, each contour plot was plotted against non-dimensional wavelength and wave height. Additional axes have been included to show the actual wave period and height. The wavelength was non-dimensionalised by the duct length (1.2 m) to provide the ratio "L/L_D" and the wave height by duct entrance height (0.15 m). The non-dimensionalised wavelength is a particularly important design parameter that was referred to throughout the subsequent physical modelling phases.

Figure 4.22 to Figure 4.27 show the comparisons between the baseline configuration and configuration 1 with a dipped stern for three different freeboards. Each of the six tests was conducted using an orifice with $\beta = 0.4$ with a sample of 296 test conditions providing a high definition of results. Of the baseline configurations tested the moderate freeboard (Figure 4.24) gave the best performance and the large freeboard had a negative effect on performance. In contrast to the intermediate scale test results, this showed that tuning the duct entry freeboard to $2/3^{rds}$ the wave amplitude was not necessary for peak performance. For the baseline configuration, it can be seen in Figure 4.22 that setting the freeboard to 5 mm benefitted the

performance for H < 30 mm and $L/L_D < 2$. The plots show two main regions of peak performance; the first between L/L_D = 1.0 and 1 .5 and the second between L/L_D = 3.5 and 3.8. Additional peaks can be seen at $L/L_D \approx 2.5$ and $L/L_D \approx 3.2$ however, these are not as pronounced as the others.

Comparing the baseline configuration and configuration #1 shows that, for a 5 mm duct entry freeboard, there is little difference between the two plots other than the baseline performing slightly better for some conditions. The comparison between the two configurations with a 15 mm freeboard shows that the baseline had higher performance peaks however, configuration #1 performed better for H < 30 mm as it enabled these wave crests to seal with the duct roof. The final comparison between the two configurations with 25 mm freeboards (Figure 4.26 and Figure 4.27) shows that configuration #1 far outperformed the baseline for all of the conditions tested. This demonstrated that by trimming the duct bow up, the dipped stern configuration was able to efficiently capture waves over the range of heights tested. The effect of increasing positive trim angle so that the duct entry freeboard exceeded 25 mm was not investigated at the time. This configuration produced peak conversion efficiencies of around 40 % which was encouraging.

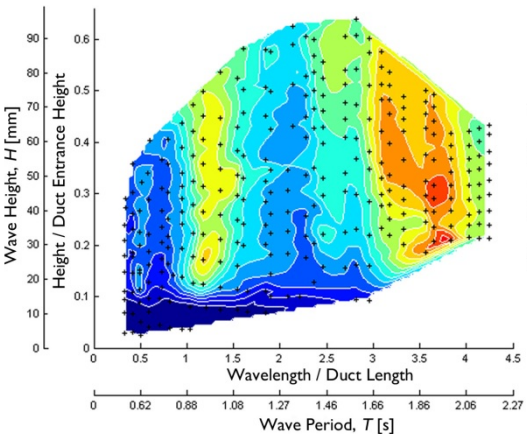

Figure 4.22, Baseline configuration with a 5 mm freeboard.

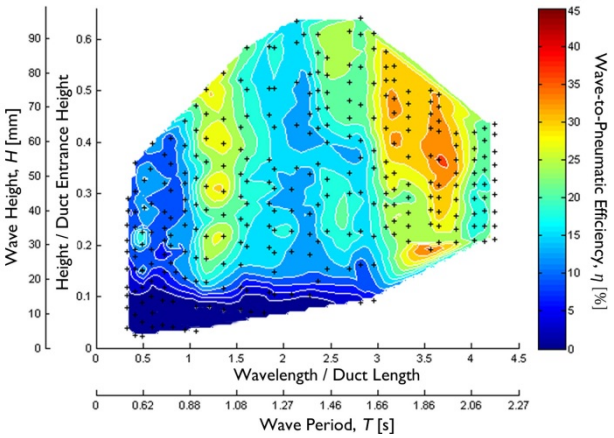

Figure 4.23, Configuration #1 with a 5 mm freeboard.

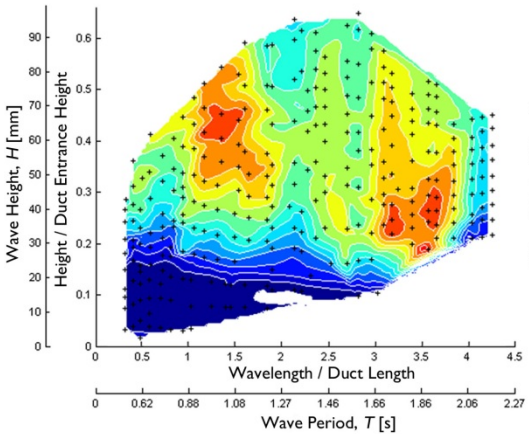

Figure 4.24, Baseline configuration with a 15 mm freeboard.

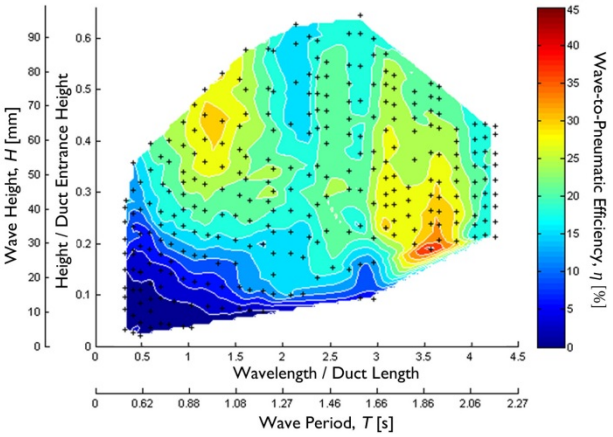

Figure 4.25, Configuration #1 with a 15 mm freeboard.

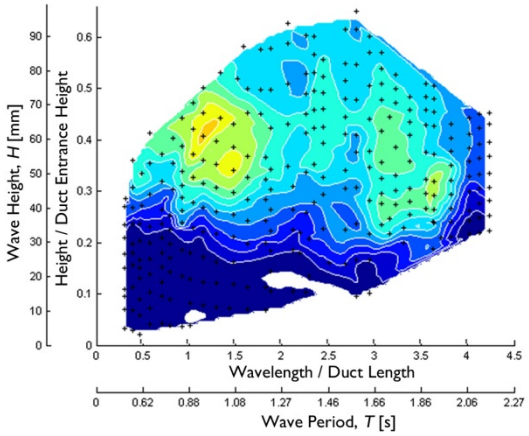

Figure 4.26, Baseline configuration with a 25 mm freeboard.

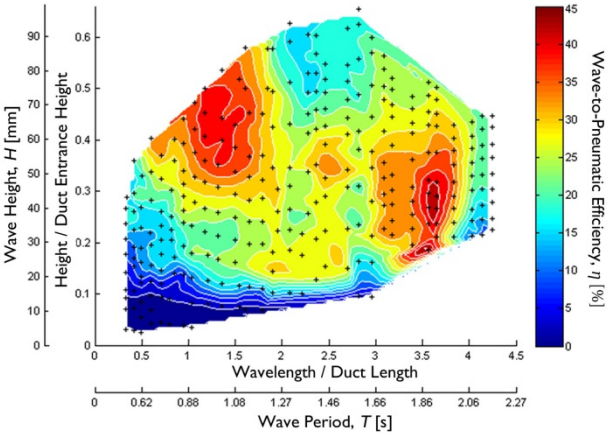

Figure 4.27, Configuration #1 with a 25 mm freeboard.

It was postulated that waves entering the OWEL duct act similarly as they would when entering a harbour: Waves within a semi-enclosed basin such as a harbour have a number of different resonant modes of free surface oscillation, due to the effect of wave reflection from the rear harbour wall and seabed causing standing waves to occur within the basin. Rabinovich (2009) provides a summary of the fundamental frequencies of free oscillation and the first modes of oscillation for several different idealised shapes of harbour.

The two most relevant examples presented by Rabinovich (2009) that can be most likened to that of the 2D OWEL model have been reproduced in Figure 4.28. The first of these two examples is for an open ended, rectangular harbour with a constant depth, d, throughout. Equation [20] shows that the longest fundamental wavelength is equivalent to four times the basin characteristic length, L. Although this example is not an accurate representation of the OWEL duct, due to the lack of inclined floor, it provides a simplified case at one extreme of the geometry. The second example in Figure 4.28 provides the other geometrical extreme; a

rectangular harbour with a floor inclined at 45°. As equation [21] shows, the fundamental wavelength for this case is greater than that for a flat bottom.

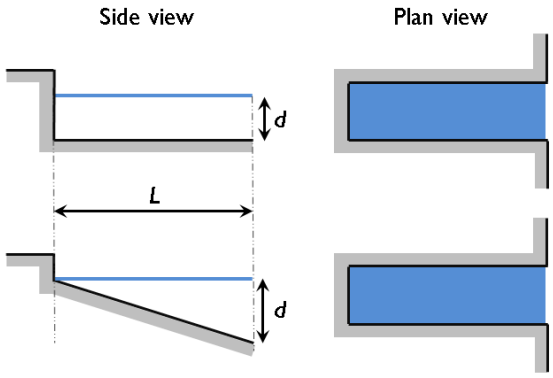

$$T_0 = 2.000\left[\frac{2L}{\sqrt{gd}}\right] \quad [20]$$

$$T_0 = 2.618\left[\frac{2L}{\sqrt{gd}}\right] \quad [21]$$

Figure 4.28, Plan and side views of two ideal harbours with their associated, longest natural periods.

Applying the geometry dimensions of the model configuration #1, d = 0.125 m and L = 1.2 m, to equations [20] and [21] and the mode ratios provided by Rabinovich (2009), yields the results in Table 5. As the OWEL model does not feature a floor sloping at 45° or a flat floor, it is likely that the corresponding resonant periods are between the values of the sloping and flat floor harbours in Table 5.

Table 5, Standing wave periods for different modes for two different basin shapes.

	Constant Depth		Reducing Depth	
Mode (n)	Ratio from T_0	Period [s]	Ratio from T_0	Period [s]
0	1.000	4.33	1.000	5.67
1	0.333	1.44	0.435	2.47
2	0.200	0.87	0.278	1.58
3	0.143	0.62	0.203	1.15

Comparing the resonant periods of the different modes presented in Table 5 with the performance contour plots in Figure 4.22 to Figure 4.27 does not identify any strong correlations. Although the fundamental standing wave period is too great to influence the conditions tested in these experiments, the first, second and third modes have periods within the testing range. It is therefore conceivable that these standing wave modes may have contributed to the peaks in conversion performance shown in the contour plots. Conversely, the unfavourable wave superposition, occurring at periods away from the standing wave modes may have led to the reduction in conversion performance. In addition to the difference in geometry between these ideal cases and the tested OWEL model, other features are likely to have contributed to the differences between the predicted standing wave periods and the periods of

peak performance; The step change transition from deep water to shallow water means that the wave speed reduces tending towards the shallow water wave speed but is unlikely to reach that value in such a short distance. The shallow water wave speed, $\sqrt{gd}$, used in equations [20] and [21] will be greater than that estimated. Furthermore, the baffle at the stern of the duct allows interaction between the internal and external waves which may further modify the internal wave dynamics. With further experimental work and following the approach by Rabinovich (2009) and Wilson (1972) it is possible that the standing wave relationships within the OWEL geometry may be obtained.

4.7.2 Optimisation of the Applied PTO Damping

It was shown in the review of small scale PTO simulators for OWCs in section 3.6 that the performance of OWCs can be sensitive to changes in the damping applied to the air flow by the PTO. Prior to these experiments, OWEL had not been tested with an orifice PTO simulator and the magnitude of damping required to maximise the conversion efficiency was not known. In order to determine the optimum damping a series of orifice sizes were tested to ascertain which yielded the highest performance over a range of wave conditions.

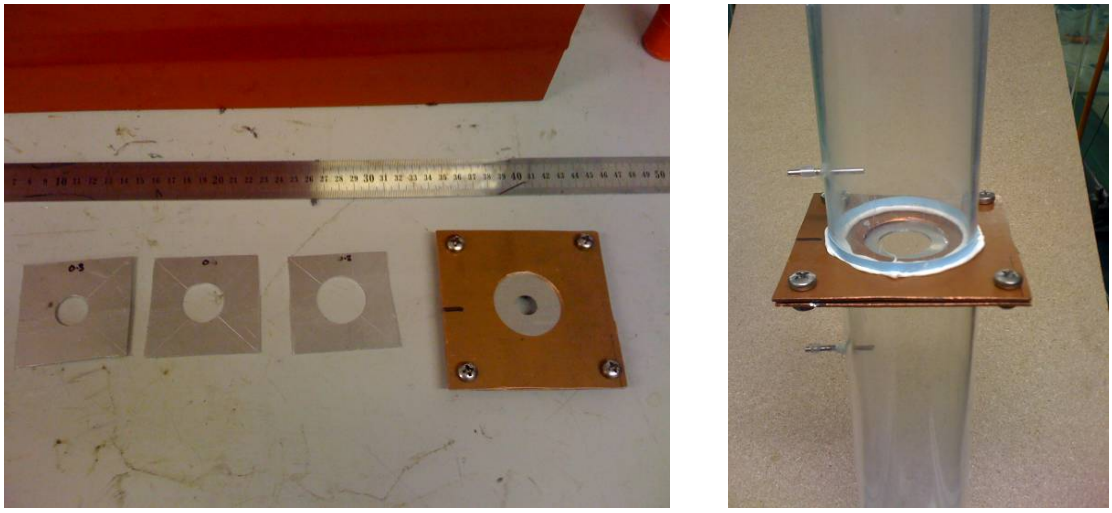

Figure 4.29, Orifice plate construction showing orifices and mounting plate in PTO tube.

Six different orifice sizes were each tested over a representative sample of 23 test conditions that were specified in order to intersect the areas of peak performance found in the initial tests. The wave height was varied whilst maintaining wave periods of T = 1.0 and 1.9 sec, then subsequently the wave period was varied for constant wave heights of H = 30 mm and 60 mm. The 23 test points are shown on the plot in Figure 4.30 which is overlaid onto a performance contour plot from section 4.7.1. The orifice sizes were specified by their β ratio (the ratio of orifice diameter to pipe diameter, which is inversely proportional to the applied PTO damping and resistance to the air flow); these ranged from β = 0.2 to 0.6. Configuration #1 was used for

all of these tests and the freeboard was set at 25 mm. The results from the two iso-height tests and iso-period tests are shown in Figure 4.31 to Figure 4.34.

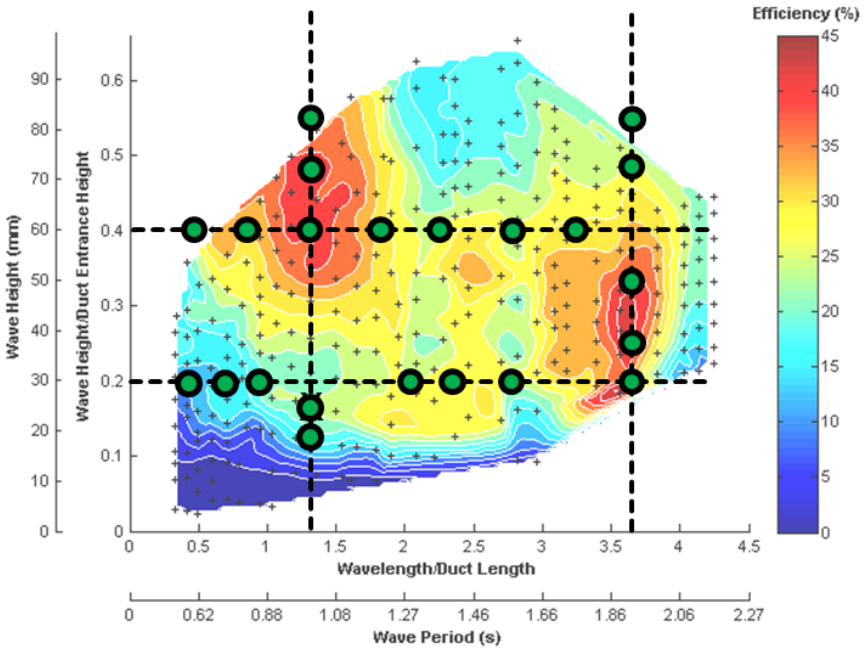

Figure 4.30, The wave H-T pairs used to investigate optimum PTO damping overlaid onto an efficiency contour plot taken from the previous tests.

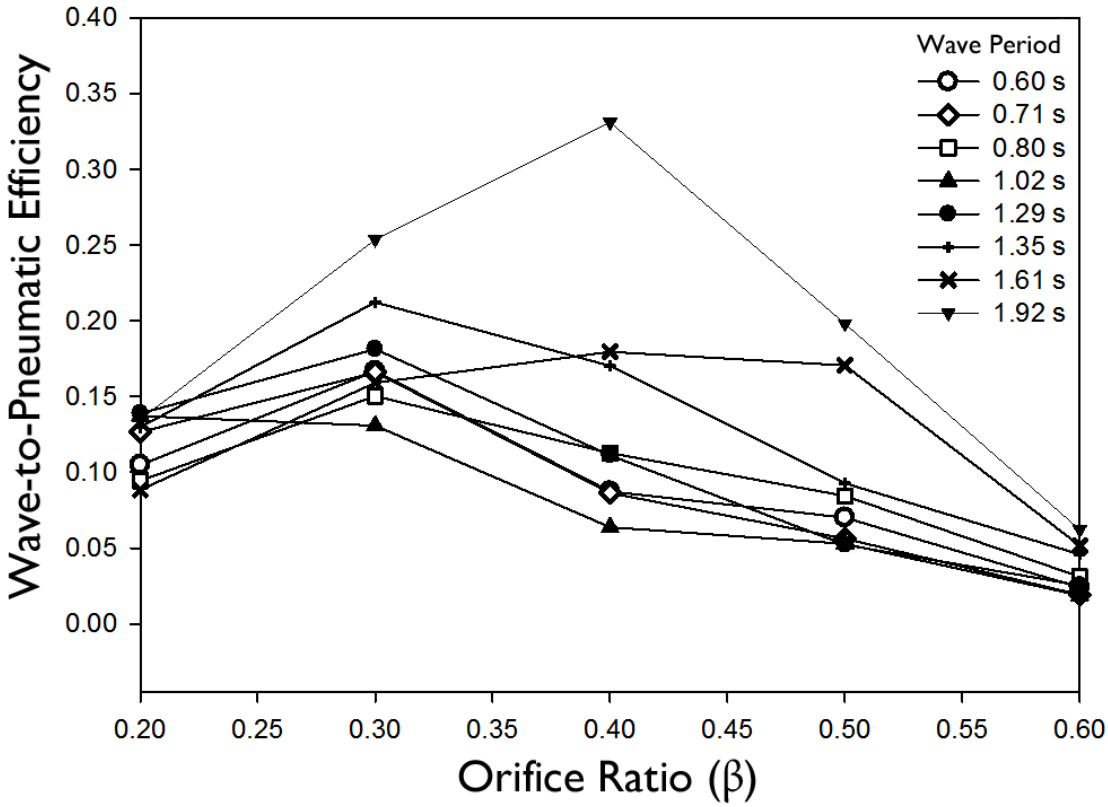

Figure 4.31, The relationship between wave-to-pneumatic conversion efficiency and the orifice size for a range of wave periods with a wave height of 30 mm.

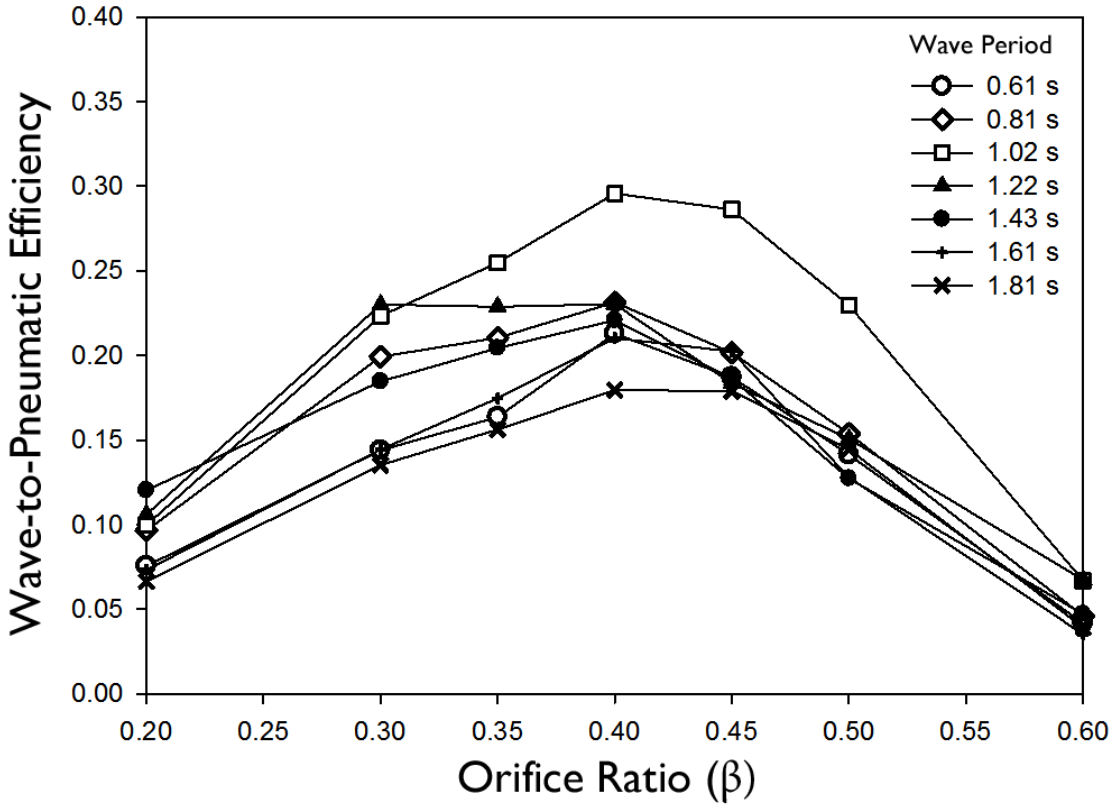

Figure 4.32, The relationship between wave-to-pneumatic conversion efficiency and the orifice size for a range of wave periods with a wave height of 60 mm.

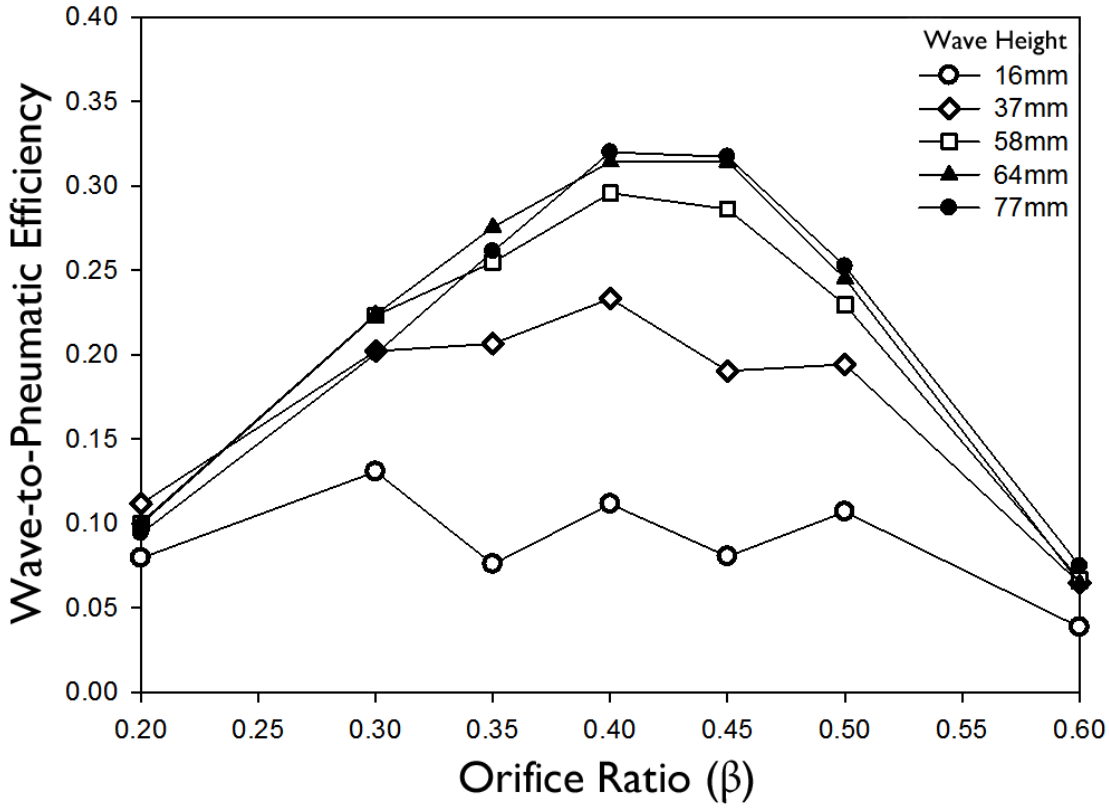

Figure 4.33, The relationship between wave-to-pneumatic conversion efficiency and the orifice size for a range of wave heights with a wave period of 1.0 s.

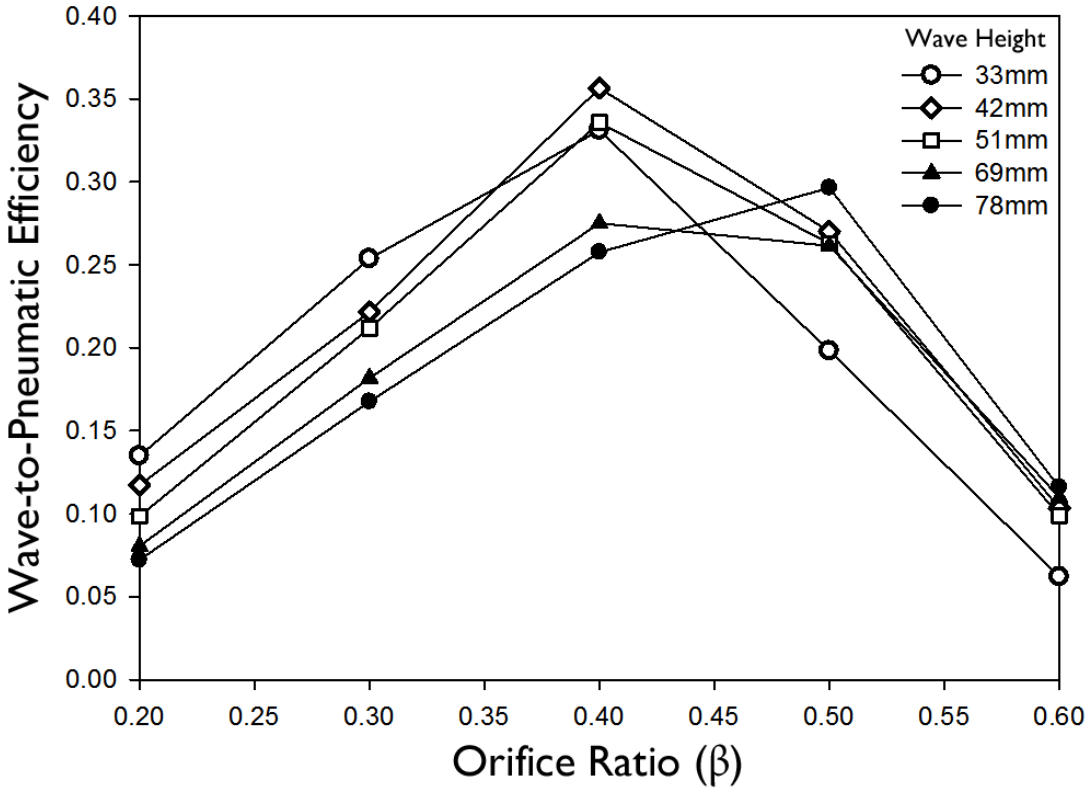

Figure 4.34, The relationship between wave-to-pneumatic conversion efficiency and the orifice size for a range of wave heights with a wave period of 1.9 s.

The graphs in Figure 4.31 to Figure 4.34 confirm that the performance of the device is sensitive to the applied PTO damping. In Figure 4.32 (H = 60 mm) for example, a wave period of 1.0 s resulted in a peak performance of approximately 30 % for a β = 0.4 orifice. An increase or decrease in orifice size to β = 0.6 or 0.2 resulted in efficiencies of less than 10 %. It was therefore concluded that the device should optimally damped to ensure the highest conversion performance. For most of the waves tested the optimum β was between 0.35 and 0.45 with the greatest majority at β = 0.4. The graphs show that as the exhaust air flow rate reduces, the ideal turbine damping increases as a smaller orifice is required to generate a sufficient pressure drop. It can be seen in Figure 4.33 (T = 1 sec) that as wave height reduces the optimum orifice ratio reduces as a higher damping is required. Similarly, in Figure 4.31 and Figure 4.32 (60 mm and 30 mm) there is a slight trend for the optimum damping to increase as the wave period decreases.

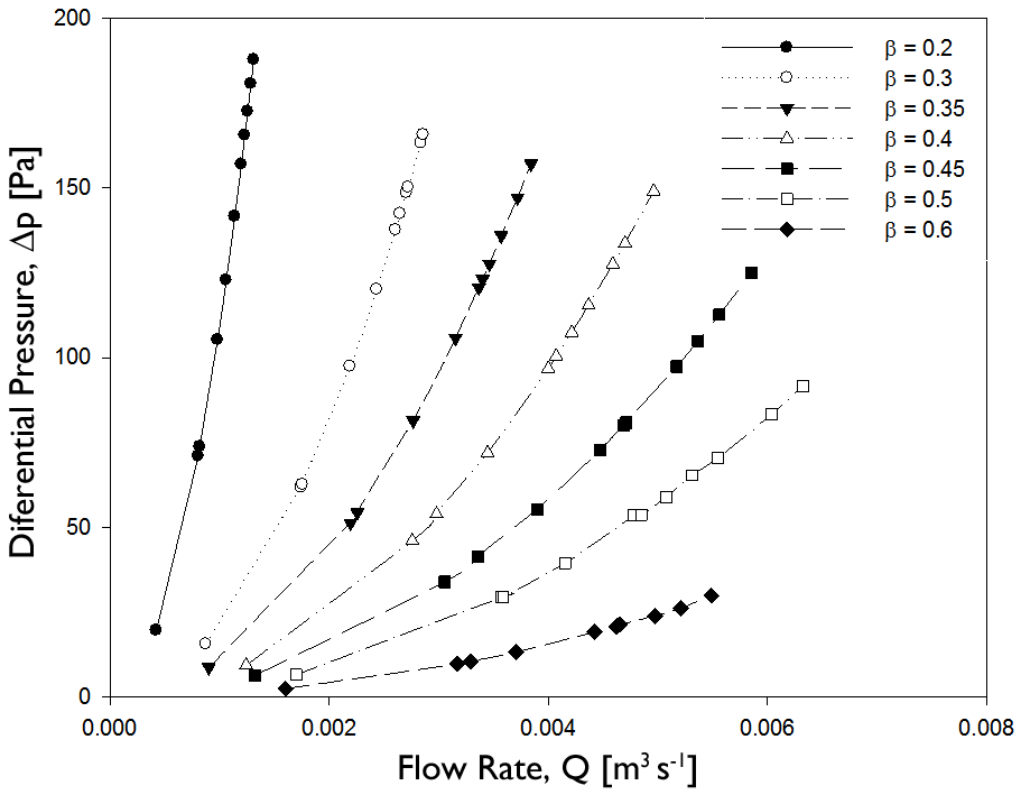

Figure 4.35, Non-linear pressure - flow relationship for the various orifice sizes tested.

It was discussed in section 3.6.1 that orifice plates exhibit a non-linear, pressure – flow relationship. Figure 4.35 displays this non-linear relationship for each of the orifice sizes tested. The damping provided by the orifice is the ratio of the pressure drop to flow rate, equation [15]. As this ratio is not of linear form, the level of damping depends on the flow rate, therefore, for a $\beta = 0.4$ orifice, the damping provided is not a single value. At the time of testing, the relationship between performance and orifice damping had not been fully understood. Configurations #2 – 4 were tested using a smaller orifice ($\beta = 0.2$) therefore providing a higher PTO damping than was optimal. This resulted in the conversion efficiencies of the duct being significantly reduced, as can be seen by comparing Figure 4.36 with Figure 4.24. Nevertheless, the results from configurations #2 – 4 remain directly comparable despite the poor efficiencies. It was assumed however, that the relationship between the changes in duct geometry and the conversion performance were not affected by the over damping of the system.

4.7.3 Configuration #2 - Energy Dispersion Methods

Results from the initial tests and observations suggested that wave reflections from the baffle were detrimental to the conversion performance. It was observed that as the reflected wave crest passed back along the duct, it collided with subsequent incoming wave crest. For some conditions this caused the incident crest to break inside the duct, therefore losing energy, or be detrimental to the sealing of the wave crest. Therefore, the focus of these tests switched to study

the effect different baffle arrangements had on performance with the thought that a reduction in the reflections would aid the conversion process and increase the efficiency.

The first modification tested was configuration #2 which was similar to the baseline configuration but had a series of coarse foam wedges attached to the baffle wall. The foam was the same that is commonly found in passive wave absorbing beaches in wave tanks and it was anticipated that it would dissipate some of the remnant wave energy in order to reduce reflections. Figure 4.37 shows the resulting performance map when the foam was included. When compared to the baseline condition in Figure 4.36, there appears to be little difference, however, by summing the average powers over the entire data set for each configuration, it was found the baseline configuration outperformed configuration #2 by approximately 10%. This

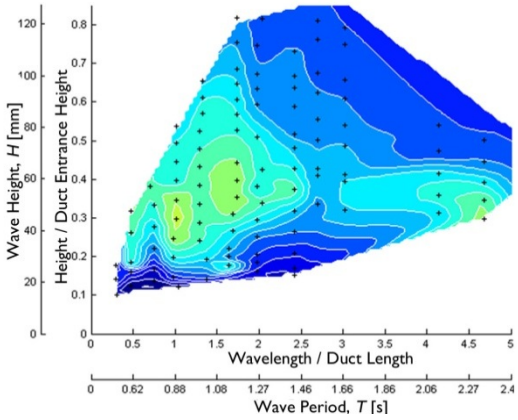

Figure 4.36, Baseline configuration with a 15 mm freeboard and orifice $\beta = 0.2$

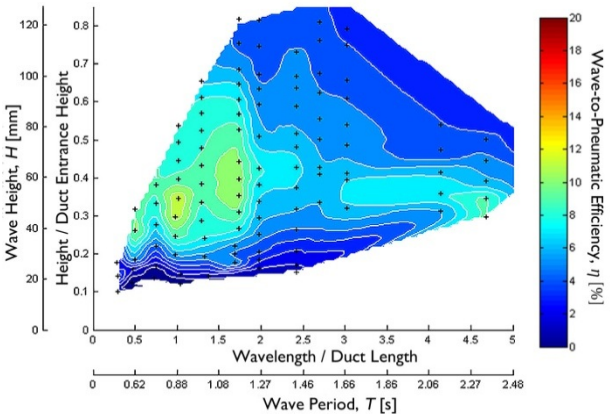

Figure 4.37, Configuration #2 with a 15 mm freeboard and orifice $\beta = 0.2$

result contradicted the previous thoughts and subsequently, further investigation was carried out. As configuration #1 had significantly outperformed the baseline it was decided to incorporate this into the subsequent configurations. Figure 4.38 shows a contour plot from configuration #1, run with a reduced wave sample focused on the shorter period waves and a $\beta = 0.2$ orifice as used in configurations #2 – 4. As with the baseline configuration with the $\beta = 0.2$ orifice, the performance was poorer than configuration #1 with a $\beta = 0.4$ orifice, see Figure 4.25, however, it outperformed the baseline configuration with a $\beta = 0.2$ orifice (Figure 4.36), thus corroborating with the results found in the previous tests.

Foam wedges were also attached onto the baffle of configuration #1 as a side experiment to see if it had a similar effect as it did to the baseline. Far more conclusively, this resulted in reduced performance as can be seen by comparing Figure 4.38 with Figure 4.39. This confirmed the conclusion that the energy absorbing foam should be rejected as an option for reducing wave reflections

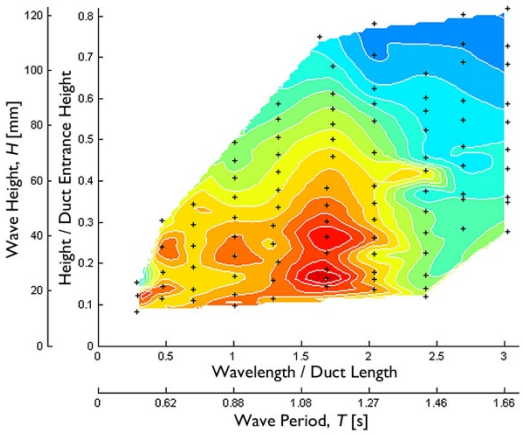

Figure 4.38, Configuration #1 with a 15 mm freeboard and orifice $\beta = 0.2$.

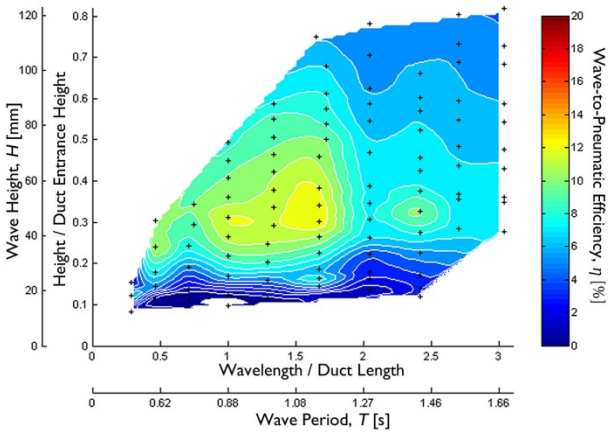

Figure 4.39, Configuration #1 with foam wedges, a 15 mm freeboard and orifice $\beta = 0.2$.

4.7.4 Configuration #3 - 45° Baffle

The next attempt to reduce wave reflections was to reduce the angle of the baffle to the incident waves. A new baffle plate was installed on the model at 45° to the duct roof to provide less of an abrupt obstacle to the wave front. Figure 4.40 shows the performance of configuration #3 with the 45° baffle and comparing this to Figure 4.38, it is again apparent that configuration #1 had superior performance.

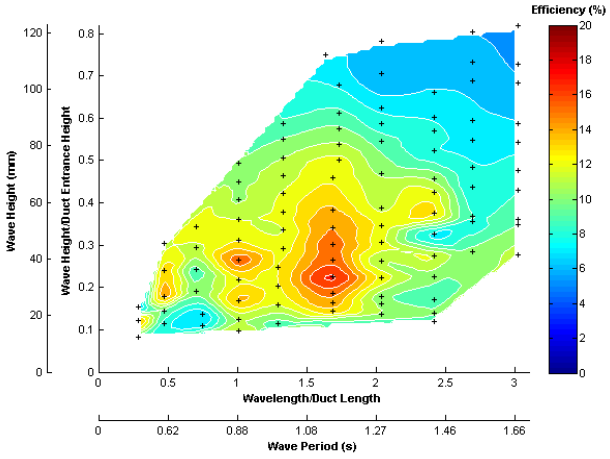

Figure 4.40, Configuration #3 with a 15 mm freeboard and an orifice with $\beta = 0.2$.

4.7.5 Configuration #4 - No Baffle

The final investigation of reducing wave reflections involved removing the baffle plate entirely. A plate extended parallel from the roof, down into the water behind the duct with the stern dipped. This was intended to allow remnant wave energy to exit the rear of the duct freely and so keeping reflections to a minimum. However, the design was found to spill air out of the rear of the duct and so the tests were aborted as it was deemed impractical.

4.7.6 Configuration #5 – Flat Plate Baffle

The previous tests, reported in sections 4.7.3 to 4.7.5, showed that reducing the wave reflections was consistently detrimental to the conversion efficiency of the model. It was therefore concluded that the internal wave reflections from the baffle were necessary for efficient energy conversion. It was postulated that, at the peak wavelengths, beneficial wave superposition occurred between the incident and reflected waves within the duct. This constructive interference led to an increase in wave height and so a better seal was made between the wave crest and the duct roof. For this reason, it was hypothesised that the performance could be increased by enhancing the wave reflections rather than dissipating the remnant energy, in order to improve sealing characteristics. Configuration #5 was used to test this hypothesis by investigating a different baffle design to promote wave reflections.

The design of configuration #5 replaced the rounded baffle with square shaped baffle plate which presented the wave crest reaching the stern of the duct with a vertical wall from which to reflect. The design was tested with an orifice with $\beta = 0.4$ over an extensive series of test conditions consisting of just over 200 *H-T* pairs, similar to those used in the earlier testing reported in section 4.7.1. The results, which are shown in Figure 4.41, were very similar to those from configuration #1 with exceptions in a few areas. Figure 4.42 shows a contour plot comparing the performance of configuration #1 with configuration #5 with the calculated percentage differences between the two sets of results. The white and light grey areas of Figure 4.42 represent an improvement in performance over configuration #1 whilst the darker areas indicate a reduction. It can be seen that configuration #5 benefited performance particularly in between the two peaks at relatively large wave heights. However, it reduced the performance at the peak for $L/L_D = 3.5$ to 3.8, the wave period spread of the peak at $L/L_D = 1.0$ to 1.5 and significantly decreased efficiencies in the shorter period, low height waves.

From this analysis, it was concluded that configuration #5 may prove to be cheaper and simpler geometry to manufacture at large scale however, its detrimental impact on key areas of performance meant that the performance of configuration #1 was favoured.

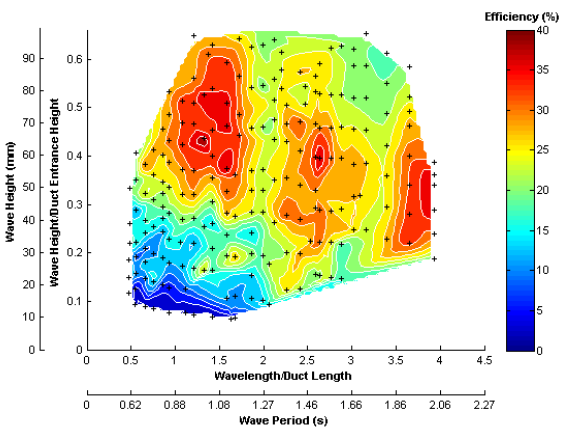

Figure 4.41, Configuration #5 performance plot with 25 mm freeboard and $\beta = 0.4$.

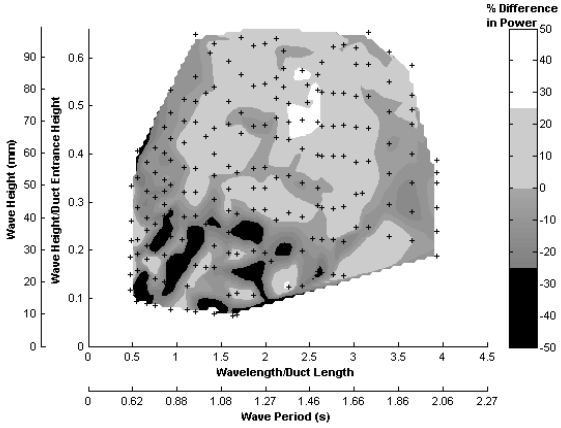

Figure 4.42, Comparison between configuration #1 and configuration #5.

4.7.7 Repeat of the Optimum Configuration

The results from the tests conducted with model configurations #1 – 5 show that configuration #1 with a 25 mm freeboard and orifice with $\beta = 0.4$ performed the most favourably. To confirm this result a repeat of this experiment was carried out at the end of the testing programme. This incorporated all of the refinements in test procedure and acted as a further repeatability check. Figure 4.43, shows the performance of configuration #1 re-run with approximately 200 *H*-*T* pairs. Comparing this with the contour plot for the original test in Figure 4.27 shows similar performance features with a reasonable comparison between the experimental results, particularly the locations and magnitudes of the performance peaks at $L/L_D = 1.0 – 1.5$, 2.5 and 3.5 – 3.8.

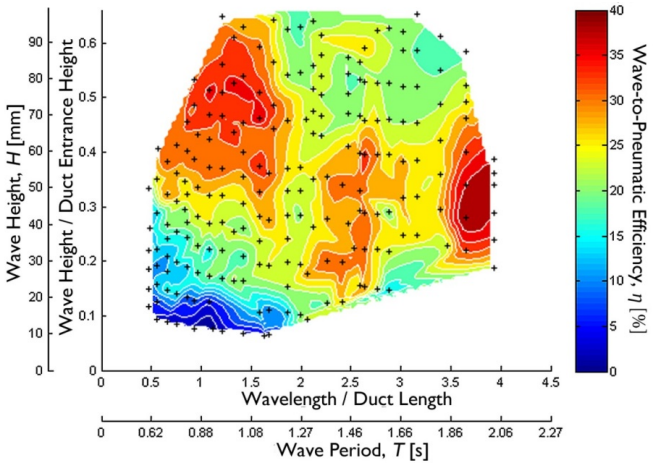

Figure 4.43, Repeat test of configuration #1, 25 mm freeboard $\beta = 0.4$ orifice.

The plot in Figure 4.44 provides examples of the repeatability of the mean performance efficiency for the duct with configuration #1. The data plotted are from two separate experiments; (A) was conducted at the start of the testing phase and is reported in section 4.7.1, the second experiment (B) was from the repeat of the optimum configuration, as discussed

previously in this section. The mean performance measured in the second experiment (B) was consistently greater than that from the first experiment. These differences are likely to have come about due to changes in the set up of the model and equipment. In between the two experiments the tank had been emptied, the model modified to different geometries and then returned to its original condition, the pressure sensor amplifier was also changed and recalibrated. Although care was taken to replicate the original test setup, difference in any of these factors may have resulted in the discrepancies between the measured performance. No other repeat runs were carried out during these tests and so observing the variation in experimental error within the results is not possible.

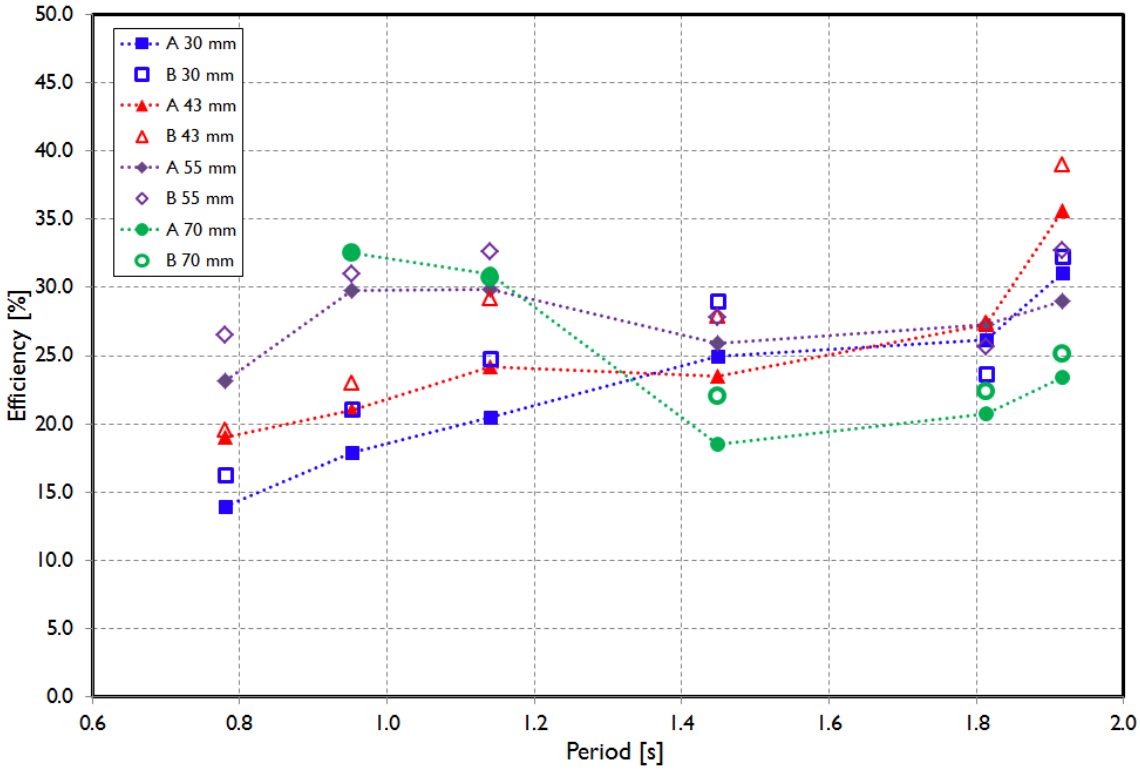

Figure 4.44, The repeatability of mean performance efficiency for four different wave heights over a range of periods taken from two separate experiments.

4.7.8 Typical Air Pressures and PTO Damping

Figure 4.45 to Figure 4.49 show the typical variation of differential pressure over two wave cycles for a range of wave periods with $H \approx 55$ mm for configuration #1 with a 25 mm freeboard and $\beta = 0.4$ orifice. The plot in Figure 4.50 shows the variation in efficiency for each of the five cases presented in Figure 4.45 to Figure 4.49 and that, for all of the cases the conversion efficiency was greater than 25%.

Figure 4.46 and Figure 4.49 are the pressure traces for waves within the two main regions of peak performance, L/L_D = 1.0 to 1.5 and 3.5 to 3.8 respectively. For the wave case, T = 0.80 s in Figure 4.45, the progression of the internal wave during a wave cycle resulted in relatively low differential pressures being developed and thus a low corresponding air flow. A number of small peaks in the pressure are present and are a likely result of small accelerations and variations in the free surface profile of the internal wave.

The characteristics of this air flow for T = 1.12 s, in Figure 4.46, are somewhat different to that of the slightly shorter wave condition in Figure 4.45. The air flow gradually increases through a wave cycle until a point approximately half way through the period and is subsequently followed by a large spike in pressure caused by the internal wave crest arriving at the entrance to the power take off tube and forcing out the remaining air at the stern of the duct. At full scale this characteristic will not be present to the same degree that is observed in small scale tests due to the effects of air compressibility. As was discussed in section 3.5, air compressibility at large scale will act to damp out sharp spikes and short time scale events, meaning the flow at the PTO will be smoother than that presented here.

The air flow behaviour for the wave case of T = 1.27 s, in Figure 4.47, was very similar to that of T = 1.12s (Figure 4.46). In this case however, the large spike in air flow and measured differential pressure occurred slightly later than the main region of air flow. The spike in air pressure is also less severe than that for the wave condition of T = 1.12 s. The profile of the air flow for the longer wave period examples in Figure 4.48 and is far more like a steady pulse. The air flow pulse for T = 1.72 s lasts for approximately 75% of the wave period whereas this reduces to around 50% for the T = 2.03 s case. These plots indicate much greater air flow and thus higher power than for the other wave cases. In the case of T = 2.03 s, this increased air flow resulted in a high efficiency that exceeded 35 %.

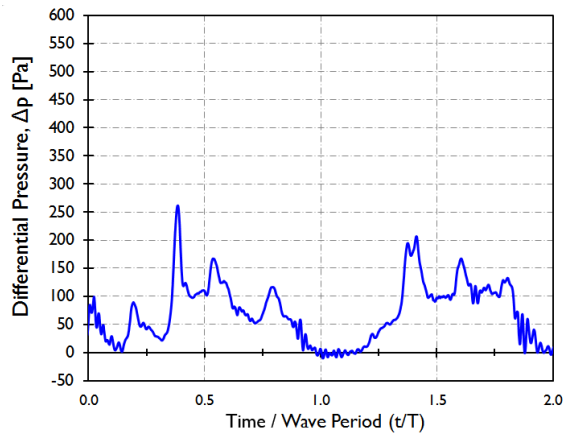

Figure 4.45, Differential pressure for T = 0.80 s.

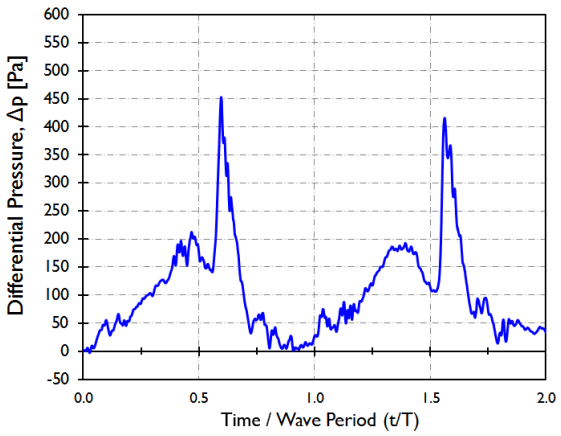

Figure 4.46, Differential pressure for T = 1.12 s.

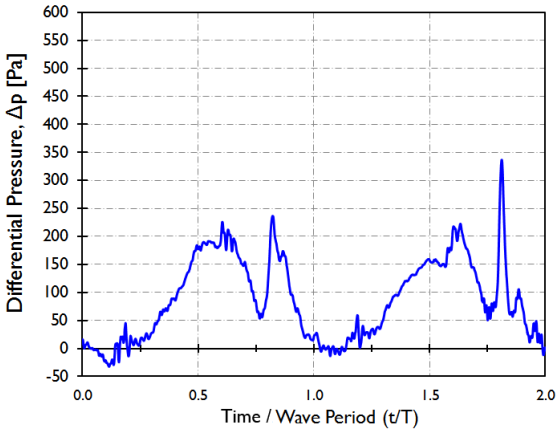

Figure 4.47, Differential pressure for T = 1.27 s.

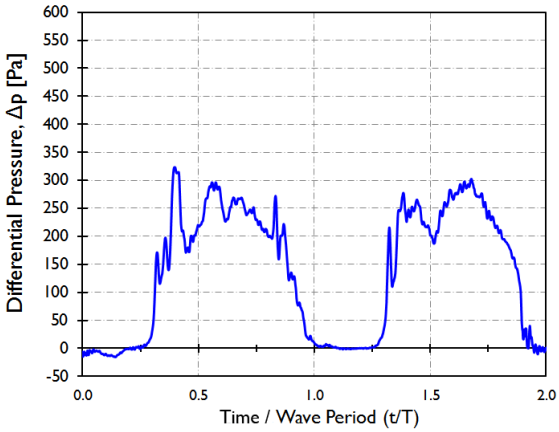

Figure 4.48, Differential pressure for T = 1.72 s.

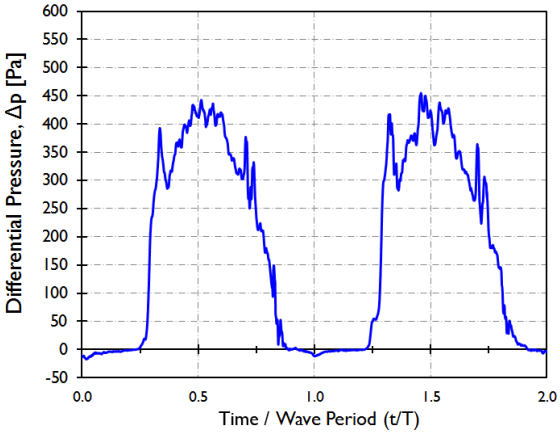

Figure 4.49, Differential pressure for T = 2.03 s.

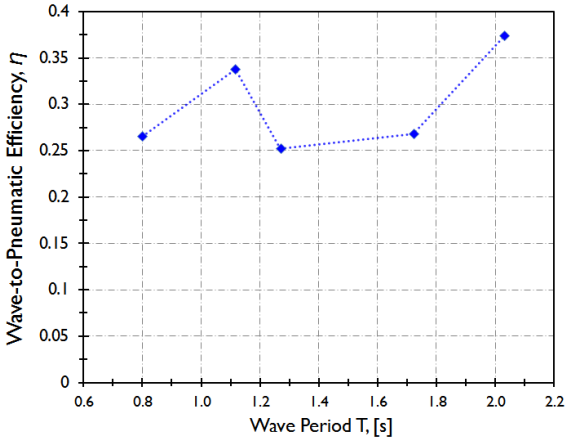

Figure 4.50, Efficiency for the wave test cases in Figure 4.45 to Figure 4.49.

The typical average pressure drop across the orifice was ranged from 66 Pa for the shortest period wave (Figure 4.45) to 180 Pa for the longest period wave (Figure 4.49) with an equivalent range of flow rates between 0.0032 – 0.0055 m^3s^{-1}. The range of average PTO damping, calculated using equation [15] was 20,000 – 33,000 $N.s.m^{-5}$. This indicates average velocities between 6-10 $m.s^{-1}$ through the 25 mm diameter orifice (β = 0.4), though these can be expected to double at peak flow. The high velocity air indicates that there may be significant losses occurring between the duct and orifice especially at rough edges. Even small changes in pressure at this scale lead to large changes in the predicted performance.

4.8 Summary

These initial wave flume tests provided the ability to study the behaviour of the internal wave and begin to understand the intricacies of the energy conversion process. The transparent sides of the tank and model allowed the conversion cycle to be observed and therefore inform the investigations to develop beneficial modifications to the model.

Over the course of the investigations, it was found:

- An orifice is a suitable PTO simulator for OWEL
- Performance was sensitive to applied PTO damping
- The relationships proposed in the previous OWEL development work were not observed
- By trimming the duct stern down, the duct roof sloped downwards meaning that waves of any height were able to seal and so performance was improved over the baseline design.
- The device was demonstrated to be frequency dependent, contrary to the original thoughts by the developer.
- Initial thoughts that the internal reflected wave was detrimental to power capture were disproved.
- Harbour wave theory of operation was postulated, meaning that internal wave reflection benefits the performance as was observed in the tests.
- Two main regions of peak performance of wave-to-pneumatic conversion efficiencies exceeding 40% were identified at the same wave conditions throughout all of the testing L/L_D = 1.0 – 1.5 and 3.5 – 3.8, with a third, smaller peak in between the two at L/L_D = 2.5.

At the end of the testing programme, it was confirmed that funding had been awarded to continue the development of OWEL. This was to include an extensive series of physical modelling in a large wave basin in realistic conditions. The findings of this initial physical modelling study were used to directly inform the design of the wave basin testing that followed on. In particular, the conclusions of this testing were used to:

- Aid the design of the multi-duct model, including the improved trim position.
- Define the range of wave conditions that should be used in the testing
- Show that an orifice PTO simulator could be used and that the damping it provided influenced the power capture of the duct.

5 Multi-Duct Platform Physical Modelling

5.1 Introduction

During 2008, OWEL was awarded a research grant from the South West Regional Development Agency (SWRDA Grant No.202307). A work package within the resulting project was to carry out an extensive, small scale, experimental programme at a wave basin. After comparing a number of facilities and their associated costs, the wave basin at the Hydraulics and Maritime Research Centre (HMRC), at University College Cork, was chosen by ITP to be the most suitable.

The objectives of the experiments were predominantly directed by OWEL and ITP however, the methodology and design of the tests was directly informed by the learning from the initial physical modelling of chapter 4. The aims were intended to support the development of a technical and economic review to provide a business case for the future development of OWEL. Whilst the model construction and testing was carried out by the staff at HMRC, the data were analysed and conclusions were drawn by the author.

A principal difference between these tests and those conducted previously, was that the model comprised five individual ducts combined in a single device. The design of the multi-duct model was carried out by ITP and is detailed in section 5.3. The concept of joining a number of ducts together to form a large platform had been considered when the original OWEL concept had been patented. The intention was to provide a number of cost reducing benefits over the deployment of many single duct units. It was postulated that a future, multi-duct platform could utilise a single power take-off, generator, grid connection and mooring system as well as providing a stable platform for maintenance. Whilst this is a reasonable design point of investigation for future commercial designs, the likelihood of being able to raise the required project finances for such an ambitious device at this stage of development was slim. It would have therefore been more appropriate to conduct this testing with a single duct model to understand its intricacies before considering the complexities of a combined array. Nevertheless, the testing provided useful insight and conclusions to aid the development of OWEL and may be of further value if a platform configuration is later considered.

Prior to this physical modelling, OWEL had not been tested in irregular waves and therefore a primary objective was to test the behaviour of the model in realistic, directional short crested, irregular sea states with a classical Bretschneider spectrum. In addition, other than the initial proof of concept tests in the Solent towing tank during 2001, no attention had been paid to

testing a floating model. These tests were the first real opportunity to experiment with the naval architecture of the device and observe its performance whilst floating in a moored state. It would have been more logical to at first test a single duct and ensure that was understood before progressing to a complex multi-duct model with many unknowns. However, the grant was awarded with the objective of evaluating the design of a multi-MW, multi-unit platform and so no provision was made to initially test a single duct.

Testing occurred over two periods; two weeks during October 2009 and four days of follow-up tests in December 2009. This provided a break for initial analysis and re-evaluation of the test schedule based on the results obtained, therefore enabling the second testing period to be better utilised. The first testing period was split into two phases of investigation; static and floating conditions. Whereas the second visit to the facility was purely for a floating model in order to fulfil the primary objective of providing realistic performance data.

5.2 Objectives

The focus of these investigations was to provide performance data from a floating model in realistic, irregular sea states in order to inform the generation of a techno-economic model. Further to this, the objectives of the basin testing were intended to increase the knowledge and understanding of OWEL;

- Determine the optimum applied PTO damping.
- Assess the performance of the static model in regular and irregular seas.
- Assess the performance of the floating model in regular and irregular seas.
- Produce data suitable to validate numerical models.
- Measure motions to investigate relationship between motions and performance.

5.3 Wave Basin Facility

The HMRC wave basin is 25m long, 18m wide and 1m deep. Therefore, depending on wavelength, it is able to produce a mixture of intermediate depth and deep water waves. The wave generation system consists of 40 flap type, wedge shaped aluminium paddles attached to the 18m side of the tank, as can be seen in the image in Figure 5.1. The wave makers were capable of generating regular and directional, irregular seas up to a significant wave height of 0.18 m and period of 2.5 s. Active absorption is incorporated into the paddle system which uses a feedback signal from force transducers to adjust paddle motion in order to absorb unwanted reflections in the basin.

Figure 5.1, General view of HMRC tank with yellow wave makers to the left.

To further minimise wave reflections, an artificial, passive beach is located at the opposite end to the paddles. Data from the wave probes, pressure sensors and motion tracking system were all sampled at 32 Hz. The regular wave tests were each sampled for 64 seconds following a period of continuous operation for approximately one minute in order to establish a quasi-steady state. The irregular wave tests were sampled for 256 seconds in order to capture all of the wave components of the deterministic wave spectrum, see Payne (2008) for further information

5.4 Model

The model geometry incorporated the learning from the initial 2D tests with principal dimensions, such as entry height and duct length, being reduced from those of the 2D model by approximately 70 %. The ducts all had roofs angled bow up, a horizontal keel perpendicular to SWL and contracting side walls at 8°. A drawing and dimensions of a single duct are given in Figure 5.2. From this, it can be seen that the characteristic duct length, L_D, was 0.831 m. The entire of the duct geometry was constructed from 10 mm and 6 mm, transparent Perspex. The air exhaust pipe was standard drainage pipe with a diameter of 52 mm and contained an orifice plate to simulate a PTO.

The drawings in Figure 5.3 show the arrangement of the five ducts on the common baseplate with the inclusion of sections of buoyancy underneath the model. When testing the static model, the buoyancy was not present and the base was flat. The duct roofs were angled upwards similarly to the configuration found beneficial in the initial 2D tests. This resulted in the freeboard at the bow being 25 mm whilst the still water level met the duct roof at the stern just aft of the PTO tube.

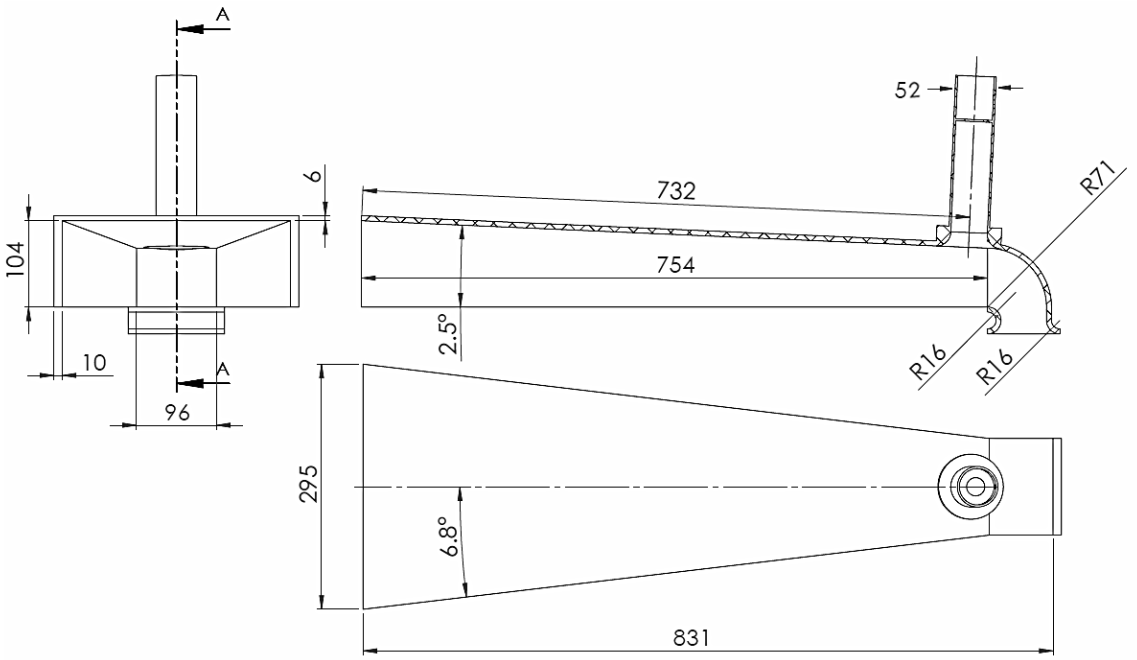

Figure 5.2, A single duct from the multi-duct model with all dimensions given in mm.

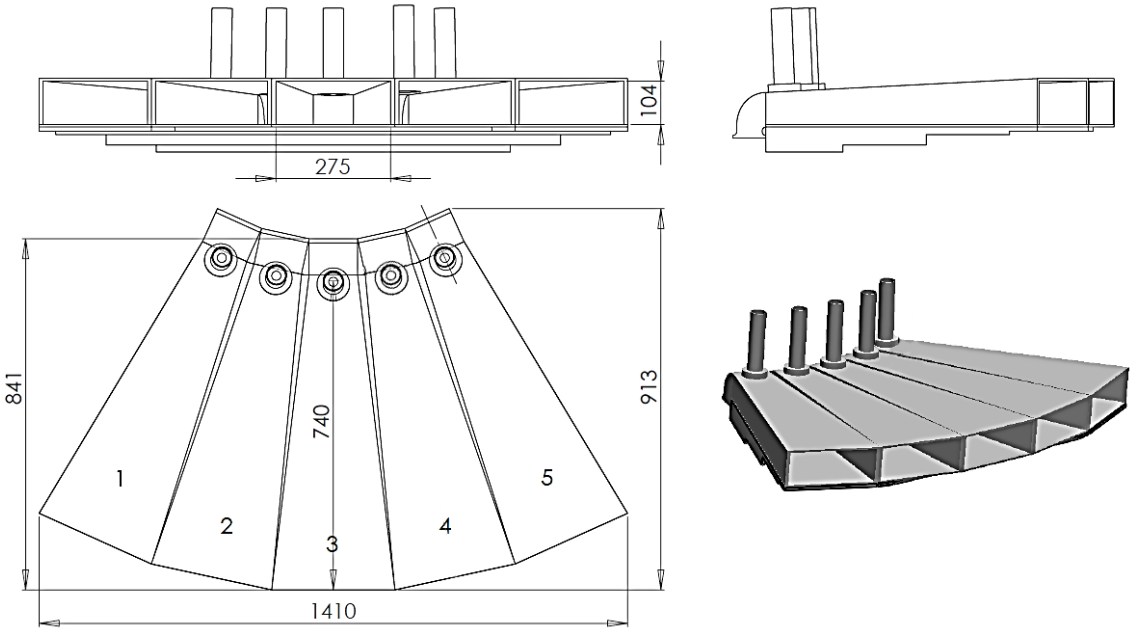

Figure 5.3, The five duct model with staggered buoyancy underneath with all dimensions in mm.

The ducts in Figure 5.3 are labelled 1 – 5. The naming convention used throughout this chapter and also during the tests, specifies the location of the duct rather than its sequential number. Therefore, each duct was named as follows:

1 – “Starboard”

2 – “Starboard Quarter”

3 – “Middle”

4 – “Port Quarter”

5 – “Port”

The particulars of the geometry configuration in the second phase are the same as those just described. The buoyancy and naval architecture design changed significantly between the test phases; this however, is described in detail in section 5.8.

The mooring arrangement used for station keeping of the floating model was a typical configuration used in the testing of small scale, floating WECs at HMRC and is shown in a schematic in Figure 5.6. It comprised three catenary lines; two forward lines with a +/- 30° spread and a rear line. Some mooring forces were recorded using a small, waterproof, tension load cell attached at the connection of the mooring line to the model however, their analysis is beyond the scope of this work.

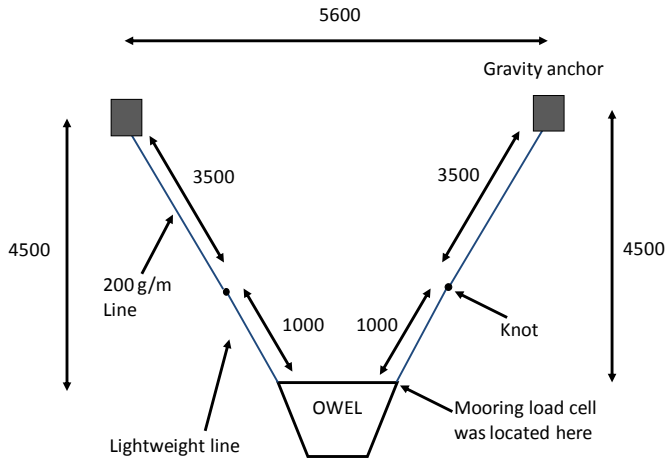

Figure 5.4, Mooring layout for the floating tests, not including the rear catenary.

5.5 Orifice Plate Arrangement

As with the previous initial testing, an orifice plate was used to simulate the power take off and provide the necessary damping and to allow the air flow to be measured. The thickness of the plates was greater than that specified by the British Standard, BS 5167-2, [British Standards Institution (2003)] but the arrangement of the pressure tappings and chamfer on the downstream side were in keeping with the standard, see section 3.6.1 for further details. Rather than using a differential pressure sensor per orifice, two separate pressure sensors were provided by HMRC to measure the pressure drop across the orifice. These were specified by ITP to have the same accuracy and characteristics as the sensor used in the initial testing as reported in section 4.5. The construction of the mounting within the 52mm diameter tubes allowed them to be easily swapped to investigate the effect of applied PTO damping on the power capture.

In addition to the model geometry, HMRC also manufactured the various orifice plates used in the testing and calibrated them to determine their discharge coefficient (C_D). The calibration

process utilised the PTO tube that the orifice was mounted in for the tests, the arrangement of the tube and orifice are shown in Figure 5.5. The tube was manually oscillated vertically in still water. The small float within the tube remained at the same vertical position at the water surface and acted as a piston within the pipe, forcing air through the orifice. Motion tracking markers were attached to the exterior of the pipe and to a thin rod which was in turn mounted on the float within the tube. This allowed the motion tracking system to record the vertical position of the tube, z_1, and internal free surface, z_2. Assuming that compressibility was negligible, the air volume flow rate, Q, was determined from the time history of the marker positions providing a change in volume from an initial time record, t_1, to the subsequent time record, t_2. The time series of air volume flow rate was subsequently calculated and combined with the time series of the measured differential pressure across the orifice. This method also assumed that the float within the tube, that the rod and marker were attached to, was directly equivalent to the position of the free surface in the tube.

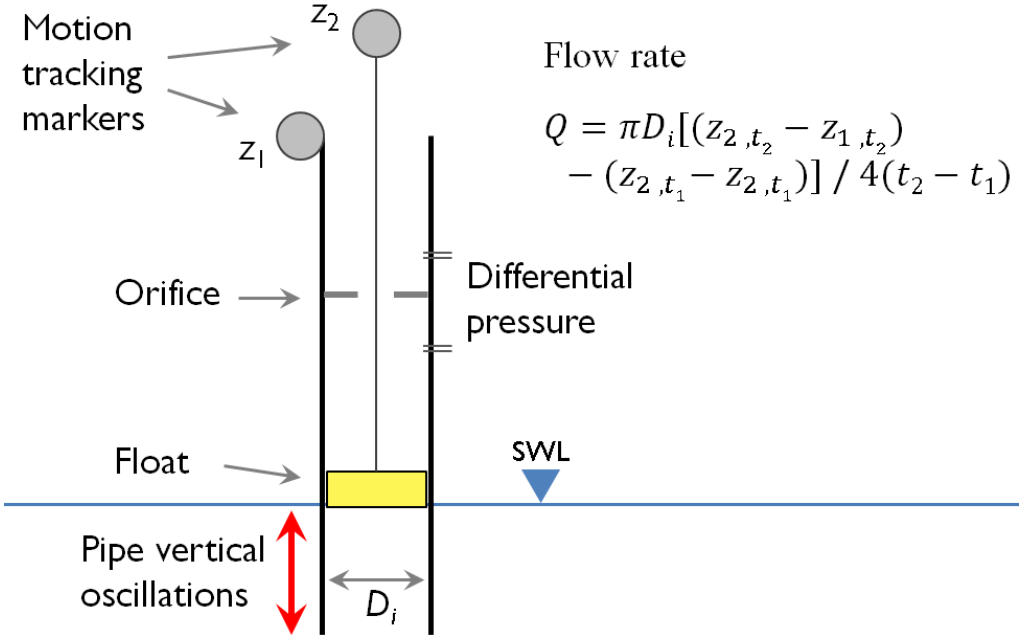

Figure 5.5, Orifice arrangement for the orifice calibrations.

The air volume flow rate through the orifice was measured and plotted against the pressure drop across it to determine the C_D as shown in Figure 5.6. This gave a C_D of around 0.65 which is higher than predicted by the British Standard reference tables which estimates a C_D close to 0.61 however, this discrepancy may have been due to the increased thickness plate. The graph illustrates the quadratic relationship of the pressure drop across the orifice and a good correlation to the theoretical curve.

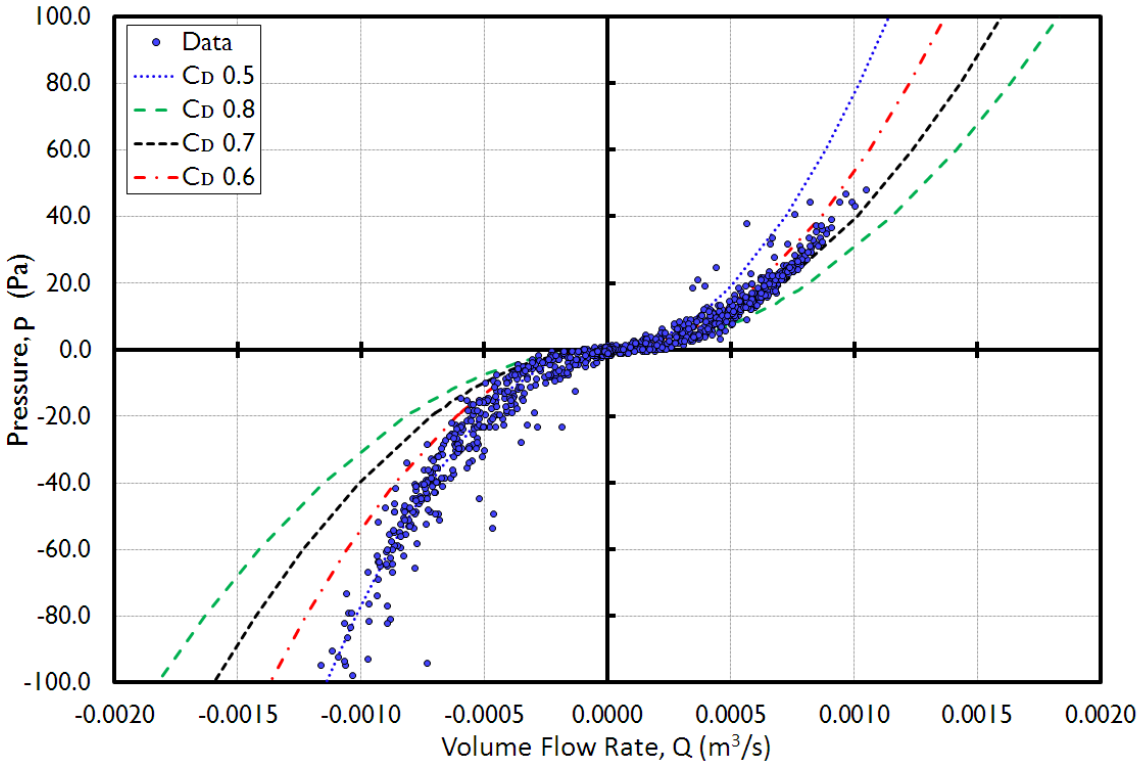

Figure 5.6, The relationship between pressure and volume flow through the orifice in order to estimate the value of C_D as carried out by HMRC.

It is worthwhile noting that the C_D value is asymmetric due to the orifice having a sharp leading edge and a chamfered trailing edge only in one direction. Flow in the opposite direction leads to a lower C_D as is seen in Figure 5.6. In the case of OWEL, only the positive flow direction is of interest and so data on the right hand side of the graph was used to determine the C_D.

5.6 Test Conditions

A total of 24 wave conditions were used throughout the testing and these are summarised in Figure 5.7. A governing factor for the choice of test waves was that the basin had to be well calibrated for each wave prior to testing. For regular waves, this is a relatively straightforward process, however, for irregular seas the measured wave spectrum had to match the required input spectrum. As each sea state comprises many wave period components and heights the process to calibrate the tank for each sea state was arduous. The limited testing time available to the project meant that only a few conditions could be specified and the majority of the waves were taken from the list of standard pre-calibrated conditions suggested by HMRC. Many of these were also similar to those recommended by Holmes (2009).

Each number (1-24) in the central region of the diagram in Figure 5.7 indicates a different wave condition in the testing. Values of peak wave period (T_p), zero crossing wave period (T_z), wavelength and significant wave height (H_s) are given along with their corresponding prototype

scale values scaled up by 1:56, based upon the full scale design dimensions that were proposed by ITP at the time. For the regular wave conditions the values for T_p and H_s were assumed to represent the input T and H of the sinusoidal wave train. The irregular seas used the T_p and H_s values as inputs for the spectrum. Due to the limitations of the tank, it was found that some of the more energetic sea states in Figure 5.7 could not be generated for irregular waves.

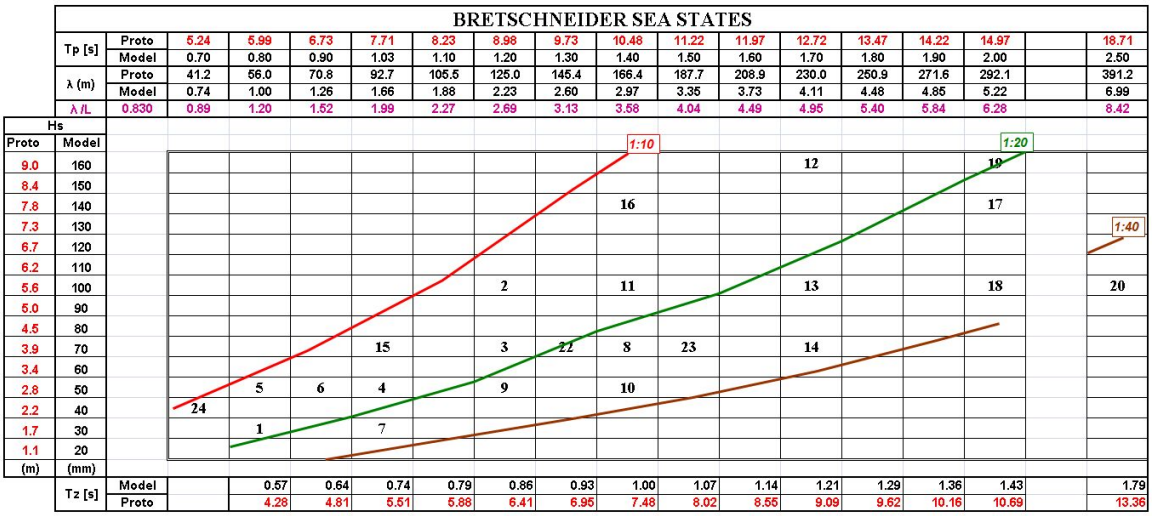

Figure 5.7, The 24 sea states used throughout the two phases of testing, modified from Holmes (2009).

For the tank calibration, the wave probes were located at the testing region in the centre of the tank and, along with all other measurements in the testing, sampled at a frequency of 16 Hz. Assurance was given by HMRC that the wave conditions that were input into the wave generation system were the same as the conditions generated in the basin. No calibration data was provided by HMRC to corroborate this statement and so it was assumed that their tank calibrations were sufficient in order to substantiate this claim. Figure 5.8 shows the quality of the wave forms and consistency in the free surface profile for the two extremes of regular wave conditions used in the testing. The depth effects of the tank are more prominent with the longer waves as their crest amplitude is up to ~20% greater than the trough amplitude.

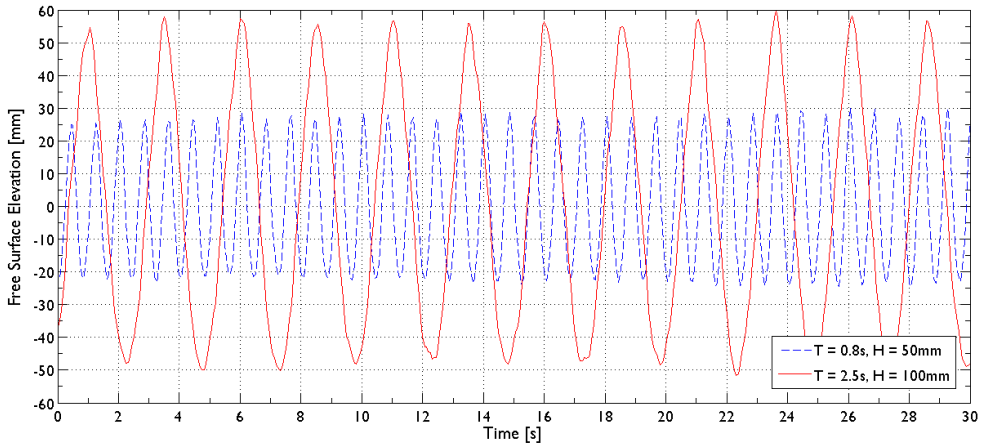

Figure 5.8, The free surface profile for a small short wave and a large, long period wave.

{Mansard, 1980 #355} presented a methodology using a least squares fit for three measurement points to calculate the incident and reflected wave spectra. This method assumes that an irregular sea can be described as a linear superposition of an infinite number of discrete wave components each with their own period, amplitude and phase. Three wave probes were positioned at the test region within the wave basin and aligned in a plane parallel to the direction of wave propagation. The methodology specifies that the distance between the first and second probes, X12, should be between L/20 and L/10 and that the distance between the first and third, X13, to be L/6<X13<L/4.5 but not L/5 or 3L/10. The results of the analysis for irregular, long crested waves are presented in Figure 5.9 and show the variation of reflection coefficient, defined as the ratio of reflected to incident wave height, over the range of wave periods tested. This shows that the reflection coefficient varied approximately from 15% to 20%. This was taken into account during the wave tank calibration to determine the actual, incident significant wave height for each sea state and wave condition tested.

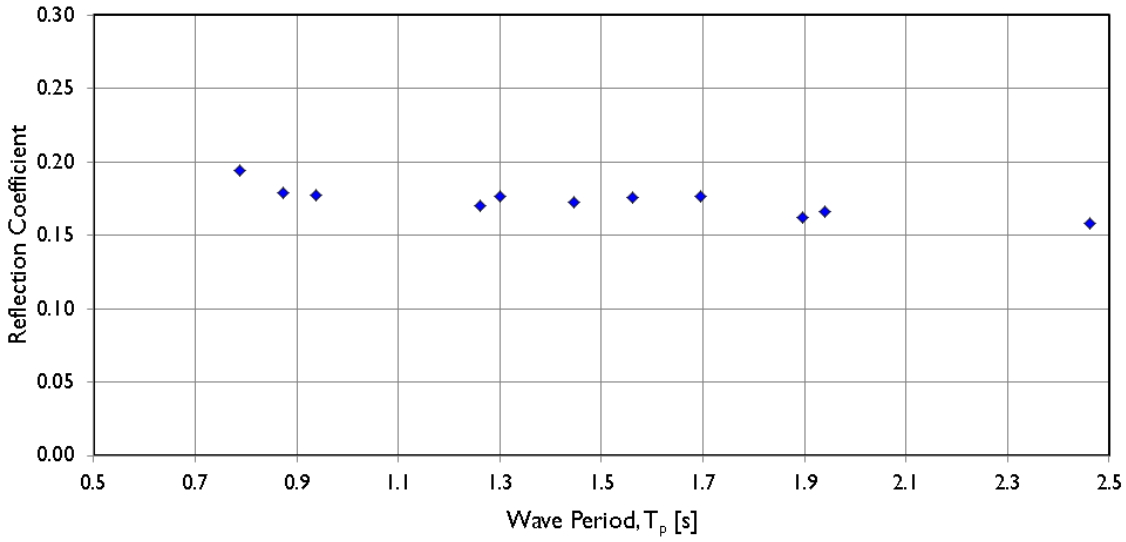

Figure 5.9, The variation in reflection coefficient with wave period measured in the wave basin

The variation in wave height across the tank was not measured. It should however be noted that the effect can be significant; O'Boyle *et al.* (2011) reported on the spatial variation in wave height in the wave basin at Queen's University Belfast. This examined the effects of phase locking, caused by the superposition of incident and reflected wave components within the basin resulting in a wave field containing nodes and anti-nodes within the basin. Further to this, it is not likely that each of the 40 paddles across the basin width would be able to produce identical wave forms and this would therefore add to the lateral variation in height. Given the relatively large width of the OWEL model tested and the sensitivity of the performance of each of the ducts to wave height, any spatial variations in height that differ from the stated significant wave height would have led to miscalculations in the efficiency.

In all test runs, the wave basin was operated with the input wave conditions for an initial period to allow the tank to "stabilise", so that the initial transient waves would not be included within the test. The duration of a test for regular wave conditions was 1 minute. For the irregular sea states, the wave generation system used the standard input employed by Edinburgh Design's wave makers. All of the irregular seas run were intended to be classical Bretschneider spectra and these tests were run for a total of 4 minutes to ensure all components comprising these spectra were present within the test. The Bretschneider spectral model is relatively simple, requiring only an input of peak wave period (T_p) and significant wave height (H_s). It assumes a fully developed sea which may not be a reality however, it is the general spectrum recommended by Holmes (2009) for long fetch sites such as those in the Atlantic. Short crested, directional sea states were used for the irregular wave investigations. These were specified by HMRC and were intended to simulate realistic conditions with a typical maximum spread of +/- 45°. This spreading function was that proposed by Longuet-Higgins *et al.* (1963) and featured the cosine-power term $cos^{2s}\theta$ to provide a weighting to the directionality of the sea state. Larger values of the spreading index, s, reduce the directional spread, so in these tests, s = 10, was used to provide some directionality [Nwogu and Demirbilek (2001)].

5.7 Phase 1 Testing

5.7.1 Static Tests

For the initial tests, the multi-duct model was positioned in the centre of the tank and attached to a rigid metal frame with adjustable height as can be seen in Figure 5.10. Large ballast weights were placed on top of the model to prevent it and the frame from moving.

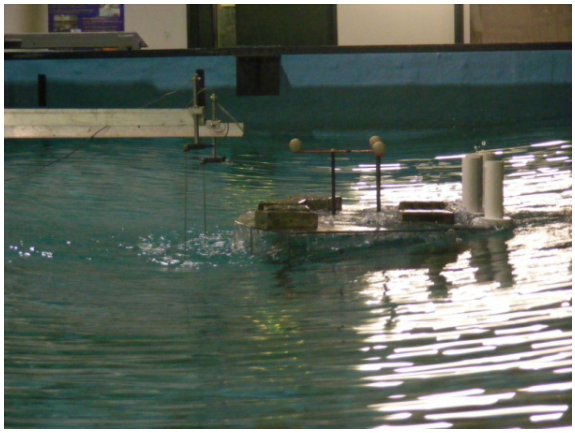

Figure 5.10, Static model under test in long regular waves, with the short PTO tubes.

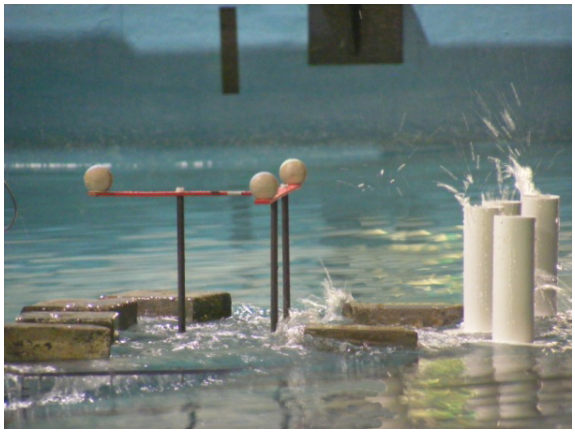

Figure 5.11, The issue of water spouting up through the short PTO tubes.

Initial tests quickly demonstrated a flaw in the experimental set up; in certain wave conditions, particularly with the more energetic waves, water exited vertically out of the PTO tubes after

having passed through the orifice. This can be seen in the images in Figure 5.11. To rectify this issue, longer PTO exit pipes were attached so that the orifice was higher above the duct exit and reduced the risk of water ingestion into many pressure sensors. Despite this however, water ingress into the ports of the pressure sensors still remained a problem throughout the course of the tests due to water splashing into the tubes. This did lead to the repetition of a number of tests due to a lack of output from the pressure sensors. Another implication of the extended tubes was to increase the height of the CoG which was to later affect the naval architecture design. One benefit of adding the tubes was to allow the airflow within them to become more steady before arriving at the orifices; the British Standard recommends that the orifice is placed between $15D_i$ and $5D_i$ downstream of changes in flow and corners in the pipe. The lengthened pipe meant that the orifices were approximately $10D_i$ downstream of the exit to the duct.

5.7.1.1 Applied PTO Damping

The first tests to be carried out with the static model were to investigate the effect of changing the applied PTO damping on the conversion performance. It was previously demonstrated in section 0 that the performance is dependent on the orifice ratio and that an optimum exists to provide the best overall power capture. An optimum level of damping exists for every sea state, however, the realms of practicality prohibited changing the orifice size for each test. The most suitable orifice size for the tests was chosen by conducting a sweep through a number of regular waves in the test schedule that lay on, or near to, the 1:20 steepness line whilst varying the orifice size. The waves used were 1, 4, 3, 8, 13 and 17 and are summarised in Table 6. The orifice diameters used were 13, 15, 17, 20 and 22 mm equating to β ratios of 0.26, 0.30, 0.34, 0.40 and 0.44 within the 50 mm PTO tube. The results of the tests are shown in the six graphs in Figure 5.12; it should be noted that whilst the legend and x axis remain constant throughout, the y axis, showing performance, varies between the graphs in order to improve readability.

Table 6, A summary of the regular wave conditions for tests # 1, 4, 3, 8, 13 and 17.

#	Wave Period [s]	Wave Height [mm]	Wavelength/Duct Length
1	0.80	30	1.20
4	1.03	50	1.99
3	1.20	70	2.69
8	1.40	70	3.58
13	1.70	100	4.95
17	2.00	140	6.28

As expected, the optimum applied damping varies with the wave conditions and hence, the resultant air flow. Similarly to the results from the initial 2D testing; smaller waves with lower associated air flow rates, particularly wave #1, benefit from a high level of damping whereas the performance in larger waves was increased by increasing orifice size and so reducing the applied damping.

A number of observations can be made from the graphs in Figure 5.12:

- The performance across the 5 ducts is not similar and can vary dramatically, even though waves were regular, were uni-directional and air flow was averaged over 60 seconds of testing.
- The smaller waves in these tests, #1 and #4, benefit from an orifice with $\beta = 0.34$.
- Waves #3, 8 and 13 benefit from $\beta = 0.4$.
- The trends for wave #17, the largest wave, suggest that a wider orifice, greater than $\beta = 0.44$ could yield an improvement in performance.

The asymmetries in performance across the five ducts of the model can be explained by the possible spatial variation in wave height across the basin that was described in section 5.6. It is likely that, even small deviations in local wave height from the measured significant wave height would have resulted in differences in the apparent performance for each duct. It was also postulated at the time of testing that the asymmetries in efficiency may have been due to each duct having a different orifice installed for the PTO damping studies. This was thought to cause each duct to perform slightly differently and in turn affect the performance of the neighbouring ducts. This phenomenon however is far less likely to have had a significant impact on the performance of the ducts than the variations in wave height distribution.

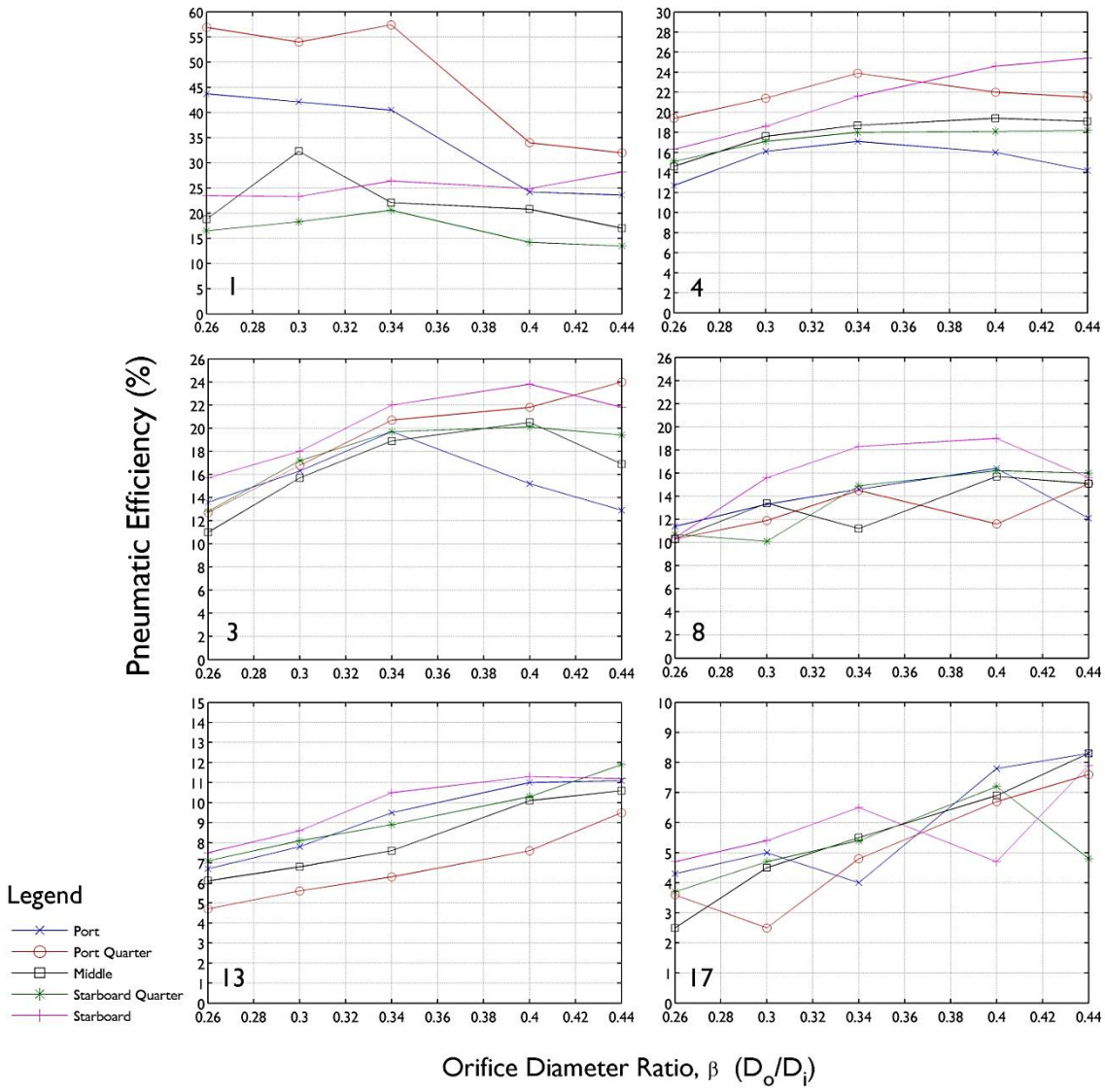

Figure 5.12, The relationship between performance and applied PTO damping for each duct in six test conditions (1, 4, 3, 8, 13, 17).

From these results, it was decided to use two orifices in the subsequent tests; $\beta = 0.34$ was to be used in the smaller wave conditions with $T < 1$ s (i.e. wave # 1, 5, 6 and 24) whereas the $\beta = 0.4$ was to be used in all other wave conditions. Over the range of wave conditions tested the $\beta = 0.4$ orifice provided a linearised damping ratio of ~25,000 – 78,000 Ns.m^{-5} as calculated using equation [15] in section 3.6. By using the smaller orifice for the tests with shorter wave periods, the damping ratio was increased from 25,000 Ns.m^{-5} to approximately 47,000 Ns.m^{-5}. The magnitude of this range was greater than that of the initial model testing, in section 4.7.8. This however, was expected as the model in the initial tests was larger than the multi-duct geometry and the damping ratio scales by $X^{-1.5}$, where X is the scale factor. The equivalent full scale ($X = 50$) turbine damping ratios provided by the $\beta = 0.4$ orifice were predicted to be ~70 - 220 Ns.m^{-5}. The smaller orifice provided a lower limit of damping equivalent to 133 Ns.m^{-5}.

The magnitude and relationship of required damping are similar to those reported by Tease *et al.* (2007) and presented in Figure 3.15, section 3.6.

5.7.1.2 Regular Waves

The static model tests were used to assess the performance and characteristics under idealised conditions and provide data for the validation of computational models. Figure 5.13 provides a series of contour plots showing the hydraulic – pneumatic conversion efficiency of each duct over 21 test waves (waves #22, 23 and 24 were test points added later in the testing as a result of initial findings). It should also be noted that, for ease of comparison, all of the performance contour plots presented in this chapter are plotted on the same scale *x* and *y* axes and with the efficiency colour bar being constant throughout.

These results show that the Port Quarter duct generally outperforms the others and has a peak performance of 34.2 % for $T = 0.9$ s, $H = 50$ mm. The Port, Middle and Starboard Quarter ducts all performed similarly with performance only slightly lower in comparison to the Port Quarter. Their peak efficiencies all occurred around a wave period of 1.2 s ($L/L_D = 2.7$) with typical peaks being between 25 % and 30 %. The Starboard duct had the lowest performance but this was not as "peaky" as the other plots, in that efficiencies of around 20 % were maintained for lower half of the test schedule and this gradually declined with the larger waves. The performance across the five ducts was far more symmetric in comparison to the lack of similarities displayed in the orifice optimisation testing in Figure 5.12. This further strengthens the theory that explained this original phenomenon due to the difference in orifices between the ducts.

The region of peak performance for all of the ducts was centralised around a wave period of 1.2 s ($L/L_D = 2.69$). Comparing the position of this peak to those of the initial 2D tests (Figure 4.43, section 4.7.7) shows that it occurred at a similar L/L_D ratio as the middle, moderate peak. The peak efficiencies in these tests however are far lower than those observed in the 2D tests. This was likely due to a number of reasons:

- The 2D model spanned the flume and so intercepted all of the incident wave energy whereas the multi-duct model was in the wave field in the basin and waves could diffract around it.
- The proximity of each duct to the others will have meant that they would have influenced each other and the performance. This could have had a detrimental impact.
- Whilst the two models were geometrically similar in terms of dimensions, the primary difference was that the multi-duct model had tapering side walls rather than being parallel. This too could have had resulted in reduced performance.

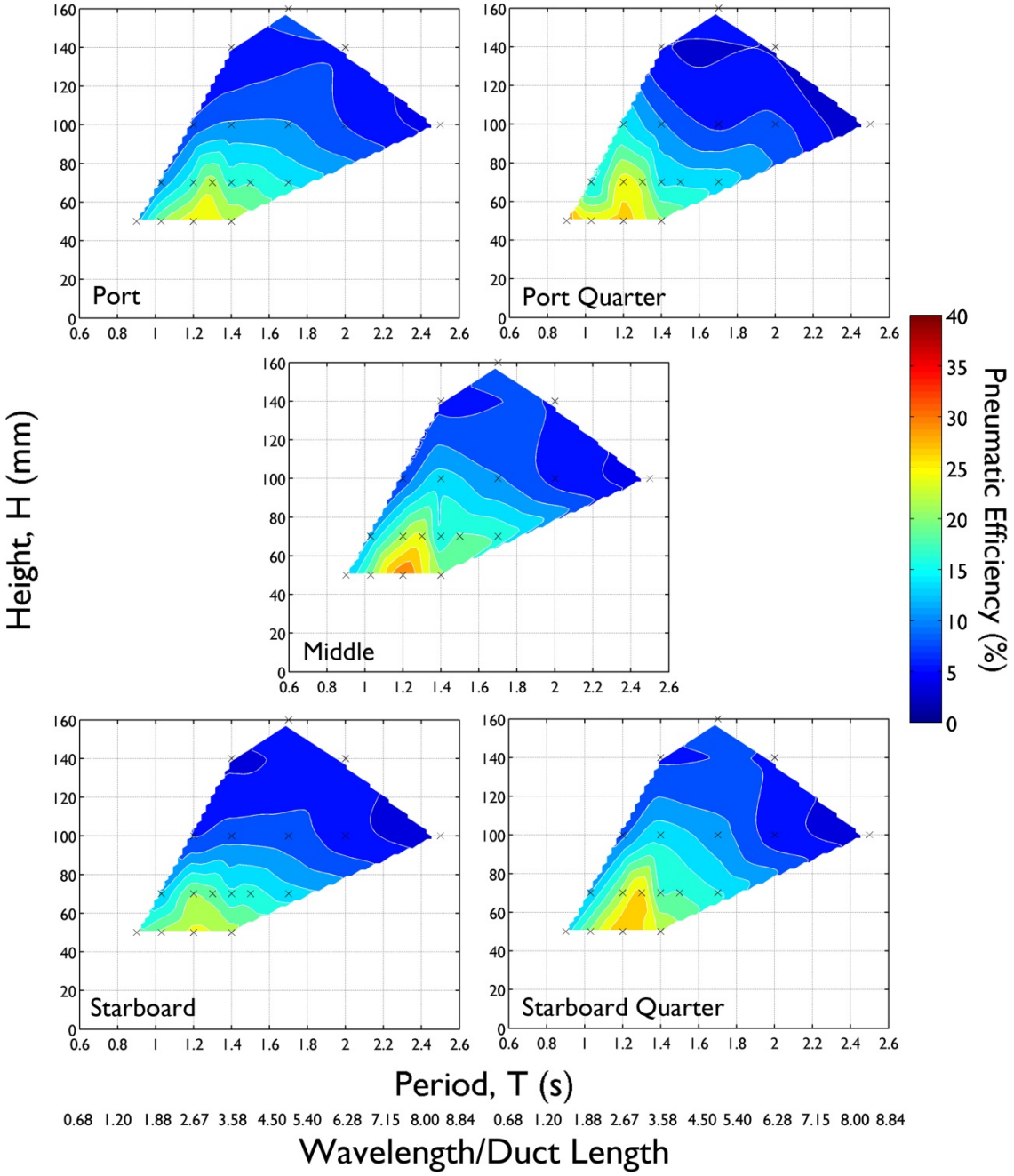

Figure 5.13, Efficiency contour plots for the static model in regular waves.

The results presented in the contour plots in Figure 5.13 have also been plotted as a scatter plot with lines of iso-height in Figure 5.14. This shows the relationship between wave period and performance for five different wave heights and for each of the 5 ducts. The sparse number of data points used to create the contour plots means that there are large regions that are heavily interpolated. This will have resulted in some performance characteristics being omitted due to the lack of data available to demonstrate all of the features. For this reason, the contour plots in this chapter could be misleading, unless the reader treats them with caution; particularly the large interpolated regions. By providing the performance data as lines corresponding to the

same wave height, it is intended to present the reader with all of the data available to observe the trends and compare the characteristics. The line plots in Figure 5.14 also help to identify anomalies such as the point in the Port Quarter duct plot, giving an efficiency of 35% at T = 0.9s and H = 50 mm. It can also be seen that the peak performance may have shifted to greater wave periods with increasing wave height, however there is not enough data to distinctly identify this.

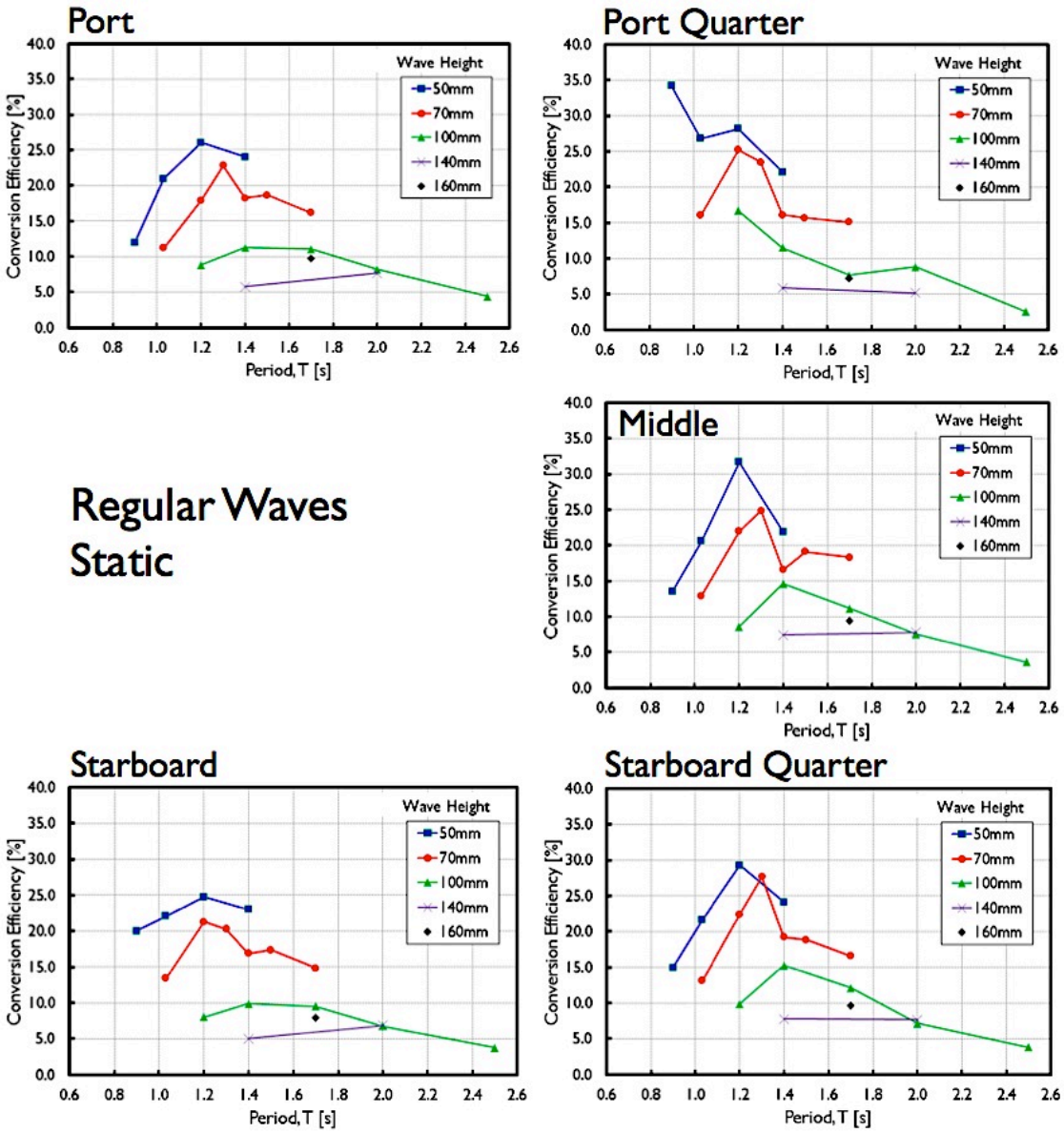

Figure 5.14, The variation in performance efficiency with wave period for five different wave heights with a static model.

5.7.1.3 Irregular, Short Crested Sea States

Following the regular wave tests, the static model was subjected to short crested irregular waves in order to examine the performance sensitivity of the device to irregular sea states. Until this

point, OWEL had never been tested with irregular waves however, it had been postulated that the efficiency of the device would reduce due to the variation in wave height and period preventing the sealing of waves with the duct roof. However, the contour plots in Figure 5.15 of the performance of the static model in short crested, irregular seas show, this was not the case.

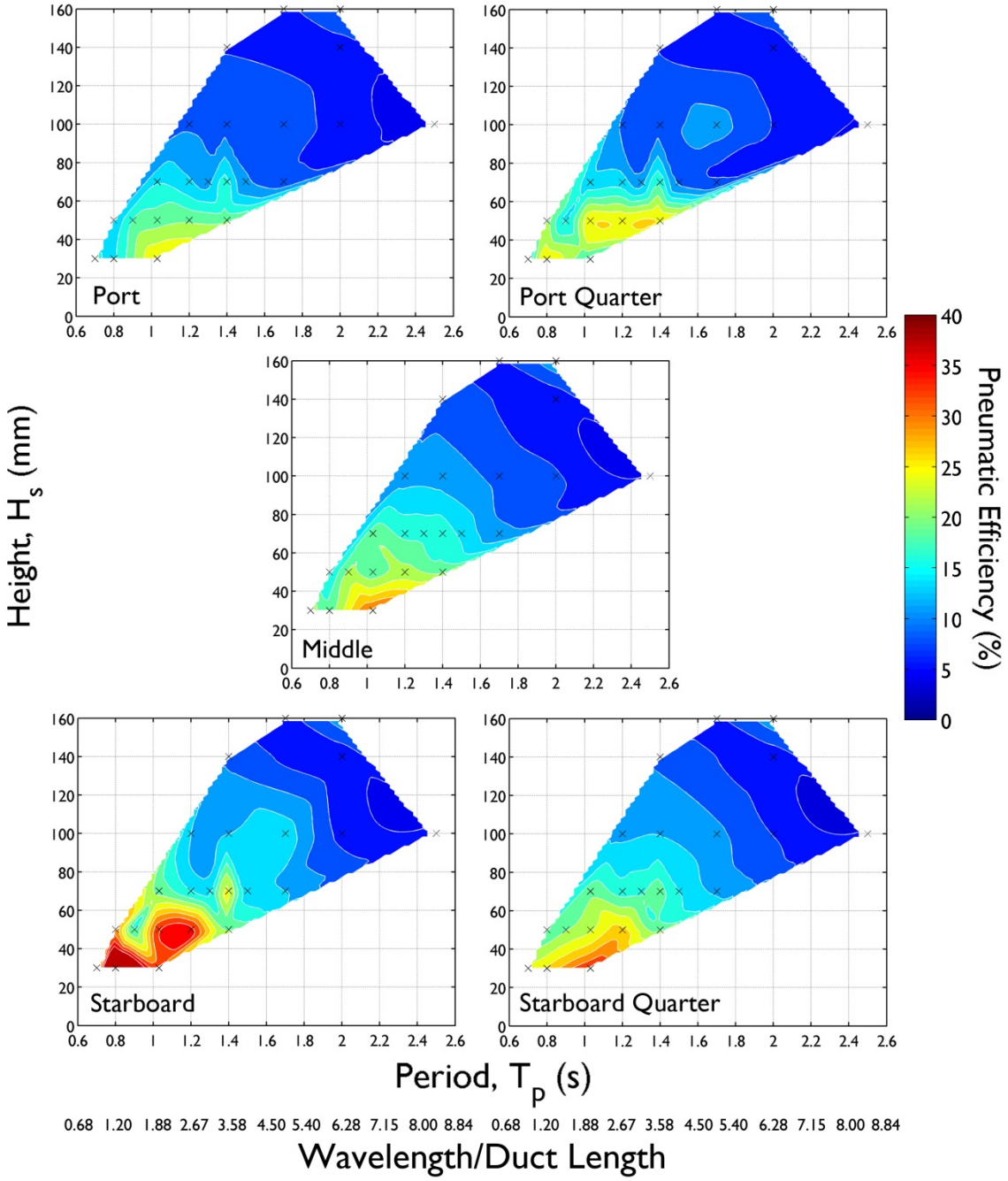

Figure 5.15, Irregular, short crested performance maps for a static model.

The performance data displayed by the contour plots in Figure 5.15 has also been plotted as lines of iso-height for six different wave heights in Figure 5.16, similar to that on the previous page. Unlike for the regular wave conditions, the trends in performance are much harder to distinguish and there appear a number of anomalous results that vary drastically from the neighbouring points. Once again, due to the lack of data points, it is difficult to ascertain the

actual relationships and which points are anomalous. For the irregular wave cases, the accuracy of the specified wave conditions could be a large contributing factor for the variation in performance. No spectral data of the tank calibration was supplied by HMRC and so spectra with varying distributions of power with wave period for different sea states may have provided the same summary data but not necessarily the same wave regime. This could have changed the performance characteristics of the ducts due to the differing components of energies within the spectra.

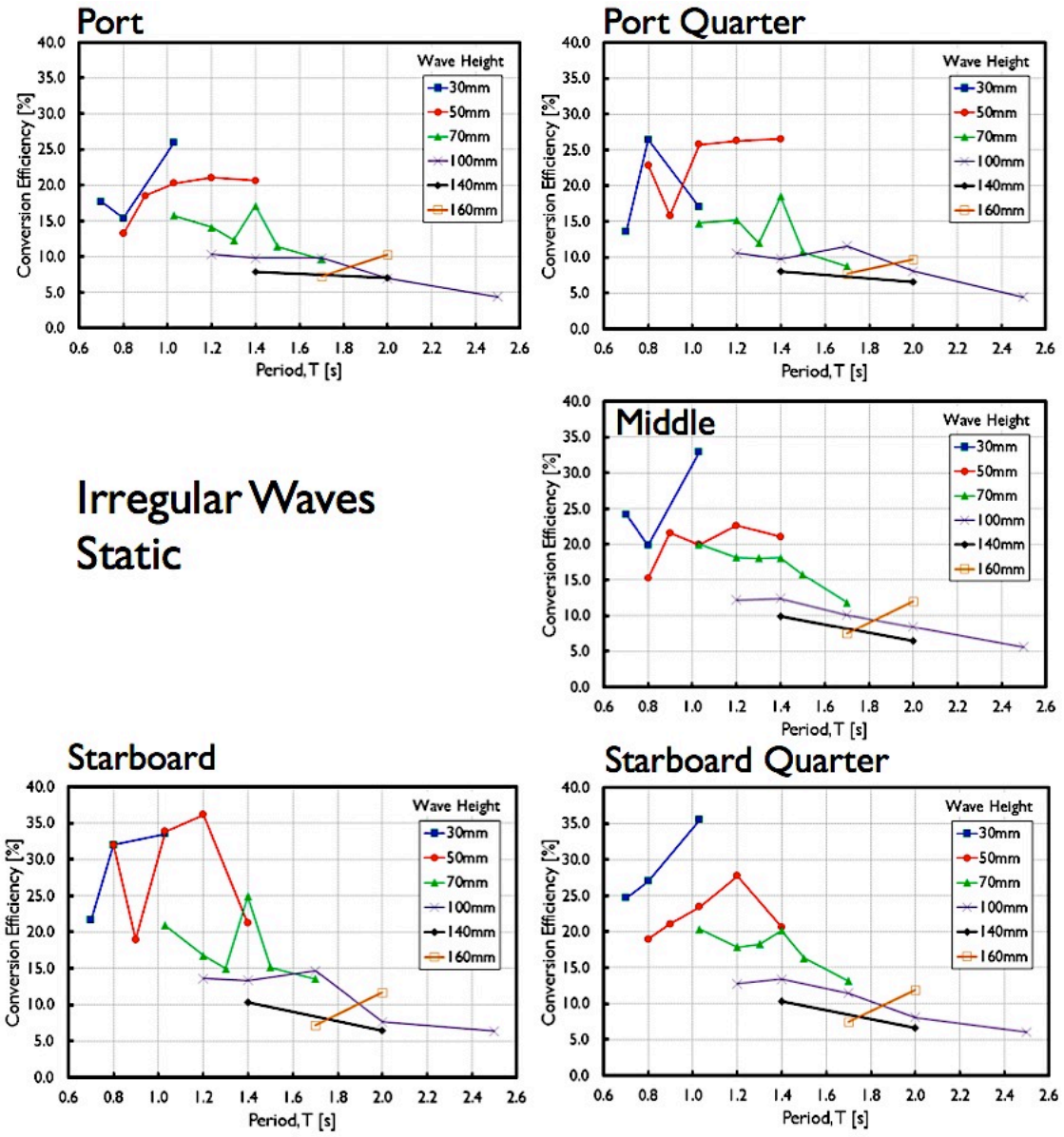

Figure 5.16, The variation in performance efficiency with peak wave period for six different significant wave heights with a static model.

In comparison to the results for the static model in regular waves, the conversion efficiencies were of similar magnitude in the two types of waves and the same trend of increased performance in smaller waves was observed. This characteristic was further investigated by the inclusion of three additional test cases at a significant wave height of 30 mm.

Perhaps the most apparent feature in the contour plots in Figure 5.15 is the high peak performance of the starboard duct. Five of the test points resulted in conversion performance exceeding 32 % which was considerably higher than the ~30 % peak recorded in the other ducts. This was a surprising results as, in the regular testing, the starboard duct underperformed in comparison to the others. After some deliberation, it was postulated that the reason for the increase in performance was due to a simple geometrical difference between the starboard duct and the other four; when specifying the construction of the model, the joint between the PTO tube and the duct roof was filleted to provide a smooth, rounded airflow passage. This was included on the starboard duct however, the additional construction time required to fillet the plastic on the other four ducts would have significantly increased the model cost and so, due to financial constraints within the project, the joints on the other four ducts were chamfered instead. This meant that air flowing from the duct to the orifice flowed around a corner with a sharp edge from the chamfer. The subsequent energy losses due to flow separation in the regions surrounding the sharp edges, were attributed to the reduced performance in the four ducts and the apparent increased performance in the starboard duct. Prior to the tests, the effect of the chamfered joints on the efficiency was not anticipated and so this phenomenon highlighted the need to reduce flow losses in small scale models, particularly where low energy airflows are present. The filleted joint of the starboard duct remained on the model for the subsequent tests and so the performance from that duct became the benchmark for the true magnitude of conversion efficiency possible. Ideally, at this point in the testing, the joints within the other ducts would also have been filleted however, as previously mentioned, this would have increased testing costs significantly and also reduced the testing time available.

5.7.1.4 Comparison of Performance with Initial, 2D Testing

The two main performance peaks in the initial 2D tests occurred at L/L_D = 1.0 – 1.5 and 3.5 – 3.8 with a smaller peak in between at L/L_D = 2.5. For a duct length of 0.83 m and water depth of 1m, these ratios should equate to the wave periods given in Table 7. However, comparing the locations of these predicted performance peaks with the results in Figure 5.13 and Figure 5.15 only shows some correlation and some apparent differences.

Table 7, Equivalent wave periods from the peak L/L_D ratios determined in the initial 2D testing.

L / L_D	Wave Period [s]
1.0 – 1.5	0.73 – 0.89
2.5	1.16
3.5 – 3.8	1.38 – 1.45

For the regular waves in Figure 5.13, the peak performance occurred at approximately L/L_D = 2.7 (T = 1.2 s) whereas for the irregular waves in Figure 5.15, the main peak appeared to be more spread, occurring between L/L_D = 1.9 – 2.7 (T = 1 – 1.2s). This should be treated with some caution as the interpolation applied to the contour plots between the sparsely located data points may have resulted in smoothed relationships and so some characteristics may not have been captured by the plots. In comparison to the numerous test conditions in the initial physical modelling phase, the reduced number of tests for the multi-duct testing was required to cover a wider range of L/L_D. Unlike the previously, well defined performance peaks, the lack of data points led to the poor definition of the relatively narrow bandwidth peaks; an L/L_D range of 0.5. Nevertheless, the location of the performance peak in regular waves is very similar to that of the smaller middle peak previously observed in the 2D testing, in Figure 4.43 (section 4.7.7), at L/L_D = 2.5 but however, with a reduced magnitude. This may have been a result of a number of factors:

- 3D effects as the model did not provide complete blockage of a narrow flume.
- A smaller model draft, thus capturing less of the water column energy, particularly in longer wavelengths.
- Deeper water in the wave basin would have altered the wave characteristics.
- The inclusion of the angled side walls and reducing duct cross section.
- Detrimental effects due to the presence of the other ducts.

The most remarkable difference however, is the absence of the main peaks of performance at L/L_D = 1.3 and 3.8. It is possible that this is a product of the aforementioned factors. A further, less likely, possibility is that the range of wave heights tested at L/L_D = 1.3 and 3.8 was not extensive enough to capture the peaks. The 2D model performance in Figure 4.43 shows that for L/L_D = 1.3, the peak performance occurred at wave heights between 50 – 90 mm, similarly, the range for the peak at L/L_D = 3.8 was 20 – 60 mm with a rapid reduction at larger wave heights. The 0.7 reduction in scale between the 2D geometry and this model could have led to these peaks shifting and so the tested wave heights at these conditions may have exceeded the conditions for peak performance. For example, the smallest height tested at L/L_D = 3.8 was 70 mm whereas the previous trends suggested that this peak significantly declined at wave heights larger than 60 mm.

The peak performance in the irregular sea states appeared to be more spread than that in regular waves. As previously mentioned this may be exacerbated by the contour plot interpolation however, it likely that this is also due to the presence of a number of wave periods featuring in each spectrum. This implies that test conditions with a T_p close to the favourable wave period of 1.2 s contain wave components within the spectrum that include waves with a period of 1.2 s. This will therefore increase the bandwidth of the performance peak however, it should also

reduce the magnitude of the peak as a spectrum with T_p = 1.2 s will also contain wave components with less favourable periods.

The differences and relationships between the initial 2D and multi-duct 3D model performance results require further investigation as no firm conclusions can be drawn from these observations. The modification of the main regions of peak performance cannot be conclusively explained.

5.7.2 Floating Tests

The design of the floating model can be seen in Figure 5.3. It was identical to the static, five duct model but a layer of foam was positioned on the underside of the baseplate. To counteract some of the buoyancy and correctly trim the model, lead weights were positioned on the top of the duct roofs. This had the undesired consequence of making the model particularly unstable and will be discussed further in section 5.8.

As a result of an unsatisfactory naval architectural design, the performance of the floating model was significantly lower than that of the static model. A selection of results is given in Table 8 to provide a comparison between the performance of the static model and the best floating configuration. For the five wave conditions, it was observed that the static model in irregular waves performed most favourably but conversely in the same five sea states, the floating model had a significantly reduced performance. Whilst some reduction in performance was forecast, the low efficiencies that were recorded for the first floating model were unexpected. Subsequently, a number of remedial strategies were suggested and trialled in an effort to improve performance.

Table 8, Comparison of the model performance in static and floating configurations for five conditions.

#	Period [s]	Height [mm]	Regular, Static Efficiency [%]	Irregular, Static Efficiency [%]	Irregular, Floating Efficiency [%]
5	0.80	50	N/A	32.0	8.0
4	1.03	50	22.1	33.8	15.3
15	1.03	70	13.4	16.8	9.8
2	1.20	100	8.0	13.6	4.1
13	1.70	100	9.5	14.7	4.5

No motions data were recorded during the phase 1 tests however, from observing the floating motions in various regular wave conditions, the model appeared to excessively pitch bow up in

all cases. As a result, the freeboard at the duct entrance became so great that only a small amount of the wave crest could enter into the duct. Reducing this effect became the primary aim of the testing and so various different configurations and buoyancy arrangements were trialled. The modifications included;

- Addition of buoyancy and ballast at the bow to increase pitch stiffness and longitudinal inertia.
- Addition of buoyancy and ballast at the stern to increase pitch stiffness and longitudinal inertia.
- Fixing a large flat drag plate, 500 mm below the keel in order to damp motion in both pitch and heave.
- A combination of damping plate and additional stern buoyancy.

Whilst these did improve the efficiency in comparison to the initial baseline, floating design, it was deemed insufficient. The results in Table 8 represent the best performance achieved from any of the floating models and so, in light of this, a decision was made by ITP to suspend the testing. This was intended to allow time to further analyse the results from the initial tests and make a better, more informed judgement on the design of the naval architecture. In hindsight, this was the correct decision to make and led to a more productive return visit to the testing facility. The primary objective of the testing was to generate performance data from a floating model in irregular seas and so this became the priority for the remainder of the testing time.

5.8 Naval Architecture Redesign

In the first testing phase, it was found that the key issue with the floating design was that its stability was poor and this resulted in the model being too sensitive in pitch. A number of design alterations were suggested by ITP in order to resolve these issues and increase the stability. This was intended to modify the motions and so improve the performance.

The drawings in Figure 5.17 show the revised naval architecture design. Four damping plates were included; each was made from 10mm aluminium and orientated 45° from horizontal. These were to provide a large opposing drag force to motions in any direction and also provided the majority of the ballast required to correctly float the model. Similarly to the initial floating design, all of the buoyancy was submerged below the model. However, because the ballast of the heave plates was also located around the same position, the centre of gravity was lowered further below the centre of buoyancy and so the stability of the model was greatly improved. In addition to these changes, sections of buoyancy were also included aft of the stern to increase pitch stiffness and provide a greater resistance to the tendency of the model to pitch bow up. The inclusion of the large drag plates with their supporting structure and the additional ballast

required to counteract the extra buoyancy, significantly increased the inertia of the model. The total mass of the new model was ~45 kg and it is likely that this would have also acted to reduce the motions as well as altering the natural frequency of their response.

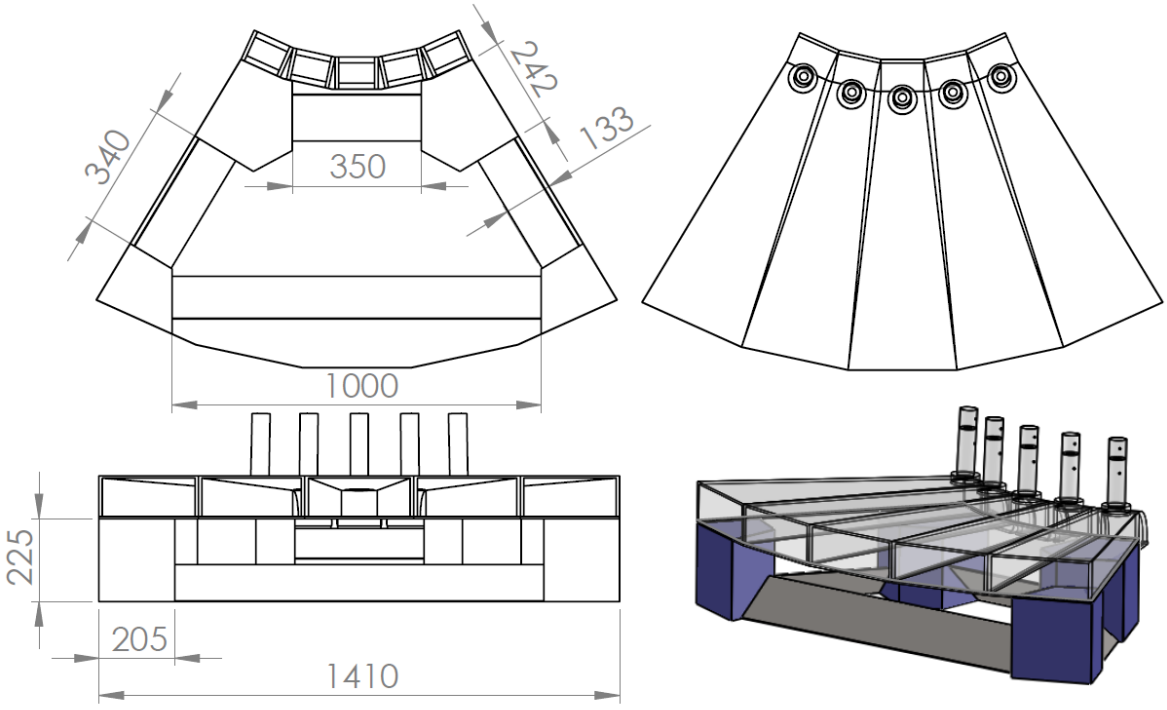

Figure 5.17, The redesigned naval architecture design for the floating model with the buoyancy blocks shown in blue and the 45° damping plates in grey.

5.9 Phase 2 Testing

The model was modified to include the changes in the naval architecture design and the testing recommenced. This phase of testing was to specifically investigate the floating performance of the model as performance from the previously tested static model had been deemed 'satisfactory'. Similarly to the static model tests in the first phase of testing, free floating investigations were initially carried out in regular waves and then in short crested, irregular sea states.

5.9.1 Floating Tests

5.9.1.1 Regular Waves

The contour plots in Figure 5.18 show the wave-pneumatic conversion efficiencies for the five ducts, tested over 22 regular wave conditions. As had been witnessed previously in the first testing phase, the performance was reduced in comparison to the static model in regular waves (see Figure 5.13). Despite this however, there was an overall improvement in comparison to floating configurations tested at the end of the first testing phase.

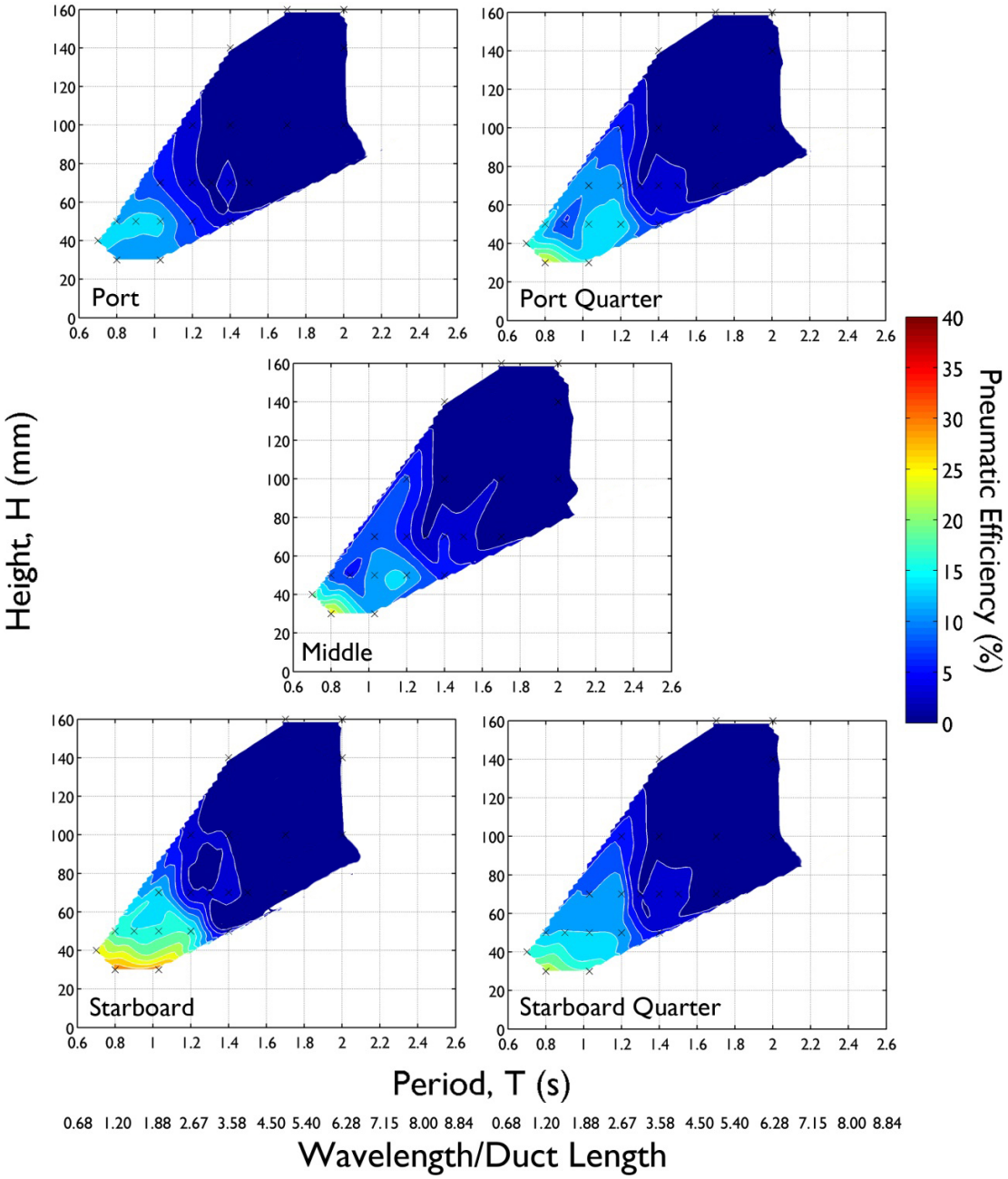

Figure 5.18, Performance contour plots for the redesigned, floating model in regular waves.

The performance data has been plotted against wave period for each of the six wave heights tested, in Figure 5.19. These show large variability in the performance in 30 mm waves between the five ducts and with no clear trends between them. For the other wave periods however, show a significant reduction in performance in wave periods of >1.4 seconds. For the larger wave heights, the performance appeared to increase with decreasing wave period, with the data suggesting a peak for H >50 mm in waves with T < 1.0 s.

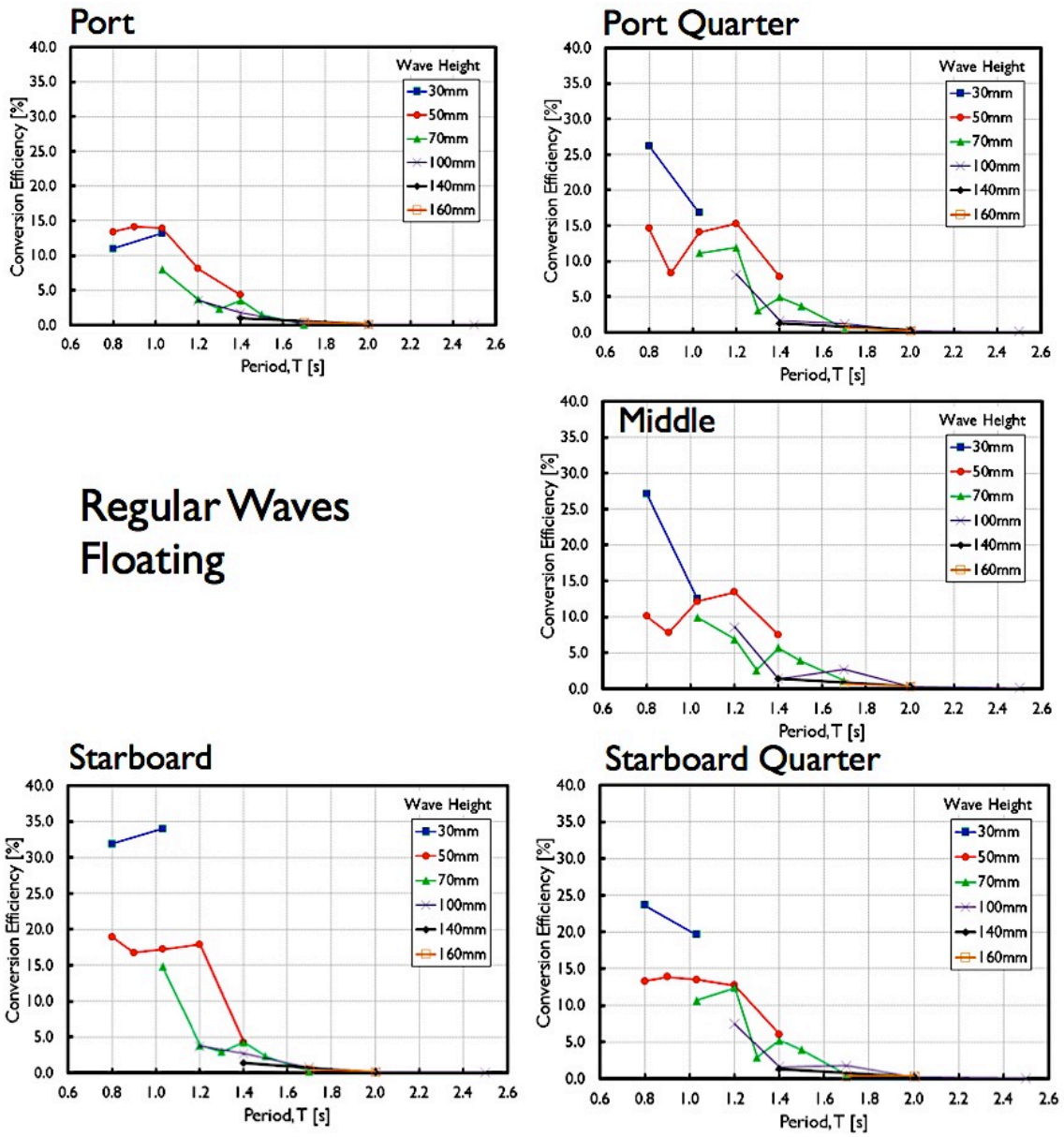

Figure 5.19, The variation in performance efficiency with wave period for six different wave heights with a floating model.

Unlike the trends of the static tests in regular waves, the results in Figure 5.18 and Figure 5.19 show that the starboard duct performed slightly better than the others. This is the same relationship that was seen in the static, irregular wave tests and so can be explained by the geometric difference of the chamfered PTO inlet. However, this could perhaps suggest that the poor performance of the starboard duct in the regular wave, static tests could have been anomalous.

In this instance however, peak efficiencies from the starboard duct were around 25 % but typical efficiencies across all of the ducts were less than 15 %. It should be noted that the apparent white voids in the contour plots are a feature of the interpolation scheme which predicts

efficiencies to be zero in these regions. With reference to the static, regular wave tests in Figure 5.13, the peak efficiencies in Figure 5.18 are of a similar magnitude but were observed in shorter period waves. The peak efficiencies of the static tests were centred about a wave period of $T = 1.2$ s whereas in these floating tests the region of increased performance occurs at wave heights less than 60 mm and between $0.7 \text{ s} < T < 1.2$ s.

The reduction in performance in longer waves with $T > 1.2$ s is likely due to the motions of the model that arise as it follows the wave profile and so it 'rides' the waves rather than capturing any wave crest into the duct entry. This phenomenon known as 'contour following' is described in greater detail in section 5.9.2.1 with reference to the motions of the model.

5.9.1.2 Irregular, Short Crested Sea States

The contour plots in Figure 5.20 show the performance of the model in short crested, irregular seas. The wave spectra and direction spread were the same as the wave conditions in the static tests and so comparisons can be made between the plots in Figure 5.20 and those in Figure 5.15. In these tests, due to a lack of testing time available and limitations in the wave makers, as mentioned in section 5.6, only 18 sea states were run.

Perhaps the most evident feature of the contour plots in Figure 5.20 is the comparatively high performance of the starboard duct. This trend has been observed in the previous results and can be attributed to the difference in PTO inlet shape. In this instance, the peak performance exceeded 40 % which is significantly greater than the maximum peak of 25 % for the Port duct. Similarly to the floating, regular wave performance, the peak efficiency occurred between $0.7 \text{ s} < T < 1.2$ s and at wave heights less than 60 mm. It is likely that the efficiency was dependent on the wave height due to the duct entry height, the heave and pitch behaviour – and so the freeboard at the bow during the wave cycle and also limited by losses that can typically increase for more energetic wave conditions.

In comparison to the performance of the floating model in regular waves, there is a less abrupt reduction in performance beyond waves with periods of greater than 1.4 s. In irregular seas the model is excited by waves of differing periods which are effectively 'random' in comparison to regular waves. Therefore, the floating body does not follow the wave contour profile but instead responds differently to each wave crest. This can have the effect of reducing the motions of the device meaning that it can capture a greater proportion of the wave crest and so have higher conversion efficiencies.

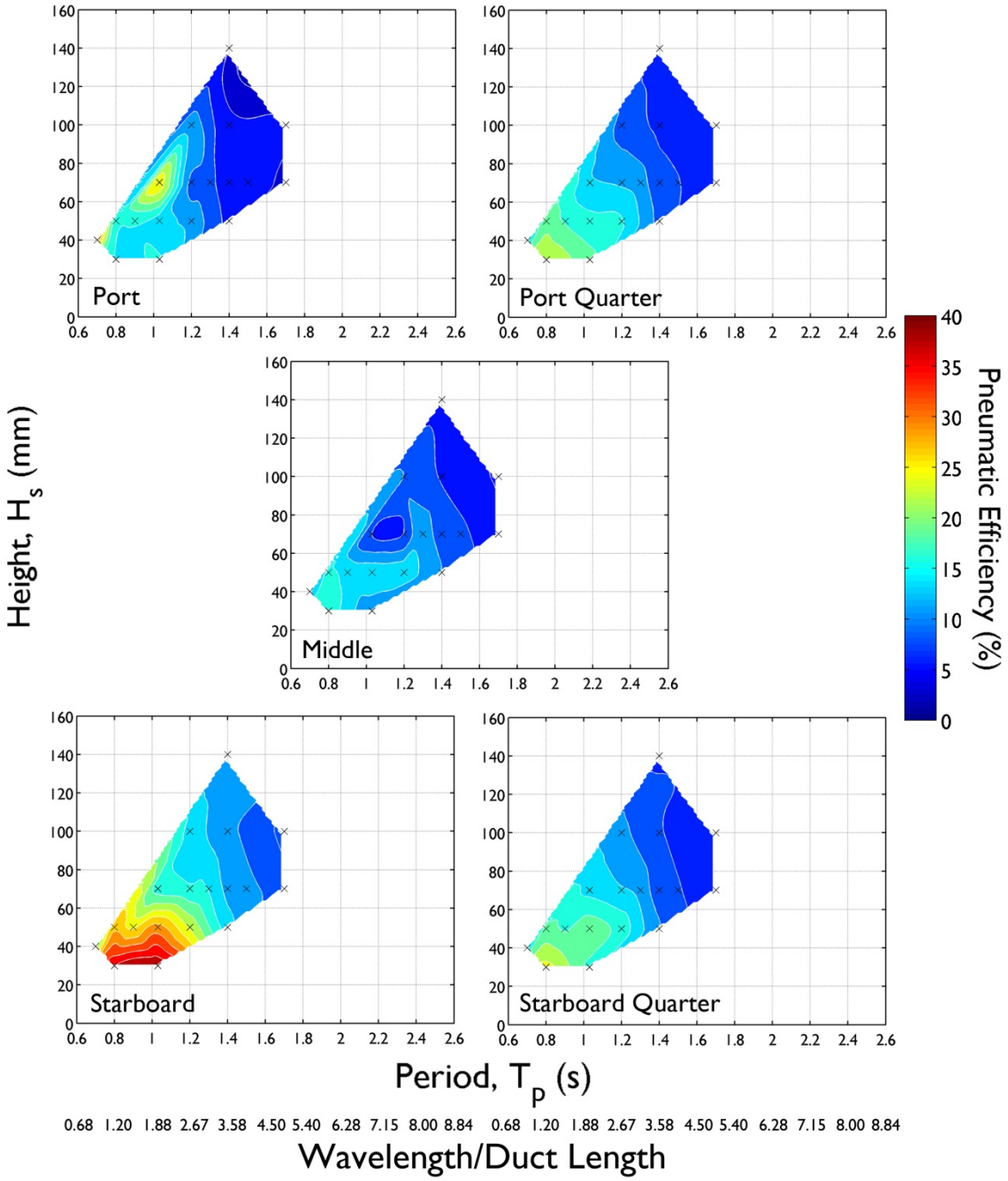

Figure 5.20, Performance contour plots for the five ducts in short crested, irregular sea states.

The performance data plotted in the contour plots in Figure 5.20 has been plotted in Figure 5.21 according to the five wave heights and over the range of wave periods tested. The general trend of the data shows that the performance decreased with increasing wave period. Similarly with the other tests reported in this chapter, there are some anomalies within the data, such as the performance of the starboard duct in H_s = 30 mm. As was mentioned previously, this may have been a result of the wave conditions within the tank; either due to the components of the spectral shape or variation in the wave height laterally across the tank. Without further data and more information regarding the wave basin calibration it is difficult to positively identify the anomalies. These results show however, that the performance of the floating platform in

irregular sea states was better than that in regular waves. This was due to the change in the behaviour of the motions of the model and will be discussed further in the subsection following.

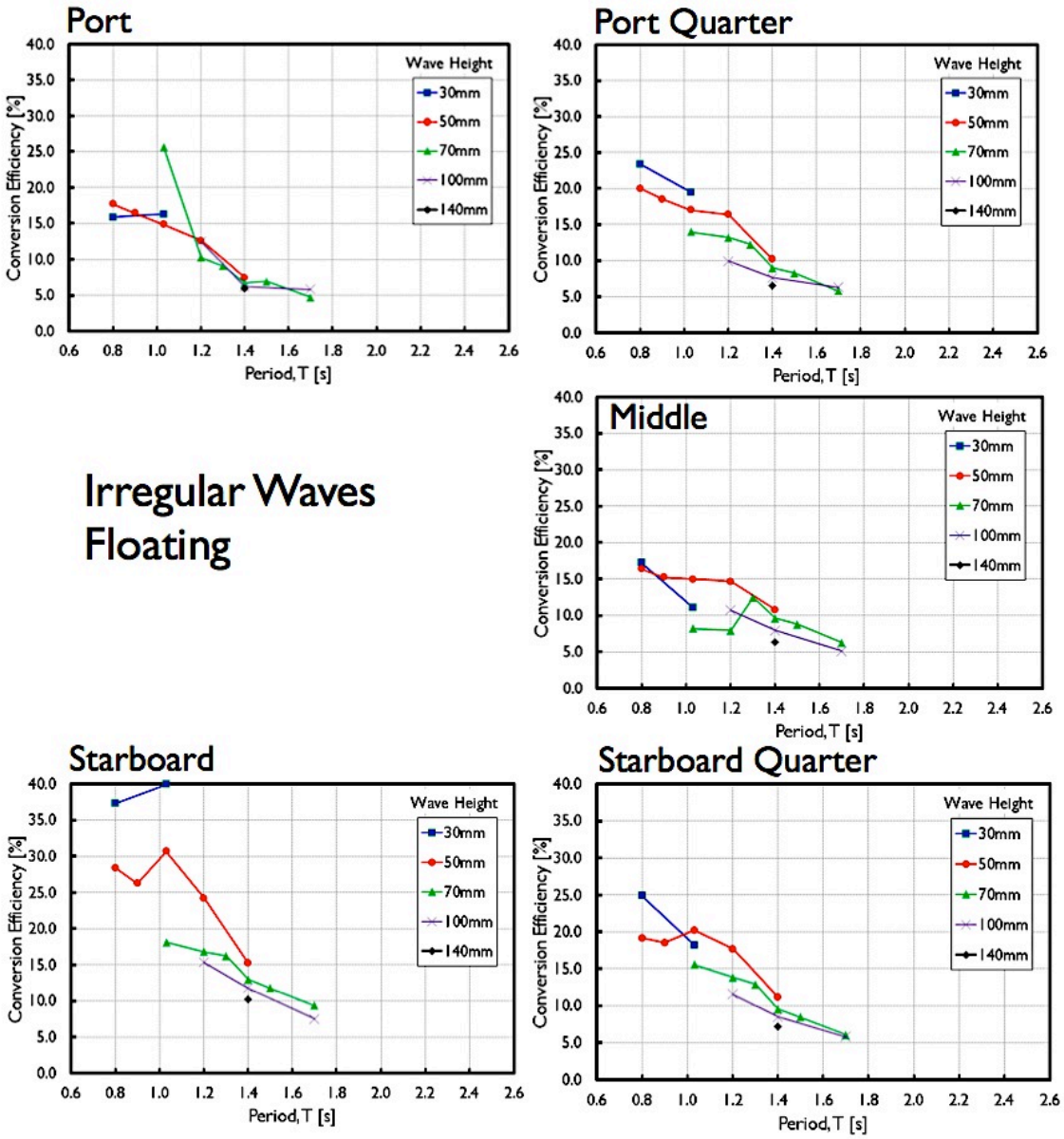

Figure 5.21, The variation in performance efficiency with peak wave period for five different significant wave heights with a floating model.

5.9.2 Motions

The behaviour of the floating motions of the model was recorded using a Qualysis™ ProReflex, non-contact 6 DOF, motion capture measurement system. This employed four high speed, infra-red cameras mounted above the tank to track the position of 3 reflective markers mounted rigidly above the model to an accuracy of +/- 1 mm. The propriety software accompanying the system was then used to convert the 3D locations of the markers to the 6 DoF motions of the rigid body about the model's CoG.

The motion tracking was used predominantly during the regular wave trials to record the resulting behaviour due to each wave period. Two methodologies have been used to study these motions; the first characterises the magnitude of response for each motion as a function of the exciting frequency. The second presents examples of the motion time series with the measured power to investigate the phase difference between the individual motions and air power recorded at the orifice. It was not possible to plot the motions as a direct consequence of individual waves as the position of the wave probe relative to the model position was not recorded during the tests and so it was not possible to infer the wave at the model. Additionally, no motions data for the model tests with the original naval architecture were measured, meaning the two designs could not be quantitatively compared.

5.9.2.1 Response Amplitude Operators – RAOs

RAOs indicate the response of a body to an applied wave excitation frequency and amplitude. These were obtained from the motions of the model in regular waves and were calculated as the ratio of the mean amplitude of the motion to the wave amplitude, as explained in Appendix A2.2.4. In the cases where multiple wave heights were tested for the same wave period, initially the RAO for each wave height was calculated. Two wave period examples are provided in Table 9 to show the difference in RAO with increasing wave height. There was generally good agreement between the RAOs and so an average over the different wave heights was taken to generate the RAO for each wave period.

Table 9, Example RAOs for two wave periods.

#	Period [s]	Height [mm]	Pitch RAO [°/mm]	Surge RAO [mm/mm]	Heave RAO [mm/mm]
7	1.03	30	0.08	1.2	0.5
4	1.03	50	0.09	1.3	0.5
15	1.03	70	0.08	1.2	0.5
18	2	100	0.01	0.3	1.0
17	2	140	0.01	0.3	1.0
19	2	160	0.01	0.3	1.0

RAOs however, do imply that a body responds linearly at each wave period for increasing wave height. In reality however, this may not be the case as non-linear and viscous effects increase with extreme motions and waves thus changing the dynamic response. The RAO therefore are most valid if they are calculated from non extreme conditions and are useful to indicate trends in the behaviour of the motions of the device.

The graph in Figure 5.22 shows the RAOs for the 6 degrees of freedom of the model over the range of 11 wave periods tested. The roll RAO would likely resemble the typical response curve however, in these tests, the waves were uni-directional and so the roll magnitude was insignificant. The most pronounced feature of the RAO plot is the peak response of surge and pitch at 1.2 seconds. This coincided with the peak in performance at T = 1.2 s that was observed in the static tests in regular waves. The absence of this peak performance feature in the floating tests with regular waves suggests that the motions were detrimental to the conversion process. Furthermore, a significant decline in performance for the floating model can be seen at T = 1.2 s in Figure 5.18. The coincidence of the peak performance and motion response was noted as a point of further investigation for subsequent experimental studies.

The heave response was small for wavelengths where the duct length was relatively long in comparison to the wavelength. The heave increased with period to about 1.7 seconds where the response and excitation almost reach unity. At this point the model effectively follows the wave contour and so absorbs less of the wave energy, which limits the energy capture. Similarly to roll, yaw and sway were also fairly insignificant due to the lack of directionality within the waves.

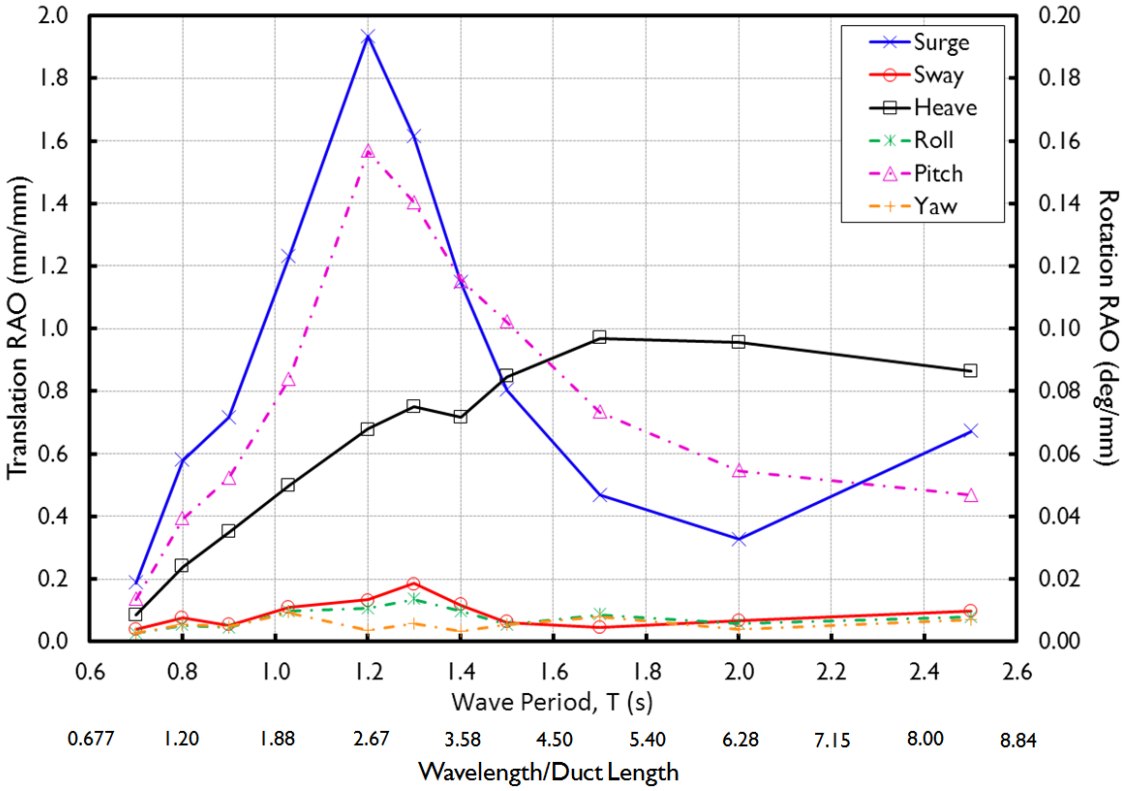

Figure 5.22, Response Amplitude Operators (RAOs) of the model for a number of regular wave periods.

Of the 6 DoF, pitch, surge and heave were thought to have the most influence on the power capture. As has been previously mentioned, yaw, sway and roll were small in comparison to the other dynamics and therefore had little effect on power capture.

5.9.2.2 Time Series Analysis of Motions and Power

The previous section presented the relationships between the magnitude of the motions with respect to the incident wave period. This however, provides little information as to what occurs during the course of a wave cycle. The energy conversion process was first observed in the static 2D duct in the images in Figure 4.21 however, this does not account for the effect of motions. Plotting the behaviour of the key motions and power generated with respect to time shows the point in cycle at which pneumatic power is generated.

The plots in shown in Figure 5.24 to Figure 5.26 are examples of a few cycles of pitch, heave, surge and pneumatic power. These were taken from the regular wave test numbers 4, 3 and 13, with power data derived from the middle duct. The positive directions of each of the three motions are shown in Figure 5.23. The wave conditions used feature around the 1:20 steepness line and are representative of the range of wave periods tested. Each of the variables plotted have been normalised by their maximum value (x/x_{max}) over the entire dataset. The amplitude of each variable is therefore relative to itself rather than any of the other variables and is plotted in this manner to improve the clarity of the figures.

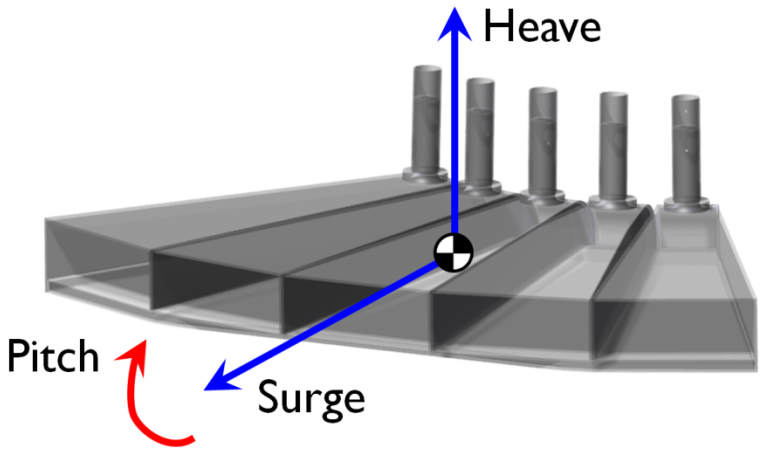

Figure 5.23, Directions of positive motion for pitch, heave and surge of the multi-duct model.

For each of the wave cases, it was observed that the pitch and surge motions had the same frequency and are 180° out of phase, meaning that the bow pitched upward whilst simultaneously surging backward. Maximum pitch and heave deviations were achieved at the same point in the cycle suggesting a strong coupling between pitch and surge.

Wave #4 in Figure 5.24 shows an "ideal" case for the phase difference between the incident wave and the pitch and surge. At 24 seconds, for example, the maximum amplitudes of pitch and surge (and heave) had just occurred and so subsequently the model began to pitch bow downward again and with a forward surging motion. As it pitched and surged forward, it encountered the next wave crest at the duct entrance. The combined pitching and surging motion aided the duct in capturing the wave front therefore creating a better seal and increasing conversion performance. The pulse of power occurred at around a $T/4$ phase lag to the pitch and was thought to be optimum. For this wave case, the regular wave, static model performance efficiency was 14.3 % whereas for the floating conditions, this increased to 17.2 %. This demonstrates that the performance was improved as a result of the device motions.

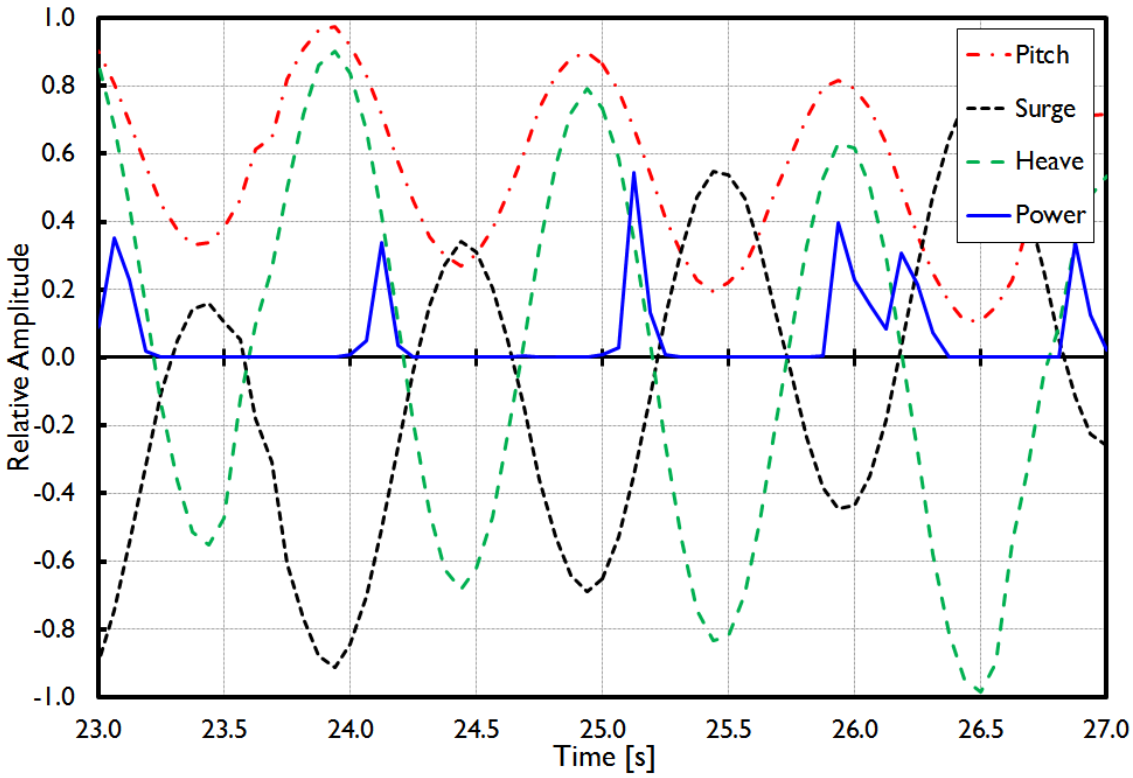

Figure 5.24, Time series data for regular wave #4 (T =1.03 s, H = 50 mm).

For longer wave periods, the airflow at the orifice was seen to shift towards being in phase with pitch. For wave #13 for example, see Figure 5.26, the airflow was generated almost concurrently with the maximum pitch amplitude. This can be explained by the process that occurs as the wave front encounters the duct; incident waves are typically deep water waves, as they enter the duct they experience a step change in depth, transforming them into a shallow water wave. This is effectively very rapid shoaling, whereby wavelength and celerity decrease, wave height increases but the period remains constant throughout. The waves within the duct may therefore travel with a slower forward velocity than the waves outside. In shorter wave periods, such as wave #4, this process happens more suddenly as the wavelength is much shorter than for wave #13 where there celerity of the wave is much higher. Unfortunately, as the

power production shifts phase with the pitch of the model, the performance is reduced and in the case of wave #13, the performance of the floating model was severely reduced in comparison to a static configuration.

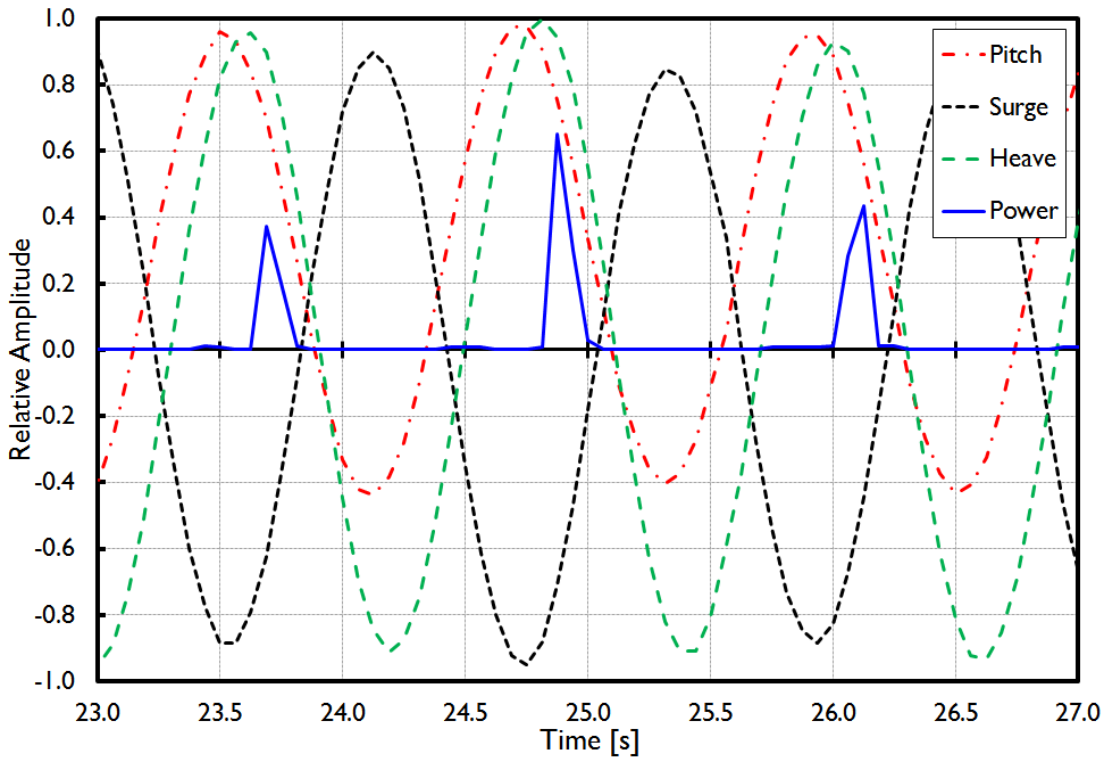

Figure 5.25, Time series data for regular wave #3 (T = 1.2 s, H = 70 mm).

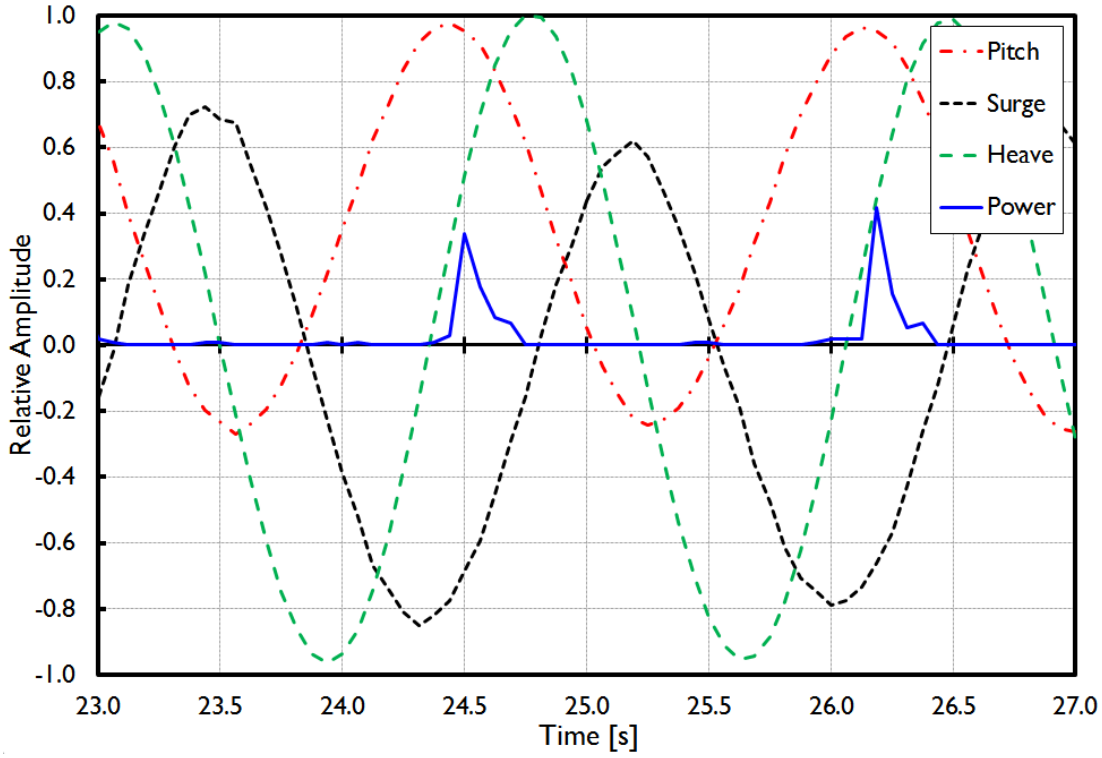

Figure 5.26, Time series data for regular wave #13 (T = 1.7 s, H = 100 mm).

In addition to the power production shifting with increasing period, the heave also shifts to become further out of phase with the pitch. For wave #4 (see Figure 5.24), heave and pitch are in phase whereas for wave #13 (Figure 5.26), they are nearly *T*/4 out of phase. For the short waves the model had a low heave response, as was shown by the RAO plot in Figure 5.22, and so the excursion was much smaller. Increasing the wave period gave a much larger heave response and so the time taken to overcome the inertia of the model was greater which likely led to the slight phase lag.

5.9.2.3 Free Oscillation Pitch Response

A displacement test was carried out to determine the natural pitch period of the redesigned model and whether it had influenced the power capture. The bow was pitched up, released and allowed to oscillate back to rest. The graph in Figure 5.27 shows the decay of the pitch oscillation after the initial displacement and shows that the natural pitch period of the model was approximately 5 seconds. This was twice the longest wave period used in the testing and so was not the cause of the peak in pitch RAO at 1.2 seconds. The graph also demonstrates the high level of damping provided by the reserve buoyancy, ballast and damping plates, only allowing two oscillations after the initial displacement. The internally radiated wave entrained within the duct, caused by the displacement of the duct, also influenced the motion of the model and further added to the damping.

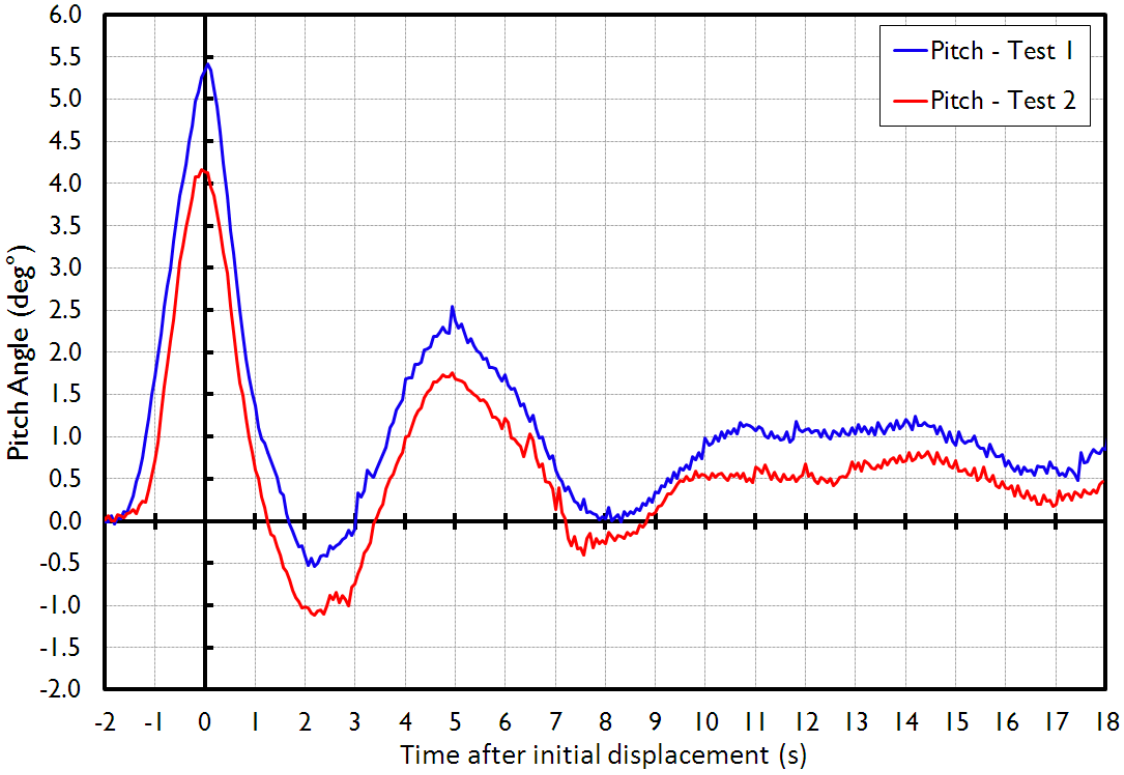

Figure 5.27, Two repeat tests of free oscillation after an initial displacement to show the natural pitch period of the redesigned model.

5.10 Discussion and Conclusions

This was the first occasion that the OWEL duct had been tested in irregular seas and also the naval architecture design considered. The results of these tests therefore provided essential learning and experience with which future, subsequent devices could be conceived. Unfortunately however, the geometry of the floating platform meant that the results from this testing were not especially applicable to subsequent models. Nevertheless, the experiments yielded a number of important conclusions:

- Testing confirmed that the performance was sensitive to the applied orifice damping.
- Providing higher PTO damping at lower flow rates and conversely, lower damping at higher flow rates, was beneficial.
- The range of typical linearised damping ratios of the optimised orifice strategy was 47,000 – 78,000 $Ns.m^{-5}$; a full scale equivalent of 133 – 220 $Ns.m^{-5}$.
- Peak efficiencies of up to 30 % were recorded for the static model in regular waves with the peak typically at T = 1.2 s, H = 50 mm, L/L_D = 2.7.
- The peak efficiency at L/L_D = 3.5 – 4.0 that had been observed in the 2D static tests, was not observed in the basin tests.
- Performance of the static model in irregular seas was comparable to that in regular waves, however the peak broadened to span L/L_D = 1.9 – 2.7.
- The performance of the floating model in regular waves was poor, with typical peak efficiencies across all of the ducts being less than 15 %. This was predominantly due to the increased motions as a result of the excitation by single frequency waves.
- The performance of the floating model in irregular waves was better than that in regular waves as the model was excited by a sea comprising multiple wave frequencies and phases, meaning that motions were reduced.
- The lack of peak performance at T = 1.2 s in the floating tests was postulated to be a result of its coincidence with the pitch RAO peak. This was identified as a point of investigation for subsequent studies.
- Certain wave conditions were thought to be beneficial to performance due to the behaviour of the model that they induced. This was also deemed important to investigate further.

This testing was a significant work package of the SWRDA funded project and fed into the technical and economical analysis of a future full scale device which demonstrated the potential of OWEL to become a commercially viable technology. This in turn led to the award of

additional funding from the TSB in order to continue the development of OWEL with the overall aim of deploying a large scale, marine demonstrator.

The challenge of designing a floating OWEL device with suitable conversion performance was realised during this testing. The effect of motions on the performance was not fully understood from these observations and so became a key objective for subsequent testing. It was also concluded that the performance of the single duct in the wave flume had been very different to that of an individual duct tested in the wave basin. Determining the performance characteristics in a wave tank with no lateral constraints was therefore also important in order to isolate the behaviour of the duct from any effects due to the tank walls.

6 Single Duct Physical Modelling

6.1 Introduction

The 2D and wave basin tests formed the majority of work in the SWRDA funded project. The successful completion of this project, coupled with the encouraging results from the physical modelling led to OWEL being awarded a large grant financed by the TSB. This was intended to part fund the continued development of the device with the overall aim of designing and deploying a large scale machine at an offshore site. The strategy devised by ITP and OWEL was to concentrate on the development of a single duct device rather than to continue with a multi-duct device. This not only made the project more feasible but reduced the capital required for construction and the overall risk in designing a large and complex WEC. Despite this however, designing a full scale device based on testing from 1:50 scale, laboratory models is not without significant risk. In the interest of de-risking the development of OWEL, it would have been appropriate to advance to an intermediate scale device rather than progressing straight from small to large scale. This would have allowed for lessons to be learnt and experience gained on a less costly and risky project. It is likely however, that funding would not have been obtained if OWEL proposed to develop an intermediate scale device.

As a single duct configuration had not been previously investigated, further modelling was required to inform the design of the demonstrator. Without a robust and reliable numerical model, the only option available was to carry out an additional series of wave tank testing studies. It was decided to take a single duct unit from the multi-duct, HMRC model and test it in the Lamont towing tank at the University of Southampton. Whilst the Lamont tank is by no means state-of-the-art, it provided invaluable research time with little pressure on time constraints for the testing that would otherwise be present at other facilities.

6.2 Objectives

In addition to studying the characteristics of a single duct model in comparison to the multi-duct configuration, the objectives of this phase of modelling were to:

- Further increase the fundamental understanding of the operating principle.
- Provide comparable results to compare single duct against multi-duct Cork model.
- Observation of the motions and power capture to draw relationships between the two.
- Optimise the physical geometry to maximise power conversion.
- Optimise the floating configuration to benefit performance.
- Produce an improved single duct configuration suitable to be designed for full scale.

6.3 Towing Tank Conditions and Limitations

The Lamont tank is 30 m long, 2.4 m wide, 1.1 m deep and has three pneumatic actuated, flap-type wave paddles, spanning the majority of the width and depth of the tank, see Figure 6.1. The water depth of 1.1 m meant that waves with $T < \sim 1.18$ sec ($L = 2.17$m) could be considered as deep water waves.

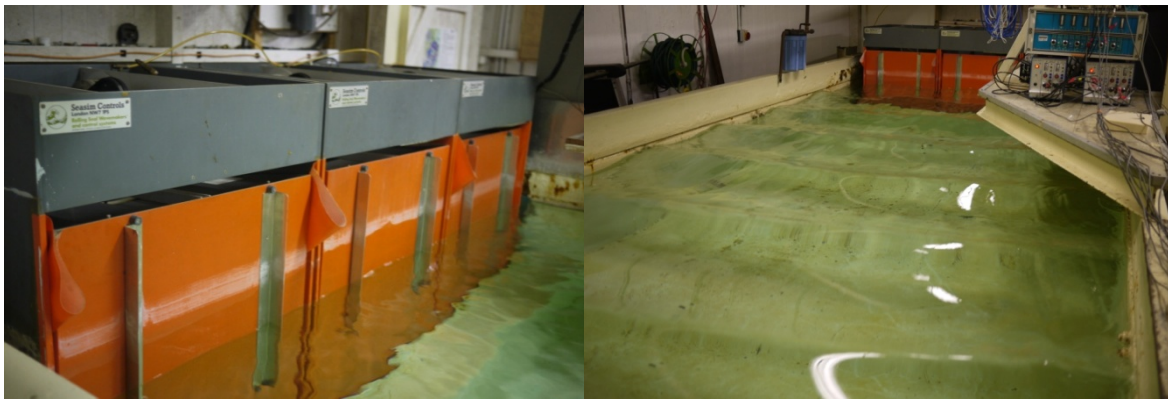

Figure 6.1, The wave generation system in the Lamont tank.

The wave absorbing "beach" in the tank consisted of a 20 mm thick sheet of open cell, coarse foam stretched over an inclined wooden frame at the far end of the tank. This was inadequate as it would likely only be able to attenuate low energy ripples. The majority of waves would therefore have had a large reflection coefficient with the incident wave trains reflecting back off the beach and wall in the direction of the wave makers. The lack of active wave absorption in the wave paddles meant that the reflected wave would then reflect off the paddles and combine with the generated incident wave. For this reason, in particular for long waves, the duration of each test was governed by the time it took for the waves to travel to the beach and back to the model. As Figure 6.5 shows, the model was positioned about 10 metres from the paddles and 20 metres from the beach. In the case of shorter waves where celerity was low, a reasonable run time could be achieved without influence from the remnant, reflected waves. The upper limit for wave period in the tank was deemed to be around 2 seconds with the associated waves having a wavelength of 5.36 m and a speed of 2.68 m/s. This allowed for about 14 seconds of useful test data from the waves passing the model to the reflected wave train arriving back at the model and influencing motions and the incident waves.

A further implication of the inadequate beach was that it was not possible to test irregular sea states in the tank. The time required to run a sea state depends on the method chosen to generate an irregular wave time series, see Payne (2008) for further information. The minimum time at small scale however, is typically of the order of a few minutes, during which the reflected waves from the beach, model and wavemakers would have traversed up and down the tank many

times. This would have significantly interfered with the testing as the contaminated waves would have modified the performance and motions of the model. It was therefore decided not to carry out any irregular tests.

Any open body of water has natural frequencies at which it will freely oscillate. These standing waves may occur in a number of different patterns depending on whether the water basin is enclosed at both ends or open at one of them. A closed basin is analogous to the body of water between the two side walls of a wave tank and its first three modes of oscillation are given in the diagram in Figure 6.2. Also given is Merian's formula for the periods of the natural oscillation modes in a rectangular basin of uniform depth.

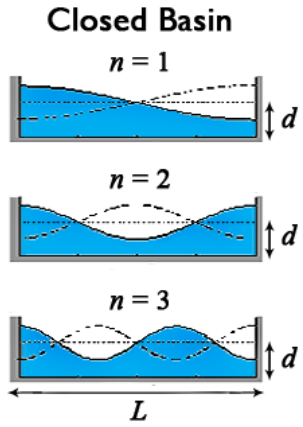

$$T_n = \frac{2L}{n\sqrt{gd}}$$

Where is the length of the basin, $L = 2.4$ m, the mean water depth, $d = 1.1$ m and the oscillation mode $n = 1, 2, 3\ldots$

Figure 6.2, Modes of oscillation of a closed basin with uniform depth.

As Figure 6.2 shows, the longer the basin length (L) or the shallower the basin depth (d), the longer the standing wave period. The values for L and d provided in Figure 6.2 are for the Lamont towing tank and using the above equation, the periods of the first five cross wave modes are given in Table 10.

Table 10, Transverse wave modes of the Lamont towing tank.

Mode (n)	Length [m]	Period [s]
1	4.80	1.86
2	2.40	1.24
3	1.60	1.01
4	1.20	0.88
5	0.96	0.78

The periods at which transverse standing waves occur in the Lamont tank, provided by Table 10, are predominantly within the range of wave periods used within the testing. It was identified after the experiments that these standing waves may have had an undesirable impact on the test results. This could have been due to the wave height measured during the tank calibrations being a combination of the incident and transverse waves leading to the wave height being incorrect due to the transverse component.

Historically, the Lamont facility had predominantly been used for the small scale, tow testing of ship hulls and so wave generation had never been the foremost concern in the experimental studies. As a result the tank was only equipped with an old signal generator to act as a drive signal source for the wave makers. This method did not allow for repeatable tests to be run and was unsuitable for use in any wave specific studies. The author developed a new wave drive signal generation system, based on a drive and data collection program written by Prof. J. Chaplin. The modified program was similar to that used in the 2D testing, therefore allowing autonomous computer control of the wave paddles and data collection enabling tests to be carried out in batches to encompass a large number of test conditions. The program sampled all of the wave probe and pressure sensor data at 256Hz through a 16-bit analogue to digital conversion unit.

During the initial calibrations of the tank, the water was observed and monitored with wave probes after each test run of waves to determine the necessary tank settling time required before commencing the subsequent test. This was significantly longer than for the 2D tests as the tank was larger and had a poorer wave absorbing beach. Similarly to the 2D testing, the settling time varied with the wave period tested, with longer times required for longer wavelength waves. This typically ranged from 4 minutes up to 7 minutes for the particularly energetic waves. The plots presented in Figure 6.3 and Figure 6.4 provide examples of the water surface elevation prior to the commencement of two typical runs. Both cases show that there may have been some very small (<1 mm) ripples in the tank prior to the run but otherwise it had mostly settled to an acceptable state. The wait time was adjusted to ensure that the water surface in the tank was similar to this before the subsequent run commenced. In all of the experiments in the Lamont tank, each of the tests only ran a wave train of between 12 to 20 full wave cycles to help reduce the settling time required and also to prevent the reflected wave train from excessively contaminating the waves at the test section.

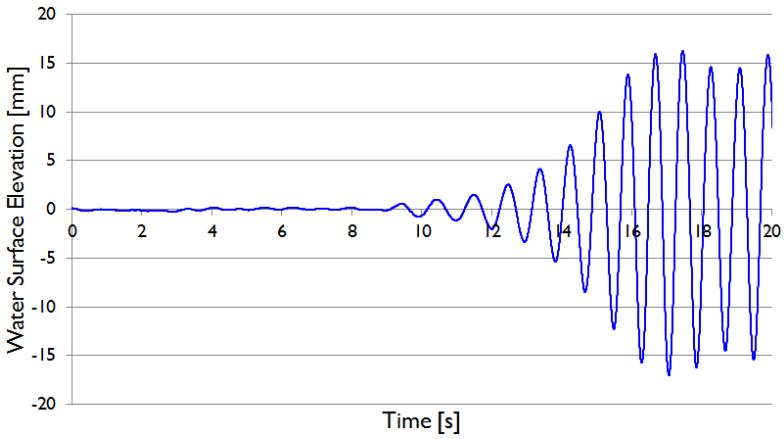

Figure 6.3, An example of the water free surface elevation preceding a run for T = 0.83 s, H = 30 mm.

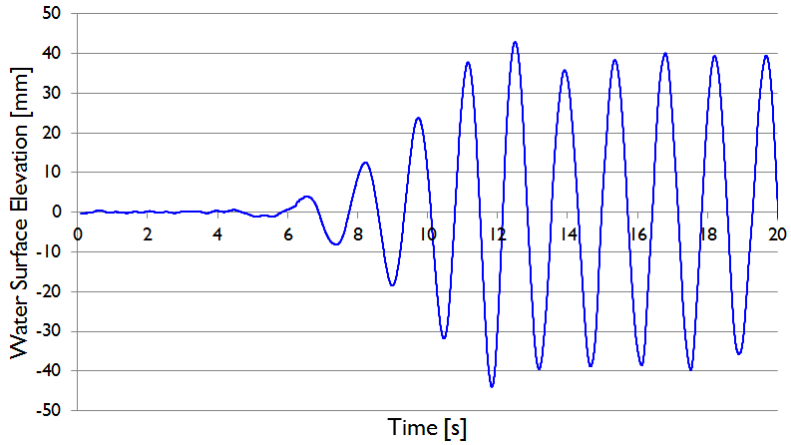

Figure 6.4, An example of the water free surface elevation preceding a run for T = 1.43 s, H = 78 mm.

6.4 Orifice

The orifice PTO simulator arrangement was identical to that used in the wave basin testing as detailed in section 5.5. The chamfered PTO tube entry from the starboard duct in the wave basin testing was also used throughout this series of tests to ensure airflow losses prior to the orifice were minimised. The differential pressure sensor used to measure the pressure drop across the orifice was a Sensor Technics HCLA 12X5 EB with temperature compensation. This was far superior to the original sensor, detailed in section 4.5, as it had a more suitable pressure range of +/- 1,250 Pa and lower error, specified as +/- 0.05% of the output span which is equivalent to +/- 1.25 Pa.

Only the $\beta = 0.4$, $D_o = 20$ mm orifice was used in these tests. It is possible that greater performance could have been achieved in wave conditions where $T < 1$ s by using a 17 mm orifice, as was the case in the wave basin testing.

6.5 Phase 1 – Baseline Configuration

6.5.1 Introduction

The first phase of testing in the Lamont testing occurred over two weeks during February 2011 and was principally intended as a preliminary set of experiments. The foremost task was to check the suitability of the facility for the testing programme and develop the testing methodology that could be used in subsequent phases. The single duct was initially fixed rigidly in the tank to investigate static model performance and the modification of the internal wave along the duct's length. Testing continued on to examine the floating performance of the duct with an initial buoyancy configuration based on the arrangement from the wave basin testing however, this was shown to be unfavourable. A redesigned buoyancy arrangement was conceived in order to improve the stability of the duct which resulted in a significant improvement in motions and performance.

The objectives of this initial testing were to:

- Establish a testing methodology and set up for the Lamont tank.
- Determine the performance of a single, static tapered duct to provide a baseline.
- Apply the naval architecture approach for the multi-duct device to the single duct.
- Determine the performance of the single duct, floating model with a mooring and buoyancy configuration that are representative of a full scale scenario.

6.5.2 Model Design

The model was a direct derivative of the model that was tested in the wave basin at HMRC, Cork. The starboard duct was removed from the previous five duct model as, due to its chamfered rather than filleted PTO inlet, it performed most favourably of the five ducts. The dimensions of the duct and PTO pipe were the same as those on the model tested at HMRC and are summarised in Figure 5.2.

Ten wave probes were used to measure the water free surface displacement in the tank and the internal water level within the duct. Figure 6.5 provides a schematic of a typical layout for the tank and sensors during the testing. Data from the wave probes ahead and to the rear of the model during the tests is not presented in this work.

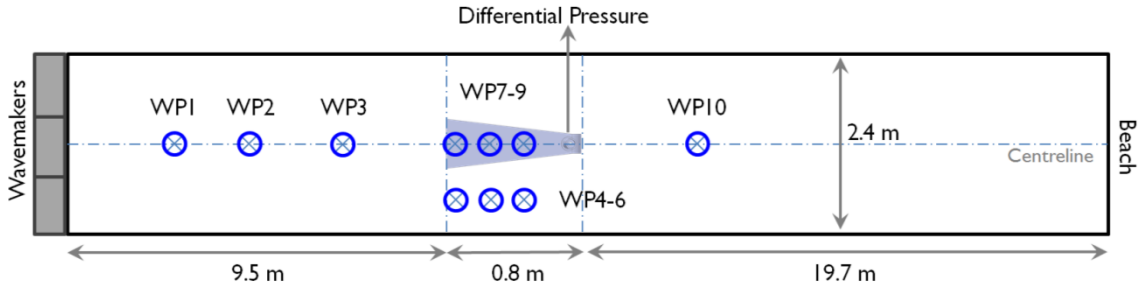

Figure 6.5, Schematic of the experimental setup showing type and location of instrumentation.

6.5.3 Wave Test Conditions

The testing was planned to cover an extensive range of wave periods and heights and additionally to include the wave conditions used in the wave basin experiments at HMRC, Cork. Prior to testing, little was known about the wave generation capabilities of the Lamont tank, therefore, much of the initial tank calibration work was to determine the limits of the wave makers. As with the previous wave flume and wave basin testing, wave height measurements were carried out prior to testing so that conditions could be checked without the model in the tank.

A lip in the side wall of the tank, located just above the still water line as shown in Figure 6.6, caused large surface ripples as the waves travelled down the tank. The ripples generated by the lip were significant in comparison to the wave height and propagated transversely across the tank. Further influence may have been a result of transverse cross waves set up in the tank at a number of different wave periods as previously discussed in section 6.3.

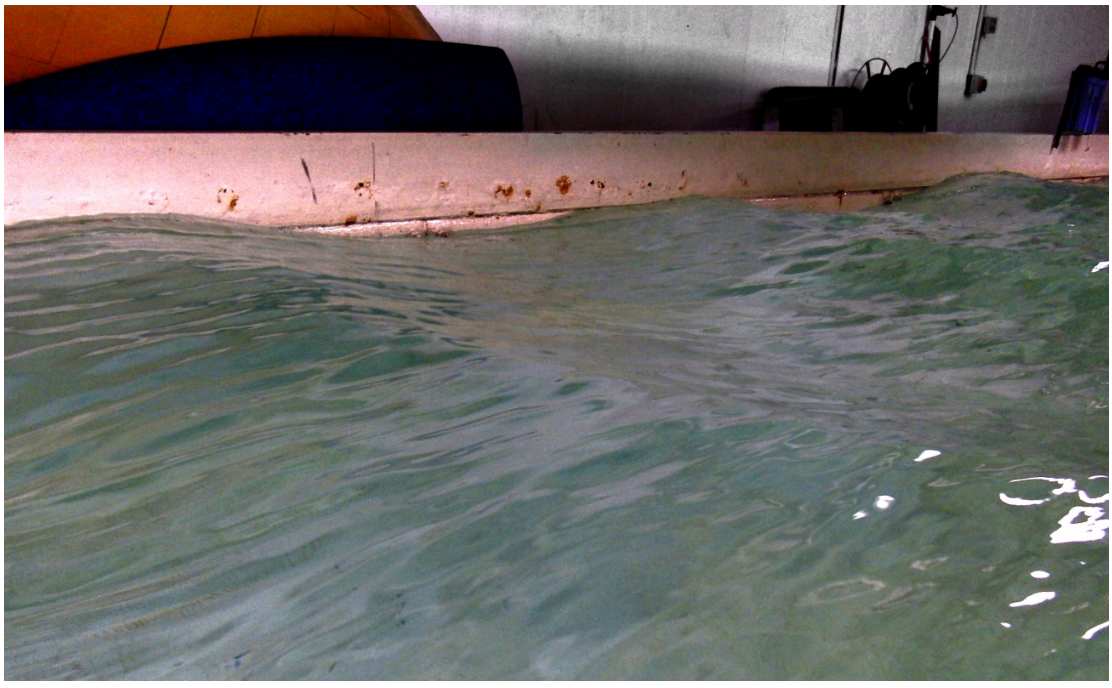

Figure 6.6, Water surface ripples propagating transversely generated by the side wall lip.

Three wave probes were positioned across the span of the tank at the same *x* location where the duct entry would be when the model was installed in the tank. Wave probes 1 and 3 (WP1 & WP3) were positioned 0.6m from each of the side walls in the tank whereas WP2 was positioned in between them, in the centre of the tank, 1.2m from the side walls. The average height from each of these probes was taken over five wave periods and the average height across the tank was calculated. In addition to the height analysis an FFT of the data was taken to calculate the peak frequency of the signal and so determine the wave period.

The data in Table 11 provide an example of the variation in wave height across the tank for a sample of 21 wave conditions that were calibrated. This shows the average wave height recorded at each of the three wave probe locations with no model in the tank. Table 11 also shows the maximum and minimum percentage variations between the actual recorded average wave heights and the mean height across the tank. The results show that the positive and negative deviations from the mean wave height across the tank did not exceed 10% of the mean wave height across the tank. The percentage deviation reduced for waves with greater height as the ripples from the side wall lip, which caused the majority of the deviation, became comparatively smaller with increasing height. For all but one of the 21 conditions summarised in , the wave height recorded at WP3 was greater than that at WP1 and WP2. This may have been an error in the wave probe calibration or possibly as a result of local wave height phenomena caused by wave superposition or that the wave paddles were not all acting equally

Table 11, Variation in wave height across the tank for a set of 21 wave conditions.

Wave Period [s]	Height WP1 [mm]	Height WP2 [mm]	Height WP3 [mm]	Mean Height [mm]	Positive percentage deviation [%]	Negative percentage deviation [%]
0.71	18.5	18.3	20.5	19.1	7.4	4.0
0.71	30.9	29.9	35.0	31.9	9.8	6.5
0.82	11.9	13.1	12.9	12.6	3.8	5.7
0.82	27.4	31.4	30.5	29.7	5.5	8.0
0.82	36.3	40.9	41.1	39.4	4.2	8.0
0.92	21.0	22.3	22.4	21.9	2.4	4.2
0.92	29.7	33.8	35.1	32.9	6.7	9.6
1.00	15.5	17.8	17.9	17.0	4.9	9.1
1.00	31.1	30.3	32.7	31.4	4.2	3.4
1.00	42.5	42.6	44.8	43.3	3.4	1.8
1.15	25.4	27.7	26.9	26.7	3.9	4.6

1.15	44.5	48.4	49.5	47.5	4.3	6.2
1.15	54.7	58.8	60.6	58.1	4.4	5.7
1.15	66.1	70.7	72.8	69.9	4.3	5.4
1.25	30.8	31.8	34.1	32.3	5.8	4.5
1.25	56.7	58.7	62.4	59.3	5.3	4.4
1.25	75.2	76.4	81.1	77.6	4.6	3.1
1.47	34.0	34.3	35.1	34.5	1.8	1.4
1.47	62.8	62.8	63.8	63.1	1.1	0.6
1.47	74.6	75.0	76.0	75.2	1.1	0.8
1.69	55.9	54.8	54.6	55.1	1.5	0.9

The time series plots in Figure 6.7 show a series of three example wave forms taken from the calibration runs to demonstrate the typical quality of the waves. As is usual with generated wave trains, the wave amplitude increases over the first few periods up to a maximum, after which the wave height stabilises. With all of the calibration and testing runs the measurements of wave height or generated air power were not analysed until at least five wave periods after the first wave crest that exceeded a positive amplitude of 5 mm. The red lines on the graphs in Figure 6.7 indicate the calibrated, average wave heights for the three cases and show good agreement with the actual waveforms.

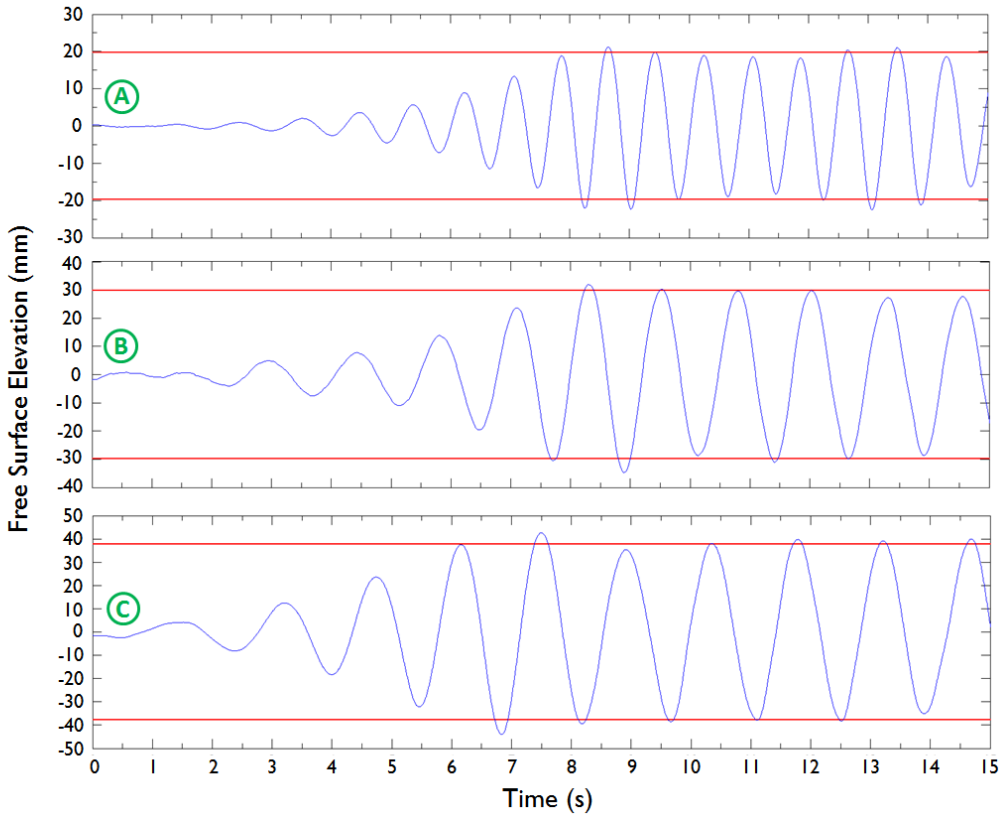

Figure 6.7, Three example waveforms from the tank calibration tests, taken from the centre wave probe; **(A)**: $T = 0.83$ s $H = 37.4$ mm, **(B)**: $T = 1.25$ s $H = 59.4$ mm, **(C)**: $T = 1.43$ s $H = 75.4$ mm.

The scatter plot in Figure 6.8 shows the 166 different wave conditions that were measured during the tank calibration runs and indicate the approximate bounds of the wave heights and periods that could be generated. From this data it was decided to limit the generation periods of the tank to 0.68 s < T < 2.0 s. Waves shorter than 0.68 s were of poor quality and for 1:50 scale conditions, these bounds were well suited to represent seas of periods 4.8 s < T < 14.1 s. For the shorter period waves, T < 1 s, the wave height was limited by their steepness. For longer periods, T > 1 s, the height appeared to be limited by the power and stroke of the wavemakers as the maximum height reduced with increasing period. For these initial tests, the repeatability of the wave height was not quantified as only one measurement test was run for each wave condition. It is likely however, that due to the large number of test conditions run, errors in the wave height giving rise to errors in efficiency would be partly smoothed out in the interpolated efficiency contour plots.

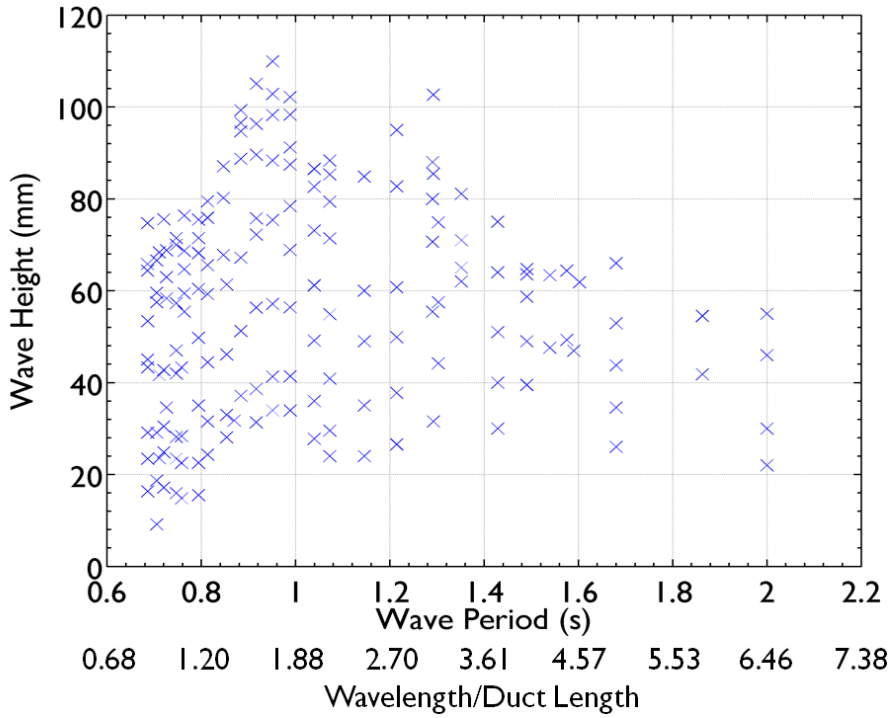

Figure 6.8, Wave test conditions used in the initial static and floating baseline experiments.

6.5.4 Static Configuration

The model was fixed rigidly in the tank and, similarly to the wave basin tests, the freeboard at the duct entrance was set at 25 mm and the stern of the model was dipped so that the internal water free surface just made contact with the duct roof directly behind the PTO tube. Figure 6.9 shows two efficiency contour plots that compare the performance results of the static model in the Lamont testing with those of the previous wave basin tests. It was found that the performance of the static, single duct model was reduced in comparison to that of the multi-duct model. At T = 1.2 s, H = 50 mm for example, there is approximately a 50 % reduction in

conversion performance from the wave basin testing (η = 24.8 %) to the single duct performance (η = 12.6 %). The main similarity between the plots is that their efficiency peaks approximately coincide at T = 1.15 s (L/L_D = 2.5). The reduced number of data points in the basin tests meant that larger regions of interpolation are required for the contour plots and so less definition is possible.

The contour plot in Figure 6.9 shows distinct bands of peak and poor performance. Particularly noticeable is the region of reduced performance between approximately 0.85s<T<1.05s. This feature may be explained by the presence of transverse, cross-waves in the tank that led to an incorrect calibration of the wave height during the wave tank calibration. Alternatively, it is possible that a local minimum wave height occurring in the tank at the duct leading to less power entering the model than was calculated from height calibration value.

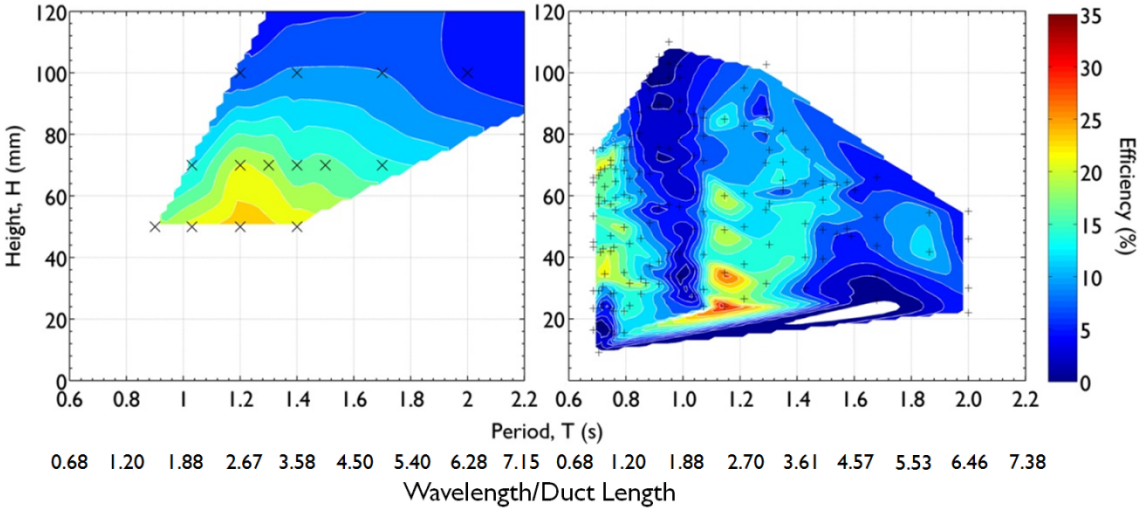

Figure 6.9, Comparison of efficiency contour plots for starboard duct in wave basin testing in regular waves in static configuration (left) and static, single duct in towing tank tests (right).

Whilst carrying out the static model tests, the free surface elevation inside the duct was recorded using the three wave probes installed within. An additional three wave probes were positioned in the open tank directly adjacent to the internal wave probes to record the undisturbed wave train. This allowed for direct comparison between the incident waves and the internal, modified free surface profile. The plots in Figure 6.10 and Figure 6.11 provide two examples of such comparisons; Figure 6.10 is for a longer wave (T = 1.2 s) and Figure 6.11 is for a shorter wave (T = 0.9 s). The blue traces (WP4 and WP5) are from the external wave probes and the red traces (WP7 and WP8) are from the internal probes with WP7 at the midpoint of the duct and WP8 being approximately 0.235 m aft of that. The flat, truncated peaks of the internal waves are where the internal wave crest sealed with the roof of the duct and so is "clipped" by the limits of the geometry.

In Figure 6.10, it can be seen that the initial lag between the two wave crests was approximately 0.5 s whereas after the wave has propagated 0.235 m to the next wave probes, the lag increased to 0.65 s. This shows that the external wave took ~0.1 s to travel 0.235 m (0.125 s calculated using the wave speed), whereas the internal wave took ~0.3 s to travel the same distance. Similarly for the wave in Figure 6.11, the initial lag was ~0.15 s which extended to ~0.5 s by the next probe. The external wave took ~0.2 s to travel 0.235 m (0.163 s calculated using the wave speed), whereas the internal wave took ~0.45 s. These results show that for the wave with T = 1.2 s, the internal wave speed reduced to ~0.78 m/s and for T = 0.9 s, it reduced to ~0.52 m/s. These estimated wave speeds are less than the theoretical, shallow water wave speed for within the duct ($\sqrt{gd} = 0.89\ m/s$) where d = 0.08 m. The wave speed of the internal wave for both cases was reduced by approximately 60% in comparison to the incident, unmodified wave conditions.

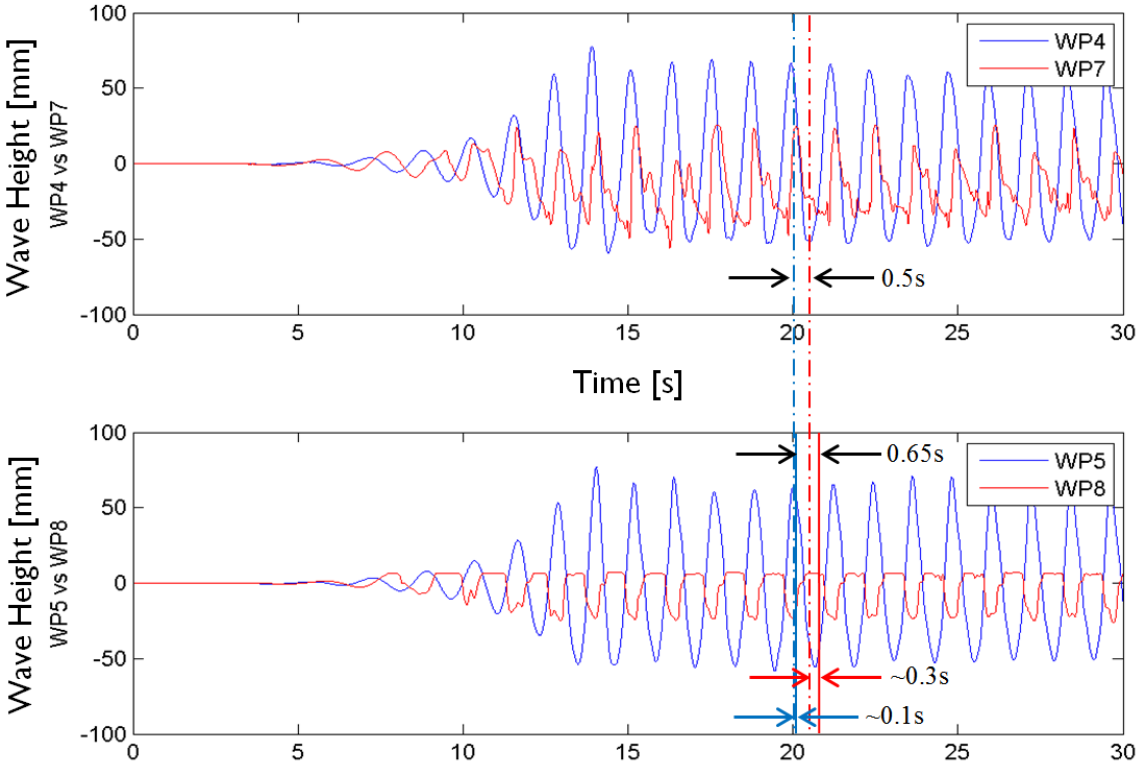

Figure 6.10, H =100 mm T = 1.21 s, L = 2.28 m, C = 1.88 m/s.

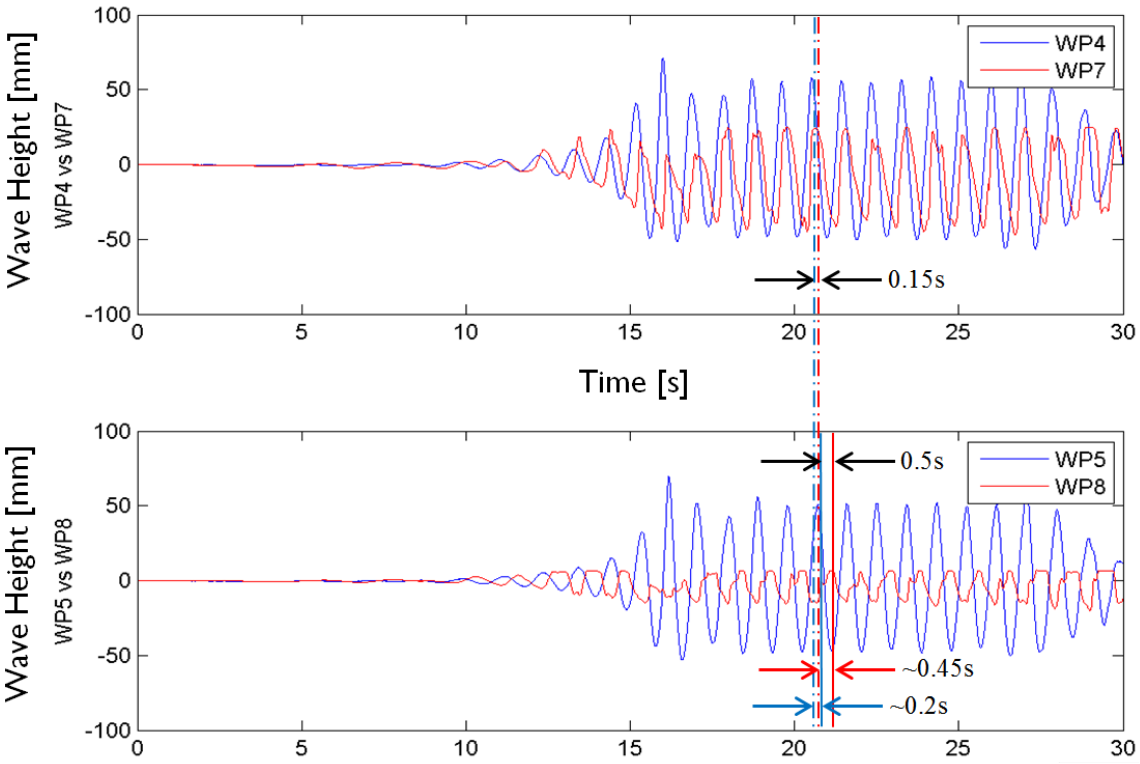

Figure 6.11, H = 100 mm T = 0.92 s, L = 1.32 m C = 1.44 m/s.

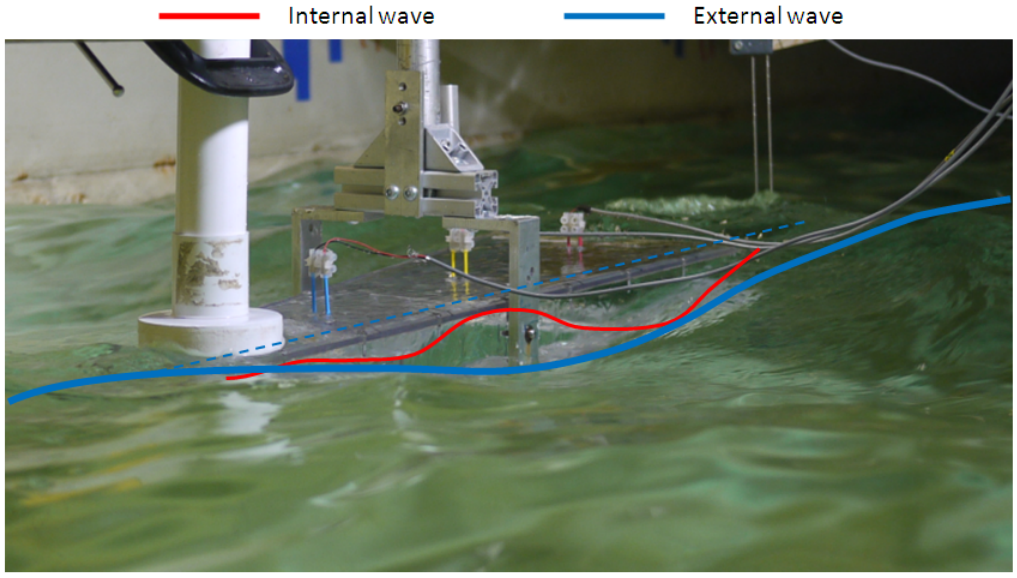

Figure 6.12, An image showing the difference in location between the internal and external wave crests.

The image in Figure 6.12 shows the difference in wave crest position brought about by the phase lag resulting from the slowing of the internal wave. The internal wave in this example arrived at the PTO in the stern of the duct at a time after the external wave crest had passed the stern. From these observations, it was postulated that, for wave conditions where the internal wave slows enough to increase the phase difference (φ) between the wave crests, the head difference created between the internal trough at the stern and the external peak, also at the

stern, causes an inward rush of water from below the duct. This causes the internal free surface to also rise at the stern which assists the advancing internal wave front in compressing and expelling the air pocket out through the PTO duct. This has been likened to having an oscillating water column at the stern interacting with the internal wave crest and it could be beneficial to conversion performance. Figure 6.13 illustrates this phenomenon and was based upon visual observations of the water behaviour from the underwater viewing window in the towing tank.

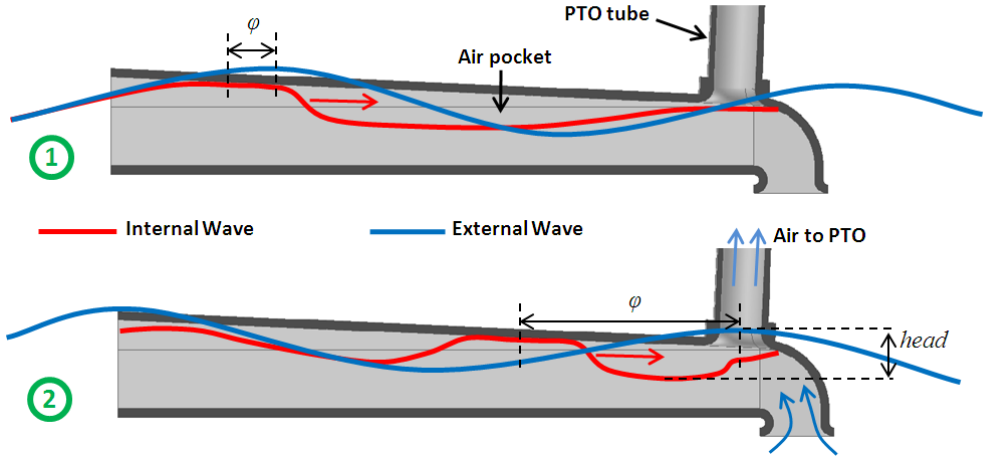

Figure 6.13, Diagram showing the observed internal fluid dynamics for $L/L_D = 1$.

Returning to the discussion of the simple, harbour wave theory introduced in section 4.7.1, further estimations of the standing wave periods within the duct for this alternative geometry may be made. Figure 6.14 and equations [22] and [23] provide the schematic of this model geometry configuration and the fundamental, standing wave period. This is similar to those previously discussed for the parallel walled duct with the flat and ramped duct floors as discussed in section 4.5.

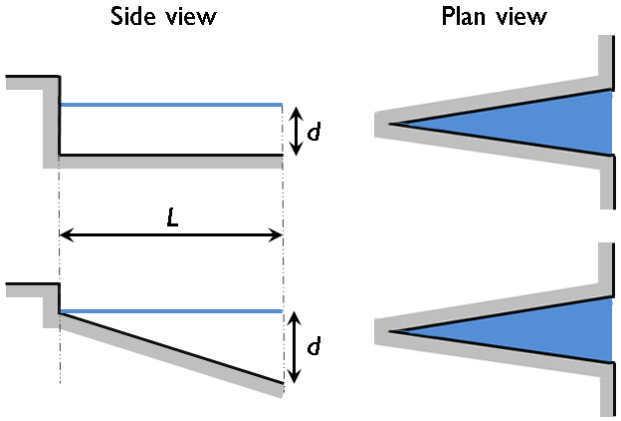

$$T_0 = 1.308\left[\frac{2L}{\sqrt{gd}}\right] \qquad [22]$$

$$T_0 = 1.653\left[\frac{2L}{\sqrt{gd}}\right] \qquad [23]$$

Figure 6.14,Plan and side views of two harbours with tapering side walls and their associated, longest natural periods, T_0.

For the case of this duct geometry, the entry depth, $d = 0.08$ m and characteristic length, $L = 0.83$ m. Using the ratio of the standing wave periods for the different modes from

Rabinovich (2009), the details of the ducts and equations [22] and [23], the periods for the first four standing wave modes for each of the geometries are given in Table 12.

Table 12, Standing wave periods for different modes for two different basin shapes with tapered sides.

	Constant Depth		Reducing Depth	
Mode (*n*)	Ratio from T_0	Period [s]	Ratio from T_0	Period [s]
0	1.000	2.45	1.000	3.10
1	0.435	1.07	0.541	1.68
2	0.278	0.68	0.374	1.16
3	0.230	0.56	0.283	0.88

Similarly to the discussion in section 4.7.1 of the application of this theory to the performance results, empirical relationships are required to determine the correct coefficients and ratios of the modal periods to the fundamental. It is likely that the actual standing wave periods for the OWEL duct in this example are between the values for the two geometry extremes presented in Table 12. Whilst this theory may be developed further with additional experimental work, the application of it to the behaviour of a floating duct may be more challenging. Nevertheless, if it can be improved to predict the wave periods at which to expect performance peaks for a static duct, this may provide better insight into the scaling of devices for full scale wave climates.

6.5.5 Initial Floating Configuration

Following the baseline, static duct testing buoyancy was attached to the keel of the duct and ballast was fixed below so that it was suspended underneath the keel. Two accelerometers were then mounted on the model, one at the bow and another at the stern, just forward of the PTO tube. As the pitch angles of the model were relatively small it was assumed that the majority of the acceleration measured would be due to the vertical motions at those points and so horizontal components of acceleration from the rotation in pitch were neglected. By integrating the acceleration signal the velocity and position of the duct could be calculated. Further to this, knowing the geometry and positions of the accelerometers, the pitch and heave magnitudes could be determined.

After some brief testing it was observed that the naval architecture design was not suitable and that the motions of the model were excessive. In shorter wavelengths, for $L/L_D < 1$ the pitch and heave were fairly negligible. However, as the wavelength was increased the pitch and heave

motions grew rapidly and at L/L_D = 2.3 the pitch motion was visibly greater than the steepness of the waves, as shown in Figure 6.15. This had a detrimental impact on the conversion performance as very little of the wave crest was actually captured by the duct and when water did pass into the duct, it was not enough to create a seal and air pocket.

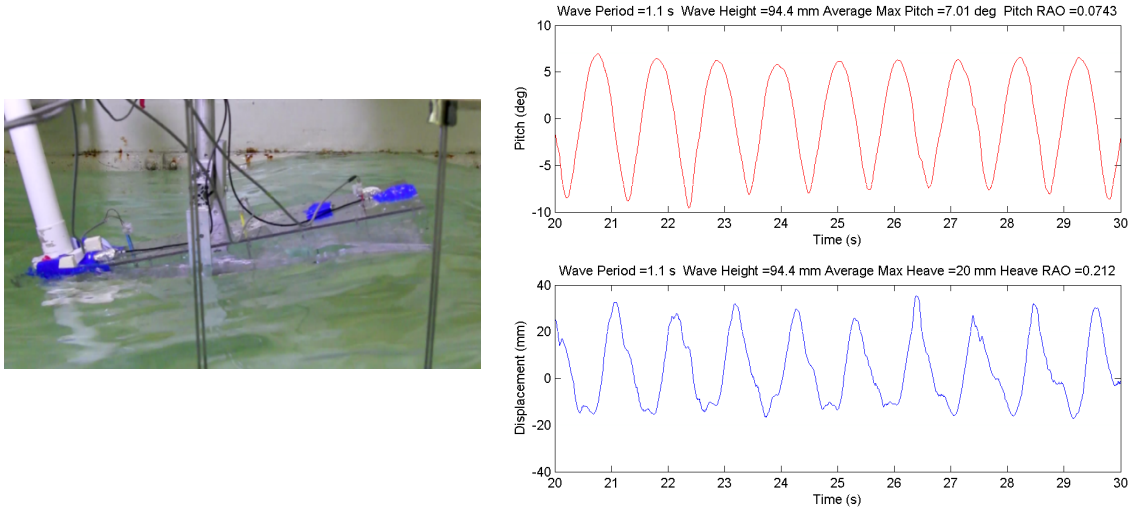

Figure 6.15, Video still with the corresponding pitch and heave motions for T = 1.1 s, H = 94 mm.

An extreme example of this excessive pitching characteristic is shown in the video still in Figure 6.16, with the dashed red line indicating the position of the wave crest.

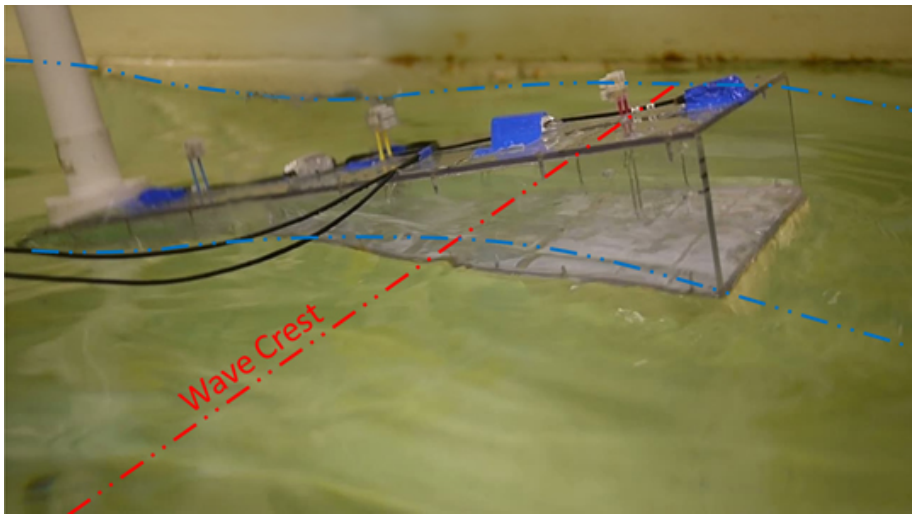

Figure 6.16, Close up video still showing the excessive pitch, resulting in a large duct entry freeboard, the wave free surface profile and the location of the crest. (T = 0.8 s, H = 65 mm)

The buoyancy and ballast arrangement of the initial floating model design was based upon the principles applied to the multi-duct model. It featured a low WPA and CoB in order to avoid changes in buoyancy due to local surface level with the intention of decoupling the motions from the waves. To reduce the resulting instability, the ballast was kept low to ensure a positive GM and bring the CoG below the lowered CoB. Additionally, the ballast was dispersed longitudinally to increase the moment of inertia and provide a higher dynamic resistance to pitch. During these initial trials it was realised that this approach may not have been the most

effective way of controlling motions for a single duct machine. It was decided to cease further testing and redesign the model and experimental methodology in order to rectify these issues.

6.5.6 Naval Architecture Redesign

The redesign of the naval architecture led to model with a much larger water plane area than had been previously tested. The majority of the buoyancy was moved from underneath the duct to the sides but with reduced buoyancy in the walls at the bow of the duct. It was seen in the previous phase that the duct had very large pitch motions in some waves which meant that it was not capturing the wave crest effectively. The lack of reserve buoyancy at the bow reduced the buoyant forces and pitching moment as the duct encountered a wave crest. Further to this, the aftward buoyancy would encourage the duct to pitch bow down into the subsequent wave crest. The two diagrams in Figure 6.19 show that the initial low WPA model would provide minimal reaction to changes in pitch or heel angle. The low WPA design therefore had a low static stability and small righting moment making it excessively tender. The revised naval architecture had an element of surface piercing buoyancy with a wide aft end and this provided, as Figure 6.19 shows, a higher transverse righting moment and roll stiffness than the previous design. The surface piercing element to the buoyancy increased the righting arm (distance GZ) for a given angle of roll by moving the centre of buoyancy a greater distance from the level roll position.

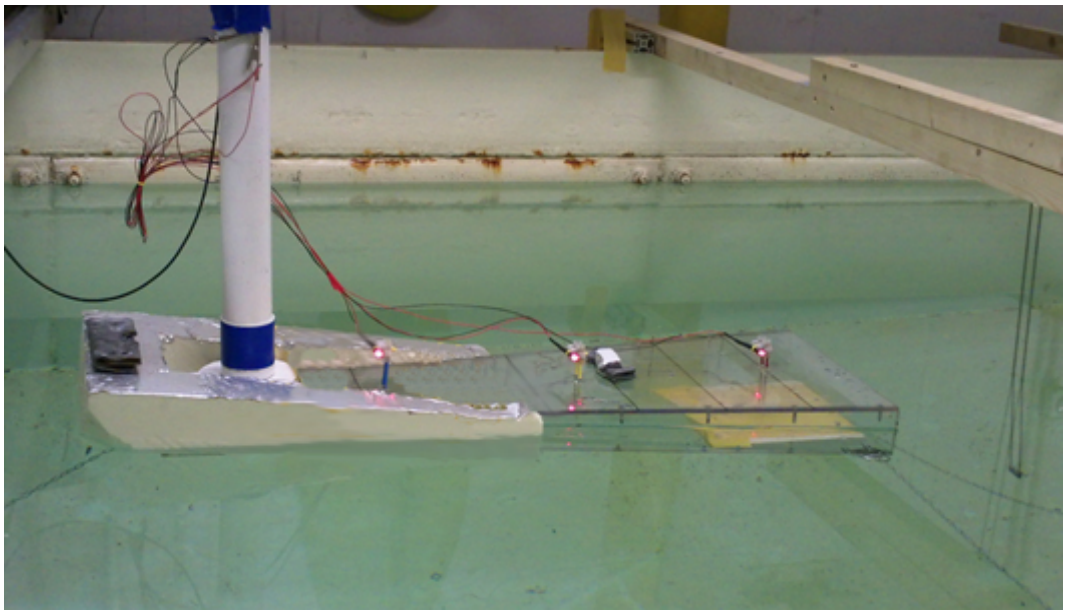

Figure 6.17, Side view of the redesigned baseline naval architecture design.

Figure 6.18, A plan view of the redesigned baseline naval architecture design.

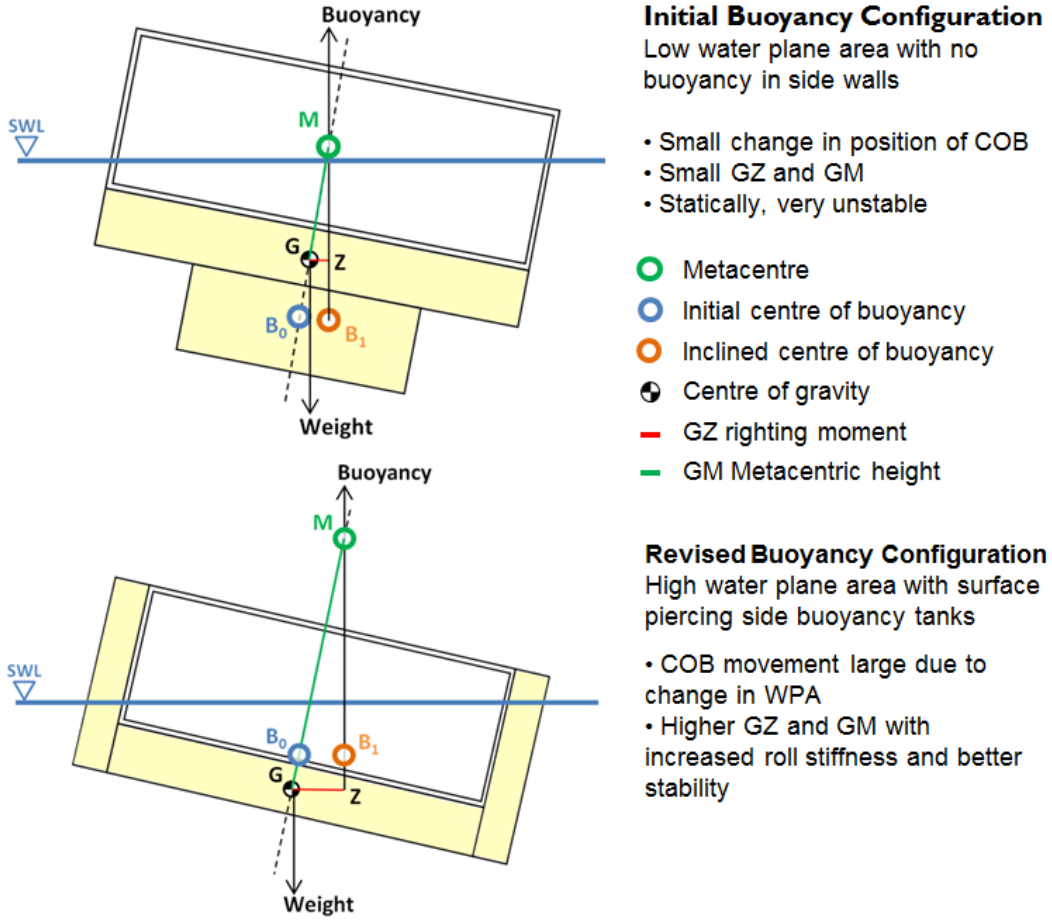

Figure 6.19: Hydrostatics of the two naval architecture designs.

The revised buoyancy distribution (visible as the silver shape in Figure 6.18) also extended the effective length of the duct; this has several immediate advantages in addition to the increased roll stiffness;

- Although the beam was slightly higher the device had a significantly lower draught.

- The natural pitch period can be maintained at a relatively long period, minimising the risk of excessive motions due to resonance. This is due to the low water plane at the forward end of the duct with a low stiffness. The mass of the entrained water also acts to damp the pitch.
- The buoyancy at the rear end of the device worked to support the duct in large differences between internal and external waves

A full scale mooring comprising 73 mm 'studless' steel chain at around 100 kg/m [Johanning *et al.* (2006)] was chosen as a suitable, initial estimate based on recommendations by Mojo Maritime, a company within the consortium for the TSB project. Scaling this down and sourcing appropriate small chain resulted in the use of aluminium chain that was around 43 g/m which was equivalent to 108 kg/m at full scale (kg/m $\propto$ scale factor^2). It was also suggested by Mojo Maritime that a rule of thumb for the "scope" of the mooring chains, that is the ratio of mooring length to depth, should be around 6 to 7. This determines how much extra chain resides on the sea bed at rest and so is the amount of allowable mooring that can be picked up in extreme conditions. In a full scale deployment it should be large enough to prevent snatching, where the mooring becomes taught and relies on the anchor for reactive force, but short enough to reduce unnecessary costs and affected sea bed deployment area. This optimum would be determined prior to deployment through calculations and modelling however, in the case of small scale testing the length of the mooring is not critical, as long as snatching is avoided. Three mooring chains, each 6 m in length, were attached to the model; two either side of the bow and one centrally at the stern. The chains were anchored with large masses at the ends and positioned at a distance away from the model as shown in the schematic of the arrangement in Figure 6.20. The dimensions of the tank limited the spread of the moorings which typically, should have been ±30° rather than the ±13° that was allowed by the tank. Nevertheless, this set up provided a suitable, initial, mooring representation upon which, later design optimisations could be based. This mooring arrangement was used for all of the subsequent testing in the towing tank.

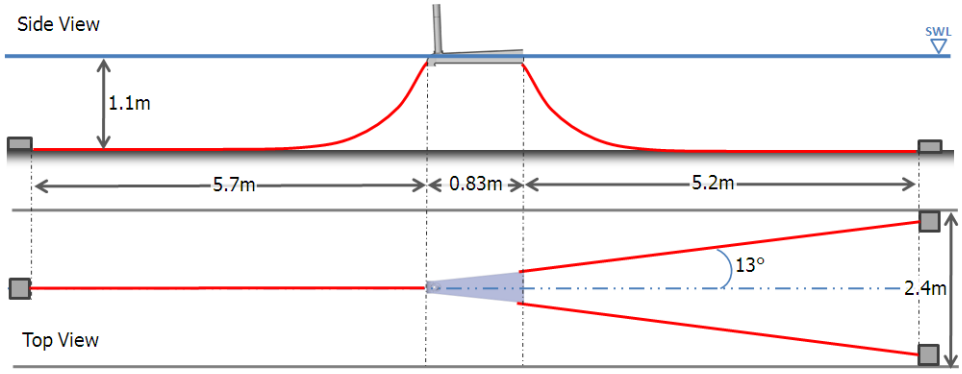

Figure 6.20, Schematic showing the mooring configuration from the side and plan views.

6.5.7 Floating Configuration

A series of batch runs were conducted to evaluate the performance of the model with the redesigned naval architecture. The results of these tests are shown in the efficiency plot in Figure 6.21. The performance of this floating configuration was improved over the initial configuration but, similarly to the static model, was reduced in comparison to the wave basin testing in Figure 5.18 (see section 5.9.1). From observations, the model appeared to behave in far less erratic manner than the previous design and with the characteristics that were anticipated.

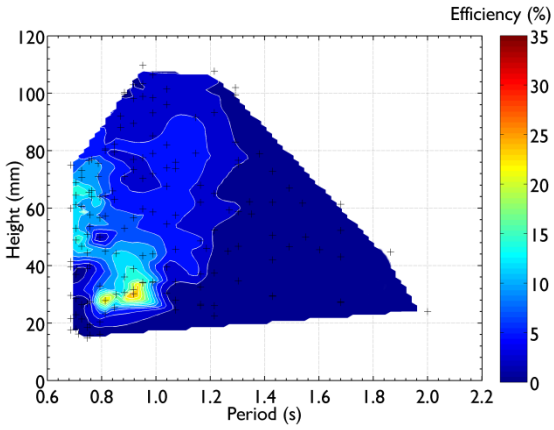

Figure 6.21, Efficiency performance plot for floating configuration.

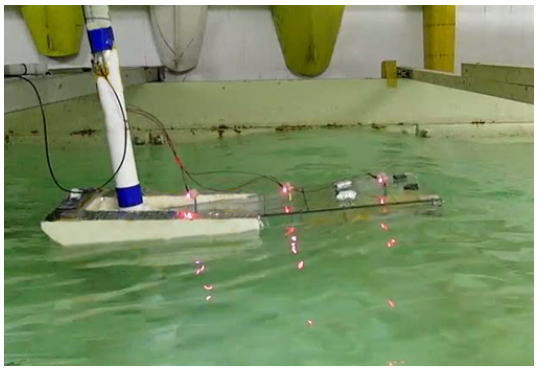

Figure 6.22, Improved pitching characteristics of the baseline, floating configuration.

The peak efficiency of the baseline, floating model was 27 %, however, the majority of the efficiency values recorded were less than 15 %. An important observation to make in the comparison between the performance of the static and floating models is that the main performance peak occurred at a shorter wave period when the model was floated. For the static model in Figure 6.9, the peak performance occurred at $T = 1.15$ s ($L/L_D = 2.5$) whereas for the floating model, this peak was not present but instead occurred at $T = 0.9$ s ($L/L_D = 1.6$). The slightly increased performance of the floating model at $T = 0.75$ s ($L/L_D = 1$) corresponds to the same peak response in performance for the static model. The efficiency of the floating duct is significantly reduced for $T > 1.2$ s.

6.5.8 Discussion

Preliminary work was necessary at the Lamont facility to improve its suitability for WEC testing. This defined the bounds of the capability of the wave making equipment, identified the limitations of the laboratory and developed a testing methodology for the subsequent modelling phases.

The calibration of the wave conditions in the tank was necessary for the testing to proceed and was beneficial to the subsequent investigations. The limitations of the tank such as the cross waves, settling time and limits of the wave paddles were also determined in this first phase of testing and aided the design of the following phases.

The cross wave resonance was thought to be responsible for the reduction in performance across a narrow band of wave periods at around L/LD = 1.7. It is likely that the cross waves caused the measured waves during the tank calibration to be greater than the actual incident wave height, this would have led to an error in the calculated efficiency.

The lessons learned regarding the naval architecture design for the multi-duct platform were applied to the design for this phase of experiments, however due to the small beam (width) of the model and low stability the motions of the duct were excessive and particularly detrimental to the performance. A new approach to the floating design was developed as a result of this testing and was subsequently used for all other floating models. This re-think has also significantly influenced the design of the full scale demonstrator.

The internal wave profile within the duct was studied using wave probes inside the model and from visual observation through the underwater viewing window in the side of the wave tank. The internal waves were seen to transform significantly in comparison to the external, undisturbed wave field. Waves slowed as they passed into the duct but to differing degrees of magnitude depending on the wavelength. The resulting lag in the positions of the internal and external wave crests led to a difference in surface elevation at the stern of the duct which caused water to enter the duct through the baffle.

The position of the internal bulk of water has implications on the floating dynamics of the duct and importantly, the loading on the structure at full scale. This is particularly the case if, in the worst-case example, external wave crests support the duct at the stern whilst the internal wave is at the midpoint of the duct coinciding with a trough outside the duct. It was identified that such load cases should be considered when designing the full scale device.

The static and floating results for the baseline geometry set the starting point from which to optimise the performance of the single duct. This provided comparisons with previous testing and confirmation that a single duct device could operate similarly to the multi-duct WEC. The low conversion efficiencies however, highlighted the requirement to increase performance in order to make the device more economically viable.

6.6 Phase 2 – Model Optimisation

6.6.1 Introduction

The first phase of testing in the towing tank concentrated on assessing the performance of the single duct, baseline configuration in order to inform the early stages of the design process within the OWEL TSB project. The power production of this duct was lower than anticipated and it was decided within the project organisation that, for OWEL to have commercial potential, the performance would have to be significantly increased in order to be competitive. This second phase of investigations was, therefore, intended to begin the optimisation of the design and to better understand the fundamental operating principles. The overall aim was to increase conversion performance through a better understanding of the effect of geometry, buoyancy distribution and moorings on the pneumatic efficiency.

Particular attention was given to observing the modification and changing dynamics of the wave crests within the duct and how subsequent waves interact with each other and their influence on conversions performance. The internal wave dynamics were briefly examined in the first phase of testing, as reported in section 6.5, and some basic conclusions could be drawn from the results. This highlighted the need for a more in-depth study of the entrained free surface to identify possible means of optimisation.

The principle objectives of this phase of testing were to:

- Examine the effect altering the floor angle has on performance.
- Improve the behaviour and performance of the floating design.
- Develop a motion tracking system to assess the floating dynamics in order to determine which motions influence power capture the most.
- Test the effect of side wall angle on the performance.

6.6.2 Geometric Configurations

Intermediate scale testing at Narec (see section 3.3.3) had concluded that the floor and side wall angle had “minor influence” on the conversion performance. During the initial 2D testing (see section 4.7.1) it had been shown that increasing the angle of the roof benefitted performance, however, that investigation simply rotated the model about a point at the stern rather than only increasing the roof angle. An implication of this was that the floor angle had been reduced and so the subsequent design by ITP for the wave basin model featured a horizontal floor and angled roof. The reduction of floor angle reduces the capture area of the duct mouth and so too the energy entering the device. By increasing the angle of the floor it was postulated that more energy could be captured, thus increasing performance. It was also thought that there would be a

change in the shoaling effect of the floor on the wave as it passed from deep to shallow water conditions.

The testing commencing with the static model studies was intended to determine the effect of floor angle on the performance. The original, baseline duct was modified to incorporate a shallow angle of the floor of the duct, initially to 2.5° followed by an increase to 5° and then to 7.5°. This is demonstrated by the schematic in Figure 6.23 and summarised by the values in Table 13. Increasing the floor angle to 7.5° increased the draught at the bow by over 100 mm and more than doubled the water cross sectional area captured. As explained in section 2.6, the wave energy available in the water column decreases exponentially (Figure 2.10) with depth and so it was postulated that, if increasing the angle of floor improved performance, larger angles would likely result in limited incremental performance gains.

Table 13, Changes to duct entrance by increasing floor angle

Floor Angle	Duct Entry Draft	Duct Entry Water Area Increase
0°	79.0 mm	-
2.5°	111.8 mm	41.5 %
5.0°	144.6 mm	83.0 %
7.5°	177.4 mm	124.6 %

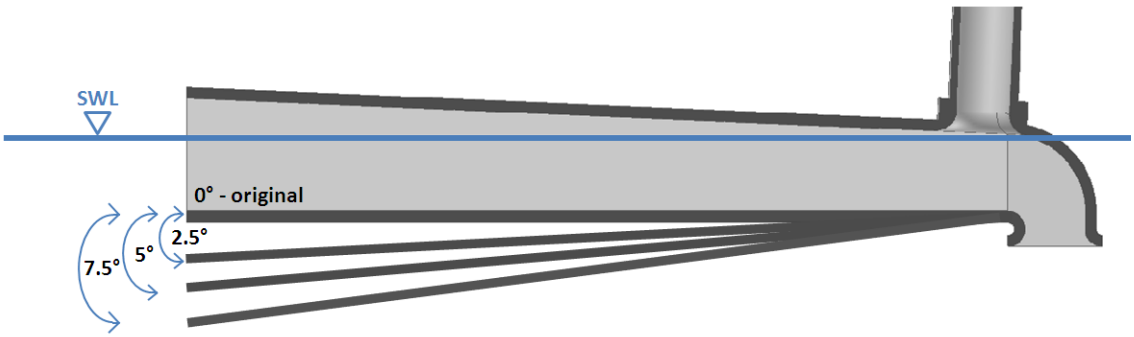

Figure 6.23, The four different floor angles tested on the baseline configuration.

After determining the optimum angle of floor, the effect of buoyancy distribution was investigated. Four buoyancy configurations were used with the intention of moving the Longitudinal Centre of Floatation (LCF), see Appendix A2.2.2, fore and aft to alter the pitching characteristics of the duct. Figure 6.24 shows the plan view of the four buoyancy configurations, A – D, that were tested.

Configuration A was the same baseline as that tested previously, as detailed in section 6.5.7. Configuration B was based upon A but had the surface piercing buoyancy more evenly distributed along the length of the duct rather than being predominantly at the stern. This was intended to be a more realisable version of configuration A as, at full scale, the duct would be better supported, thus reducing structural loads, leading to a more economic design.
Configuration C featured the stern sections of buoyancy from configuration B relocated along the duct towards the bow. There was no surface piercing buoyancy in the rear 1/3rd of the duct closest to the stern and so can be likened to a reversed configuration A.
Configuration D was intended to be a more practical version of configuration C. Unlike C the buoyancy was more evenly distributed buoyancy and so, as was intended with configuration B, the full scale structural loads would likely be reduced.

It should be noted that whilst these four configurations alter the LCF, they also varied the roll stability of the design by changing the beam and righting moment arm. This however, was thought to have less of an impact on performance than the pitch behaviour particularly in the case of regular, uni-directional head waves.

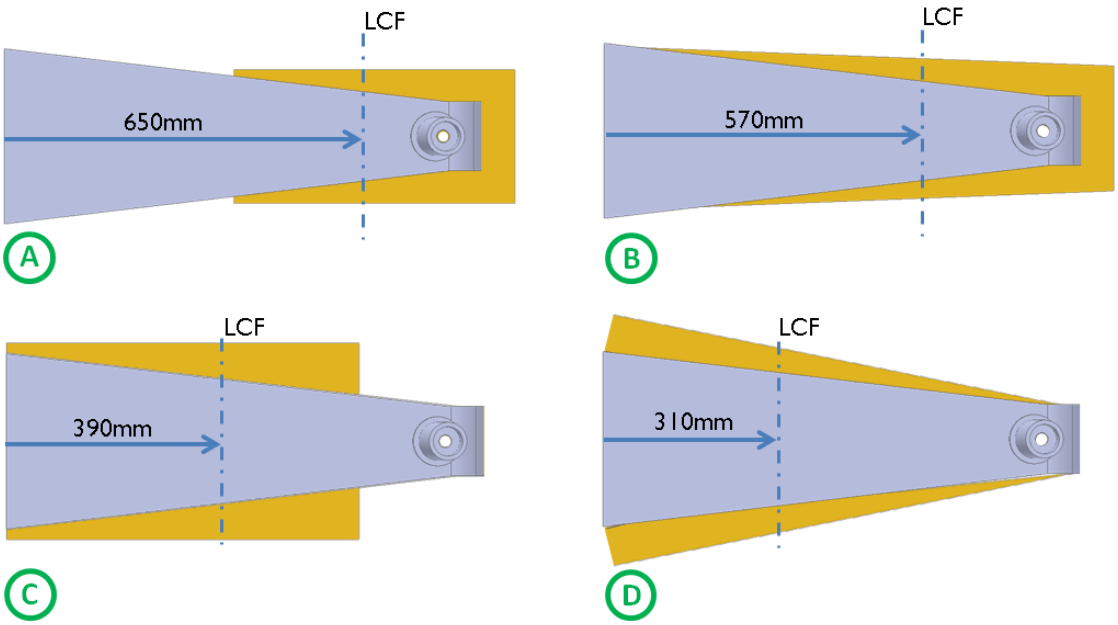

Figure 6.24, The four buoyancy configurations, A-D, tested to investigate the effect of changing the LCF.

Whilst the buoyancy investigations were being carried out, a new plastic model was constructed with parallel walls. The testing time available was limited and so it was decided to only test a straight sided model, rather than a selection of wall angles, much the same as that tested in the initial 2D experiments in section 4. This model featured the same duct entry dimensions and duct length as the other models in this testing phase and was identical apart from the beam at the stern being the same as that at the bow. The results of floor angle tests were known at the time

of designing this model and, as the 7.5° floor angle proved to be most beneficial, it was incorporated into the design. A drawing of the straight sided model is shown in Figure 6.25 with the principal dimensions given. The majority of the dimensions are the same as those for the other model used throughout this testing as detailed in Figure 5.2, section 5.4.

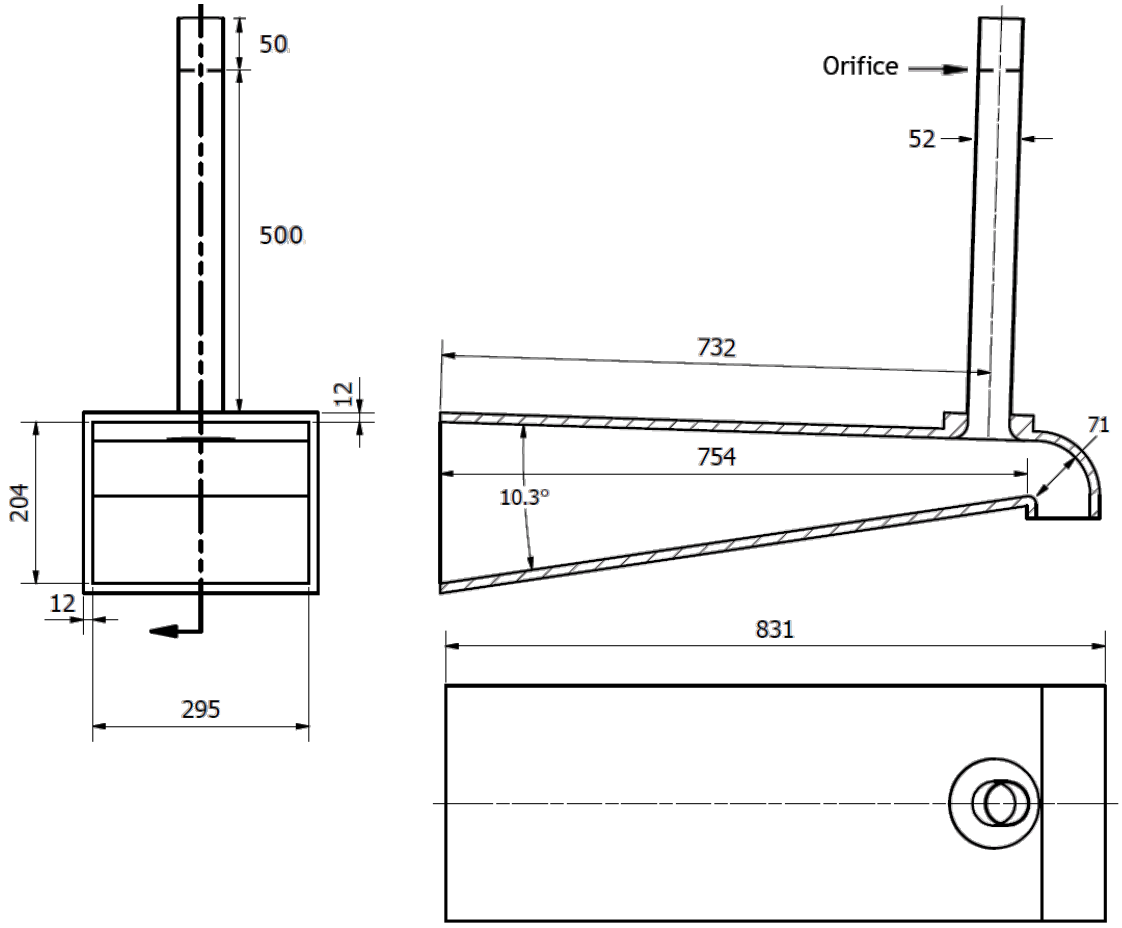

Figure 6.25, A drawing of the straight sided duct with dimensions in mm.

6.6.3 Wave Conditions

Rather than running large batch sets of test conditions as had been done in the baseline tests, 20 test wave conditions were chosen to represent the typical scatter of an offshore site. These were specified in order that they coincided with similar test points that had been used in the previous studies. It was also intended that they reside within the 1:10 and 1:50 wave steepness range to encompass wave climates typical in a real sea and be approximately distributed along lines of constant steepness. The 20 chosen conditions are plotted as red crosses in Figure 6.26. The smaller markers indicate test waves from the previous physical investigations, indicating the points at which information existed to back compare to test for improvement and also show the capability limits of the wave makers. Also plotted are a series of curves showing lines of

constant wave steepness and lines of constant wave power. The steepness curves show that the test points were selected to reside on four of them in particular; 1:15, 1:20, 1:30 and 1:40.

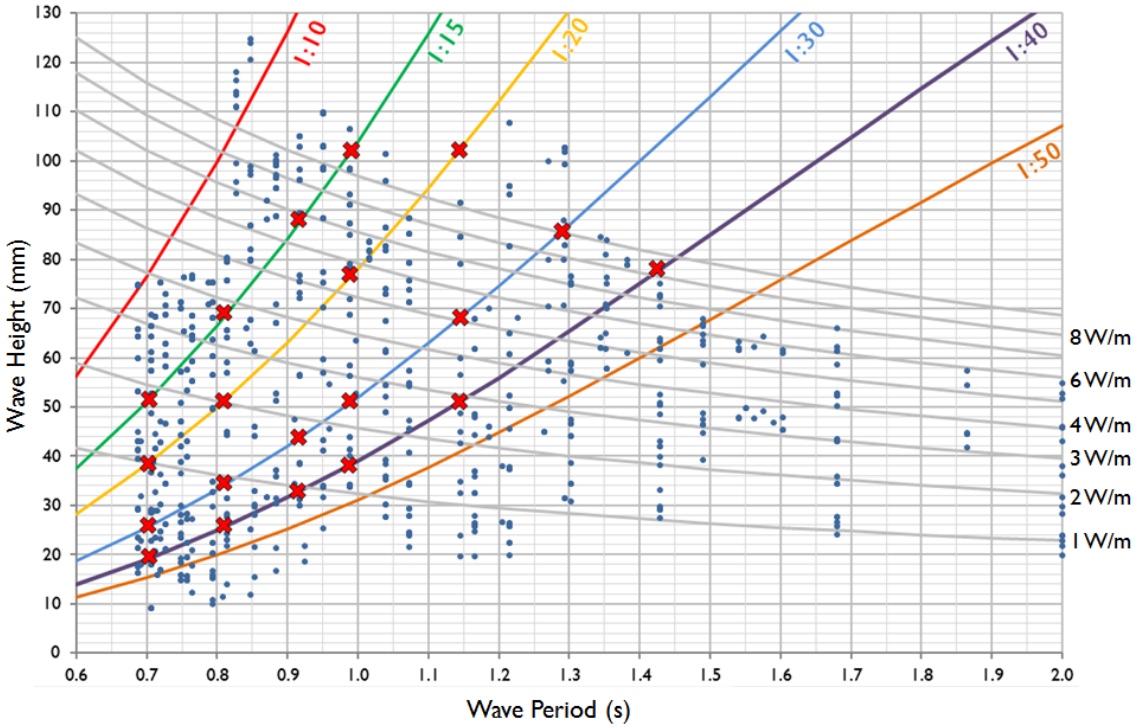

Figure 6.26, A plot indicating the 20 test waves (red crosses) specified for this testing phase, in addition to data points from previous tests (blue markers) and isolines of constant wave steepness and wave power.

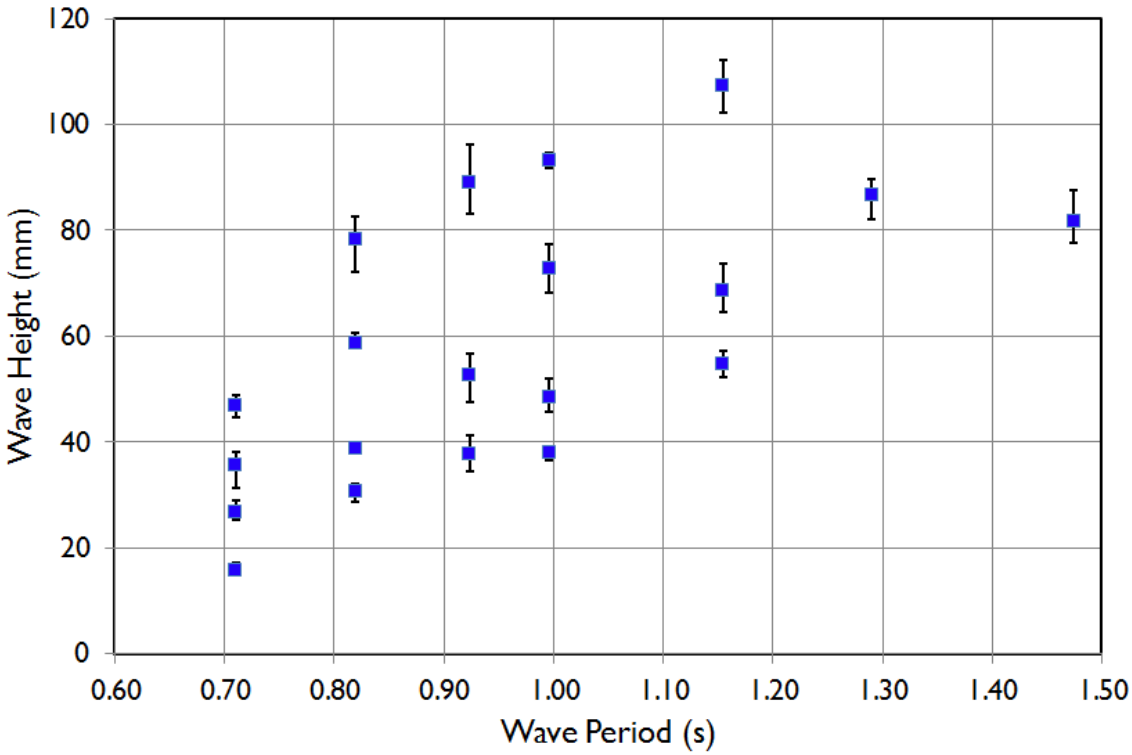

Figure 6.27, The results from the calibration of the wave tank, showing the 20 test points with the maximum and minimum variations in measured height over four repeat runs.

The wave tank was calibrated prior to testing with the model to ensure that the input conditions reliably produced waves that were the same as those specified by the test plans. Due to the limitations of the wave tank, as explained in section 6.3, repeatability for some waves was poorer than anticipated with some cases having variations of ±10 %. Perhaps the greatest contributing factor to this was the generation of large ripples caused by a lip in the sidewalls of the tank which protruded just above the waterline. This caused disturbances that propagated across the tank creating an undulating water surface with local maxima and minima making accurate and repeatable wave height measurements challenging. The graph in Figure 6.27 shows the averages of four calibration runs for the 20 test waves along with the error bars signifying the maximum and minimum wave heights recorded for each of the calibrations. The poor repeatability of some of the wave test conditions should be considered when examining the performance results presented in this section.

The 20 test wave conditions are frequently referred to by their test number throughout this section therefore this is included in the test summary in Table 14 along with the actual recorded heights and periods of each wave.

Table 14, A summary of the properties of the 20 wave test conditions.

Test #	Wave Height [mm]	Period [s]	Wavelength [m]	Wavelength/Duct Length
1	15.72	0.71	0.79	0.95
2	26.83	0.71	0.79	0.95
3	35.56	0.71	0.79	0.95
4	46.79	0.71	0.81	0.95
5	30.53	0.82	1.05	1.26
6	38.71	0.82	1.05	1.26
7	58.66	0.82	1.05	1.26
8	78.31	0.82	1.05	1.26
9	37.67	0.92	1.33	1.60
10	52.55	0.92	1.33	1.60
11	89.09	0.92	1.33	1.60
12	37.94	1.00	1.55	1.86
13	48.52	1.00	1.55	1.86

14	72.74	1.00	1.55	1.86
15	93.21	1.00	1.55	1.86
16	54.78	1.15	2.08	2.49
17	68.50	1.15	2.08	2.49
18	107.24	1.15	2.08	2.49
19	86.52	1.29	2.59	3.11
20	81.69	1.47	3.35	4.02

6.6.4 Effect of Duct Floor Angle

It was postulated, prior to testing, that increasing the floor angle would increase performance as more of the water column would be captured by the duct entrance. This trend was observed in many of the test cases for the four floor angles examined and this can be seen in the graph in Figure 6.29.

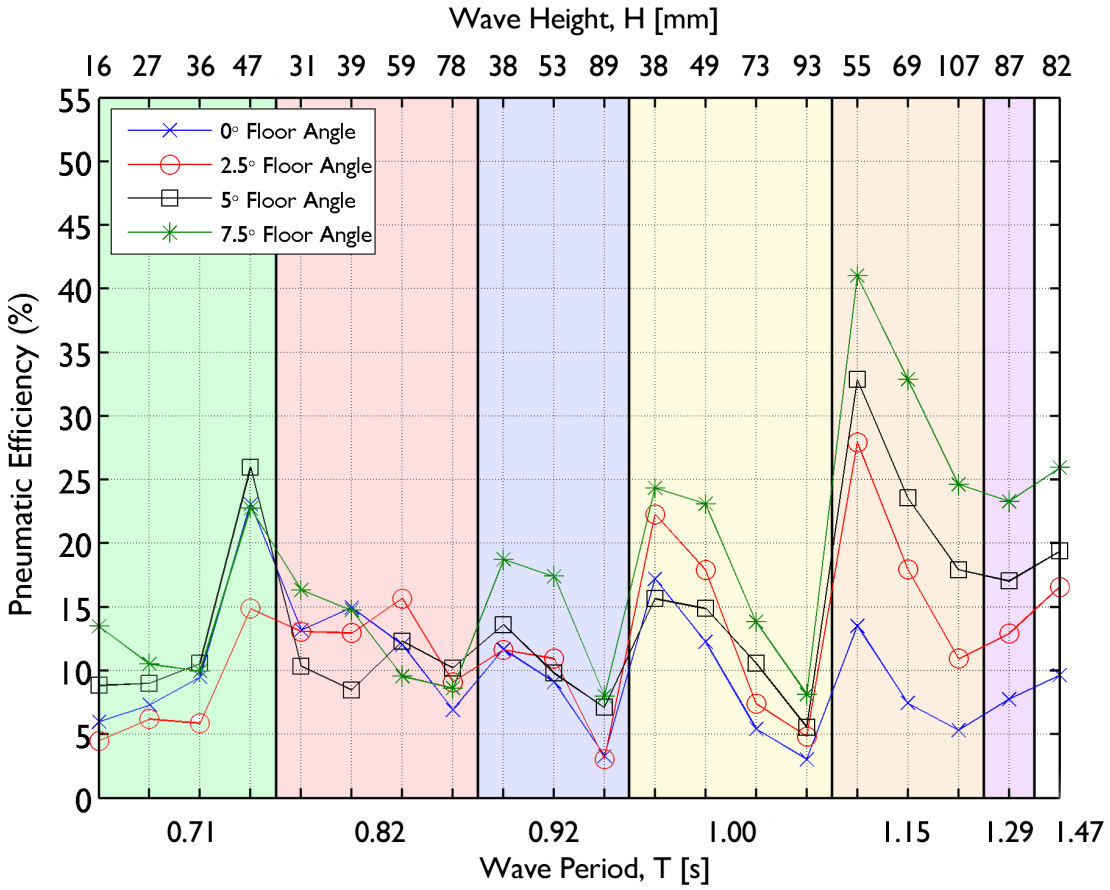

Figure 6.28, Comparison of performance for the four floor angles. [N.B. Band colours are only to aid the identification of data points with the same wave period]

In order to further reduce the likelihood of anomalous results three repeat runs of the 20 waves were conducted for each ramp angle. The results presented here are an averaged value of the three results. The plot is arranged according to the wave period each group of data points corresponds to. Within each coloured band, the wave height increases with increasing x position, but then reduces to the lowest height in the next band of wave period.
In all but one test cast (wave #7) the performance of the duct with a 7.5° floor exceeded or equalled the efficiency of the flat floored, baseline duct. In the case of wave #16, a three-fold improvement was observed with peak efficiency exceeding 40%. The four comparative efficiency contour plots in Figure 6.29 provide further evidence to demonstrate the improvement in performance and especially shows the increase in efficiency at T = 1.15 s (#16 - 18) through the progression of these tests. The contour plots in Figure 6.29 should be viewed with slight caution due to the sparseness of the data points. This means that the large regions in between the data points are heavily interpolated to provide the fill for the contour. This may have led to features in the performance being omitted and so the interpolated regions should not be considered to be an accurate representation of the performance associated with those conditions. It should also be noted that the contour fill in these examples does not extend to the bounding points and that this is a peculiarity of the contour plotting method. Nevertheless, these plots provide a good visual comparison to observe the general trends and compare the changes in performance between the model configurations.

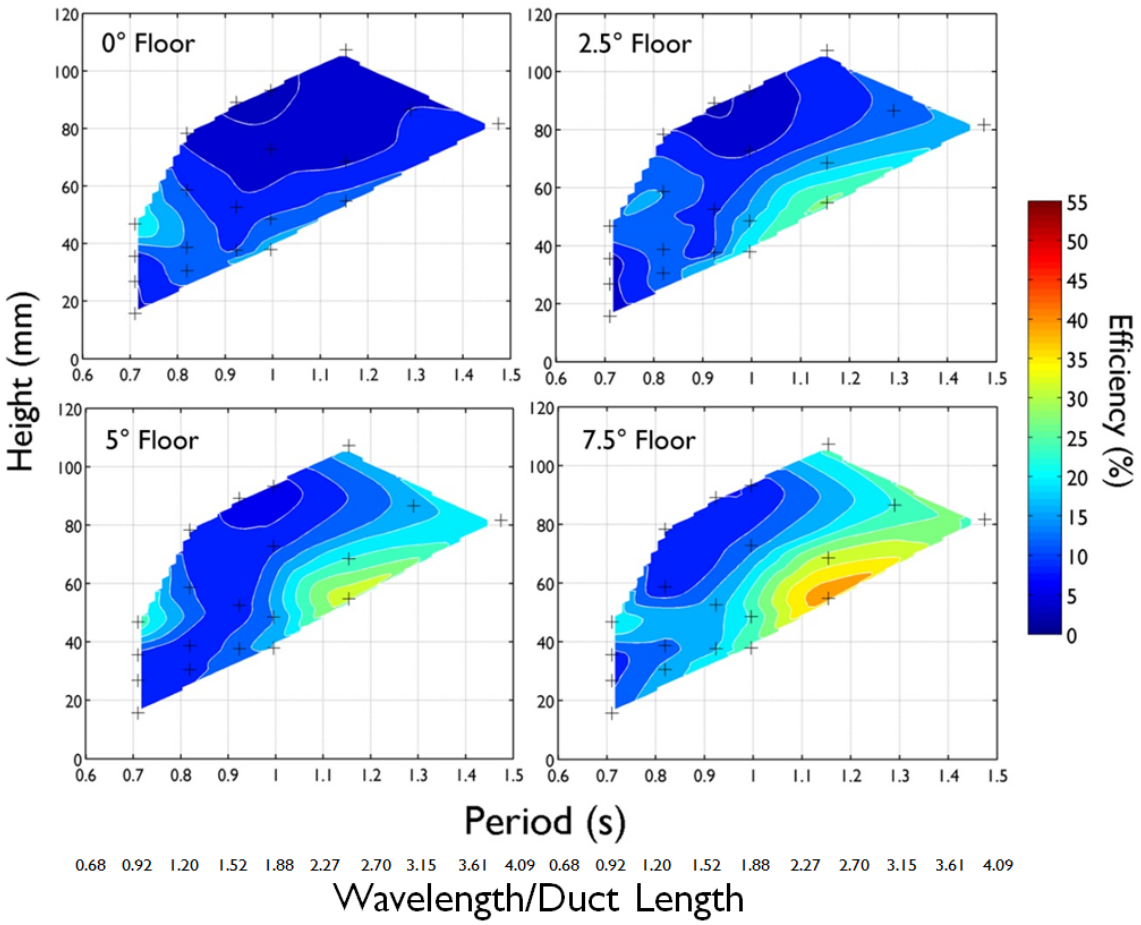

Figure 6.29, The effect of changing floor angle on conversion performance for a static duct.

The increased performance due to increasing the floor angle is likely to have resulted from a number of effects:

- A larger depth of the water column was captured by the duct entrance meaning less wave energy passed underneath the duct.
- The steeper beach had a more gradual "shoaling" influence on the waves entering the duct rather than the rapid step change from deep water to shallow water wave conditions as was with the horizontal floor.
- Less wave breaking occurred within the duct.
- Reduced frictional losses due to bottom effects.

The inclusion of a larger ramp has additional implications for the full scale device. The size and draught of the duct are substantially increased in comparison to the baseline configuration; this will lead to the requirement for additional material, larger displacement and greater structural and mooring forces. The primary aim for the WEC is to generate electricity and so, particularly at small scale, this focus has to be held above all. If a techno-economic analysis later indicates that the cost versus power benefit of the larger floor angle is not great enough to overcome the associated disadvantages then an alternative configuration may be selected. At this point however, it was decided that, as the 7.5° floor provided such an increase in performance, it

would remain a feature of subsequent models in the testing and the practicalities of its realisation at full scale would become a challenge for later investigation.

6.6.5 Effect of LCF Position and Buoyancy Distribution

Of the six degrees of freedom, pitch is one of the most influential on power capture, as changes in pitch angle result in a change in bow freeboard and forces acting on the wave within the duct. A number of factors affect the pitch behaviour of the duct; these have been summarised in the review of relevant aspects of naval architecture in Appendix A1.2. These tests were intended to investigate the changes in performance for four different LCF positions as summarised in Figure 6.24. The performance for each of the four different LCFs is presented in the graph in Figure 6.32 and contour plots in Figure 6.33. Once again, the results are an average performance taken from three repeat runs of each test condition.

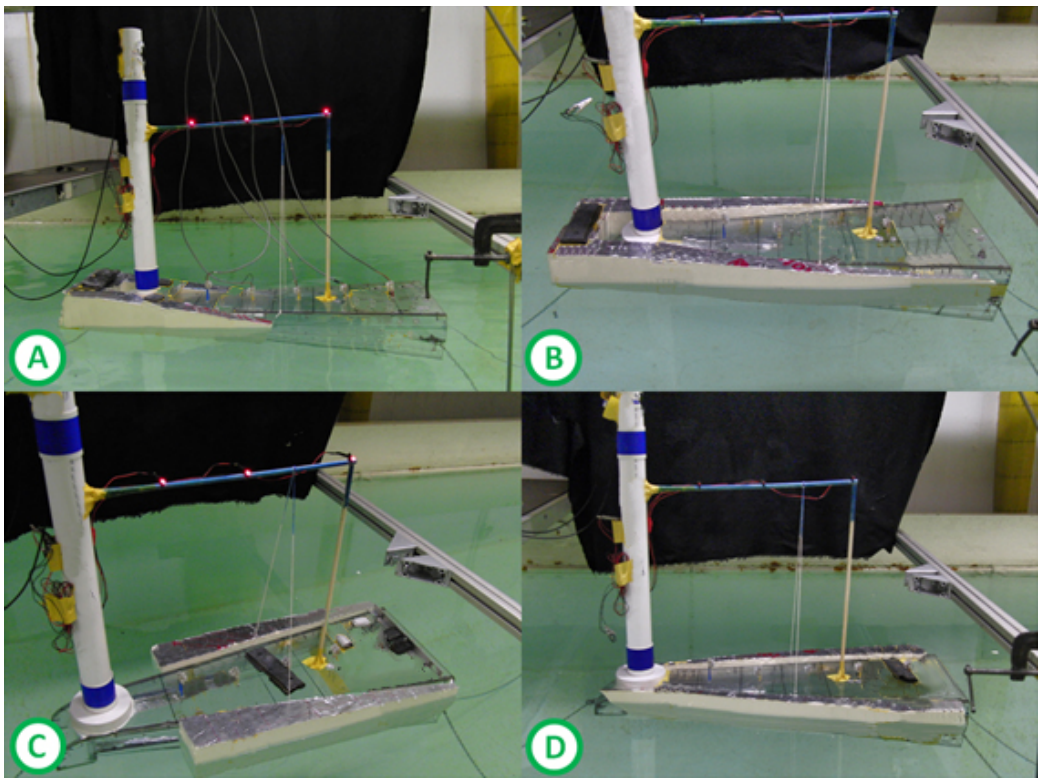

Figure 6.30, Photographs of the four buoyancy configurations (LCFs A-D) for the floating model.

The first configuration, LCF A, had the same buoyancy configuration as the baseline floating model tested throughout the first phase of testing, reported in section 6.5. The contour plots in Figure 6.31 provide a comparison between the floating performance of the baseline geometry and 7.5° floor geometry for buoyancy configuration A. It was found from the developed power over the conditions tested, that increasing the floor angle to 7.5° approximately doubled the overall performance. This also demonstrates that the performance gain from the change in floor angle benefitted floating power capture in a similar manner as for the static model.

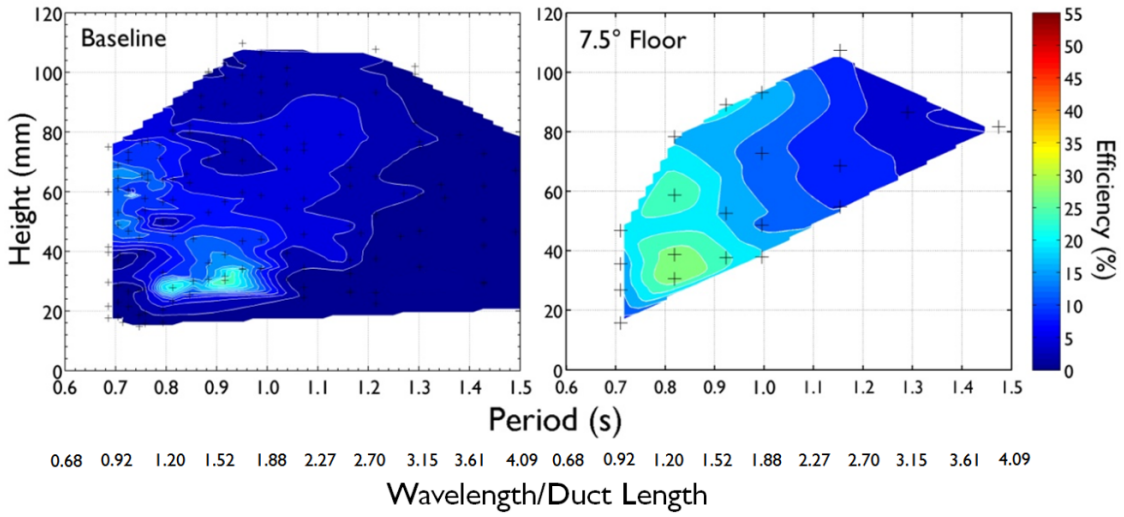

Figure 6.31, Comparison between the baseline and 7.5° floor geometries both with buoyancy configuration A.

Configuration B had a reduction in performance for all but two wave conditions in comparison to configuration A. This is demonstrated in the plot in Figure 6.32, which has been plotted in a similar manner to that of Figure 6.28; coloured bands have been used to group the data points with the same wave period. In each band the wave height increases along the axis.

Configuration C featured a far more pronounced peak in performance in the shorter wave periods of between 0.8 and 0.9 seconds than configurations A or B. It outperformed configuration B for the majority of waves but was slightly inferior to configuration A, particularly in the longer wave period conditions such as tests 14 – 20. This is likely to have been as a result of the different pitching characteristics between configurations A and C; configuration A had no surface piercing buoyancy for the first half of the duct meaning that as the duct encountered a wave crest the duct entrance, it was observed to 'pierce' the wave rather than reacting to it if there were buoyancy towards the bow.

Configuration D had very similar performance characteristics to configuration C however, was slightly inferior in a number of test conditions. However, due to it being a more realistic full scale buoyancy configuration, configuration D was favoured for the remainder of the tests in preference to the other configurations.

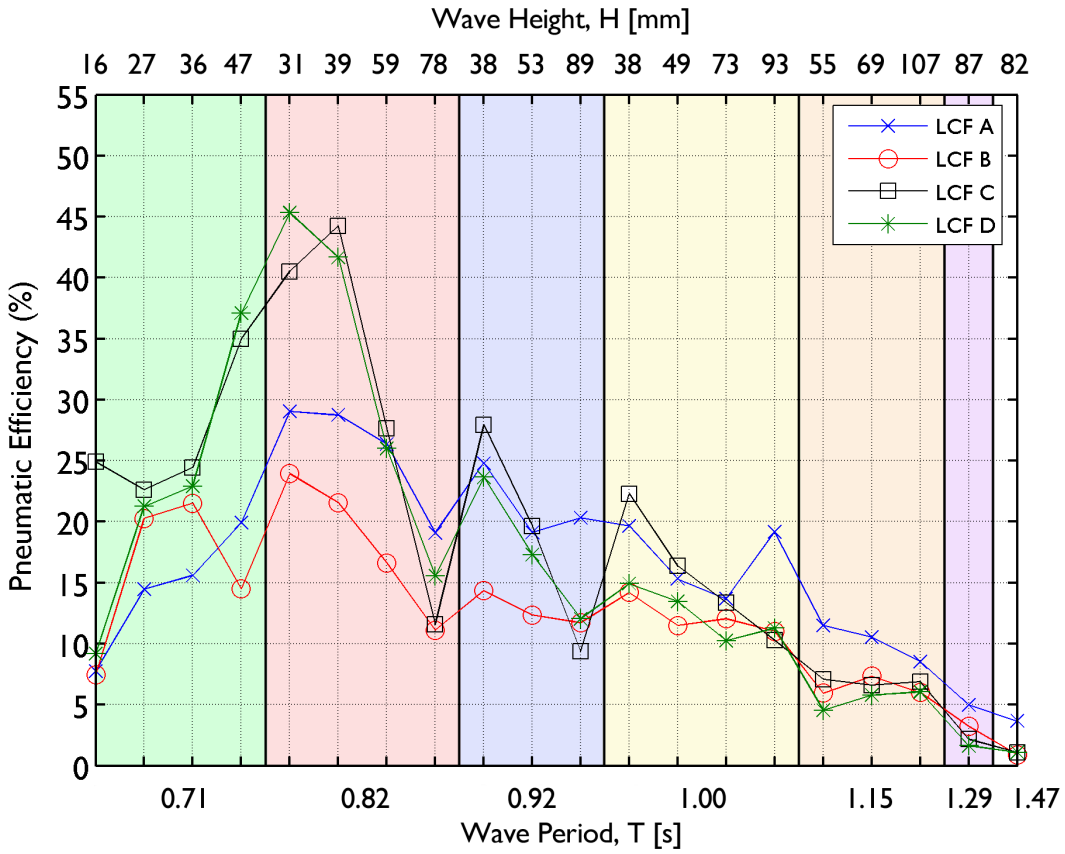

Figure 6.32, The effect of LCF position on conversion performance for the 20 wave cases. [N.B. Band colours are only to aid the identification of data points with the same wave period].

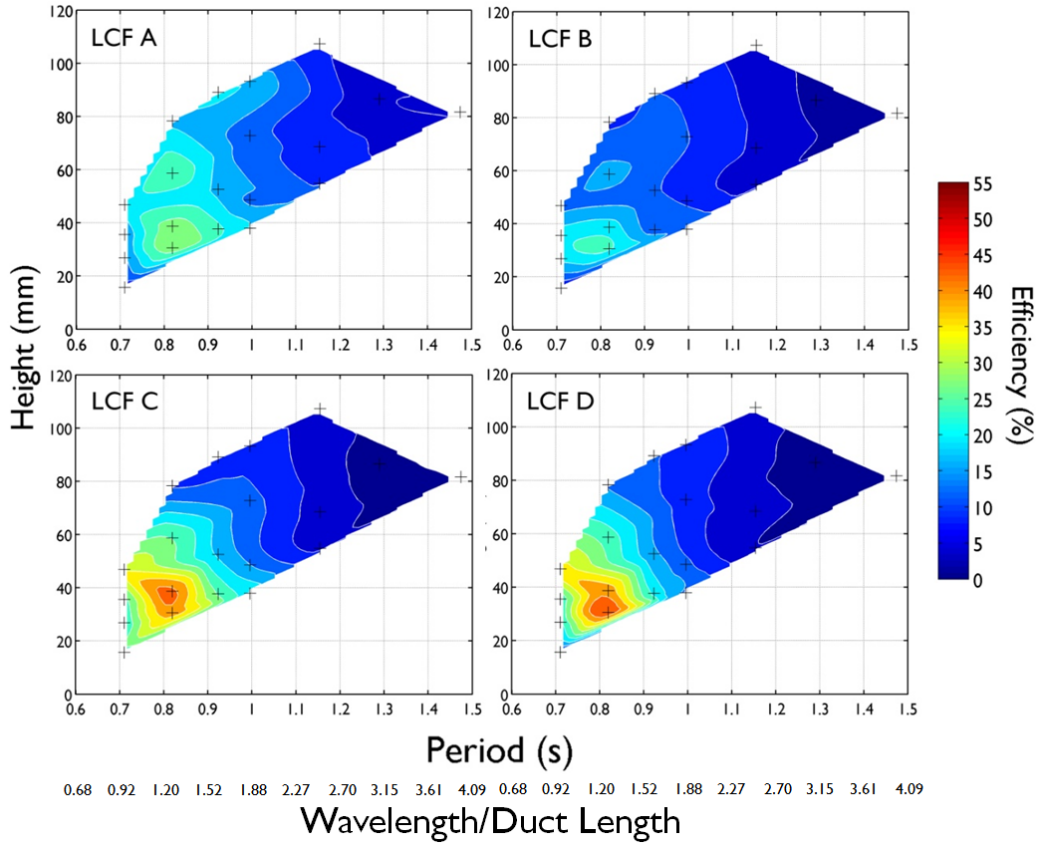

Figure 6.33, A comparison of efficiency contour plots for four different LCF cases (A – D).

Further comparisons can be made between the performance of the static and floating 7.5° floor models by examining the results in Figure 6.28 and Figure 6.32; In tests 1 – 10 the performance of the floating model typically exceeded that of the static model, whereas in waves 11 – 20 show a significantly reduced performance for the floating model. These trends are further evident when comparing the contour plots in Figure 6.29 and Figure 6.33 which show the performance of the static and floating configurations. This result has significant implications on a full scale, floating device as the peak performance that is typically identified at $L/L_D = 2.5$ in the static models is not evident. The only performance peak observed in the floating model efficiencies occurs at shorter period waves at around $L/L_D = 1.2$. The consequence being that, when deployed in a marine environment, the duct length would double in order to 'tune' the peak performance to occur at the peak wave energy conditions. This implication is discussed further in section 8.2.

One limitation was that, although a very similar mass of ballast was used for each of the four configurations, the distribution of the ballast differed, as can be seen by the position of the black weights in Figure 6.30. This would have changed the longitudinal inertia of the duct and therefore, also the pitch stiffness and position of the CoG. The weight of the ballast was approximately 500 g, equivalent to < 5 % of the un-ballasted model mass of 11 kg. The different distributions were necessary to correctly trim the model for the different buoyancy arrangements in order to ensure a freeboard of 25 mm at the duct entry. It was therefore not possible to vary the buoyancy distribution without altering the ballast distribution accordingly.

In addition to the buoyancy configurations reported here, other similar arrangements were briefly tested but failed to provide suitable floating characteristics, resulting in poor performance.

6.6.6 Motion Tracking

Through comparisons between the static and floating efficiency results, it is apparent that the floating dynamics of the duct significantly modify the performance characteristics of the converter. A motion tracking system was developed by the author in order to study the dynamics of the floating body and attempt to explain the causes of these differences in power production.

Three red, 5 mm diameter LEDs were attached rigidly to the model at a distance above the water surface and the deck of the model to prevent reflections. A matt black sheet was hung behind them to provide a contrasting and plain background. The motion of the LEDs was filmed

with a digital camera, shooting at 30 frames per second with a resolution of 1920 x 1080 'High Definition'. The camera was mounted on a tripod approximately 3 metres from the LEDs, in line with the duct and at the same vertical level as the LEDs. The LEDs can be seen mounted above the models in the photographs in Figure 6.30. The resolution of the camera meant that, at the model location, the typical resolution was approximately 1.43 pixels per mm meaning that each LED was represented by a width of approximately 7 pixels. The associated error in determining the location of the LED centre point was therefore approximately 14 % of the LED diameter equivalent to 0.7 mm. This error was further mitigated by taking the straight line average through the centre of the three LEDs.

A video processing code was written in Matlab™ which initially determined the position of the three LEDs and then tracked the position of the centroid of the group of pixels that represented them. By determining the position of two points on the line between the LEDs, knowing the distance between them and the position of the LCF the pitch, heave and surge motions of the model could be inferred. It was assumed that the heave and surge translations acted directly through the LCF and that the pitch rotations were about that point. As pitch, heave and surge were deemed the dominant motions most influential of power capture, yaw, sway and roll were not investigated. This would have required at least one other camera and significantly more data processing. In addition, the uni-directional nature of the regular wave crests meant that motions in yaw, sway and roll were small.

Figure 6.34 shows the typical outputs from the analysis of a video file, including the time series results for the recorded motions with their average amplitude. The green lines in the first two plots show the average amplitude of the pitch and heave motions. Each of the three plots shows an initial transient state where the model progresses from a still condition at rest to a more dynamic but steady state where the model moved back to oscillate on the mooring lines. The RAOs were determined for each run from the average amplitude of the motions and the recorded wave amplitude in the tank. The individual RAOs for each wave condition were then averaged across each wave period to determine the response of the model as a function of the period. In this phase of testing the motions were recorded for buoyancy configurations A and C. The pitch, and heave RAOs for these two configurations, compared in Figure 6.35, show that configuration C typically had a greater pitch and heave response than configuration A. The period at which the heave response peaked for both configurations, $T = 1.15$ s, coincided with the dominant peak in performance that was observed for the static model in Figure 6.9. Furthermore, the pitch response for configuration C also peaked at $T = 1.15$ s and the value for configuration A was also high at this period. The performance peak at $T = 1.15$ s occurring in

the static tests did not feature in any of the floating tests and its absence was therefore likely a result of the duct motions.

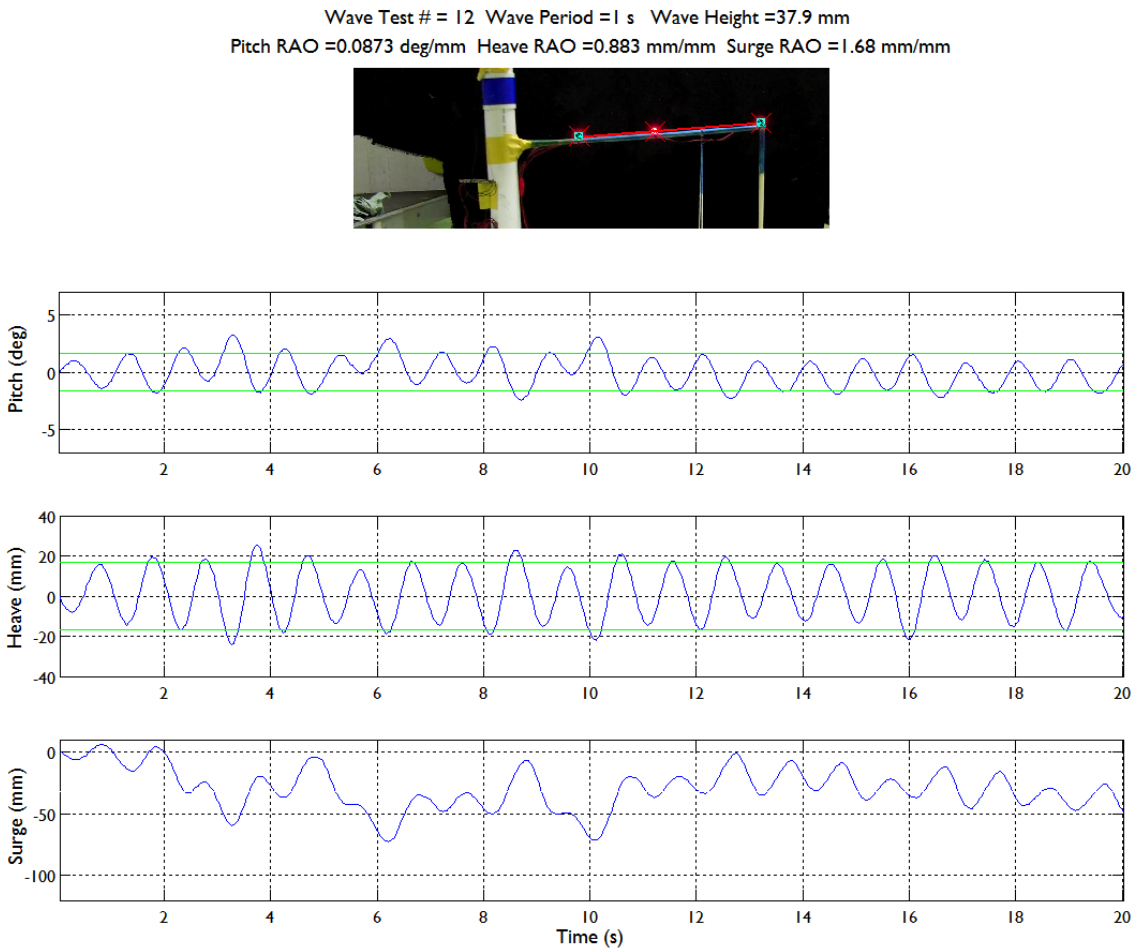

Figure 6.34, Typical motion analysis outputs, in this case for wave # 12 with buoyancy configuration A.

The pitch and heave motion time series for two configurations tested at two wave conditions are shown in the examples in Figure 6.36 and Figure 6.37. The behaviour of the two configurations in wave #6, Figure 6.36, shows the variability in the magnitude of the motions. The phase lag between pitch and heave peaks of configuration A was greater than that for configuration C. This was a result of the different longitudinal buoyancy distributions. Other than their magnitudes, the relationships between pitch and heave for the two configurations with wave #15, shown in Figure 6.37, were very similar.

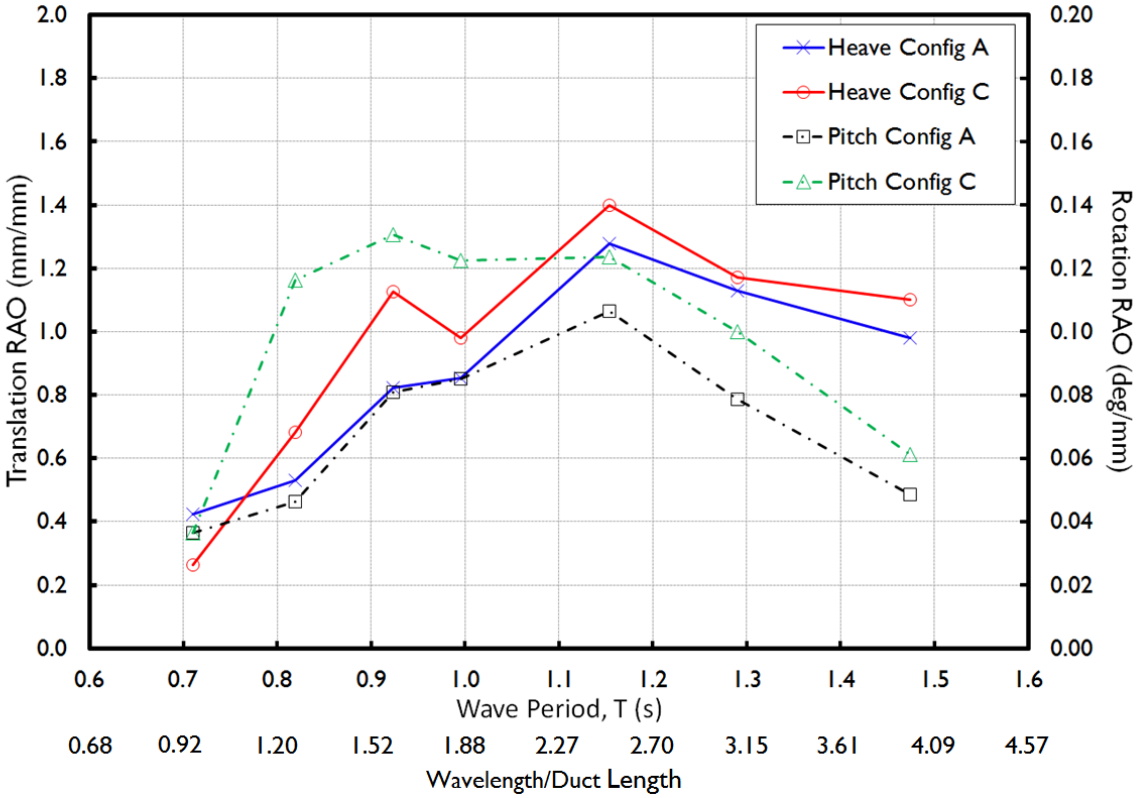

Figure 6.35, A comparison of heave and pitch response amplitude operators for configurations A and C.

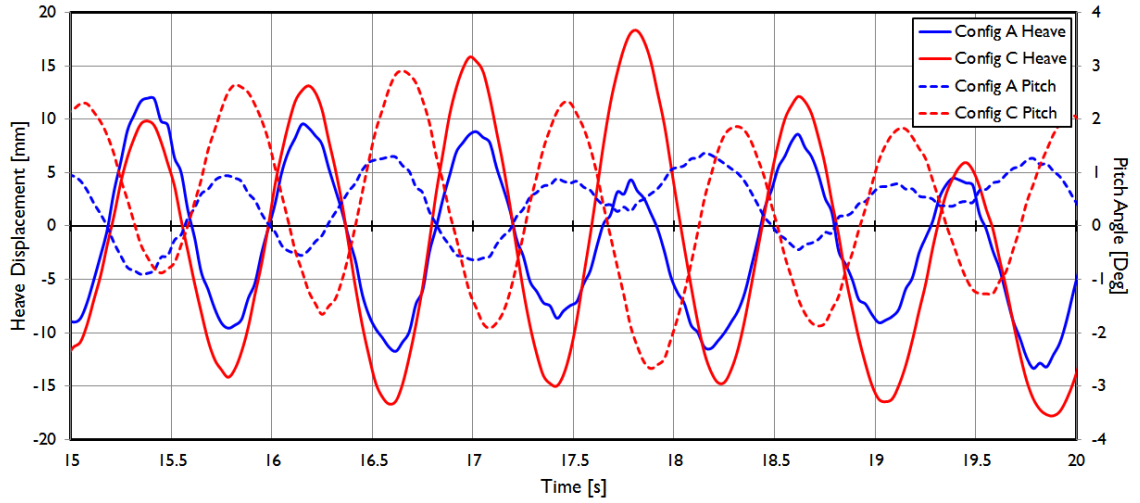

Figure 6.36, Time series of heave and pitch motions for wave # 6, $T = 0.82$ s, $H = 39$ mm for buoyancy configurations A and C.

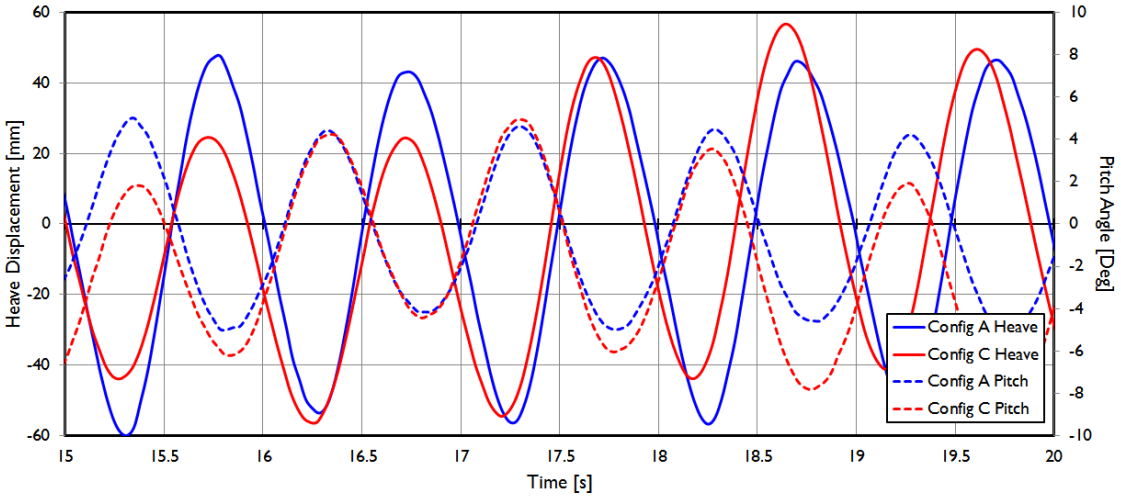

Figure 6.37, Time series of heave and pitch motions for wave #15, T = 1.00 s, H = 93 mm for buoyancy configurations A and C.

6.6.7 Effect of Sidewall Angle

Similarly to the parameter of floor slope angle, the effect of sidewall angle had only been briefly considered in earlier tests (see section 3.3.3). The choice of sidewall angle for all of the models previously tested during the development of the device had been relatively arbitrary as it was thought that the angle had little effect on the performance. However, it had always been thought that a tapered duct benefitted power conversion through focusing the internal wave towards the PTO and inducing a rise in wave height. It was therefore decided to reinvestigate this parameter in order to test these theories and conclusion from the intermediate scale tests at Narec.

The model constructed with parallel side walls (Figure 6.25) included a 7.5° floor as it had proved to be successful for the static and floating tests in this phase of modelling. This non-tapered model was rigidly fixed in the tank in the same position as the previous tests and the 20 wave cases were run three times. The averaged results of these tests are plotted in comparison to the performance of the static tapered model in Figure 6.38.

The results of these tests show that, contrary to previous theories, the tapered side walls were detrimental to the conversion performance. In all but one of the test wave conditions (#20) shown in Figure 6.38, the straight sided duct performed better than the tapered duct. The most noticeable improvements were in the shorter period waves; efficiencies in wave #3, for example, were increased by a factor of 4.5 times over the already improved, 7.5° tapered duct. Comparing the two contour plots in Figure 6.39 further highlights the performance increase across the test wave conditions when the side wall taper was removed.

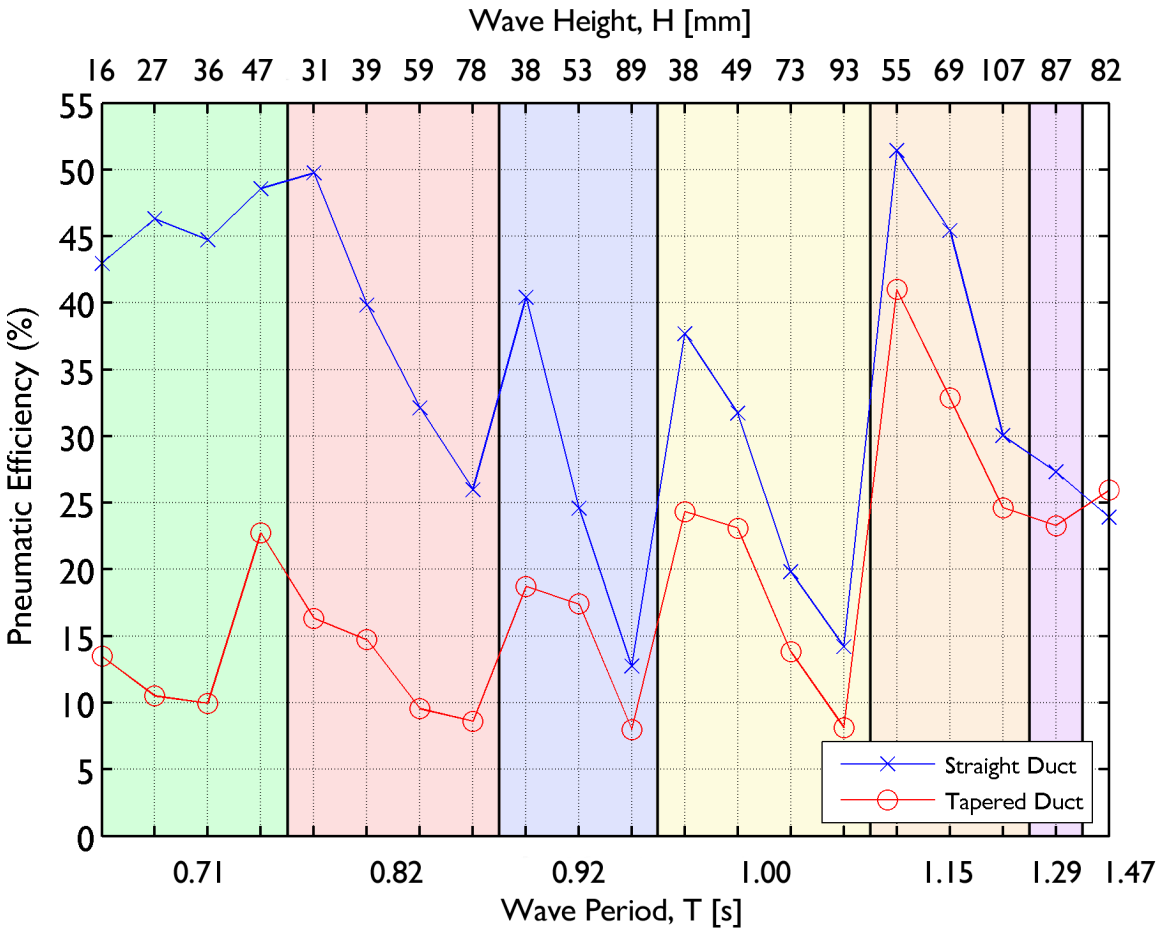

Figure 6.38, The effect of removing side wall taper on the conversion performance. [N.B. Band colours are only to aid the identification of data points with the same wave period]

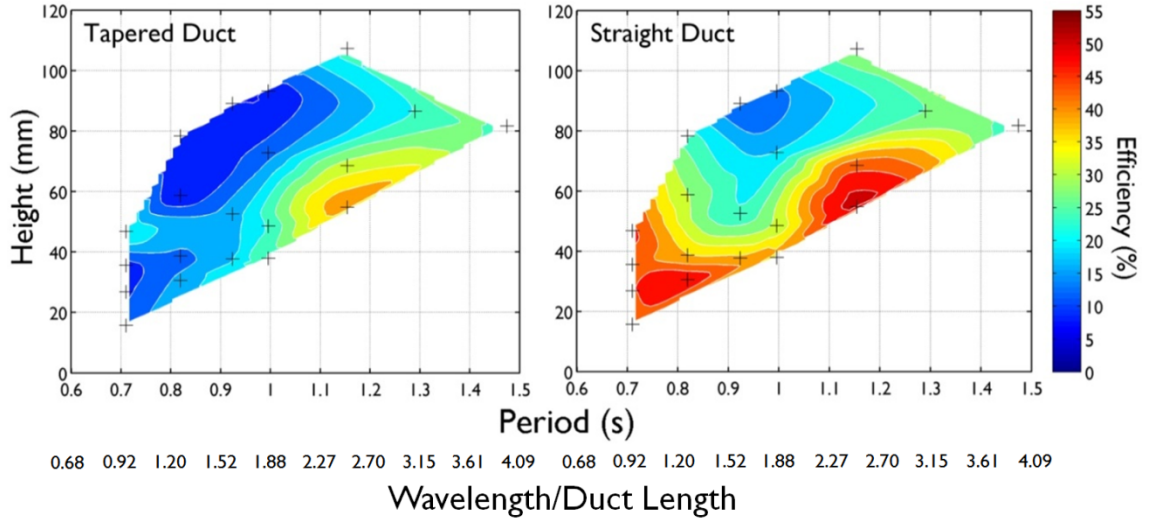

Figure 6.39, Performance contour plots comparing the efficiencies of a tapered and straight sided duct.

The reasons for the parallel walled duct outperforming the tapered duct were unclear from visual observation. It was however, postulated that as the tapered side walls reflect a small component of the advancing wave crest in towards the duct centreline this interacts with the

propagating wave. This may have influenced the shoaling of the wave crest and its ability to seal with the duct roof.

In order to better study the internal wave behaviour for the parallel sided model, the HD camera, described in section 6.6.6, was used to film each run from the underwater viewing window in the towing tank. Three sets of video stills and pressure time series data are presented in Figure 6.40 to Figure 6.42. To aid in the visualisation of these internal wave profiles, the free surface within the duct has been traced in yellow, whilst the duct entrance and roof have been traced by red lines. A single wave cycle is presented in each figure, with the step between each frame being $T/4$. Figure 6.40 shows the progression through a wave cycle for wave #5 with a wave period of 0.82 s. The performance in this wave case increased from ~15 % for a tapered duct to ~50 % for the straight duct. The video stills show that as the wave passed into the duct, it created an initial seal but this was intermittent for the first half of the duct due to the small wave height. As the wave progressed further along the duct and the internal freeboard decreased due to the angled duct roof, the seal strengthened resulting in the larger pulse of air flow in the final 40 % of the wave cycle. The relatively short wavelength meant that, from the relationship shown in Figure 2.10, at least 85 % of the energy within the water column was captured by the duct entrance. The small wave height meant that no energy was lost through overtopping and so this led to a high conversion efficiency despite the initial intermittent sealing.

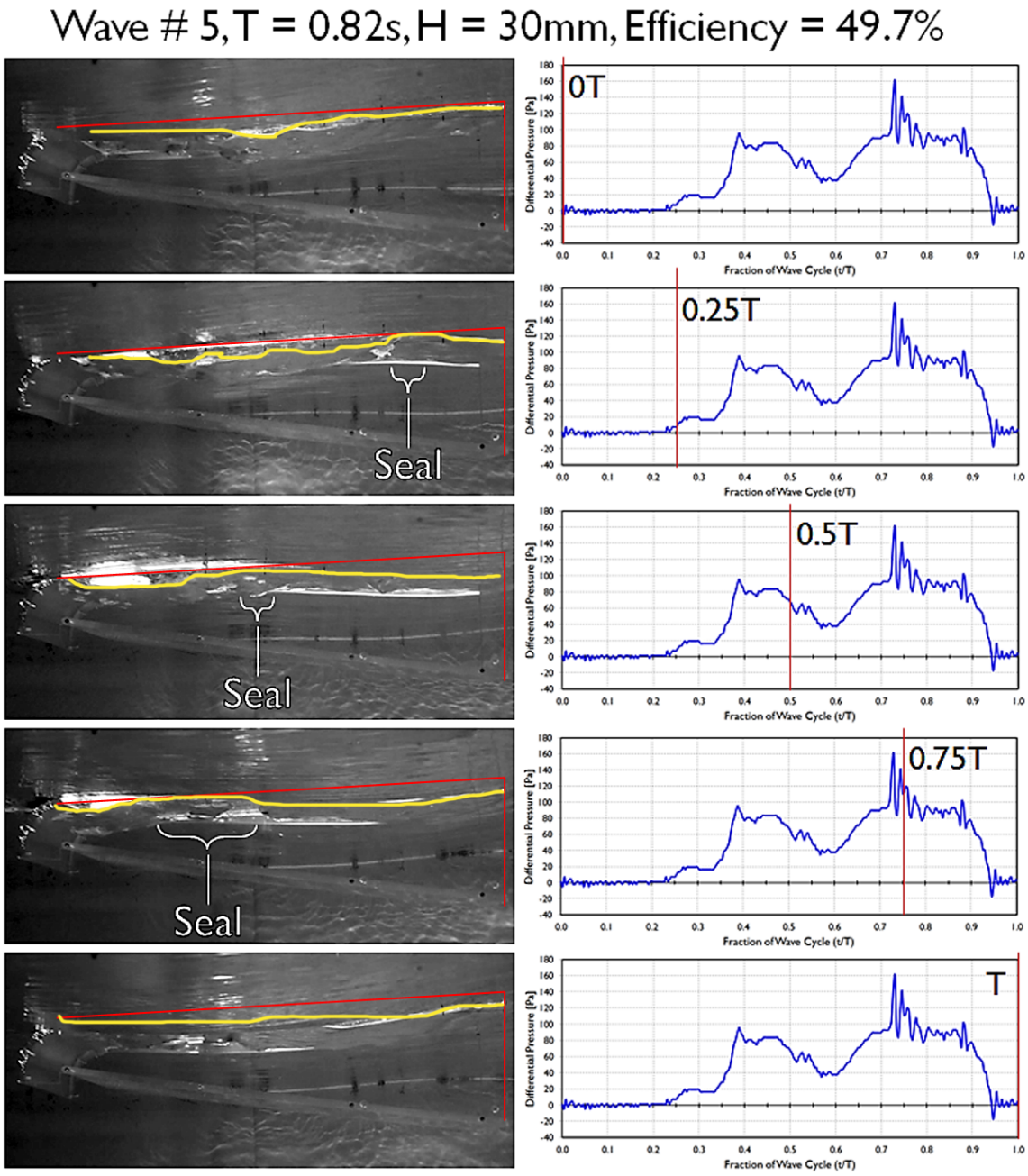

Figure 6.40, Time series of wave #5, $L/L_D = 1.27$.

The wave in the frames in Figure 6.41 had a period of 1.15 s and coincided with the performance peak at $L/L_D = 2.5$ observed in Figure 6.39 and throughout the static model investigations. This had a similar conversion efficiency to wave #5 despite only capturing ~70 % of the energy in the water column and experiencing some wave overtopping. It can be seen in the video stills that the sealing characteristics in this wave were much better than previously observed in wave #5. At the midpoint of the wave cycle, the wave crest had formed a seal with at least 50 % of the duct length and some slight wave breaking can be seen at the wave

front. The OWC type effect that was initially described in Figure 6.13 also occurs at the midpoint in the wave cycle as the external water surface was much higher than the internal water level. This resulted in an inflow of water through the baffle which assisted the advancing wave crest in forcing the air out through the orifice and this caused the larger air flow region in the wave cycle. The reflected component of the wave from the baffle passed back along the duct towards the bow creating the slight inflow of air through the orifice as the volume within the duct refilled with air.

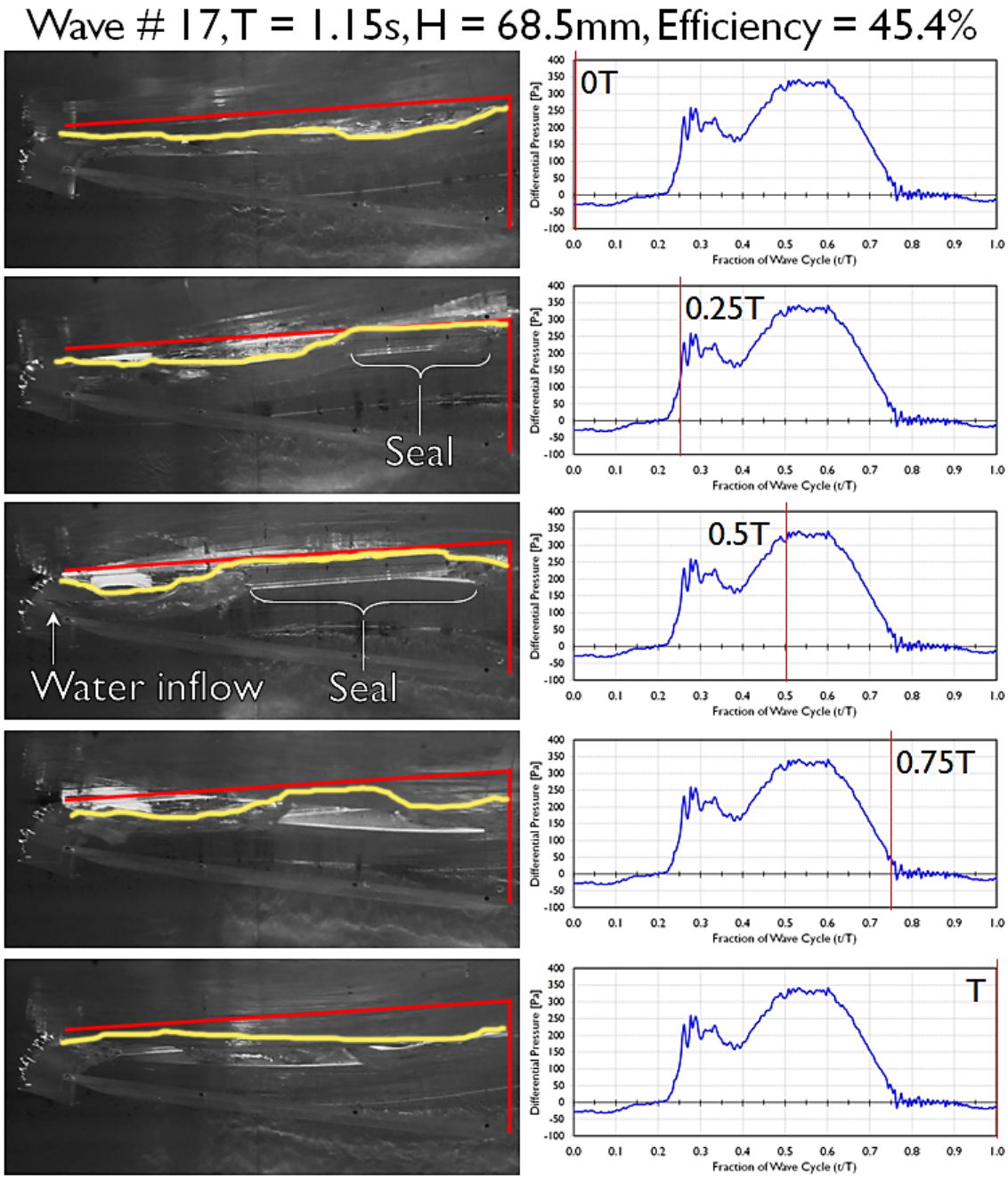

Figure 6.41, Time series of wave #17, $L/L_D = 2.48$.

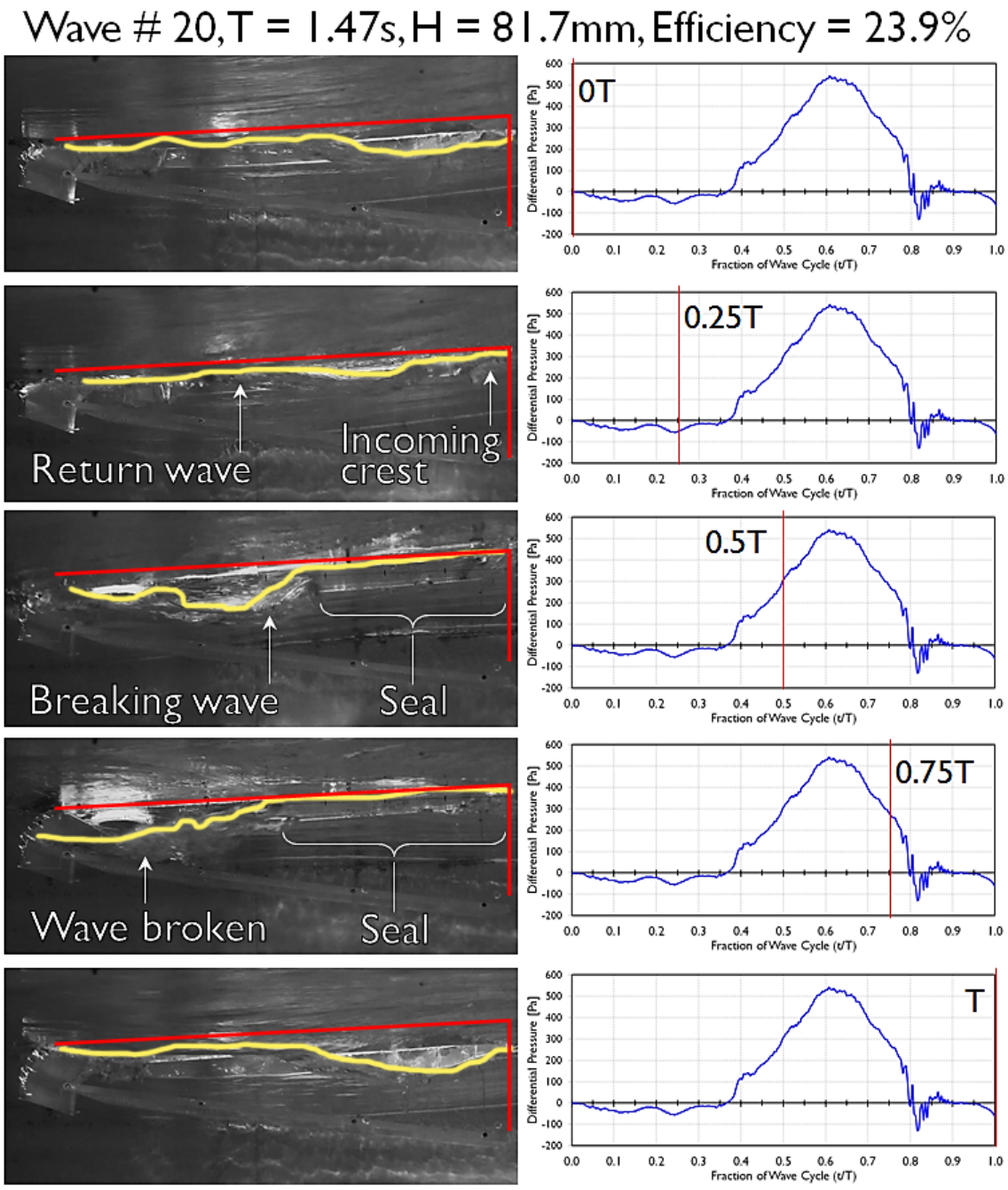

Figure 6.42, Time series of wave #20, $L/L_D = 3.95$.

Of the 20 wave conditions tested, wave #20 was the only test in which the straight sided duct performed worse than the tapered duct. The progression through the wave cycle is shown in Figure 6.42. Initially, the reflected wave from the previous wave cycle can be seen progressing along the duct towards the bow and the subsequent wave crest. This caused air to flow through the orifice into the duct, creating the negative differential pressure for the first third of the cycle. The reflected wave crest met the incident wave crest at the midpoint in the wave cycle and at approximately 40 % of the duct length from the bow. The superposition of the wave crests resulted in a good seal with the duct roof but however, this caused the wave to break within the duct. The seal with the roof then only extended to approximately half way along the duct with

the breaking wave continuing to surge ahead. The lower conversion efficiency of this test can be attributed to the losses arising from the wave crest breaking and the large amount of overtopping due to the wave amplitude being much greater than the duct entry freeboard.

6.6.8 Discussion

This was the first time that the 3D geometry of the duct had been altered to test the effect of different parameters on the performance. Furthermore, this was also the first occasion that the new buoyancy design had been modified to test its effect on performance. The two studies lead to a design that performed better than the baseline configuration. The greater duct entry area and parallel walled design were both incorporated into subsequent models and also the full scale demonstrator design.

It was noted that designs to reduce the wave breaking within the duct were beneficial and they should therefore be investigated further to inform other geometry designs.

The observation of the internal wave behaviour led to the development of theories regarding the operating principles of OWEL. These observations also highlighted the complexities of the conversion process and the difficulties that the development of a mathematical model would face.

A new methodology to measure the device motions was implemented using an HD camera to film the movement of three LEDs mounted to the model. This was then applied to the subsequent tests to compare with

The significant increase in performance over the baseline design suggested that the new design features should be included in the full scale design. This had the caveat that their additional structural cost implications should not outweigh their benefits to the power generating capability of the device. During the testing, there was only sufficient time to test the static configuration of the new geometry. Determining the floating performance of the straight sided duct was therefore the primary aim of the subsequent testing phase.

6.7 Phase 3 – Further Optimisation

6.7.1 Introduction

The second phase of testing demonstrated that a duct with parallel sides and 7.5° floor significantly improved the performance in comparison to the baseline design. The effect of

buoyancy distribution on the conversion efficiency had been investigated for a tapered sided duct but had not been confirmed for the new geometry. The primary aim of this final phase of testing was to confirm that the findings of the initial buoyancy study were applicable to the new geometry. Three buoyancy distributions, similar to those used in phase 2, were tested to investigate this relationship.

A further aim was to investigate the effect of duct trim on the conversion efficiency for a floating configuration. This was intended to inform the design of the full scale device to determine whether a control system to adjust the trim of the duct was worthwhile and necessary. Three different trims were tested with the new geometry to examine the effect on performance. The overall objectives for this phase of investigation were to:

- Test the naval architecture design approaches for the duct with parallel sides.
- Improve the floating performance of the single duct and use the previously developed motion tracking system to establish the optimum relationships.
- Alter the trim of the floating duct to assess its affect on power capture and determine whether there is merit in incorporating active trim control into the full scale device design.

6.7.2 Model

The geometry of the duct was identical to that previously tested at the end of phase 2 and is detailed in Figure 6.25. As with the previous buoyancy investigations, the amount of buoyancy remained constant for each configuration meaning that the ballast required was constant. The total mass of the un-ballasted model was ~11 kg and therefore the dimensions of the buoyancy were calculated in order to buoy up this mass including approximately 0.8 kg of additional ballast mass. The position of the ballast was slightly altered for each configuration to ensure a 25 mm freeboard at the bow of the duct and zero freeboard at the stern. Schematics of the three buoyancy configurations and their LCF positions are summarised in Figure 6.43. The results in section 6.6.5 showed that floating configurations with the surface piercing buoyancy concentrated towards the stern were less favourable than distributions skewed further forward towards the bow. Therefore, the three designs that were conceived for this phase of testing had the surface piercing buoyancy arranged to position the LCF at the midship or towards the bow. From the perspective of a full scale design, configuration B with evenly distributed buoyancy would likely be the simplest to construct. Configuration A was conceived to have the same LCF as configuration B but have the buoyancy concentrated around the midship. This was intended to have a longer natural pitch period and be less stiff in pitch due to the reduced righting moment and restoring force. Finally, configuration C was intended to be similar to configuration

D in the phase 2 testing and move the LCF closer towards the bow with the intention of replicating the favourable performance that had been previously observed.

In order to investigate the effect of trim on performance, the amount of lead ballast used to trim the model was varied to ensure that the freeboard at the bow was altered whilst maintaining the same freeboard at the stern. Whilst this may not have been a scaled representation of the full scale scenario, it was intended to determine the general trend and whether it would warrant further investigation.

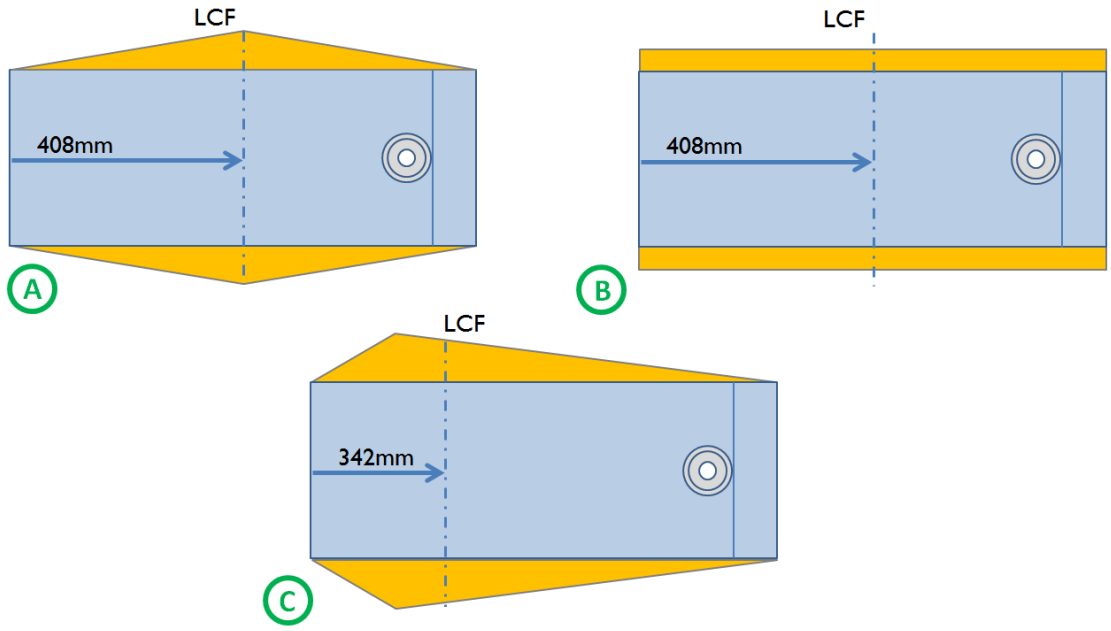

Figure 6.43, Three drawings showing the three different buoyancy distributions tested along with their associated LCF positions.

6.7.3 Wave Conditions

Initially, the buoyancy configuration trials were tested with 21 wave conditions similar to those used in the previous phase of testing. Following the choice of the most favourable buoyancy configuration 20 additional waves were included into the test programme. These extra test points were used to provide a greater spread of wave scatter when investigating the effect of duct trim on the conversion performance. The initial 21 points and the additional wave conditions are plotted in Figure 6.44 . This includes the 'error' bars that indicate the spread of wave heights recorded from the average during the tank calibration in which four repeats of each wave were run. The repeatability of the initial test waves was good whereas this was reduced for the additional wave test conditions, particularly at the shorter wave periods. Comparing these calibrations to the calibrated conditions in the phase 2 testing, see Figure 6.27, yields no discernible trends in the repeatability of the waves. Waves with T = 0.92 s, for example, had a range of ±0.1H for the phase 2 calibrations whereas the average wave heights in

each of the four runs for the 3rd phase calibrations were almost identical. Nevertheless, the average wave heights taken from the tank calibrations were used as the incident wave heights for the data analysis. Performance results from test waves with the large 'error' bar spread should be treated with caution.

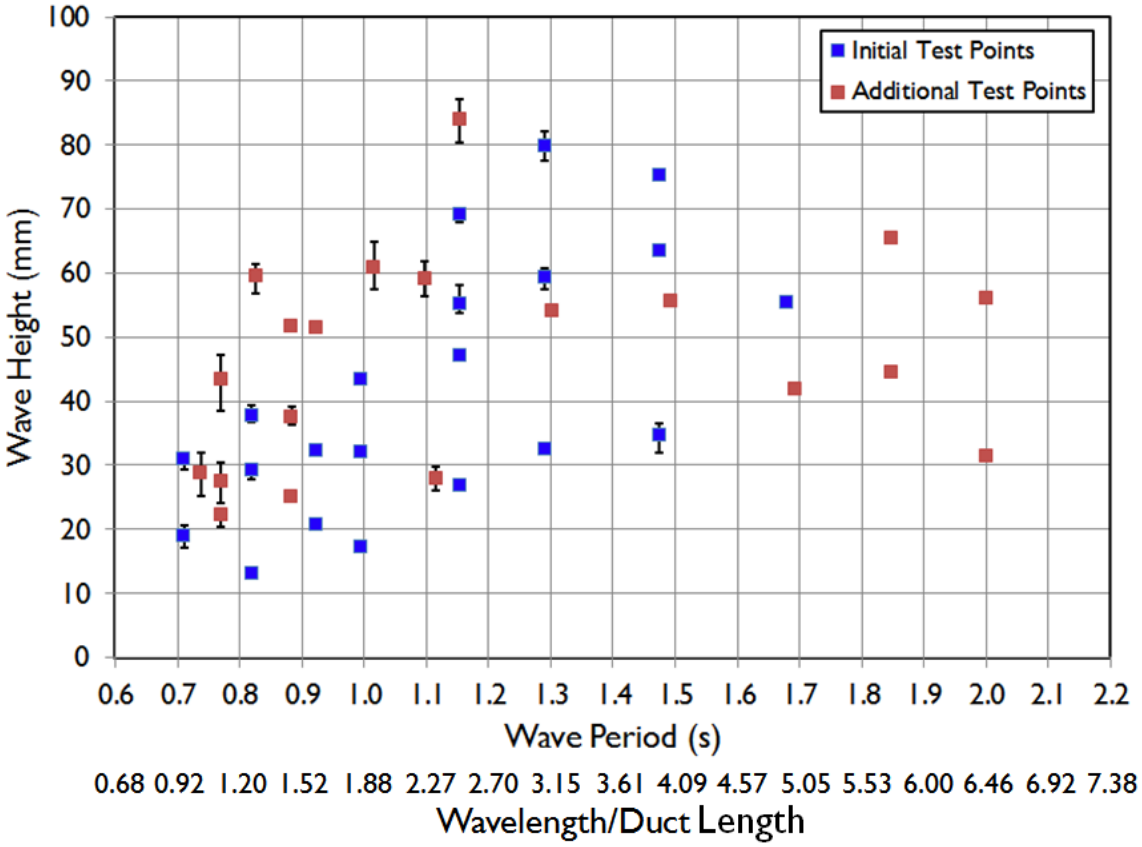

Figure 6.44, Scatter plot of the initial 21 test waves with their associated absolute deviations and the additional 20 test points included in the latter tests.

6.7.4 Buoyancy Configurations

Each of the three buoyancy configurations were tested with the 21 wave conditions. The scatter plot in Figure 6.45 shows fairly comparable conversion efficiencies for each configuration but with configuration C, with the forward LCF, having the highest peak values, as was expected.

The performance data presented in the contour plots in Figure 6.46 shows the effect of wave period and height on the conversion efficiency for the three buoyancy configurations. Comparing the three plots shows that configuration C had the highest and most defined peak of performance.

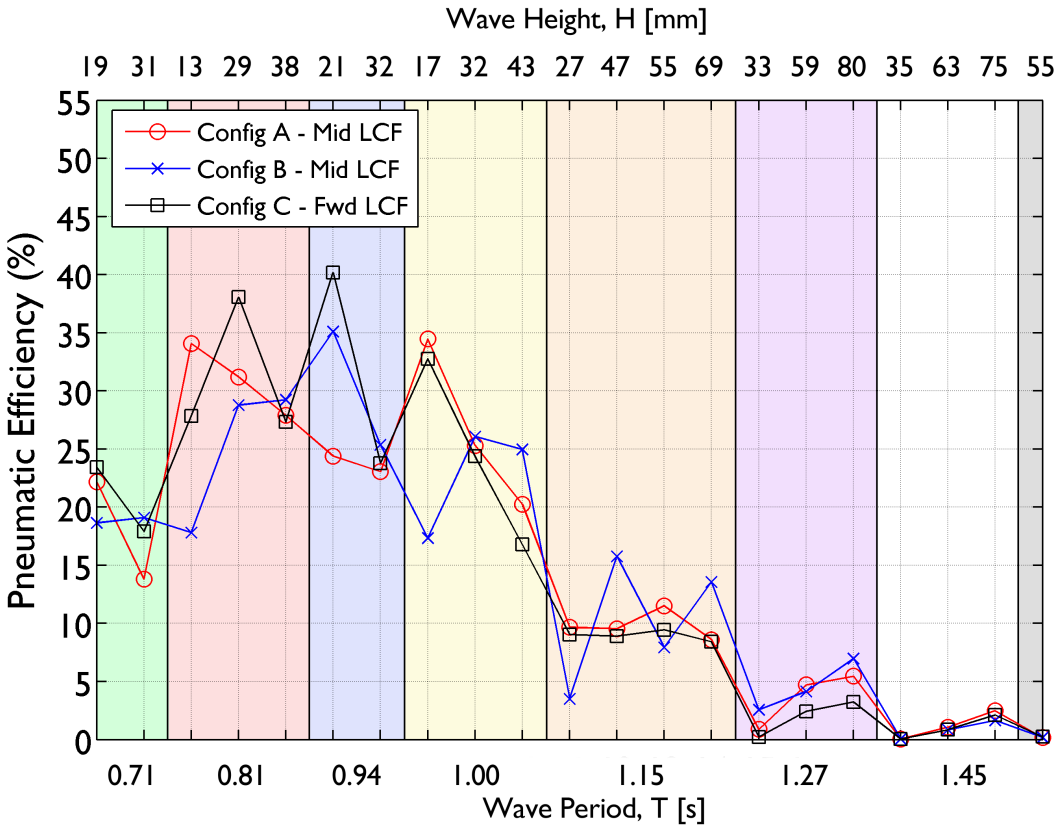

Figure 6.45, Conversion efficiency across the 21 initial test waves for the three buoyancy configurations. [N.B. Band colours are only to aid the identification of data points with the same wave period]

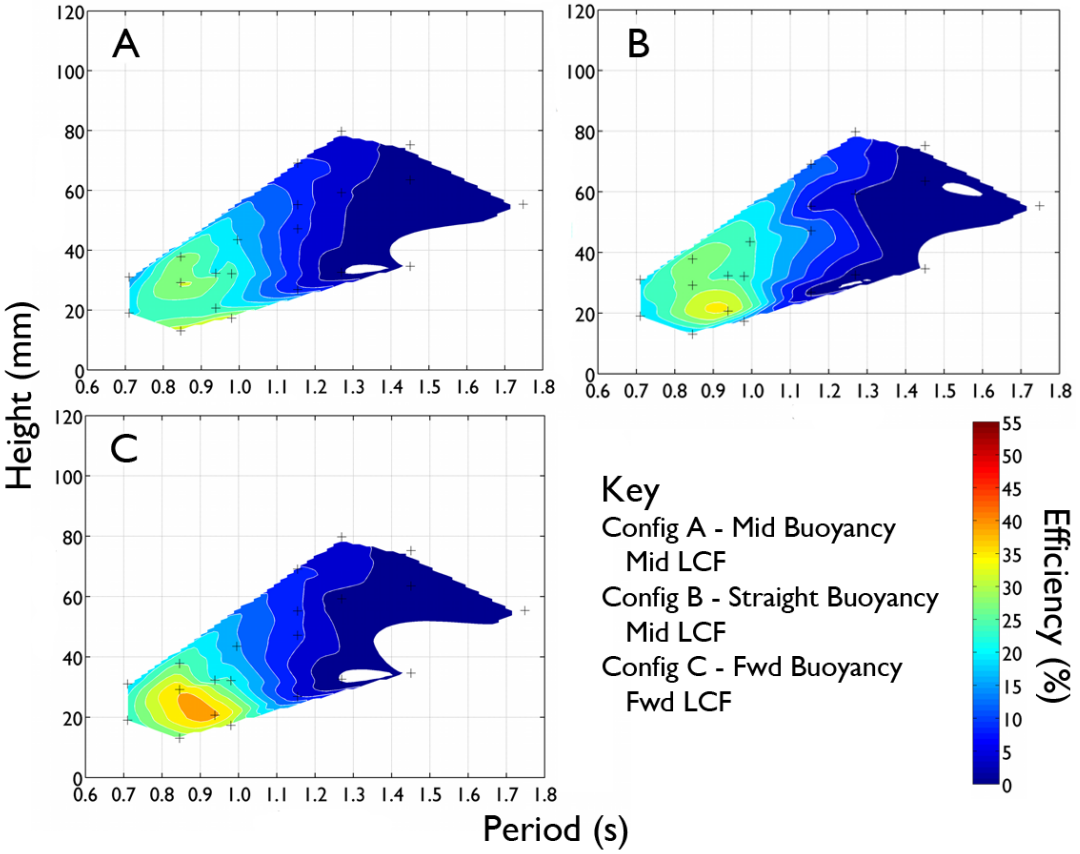

Figure 6.46, Efficiency contour plots for the three buoyancy configurations (A – C).

The contour plots in Figure 6.47 provide a comparison between the performance of the tapered duct, from the previous testing phase, and the straight sided duct with the same forward distributed buoyancy configuration. The overall efficiency plots indicate fairly little difference between the floating tapered and parallel sided geometries despite the significant performance increase observed for the static conditions. It is therefore questionable as to whether the straight sided duct could be sufficiently beneficial over the tapered duct to warrant the additional cost of materials. Nevertheless, the favourable performance of the straight sided duct, with the performance peak extending into longer waves, meant that its geometry was used for the subsequent trim optimisation experiments.

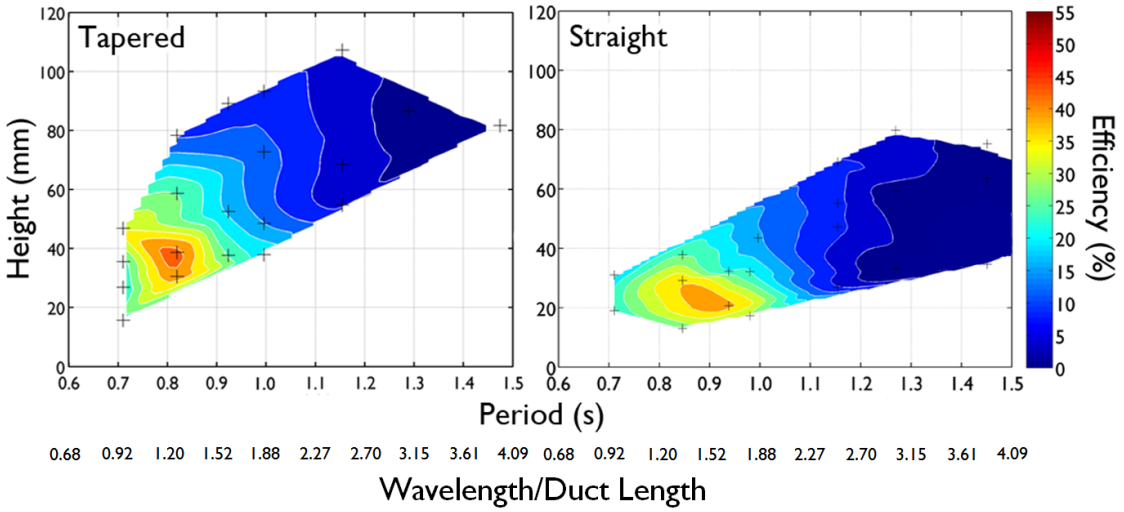

Figure 6.47, A comparison between the performance plots of tapered and straight sided ducts with the forward LCF buoyancy configuration.

6.7.5 Pitch and Heave Motions

Motions were only captured for two of the three configurations. The methodology used was identical to that described in section 6.6.6. As before, the RAOs were derived by taking an average of the individual RAOs from each test condition with the same wave period. The results for the pitch and heave RAOs for buoyancy configurations B and C are shown in Figure 6.48. There is little difference between the trends of the two configurations however, configuration B predominantly had a lower pitch and heave response than C. In comparison to the RAOs of the tapered duct geometry in Figure 6.35, the peak heave response of both geometries occurred at a wave period of 1.15 s. The magnitude of the response of the straight duct configurations however, was consistently less than that of the tapered duct configurations, whereas for pitch, the response of the parallel sided duct was greater. The reduction in heave response of the parallel walled model may have been a result of larger volume of water within the duct which would have increased the added mass and resistance to the heave displacement.

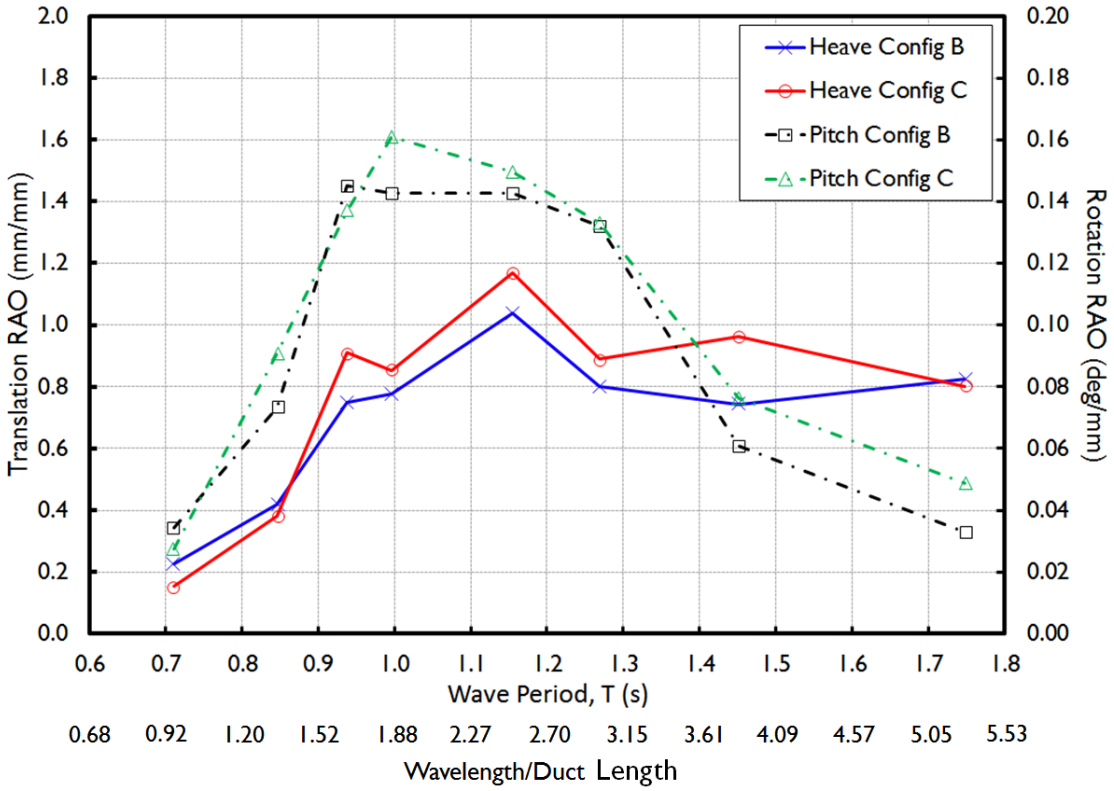

Figure 6.48, Comparison of heave and pitch RAOs for configurations B and C.

The time series plots in Figure 6.49 and Figure 6.50 show the heave and pitch motion time series for configurations B and C. These can be directly compared to the time series for two of the phase 2 floating configurations shown in Figure 6.37 and Figure 6.38. The relationships between pitch and heave across the two testing phases are very similar.

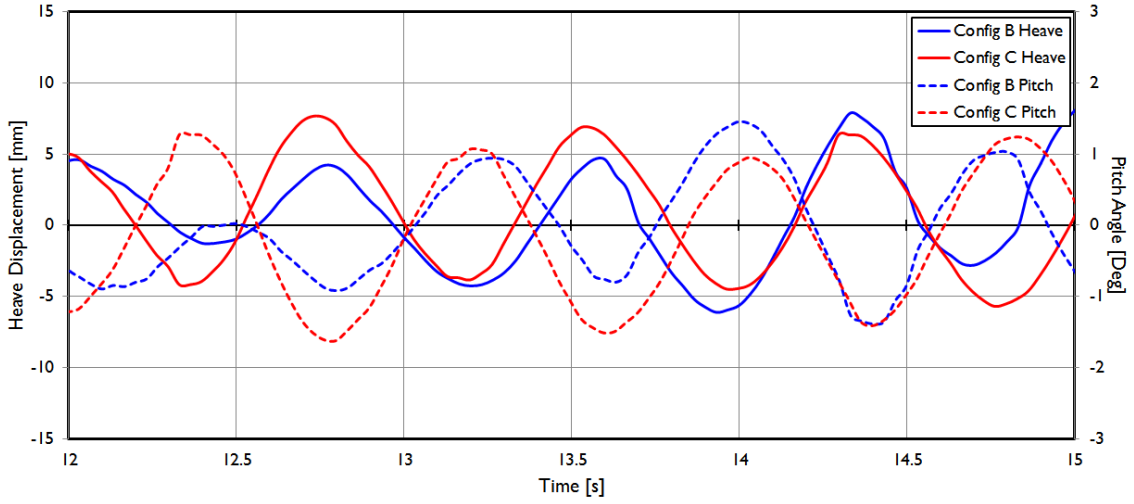

Figure 6.49, Time series of heave and pitch motions for wave # 4, T = 0.85 s, H = 29 mm for buoyancy configurations B and C.

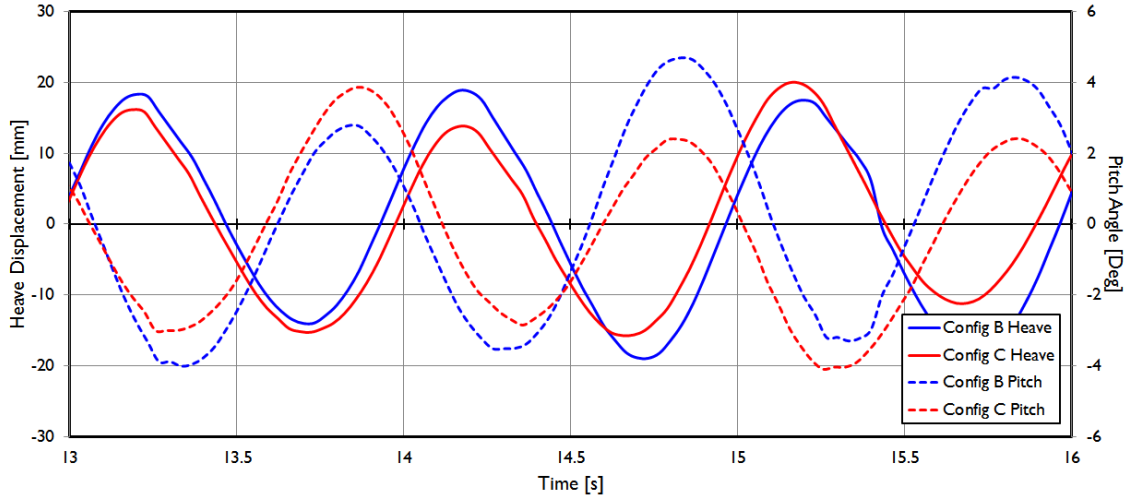

Figure 6.50, Time series of heave and pitch motions for wave # 10, T = 1.0 s, H = 44 mm for buoyancy configurations B and C.

6.7.6 Trim Variation

It was hypothesised that the performance may vary depending on the freeboard at the entry to the duct. This was initially investigated in the initial 2D tests in section 4.7 and concluded that, for the angled roof configuration, the largest bow up trim that was tested was the most beneficial. This investigation was intended to examine the effect of trim for the floating model and determine whether a relationship existed between the trim and wave conditions in order to maximise the power capture.

Throughout the testing of the single duct geometry the model was trimmed to have a 25 mm freeboard at the duct entry. An initial series of test cases were run for the 10 mm and 35 mm trim to compare with the 25 mm results. It was found that reducing the bow freeboard to 10 mm for wave periods greater than 1.05 s and increasing it to 35 mm for periods less than that, the performance could be improved. The results across the 41 test conditions for the 25 mm trim configuration are shown in Figure 6.51 for direct comparison with the results achieved by increasing and decreasing the trim. Similarly to other plots in this chapter, the results have been organised into bands of wave period and coloured to ease comparison. Including a label to show the individual wave heights of each of these tests would have compromised the readability of the graph and so it should be noted that, for each band, the wave height increases along the axis.

These results show that for the majority of cases where T < 1.05 s the 35 mm trim provided better conversion efficiencies than the 25 mm trim. Similarly for T > 1.05 s, the 10 mm trim generally led to higher performance than the 25 mm. The results from the 10mm and 35 mm trim tests were combined into one contour plot and compared against the performance plot for the 25 mm trim tests in Figure 6.52.

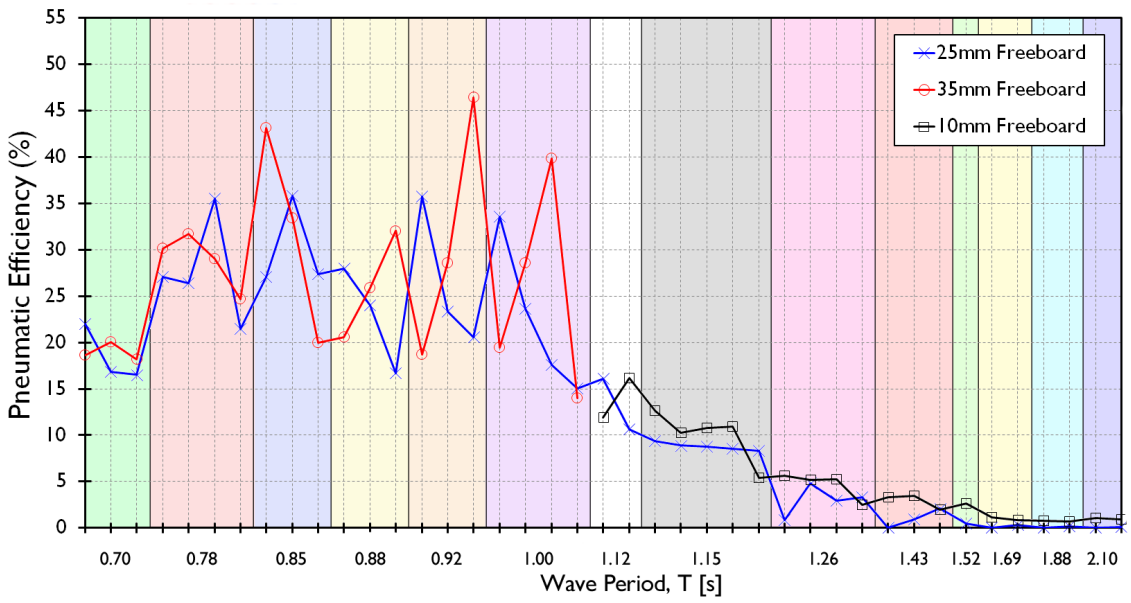

Figure 6.51, A comparison between the conversion performance for the 25mm trim and the modified trim configuration across the 41 test cases, (1 – 20, $T < 1.05$ s and 21 – 41, $T > 1.05$ s) [N.B. Band colours are only to aid the identification of data points with the same wave period].

These trends are contrary to previous conclusions from the intermediate scale testing that the duct should be trimmed depending on the wave height. Furthermore, a smaller freeboard was required for the longer wavelength waves whereas it was postulated that at longer periods, performance could benefit from a larger freeboard as a greater volume of air would be available to be compressed. These conceptions may well have been true for a static duct however, it was observed that for the floating model, the motions of the duct were the reason for the variation in trim with period. In waves with $T < 1.05$ s, ($L/L_D < 2$) the motions of the duct were comparably small which meant that a large freeboard enabled a greater volume of air to be captured. For the longer period waves therefore, the contour following nature of the duct meant that a poor seal was made with the duct roof when the trim was large. Therefore, a reduction in the bow freeboard to 10 mm meant that waves could more readily seal with the duct roof and so generating a greater air flow. The trends in performance with relation to wave period were however, not altered significantly and similarly to the 25 mm trim tests, the performance of the combined trim strategies rapidly reduced in periods greater than ~1.2 s. Nevertheless, the performance of the combined trim strategy was greater than for any of the other floating, single duct configurations within this phase of testing.

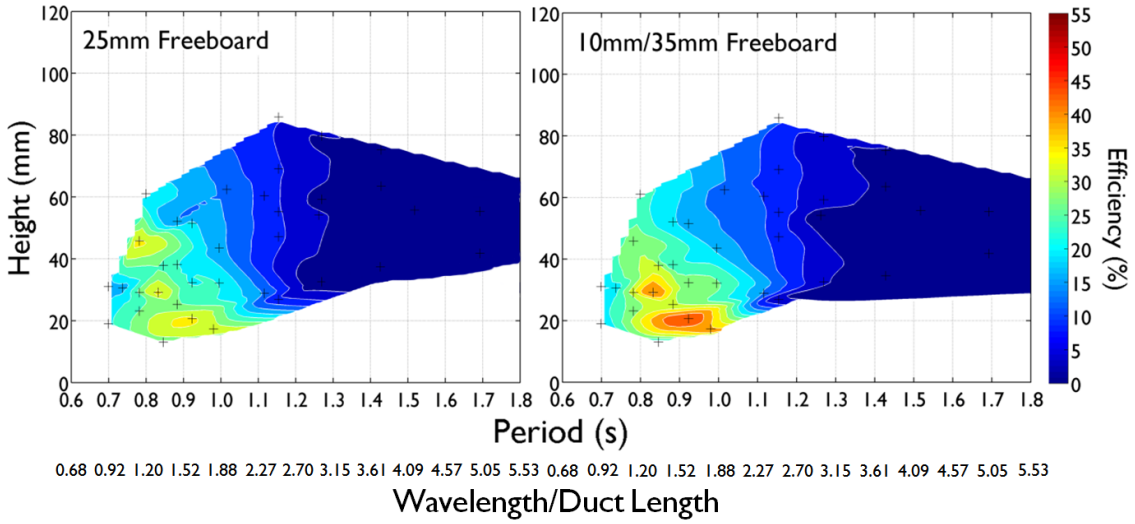

Figure 6.52, Floating model with 25 mm bow freeboard (left) and (right) a combination of 35 mm bow freeboard for short period waves ($T < 1.05$ s) and 10 mm for longer period waves ($T > 1.05$ s).

These results highlight the performance gains that are achievable if the appropriate trim is set. For a full scale device, a control system that allows the trim to be varied by sea state could be used to maximise the power output. Further investigations are required to investigate the performance with other trims and in irregular sea states in order to predict the full scale energy yield benefits that could be achieved.

An assessment was made to determine the potential absolute deviation in the calculated wave-to-pneumatic conversion efficiencies of the final model configuration, with the combined trim strategy, due to range of measured wave heights from the tank calibration. The variation in conversion efficiency was calculated from the maximum, mean and minimum average wave heights measured over the four repeat calibration runs for the 21 wave conditions in section 6.7.3. The results of the analysis, presented in Table 15, show that predominantly, the largest discrepancies are more likely for the shorter wave period tests. For wave conditions with T > 1.0 s, the range of mean wave calibrated heights reduced and therefore, so did the absolute error range of the calculated conversion efficiency.

Table 15, The implication of the range in calibrated wave heights on the calculated wave-to-pneumatic efficiencies.

Test #	T [s]	Mean H [mm]	– Deviation of H [mm]	+ Deviation of H [mm]	Efficiency max. H	Efficiency mean H	Efficiency min. H
1	0.70	19.0	1.9	1.5	15.0%	18.2%	21.6%
2	0.70	31.0	1.6	0.9	17.0%	18.6%	19.9%
3	0.83	29.2	0.4	0.3	41.1%	43.1%	46.7%

4	0.85	13.0	1.3	0.5	19.6%	20.0%	21.8%
5	0.85	37.8	1.0	1.6	32.3%	33.4%	37.0%
6	0.92	20.7	0.5	0.4	44.4%	46.4%	48.5%
7	0.92	32.3	0.7	0.5	27.5%	28.6%	29.8%
8	0.98	17.3	0.4	0.4	37.6%	39.9%	41.0%
9	1.00	32.1	0.8	0.5	27.5%	28.5%	29.7%
10	1.00	43.5	0.7	0.8	18.8%	19.4%	20.1%
11	1.15	26.9	0.5	0.8	5.2%	5.4%	5.7%
12	1.15	47.1	0.7	0.3	10.7%	10.9%	11.2%
13	1.15	55.2	1.4	2.9	10.0%	10.8%	11.7%
14	1.15	69.1	1.3	1.0	9.9%	10.2%	10.6%
15	1.27	32.6	0.5	1.0	4.9%	5.2%	5.4%
16	1.27	59.3	1.7	1.5	5.3%	5.6%	5.9%
17	1.27	79.8	2.3	2.4	4.8%	5.2%	5.4%
18	1.43	34.6	2.7	1.9	1.7%	2.0%	2.2%
19	1.43	63.5	0.4	0.3	3.3%	3.4%	3.4%
20	1.43	75.2	0.4	0.2	3.2%	3.2%	3.2%
21	1.69	55.3	0.5	0.4	1.1%	1.2%	1.2%

6.7.7 Discussion

The results from this final phase of physical modelling provided further insight into the operation of the single duct device and the conclusions assisted in making decisions for the full scale design.

Despite the large performance gains of the static, parallel sided duct over a static, tapered duct, the performance of the two geometries when floating was very similar. It is therefore possible, that the energy productivity of parallel sided device could be comparable to that of a tapered sided device and that the additional cost for the larger structure may not be mitigated. Further investigations including a full scale annual energy generation assessment will be required to determine the most beneficial device configuration.

Similarly to the conclusions for the tapered duct, the buoyancy configuration for the floating, parallel sided duct that provided the highest peak performance had the majority of the surface piercing buoyancy concentrated towards the bow of the duct. As a result of this conclusion, it was decided by ITP to incorporate a similar buoyancy distribution into the design for the full scale demonstrator.

The motions of two of the buoyancy configurations tested were similar for pitch and heave. The peak heave RAO for both configurations occurred at $T = 1.15$ s which was the same as for the tapered duct configurations in the previous testing phase. It was again postulated that the heave characteristics of the device were detrimental to the predominant peak performance observed with the static duct. This was a result of the period of peak heave RAO coinciding with the period of peak efficiency.

From this conclusion it was postulated that modifying the natural period of heave, T_{heave}, to a period outside of the normal operating envelope could improve the power capture. This would mean that the peak in heave RAO would not coincide with the period of peak efficiency of the collector. The equation to calculate the natural heave period of a floating body is given by equation [26];

$$T_{heave} = \sqrt{\frac{M + M_a}{\rho g A_{wp}}} \qquad [24]$$

Where M is the mass of the floating body, M_a is the added mass of water caused by the vertical motion of the body through the water, A_{wp} is the water plane area. From this equation it can be seen that the most suitable ways of changing T_{heave} are to either increase the mass of the body or increase the waterplane area. The most effective way to test the effect of changing the natural heave period on the conversion performance in future tests would be to increase the mass of the model. However, changing either the mass or waterplane area is likely to have implications on the stability of the hull and so change its responses in pitch and roll. To prevent this, additional mass should be added as close to the current CoG as possible and additional buoyancy be added below the waterline but in a way not to significantly lower the centre of floatation.

In addition, altering the natural pitch period, T_{pitch}, of the duct was also suggested as a further area investigation for future work. Similarly to the reasoning for changing the heave period, changing T_{pitch} would move the peak in pitch RAO outside of the operating envelope of the device. Equation [25] provides the natural period of pitch for a floating body;

$$T_{pitch} = \sqrt{\frac{I_{xx}}{M\ g\ \overline{GM_L}}} \qquad [25]$$

Where I_{xx} is the longitudinal second moment of inertia, M is the mass of the body, and $\overline{GM_L}$ is the longitudinal metacentric height of the body. The relationship in equation [25] shows that the pitch period can be modified by altering the longitudinal inertia, mass or longitudinal stability of the body. Perhaps the most suitable method to test the effect of increasing the pitch period of the model in future experiments would be to increase the longitudinal inertia of the model by moving the ballast weights further from the centre of gravity. As an extreme case, the ballast weight could be split evenly and each half be positioned at a distance from the bow and stern of the model supported by a beam. This would increase the pitch period far beyond the range of periods within the test schedule.

The investigation into the effect of trim on the power generation of the floating model showed that, contrary to prior predictions, there was no clear relationship between optimum trim and wave height. It is likely that the power generation in real seas can be maximised by modifying the trim depending on the typical wave period for each sea state. If this is the case then active control of the duct trim, through variable buoyancy and ballast tanks, would be beneficial at full scale.

The variation in the calibrated mean wave heights was found to have likely affected the efficiencies in shorter period waves $T < 1$ s, greater than for longer periods. Whilst this was not excessive, it was deemed relatively significant and was therefore a limitation of the quality of the test conditions available in the towing tank.

6.8 Further Discussion and General Conclusions

The results and learning from this series of experiments has directly influenced the design of the full scale OWEL demonstrator that is being designed by a commercial consortium and funded by the UK TSB.

The performance characteristics for a static model are very different from those with a floating model. Focusing on studying the performance when the model was static was originally thought to simplify the process, however it led to misleading results. Future experiments should only consider floating configurations of the duct as little useful information can be obtained from a static duct.

As these tests were carried out at small scale, care should be taken when transforming these findings to a full scale scenario. The performance will be particularly affected by air flow scale affects such as compressibility and disproportional losses from the lack of Reynolds similitude between the small and large scale devices. Compressibility will act to reduce the effective performance at full scale whereas the lack of Reynolds similitude will mean that losses at small scale are comparatively greater than for a full scale device. Hydrodynamically, this also implies that viscous losses at small scale are greater than for full scale and so motions at full scale are likely to be comparatively greater.

The main conclusions from these experiments were:

- The performance of the initial baseline design was improved by a series of modifications to the geometry whilst the duct was static.
    - Increasing the duct entry depth.
    - Changing the duct sidewall angle from a taper to be parallel sided.
- The performance gains from the basic geometry optimisation in static conditions did not directly translate to the same performance gains for a floating model configuration.
- The naval architecture for the duct that was originally applied from the lessons learned in the Cork basin tests was not suitable for a single duct and so was redesigned.
- Basic optimisation of the buoyancy arrangement found that concentrating the longitudinal surface piercing buoyancy towards the bow of the duct improved performance.
- Small performance gains could be obtained by altering the duct entry freeboard for different wavelengths.

These experiments also led to the development of wave generation and data collection software applicable to the Lamont wave tank, which was not previously available. Furthermore, a methodology and software for the tracking of LEDs using HD video was also developed by the author. This may be applied to problems where the motions of a body in two dimensions need to be tracked.

The modifications made to the single floating duct, resulted in the performance of the final improved configuration far exceeding that of the initial, baseline model. The testing identified the parameters that the performance of a single floating duct was sensitive to. This also provided performance data suitable to inform the design decisions of the marine demonstrator and to make estimations of full scale power generation.

7 Numerical Modelling Approaches

7.1 Introduction

Numerical models can be powerful tools in the development of wave energy converters. They can be used to study the behaviour of a device at a much lower cost and in a shorter time frame when compared with laboratory investigations. A typical application would be to optimise design parameters such as geometry or power take-off characteristics without having to rebuild or modify a physical model. Whilst numerical models can provide many advantages over physical testing, they should always be thoroughly validated by empirical data before being used as a design tool. Modelling methods for devices such as point absorbers and OWCs are well established and have been continuously developed over the past few decades [Evans (1978), Falnes (2002)] For devices such as OWEL, with a novel energy conversion principle, it is necessary to consider the physics to be modelled in order to determine the most suitable approach.

In previous OWEL research, two different numerical modelling approaches were made and have been reviewed in sections 3.3.2 and 3.3.4. The first approach, developed in the initial, proof of concept OWEL project, was a simplified, analytical model that had many inherent limitations. It neglected a number of the physical processes important in the energy conversion cycle and coupled with the simplifying assumptions made, the results did not agree well with the experiments. A simplified CFD model that was created for the intermediate scale, Carbon Trust project was intended to better simulate the internal flow physics within the device. This also had many simplifications, such as only modelling the flow within the duct, and so little was concluded from it.

7.2 Objectives

The objectives of the work in this chapter were to;

- Define the ideal outputs of a numerical model of OWEL.
- Describe the energy conversion process and the modelling requirements to capture the physics.
- Review typical numerical modelling methods for OWCs with reference to their suitability to be used in the modelling of OWEL.
- Implement the most suitable modelling approach and make comparisons between its results and the physical modelling data.

7.3 Requirements of a Numerical Model

A significant work package within the OWEL TSB project was to conduct numerical modelling of the device in order to inform the full scale design. Much of the work presented in this chapter was a precursor to the commencement of the numerical modelling work package and was used to directly inform the subsequent investigations. The specific functional requirements of the model were partly led by ITP and OWEL and evolved throughout the course of this research and the project that ran in conjunction with it.

For the model to be a useful design tool, the high level requirements of an ideal model were initially considered. The primary outputs of the model were deemed to be:

- *Power* – analogous to air flow out of the device through the PTO. This was a requirement to assess the performance of OWEL.
- *Motions* – the model should determine the floating dynamics of the device in order to determine their effect on power capture.
- *Loads* – an ideal model should be able to calculate the loading on the structure in order to inform the engineering design.

For the model to be used to carry out investigations, it would be required to determine how a series of variables affected the three outputs. The key variables in the design on which the outputs depended were identified as the geometry; mass and buoyancy distributions; mooring characteristics; PTO damping; and importantly, the scale so that the model could be validated from the small scale testing data. Finally, the model should be able to simulate different wave input conditions from idealised, regular waves to realistic, irregular sea states up to the extreme conditions for a site in which the largest loads will be experienced.

To develop a numerical model that included each of these ideal, desirable features would be particularly ambitious and would likely take years to create, without any guarantee that it would accurately model each aspect. It was therefore decided that the scope of this work should be to investigate ways in which a realistic performance model could be developed with the objective of being able to include floating dynamics and irregular wave conditions. Creating a model capable of calculating structural loads was regarded as beyond the scope of the work.

7.4 Description of the Energy Conversion Process

The performance of OWEL is reliant upon the interactions between the water and air within the duct geometry. From the physical modelling observations reported in section 6.5.4, it was shown that the internal flow physics was significantly more complex than that of the external, regular wave.

Through visual observations and data collected from the physical modelling, four key processes occurring within the energy conversion cycle were identified:

- The incident, regular wave crest enters the duct and immediately experiences a step change in depth whilst the external wave continues to propagate either side of the duct. Wave energy passing under the keel of the duct or overtopping the deck is not captured by the duct entry.
- The wave crest interacts with both the geometry and the exiting wave crests reflected from the baffle at the stern of the duct. This increase in wave height due to shoaling and interaction with reflected waves causes the crest to form a seal with the roof of the duct. The position, duration and integrity of the seal are dependent on these interactions as, in some instances, this can be a beneficial process where the two waves combine to strengthen the seal. However, in other cases, the reflected wave crest collides with the incident wave, causing it to break and not form a seal.
- As the internal wave progresses along the duct, it transfers energy to the volume of air ahead of it. The energy it imparts to the air is dependent on the force applied by the wave, the reactant force and damping of the PTO and the structure. In addition, the volume of air interacts with and deforms the wave crest. This can lead to the seal being broken and air passing between the duct roof and wave crest. As energy is transferred from the wave crest to the air volume it is acting upon, the speed and energy of the wave reduces.
- The final process that can occur involves the vertical inflow and outflow of water from the baffle at the stern. As the wave crest passes from deep water to the shallow water within the duct it shoals, therefore, further decreasing its velocity. This results in a difference between the position of the internal and external wave crests. In some instances, where the lag is large, the external wave crest may arrive at the stern whilst the internal wave is still propagating along the duct. Similarly to the operating principle of an oscillating water column, this causes a difference in internal and external water level at the stern and so there is an inflow of water through the baffle. This additional volume change contributes another force on the internal air volume. This phenomenon can be seen in the image in Figure 6.12, taken during small scale, physical tests.

The additional fluid-structure interactions that occur when the motions of the body are included, further influence the fluid behaviour inside the duct. The motion of the water entrained within the duct is therefore strongly coupled to the vessel dynamics. It has been shown throughout the experimental investigations that the performance characteristics of the device differ between static and floating configurations. Whilst considering the fundamental operating principles using

a static duct may be sufficient, it is imperative to couple this with the floating dynamics to obtain a realistic representation of the conversion characteristics.

To visualise the energy transfers and physical processes occurring around and within the device the flow chart in Figure 7.1 was conceived. This shows that the influx of wave energy either forces the duct motion, enters into the duct or passes around the duct. A proportion of the energy entering into the duct is converted into air flow whilst the remainder is either reflected back out of the duct or baffle, or lost to viscous effects. The key flows of energy, from wave to pneumatic, are shown as red arrows on the diagram and can have a magnitude exceeding 50% of the wave energy entering the duct. It was not possible to quantify the proportions of each flow of energy based upon the measurements taken in the experiments.

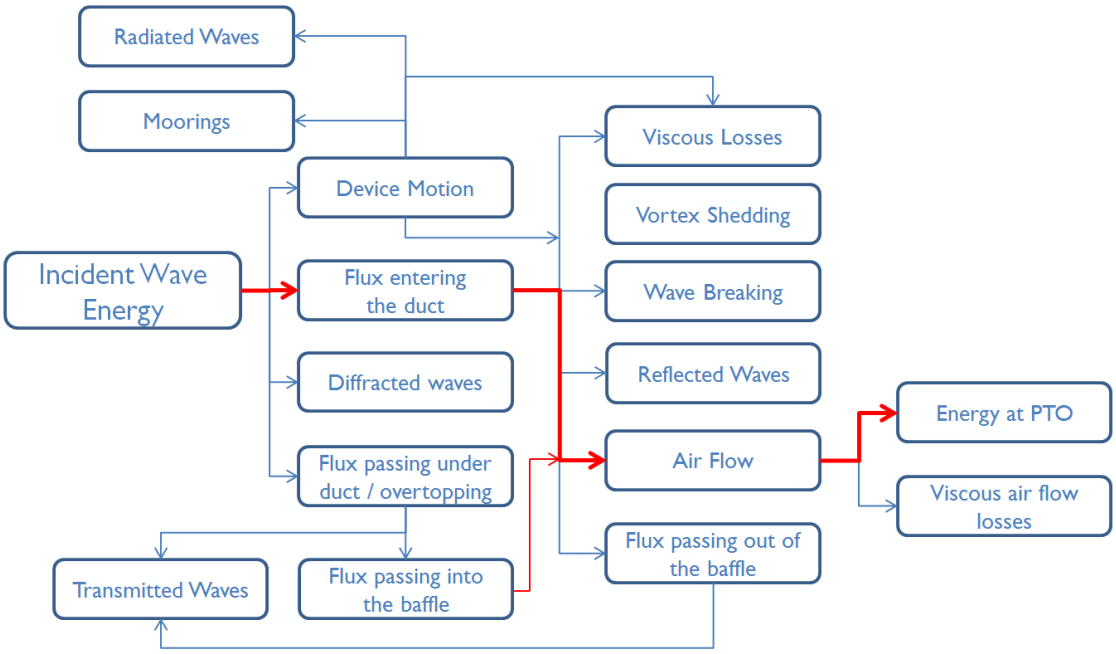

Figure 7.1, An energy conservation model for a dynamic, floating OWEL showing the inputs, losses and outputs of energy occurring through the conversion process.

7.5 Theoretical Modelling Methods for OWCs

7.5.1 Introduction

It was concluded in the literature review in chapter 0 that, of the various types of WEC, OWEL shares the most similarities with OWCs. Therefore, in the same way that the physical modelling of OWCs was reviewed in section 3.4, it is pertinent to review the numerical modelling approaches applied to OWCs in order to assess the applicability of each methodology to model OWEL.

The first theoretical model of an OWC was presented by McCormick (1974a), McCormick (1974b) and was based upon the early OWCs used as navigation buoys, experimented upon by Masuda (1971). McCormick considered a floating axisymmetric OWC comprising a float with a central pipe containing the water column and bi-directional turbine. These early studies investigated the fundamentals of the OWC operating principle and were partially empirical as they relied upon experimental values for their damping and flow loss terms. Nevertheless, they paved the way for numerous models and approaches to the hydrodynamic modelling OWCs that have since followed.

There are three typical approaches to the theoretical, hydrodynamic analysis of OWCs, as summarised in Figure 7.2: increasing in complexity (a) the massless, rigid plate model (b) linear hydrodynamic approximations using excitation and radiation coefficients with potential flow theory, (c) solution of the full fluid dynamics equations throughout the entire domain by using CFD.

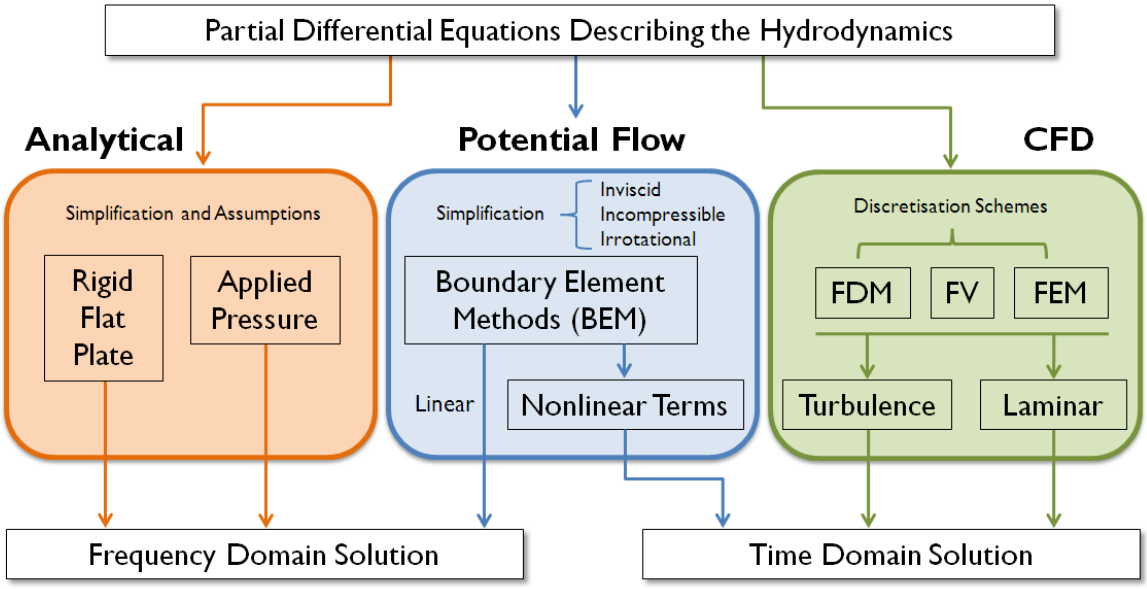

Figure 7.2, Theoretical modelling approaches for OWCs modified from Hals (2010).

7.5.2 Analytical Models

Following on from the leading work of McCormick and Masuda on OWC navigation buoys in the early 1970s, Evans (1978) conceived and presented the idea of a thin, rigid plate to model the system. The dynamics of an OWC were approximated by an oscillating, flat plate representing the free surface of the water column. Adapted directly from the theory of rigid heaving bodies; this approach is directly analogous to a mechanical mass-spring-damper type system. The free surface is assumed to be a rigid plate, with the water volume of the chamber, included in the added mass terms, oscillating under the influence of spring and damping terms, as summarised by Figure 7.3. The power entering the air chamber is therefore the product of the

net force acting on the plate and its vertical velocity. The model is limited to idealised cases where the horizontal dimension of the water column is short in comparison to the wavelength therefore, implying relatively little variation in the internal free surface profile.

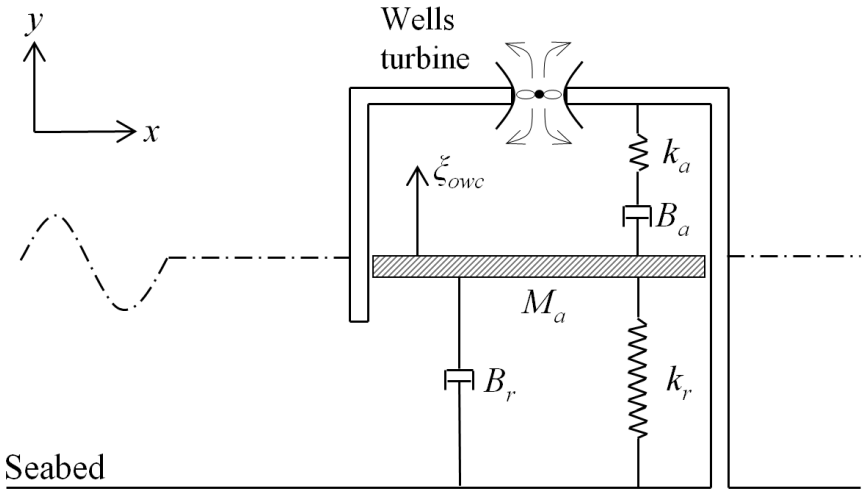

Figure 7.3, The idealised spring-mass-damper system of an OWC for theoretical models.

The fundamental equation governing this model is a description of the forces applied to the thin, rigid plate:

- Forces due to the incident and diffracted waves, $F_d(t)$.
- Hydrodynamic forces from the radiated waves generated by the motions of the plate, $F_r(t)$. This comprises added mass and radiation damping terms.
- Hydrostatic forces from the hydrostatic pressures of the water column.
- Applied force due to the pressure differential across the PTO.

This can be written as a generalised form of a linear, second order, differential equation for a mass-spring-damper system;

$$m\frac{d^2\xi_{owc}}{dt^2} + B_a\frac{d\xi_{owc}}{dt} + (k_a + k_r)\xi_{owc} = F_d(t) + F_r(t) \qquad [26]$$

Where the force term is separated into two components; one due to wave diffraction (excitation force from the waves with the plate held statically), $F_d(t)$ and the other from wave radiation, $F_r(t)$ (the force due to the oscillation of the plate in an undisturbed fluid). Here, ξ_{owc} is the displacement of the plate, m is the mass of the thin rigid plate, B_a is the applied damping coefficient from the air within the chamber and PTO, B_r is the radiation damping, k_r is restoring coefficient and k_a is the applied, air spring constant which is the stiffness of air. In many of these simple, OWC models, air is assumed to be incompressible and so implying that the stiffness of air is infinite, $k_a = \infty$.

Later, Evans (1982) commented on the limitations of the rigid plate model and extended his theory by introducing the concept of a variable, oscillatory, pressure distribution at the interior,

free surface of the chamber. In this modified model, the power entering the air chamber is the product of the net volume flux of the interior water surface and the air pressure in the chamber. Unlike the rigid plate model, which requires the free surface to be flat, this model allows for spatial variations of the surface and so is applicable to shorter waves. This theory and most subsequent models are commonly known as the 'applied pressure' or 'pressure distribution' models. These assume that the pressure at the air-water interface is equal to the air pressure, p_a.

These early analytical methods were developed further by Falnes and McIver (1985) to provide a generalised theory, applicable to other systems of oscillating bodies. Greater attention is paid to the internal, oscillating pressure and variations of the free surface in the 2D theory for a simple geometry presented by Sarmento and Falcão (1985). Comment is also made upon the spring-like compressibility of the air within the OWC chamber at large scale and a linearised term to represent these effects was reported. More recently, Brendmo *et al.* (1996) presented some additions to the rigid plate and applied pressure models to include some account of the viscous and frictional losses present in the system. Analogies between these models and mechanical and electrical systems are also suggested along with experimental techniques to approximate the added loss parameters for a 2D OWC.

Whilst these simple, analytical models cover the key features of the behaviour of an OWC, they have limited applicability to real, 3D devices. After reviewing these methods that have developed over the past four decades, little synergy was found between the simplified operating principle of an OWC and that of OWEL. The forward advancing wave front, contained within the duct of the device could be likened to a piston moving with a velocity similar to the deep water wave celerity but tending to the shallow water limit of $\sqrt{gd}$. The variability of the internal wave speed due to shoaling effects and the exchange of kinetic energy within the wave to the air, has been shown in the experiments reported in section 6.5.4. With knowledge of the volume of entrained air ahead of the wave front, an estimate of the airflow rate through the PTO could be made and would provide an approximate order of magnitude result. This however, would likely be similar to the previously developed mathematical model and would be of limited use. The importance of the intricacies of the complex physics within the fluids necessitates the requirement for a more detailed model.

7.5.3 Linear Potential Flow Theory

A current, standard approach for the modelling of OWCs is by the use of panel methods to calculate the hydrodynamic parameters of a geometry from the solution of the velocity potential over the wetted boundaries of the body and fluid. As the name of the theory suggests, the

characteristics and responses of the models implementing these methods are linear. An exception to this, which will be discussed further, is the ability to include some small non-linear terms by solving the problem in the time domain. A number of assumptions and limitations are typically imposed;

- Incompressible fluid.
- Inviscid – fluid has no viscosity,
- Irrotational flow
- Small amplitude waves.
- Small amplitude motion of the floating body.

Using a Boundary Element Method (BEM) only the boundaries of a potential flow model are discretised and the linear partial differential equations solved for each element. Solutions for the velocity potentials over the boundaries are used to determine the pressure at each panel which can be integrated over the surface to determine the total body force. A keynote review paper by Newman (1992) provides a comprehensive review of the basic principles of BEM panel methods for marine applications.

A wide variety of commercially available BEM codes are in existence however, only a few have been modified to make them suitable to be applied to OWCs. A recent review by Sarmento (2010) provides a comprehensive overview of such modifications in applications of BEM to OWCs. Additionally, an in depth review of theoretical models for OWCs is given by Cruz (2008).

Solving a potential flow model in the frequency domain provides the most computationally efficient results but is restricted by the assumptions imposed on it. The model comprises two discrete parts; a diffraction part where the body is static within the incident wave field and a radiation part where the body is forced to oscillate in still water. The sum of the diffraction and radiation potentials yields the total velocity potential which takes into account the exciting forces from the incident waves and the hydrodynamic added mass and damping of the body. From the velocity potential and coefficients, the RAOs and body motions can be determined. This approach tends to be the most common for OWC problems. One of the first applications to an OWC was an early use of WAMIT™, a three-dimensional panel method, with a low order method, [Lee *et al.* (1996)] to study a simple OWC. Two regions of resonance were noted; a low frequency mode with the free surface acting as a ‘piston’ and a high frequency ‘sloshing mode’, although the results were not validated by experiment. Perhaps the simplest of OWC problem is that of a static device. With the construction of a number of static OWCs at around the turn of the century, various subsequent numerical studies of these types of device were presented. Brito-Melo *et al.* (2000) were the first to implement the 3D, radiation-diffraction

boundary element code, AquaDyn and simulated the Pico OWC with its bathymetry using linear wave theory. Following this study, Delauré and Lewis (2003) modelled a similar, shoreline OWC using WAMIT and compared their results to experiments and against an independent approximate potential flow model. A good level of agreement between the three sets of results was achieved particularly in small amplitude waves and with an open chamber. More recently, attention has been drawn to breakwater OWCs of which a number of examples have been planned [Martins *et al.* (2005)] or built [Torre-Enciso *et al.* (2009)] in the past decade. Pontes *et al.* (2005) used WAMIT to model the proposed OWC breakwater at 'Foz do Douro' in Portugal. A vast range of site specific wave conditions and directions were used in the modelling to predict power output for two different directionality regimes. Boccotti (2007) created a model to study a U-shaped OWC arrangement for deployment as a breakwater in the Mediterranean. The results from the modelling were then validated by small scale physical results in Boccotti *et al.* (2007) showing that the BEM model compared well to the experimental data.

Frequency domain solutions can quickly determine the hydrodynamic coefficients of a particular geometry such as the added mass, radiation damping and incident wave forces and can be a useful tool in the early development of WECs. However, as geometries become more complex and the requirements of the model change to investigate more realistic scenarios, non-linear effects can comprise significant portions of the model. In these instances, their impact on the model must be taken into account and so a time domain solution can be implemented to incorporate some of these phenomena.

The modification of potential flow codes such as WAMIT and AquaDyn to model the behaviour of OWCs has meant that the use of these tools has been fairly limited. The majority of studies have been conducted using linear, frequency domain methods and only a couple of examples exist where time domain models have been implemented. Solving in the time domain allows for the inclusion of non-linear terms into the equations of motion of the body. These may include for example non-linear PTO systems or control systems. As the problem is solved at each time step, it is particularly appropriate for the testing of control algorithms, although these experiments have only been used in the study of hydrodynamically simpler, point absorber WECs such as SEAREV [Josset *et al.* (2007)].

A novel approach was taken by Josset and Clément (2007) to develop a BEM code called ACHIL3D, to model the Pico OWC in the time domain. The method split the internal and external problems into two and solved each separately. The model allowed the dedicated analysis of the air within the chamber and its dynamics with a Wells turbine and control valve. Although this provides significant advantages and accuracy over simpler, frequency domain

models, it does not account for the non-linearities in the free surface of the water column and so is restricted to idealised cases.

Further complications in modelling an OWC arise when floating dynamics and non-linear mooring forces are considered. The solution of the problem at each time step means that these models are typically computationally expensive and so it has only been in recent years, since the development of faster computing, that floating OWC models have become practical. Kurniawan *et al.* (2011) presented two similar models of a floating Backward Bent Duct Buoy (BBDB), one in the frequency domain and the other in the time domain. Although the time domain model is still under development, body motions and converted power were presented. Comment was made on the long run times of the time domain model and its computational expense.

Whilst the time domain solution of potential flow models allows for the addition of non-linear, external forces, it does not cover non-linear hydrodynamic forces: Considering the water flow around small structures during breaking of waves for example, the flow becomes strongly rotational and therefore the irrotational assumption of potential theory is invalid. Furthermore potential theory collapses in extreme wave conditions and shallow water regions due to the significant non-linearity of waves in such cases. In resonance situations, where the incoming frequency of the waves is similar to the natural frequency of the WEC, the displacement amplitudes of the device become much larger than in normal operation. For those large amplitudes, the small motion assumption of linear theory is invalid.

For the modelling of other WEC types, work has been carried out to develop improved potential flow theories with added terms to represent some viscous, vortex shedding effects [Folley *et al.* (2007)] and hybrid methods to enable the modelling of large amplitude body motions [Gilloteaux *et al.* (2007)]. These improved models have not yet been extended to include OWCs and so will not be discussed further. For cases where a fully non-linear, viscous solution is required, a model that solves the full Navier-Stokes equations should be implemented. Codes that solve these equations are commonly referred to as CFD solvers.

7.5.4 Computational Fluid Dynamics

For many OWC cases, where simple geometries need to be optimised or power estimates made, potential flow approaches in either the frequency or time domains may be sufficient. For realistic scenarios however, a more complex approach such as CFD may be required to provide the necessary accuracy and resolution of flow physics in the results. Unlike potential flow models, which solve at the fluid and geometry boundaries, the entire fluid domain in CFD models is discretised and a full set of nonlinear, partial differential Navier-Stokes equations are

iteratively solved throughout; see Anderson (1995) for additional background information. This method accounts for mass, momentum and energy conservation within the fluid and consequently is far more computationally demanding than the potential flow methodology. The financial and computational expense of CFD models, particularly for wave energy applications, has meant that their use in modelling OWCs has been limited. In recent years, as computational costs have reduced and processing speeds have increased, the possibility of CFD modelling has become far more reachable in many research and development projects. The change in computing resource has been coupled with the realisation from commercial CFD code developers that their software could be of benefit to the marine industry. Off-the-shelf CFD packages now offer built in user functionality to create wave input boundaries, wave absorption regions and even the possibility to incorporate 6 DoF, rigid body motions. ANSYS FLUENT™, for example, has been recently used in a number of projects to model OWCs: In a study by Marjani *et al.* (2006), a relatively simple, static, shoreline OWC was modelled using FLUENT with a linear, porous loss region used as a turbine simulator. The model was simplified as the input to the water column was defined as an oscillating base rather than a true wave input. This model was further developed in Marjani *et al.* (2008) with the inclusion of a moving impulse turbine connected to the air outlet of the OWC. This employed a sliding mesh to simulate the motion of the turbine. Numerical results were compared with experiment and show a reasonable level of agreement. A similar study was conducted by Horko (2007), but included the full fluid domain in order to model a Stokes 2nd order nonlinear wave regime. The CFD results were compared with small scale, experimental test data and classic oscillating plate theory. Whilst the OWC theory over predicted performance, the efficiencies from the physical and CFD models were comparatively similar. Another FLUENT based model by Paixão Conde and Gato (2008) was used to investigate the air velocity gradients and spatial distribution at the turbine. A geometry alteration was designed using the model to prevent the generation of water spray from the inward flow, which would otherwise be detrimental to the turbine. Other similar, static, shoreline OWCs have also been modelled in FLUENT, for example a series of studies by Liu *et al.* (2011), Liu *et al.* (2010a), Liu *et al.* (2010b) and an initial investigation by Şentürk and Özdamar (2011).

The necessity of using viscous models for OWCs has been highlighted by independent experimental studies by Morrison and Greated (1992) and Müller and J.T. Whittaker (1995) and CFD studies by Alves (2005) and Zhang *et al.* (2012). The results from each of these investigations have all shown the formation of significant vortices in the water at the lip of the entrance to OWCs. Morrison (1992) estimated that around 8% of the total energy of the incident wave was contained within the vortex shed from the lip and therefore subsequently lost. Further to this, visualisation of oscillating flows in a tube containing a water column excited by regular

waves by Knott and Flower (1980) and Knott and Mackley (1980) have shown the significant formation of vortices at edges of the geometry. These vortices are an indication of undesirable energy losses and would not be captured by potential flow models.

An early comparison of the suitability of two commercial CFD codes for the modelling of surface water waves was made by Westphalen *et al.* (2007). A 35 m long Numerical Wave Tank (NWT) was modelled in Star-CCM+ and ANSYS CFX and the waveforms were compared as they propagated along the domain. Both solvers were shown to be capable of modelling water waves in the simulations although a degree of 'numerical diffusion' was observed as the wave height was damped as the crests progressed. It was also reported that the run time of the CFX model was around 20 times that of the STAR-CCM+ model, although this was attributed to the computational resource available. A further comparison study by Aggidis and Mingham (2009) was made between CFX, FLOW-3D and STAR-CCM+ incorporating the WRASPA device; a surging point absorber. The abilities of these packages to model water waves and wave-structure interaction were compared in terms of accuracy and robustness. At that time however, STAR-CCM+ was not capable of excessive mesh deformation in surge and so was not considered. Similarly to the study by Westphalen *et al.* (2007), issues were encountered with the model created in CFX:

- A high level of wave height dissipation was recorded, which provided difficulties in determining the wave height at the device.
- Wave reflection from the domain outflow was problematic and unwanted waves travelled back towards the device.
- Long run times were observed although the solution was being run on a comparatively low specification, desktop system rather than a dedicated HPC.
- Issues with model set up and meshing were also reported as the device protrudes above the free surface, through the prism inflation layers of the grid.

It was concluded that FLOW-3D was preferred solver for the simulations as it provided the modelling capabilities required without the drawbacks of CFX. Bhinder *et al.* (2009) continued the modelling using FLOW-3D and found that the code provides significant advantages over many other standard methods; the regular mesh is fixed and does not deform, instead the solver computes the position of the body within the mesh, much like a volume fraction technique. This avoids the complex process of mesh deformation with the motion of the body and aids in the reduction of computational time. In addition, the air phase of the domain can be modelled as a void at atmospheric pressure, meaning that the air is not solved for, again increasing computational efficiency; this however, would not be a useful feature for the modelling of OWCs or OWEL.

7.6 Development of a Preliminary CFD Model

From the review of the various modelling options for OWCs it can be seen that analytical and potential flow approaches for modelling OWEL would be of limited use. Neither of these methods would take much of the flow physics dominating the internal wave into account. It is therefore likely that such models would not accurately represent the behaviour of the internal wave and therefore would incorrectly model the energy conversion. It was concluded that CFD is the most suitable method to model OWEL as it is able to solve the effects important in the energy conversion cycle and internal wave.

A preliminary CFD model was set up to simulate the physical model tests of the single, static duct from the Lamont towing tank. This investigation was intended to examine the suitability of CFD to model OWEL and begin to develop the methodology that could be used by subsequent studies. It was, therefore, expected to provide a starting point on which further work could be carried out and make suggestions to improve the agreement between the physical and computational models.

The commercial CFD package, ANSYS CFX 13.0 was selected as a suitable code to create a preliminary model of OWEL. CFX is a coupled finite volume RANS solver that uses a Volume of Fluid (VOF) method to model multiphase fluids, such as an air-water interface. Further information on the theory and methodology of the solver can be found in the product documentation [ANSYS (2010)]. This software was chosen for a number of reasons; the previous CFD studies, as reviewed in section 3.3.4, used an early version of CFX-5 and so there was some pre-existing knowledge within ITP about the setup of the model and boundary conditions. Furthermore, the University of Southampton had approximately 50 ANSYS CFD licences available and a further 200 dedicated High Performance Computing (HPC) licences for use on their IRIDIS computing cluster. This allowed the simulations to be run on between 4 and 12 processors on a single computing node, depending on the licences and resource available. The development of a rigid body, moving mesh model to allow floating motions to be modelled was deemed beyond the scope of this initial work. At the time, it was noted however, that ANSYS CFX had this functionality and so further, future development of the CFD model could incorporate this. Since the completion of this initial modelling, Mojo Maritime, a consortium partner company in the OWEL TSB project, have continued the development of this model in conjunction with ANSYS. This has used a methodology incorporating the learning and boundary conditions that were achieved through the development of this model. In addition, rigid body motion has been included into the model to allow vessel motion in 3 DoF to be modelled with representative mooring characteristics.

7.7 Boundary Conditions

Two methodologies are typically employed to generate waves at a boundary in CFD; either a motion is applied to the domain boundary set as a wall to act as a wave maker [Maguire and Ingram (2009)] or the fluid motion at the domain boundary can be prescribed [Westphalen *et al.* (2007), Horko (2007)]. The work by Maguire provided a good example of a moving domain wall to generate waves and this concentrated on applying wave maker theory to correctly specify the waves. A disadvantage of this method is that a region of the mesh in the fluid domain is required to deform as the solid wall moves. This can therefore introduce additional complexity to the model and increase the computing time required to solve each time step due to the addition of the mesh deformation calculations.

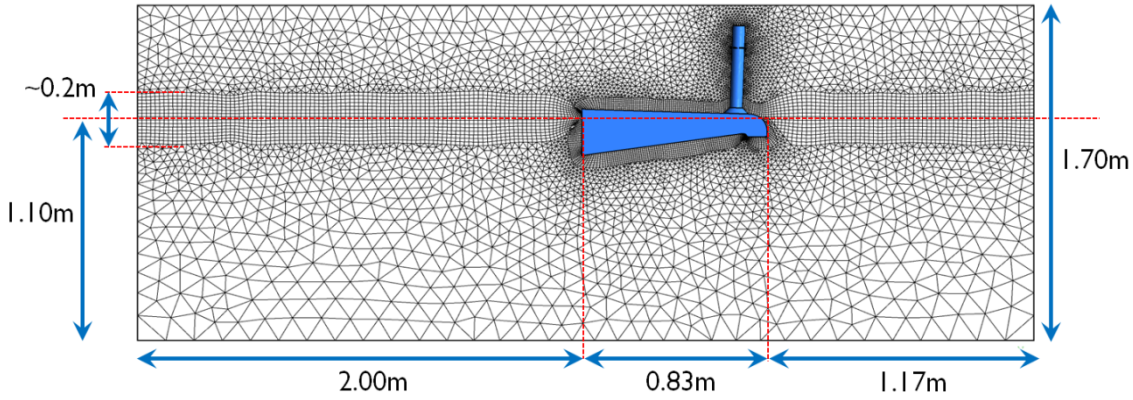

Figure 7.4, The principal dimensions of the domain, showing the position of the model and location of the SWL.

Both of the wave conditions that were tested were found to have non-linearities, see the wave type graph in Figure 2.1, particularly due to their 'steepness' factor (H/gT^2). This meant that Stokes' 2nd order theory was the most suitable wave theory to represent these wave conditions and the majority of the conditions used throughout the physical modelling. The horizontal and vertical velocities within a Stokes' 2nd order wave are defined in equations [27] and [28]. These were applied as the Cartesian velocity components at the wave generating boundary of the domain,

Particle velocity *x* direction (horizontal)

$$u = \frac{\pi H}{T}\frac{\cosh k(d+z)}{\sinh kd}\cos(kx-\sigma t) + \frac{3(\pi H)^2}{4TL}\frac{\cosh 2k(d+z)}{\sinh^4(kd)}\cos 2(kx-\sigma t) \qquad [27]$$

Particle velocity *z* direction (vertical)

$$w = \frac{\pi H}{T}\frac{\sinh k(d+z)}{\sinh kd}\sin(kx-\sigma t) + \frac{3(\pi H)^2}{4TL}\frac{\sinh 2k(d+z)}{\sinh^4(kd)}\sin 2(kx-\sigma t) \qquad [28]$$

Where H = wave height [m], T = wave period [s], d = mean water depth [m], z = vertical co-ordinate [m], x = horizontal co-ordinate [m], L = wavelength [m] and t = time [s]. When plotted,

these particle tracks are circles below the wave crest with a radius that decreases with increasing depth.

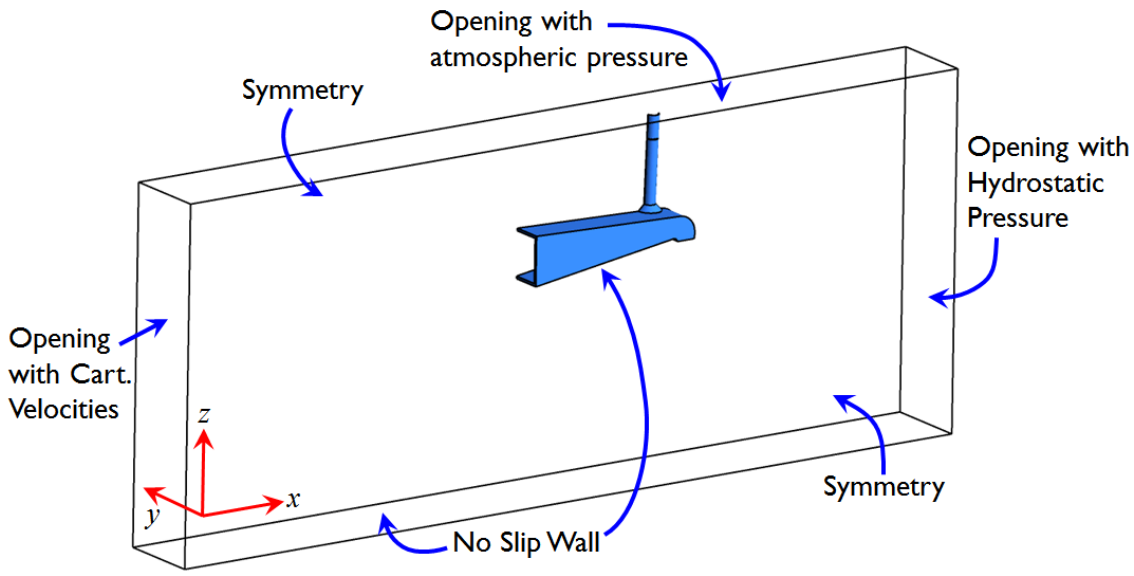

Figure 7.5, A summary of the boundary conditions for each of the six faces of the fluid domain and the co-ordinate system used.

The circular motion of the water lead to inward and outward flow across the domain boundaries; for this reason, the 'inlet' and 'outlet' of the domain were set as openings. This allows the bi-directional fluid flow as the fluid is presented with a predetermined hydrostatic pressure distribution rather than a uni-directional boundary condition. Additionally, CFX also requires the volume fraction, the ratio of air to water, to be set at the opening boundaries. For the inlet, the wave free-surface profile for a Stokes 2nd Order wave, ξ, as defined in equation [8], was used to specify the vertical distribution of volume fraction at the boundary for each time step. At the outlet the still water depth was used in equation [29] to calculate the hydrostatic pressure distribution with respect to the z position in the water column.

$$p(z) = \rho g z \qquad [\mathbf{Pa}] \qquad [29]$$

Where ρ = density of water [kg.m^{-3}], g =gravitational constant [m.s^{-2}].
Setting the side boundary opposite the geometry to be an opening with a hydrostatic pressure distribution proved problematic as the distribution changed with the oscillating free surface elevation. This led to the solver expecting a hydrostatic pressure at the boundary that was different to the pressure that occurred as a result of variations in the surface elevation. As a result, the free surface profile was modified at the side boundary which meant that the wave height was not uniform across the domain width. Both of the side boundaries of the domain were therefore set as symmetry planes and this issue was alleviated. The top boundary of the domain was defined as an opening with the pressure set equal to atmospheric pressure. The bottom boundary of the domain and the model geometry were all set as 'no slip' walls.

Westphalen and Maguire had both experienced issues with waves reflecting off the outlet, opening boundary of the domain and had suggested that a way to reduce this effect was to progressively coarsen the mesh towards this boundary. This was in order to gradually introduce errors in the fluid calculation across that domain region in order to "numerically diffuse" the water velocity. Whilst this was reported to work well in their models, it increases the domain size and mesh elements required. As an alternative therefore, a subdomain was included within the fluid domain that included additional momentum source terms to reduce the momentum of the flow within it. The subdomain region was the final 1m section of the domain, downstream of the model geometry. Negative momentum source terms were specified for the *x* and *z* directions and the magnitude of their coefficients was increased quadratically as shown in Figure 7.6. This was intended to introduce these loss terms in a gradual manner to prevent reflections from occurring off rapid changes in velocity. This method was based on initial advice by ANSYS and further developed through test runs in a 2D domain to determine the suitable momentum source coefficient and characteristics of the function.

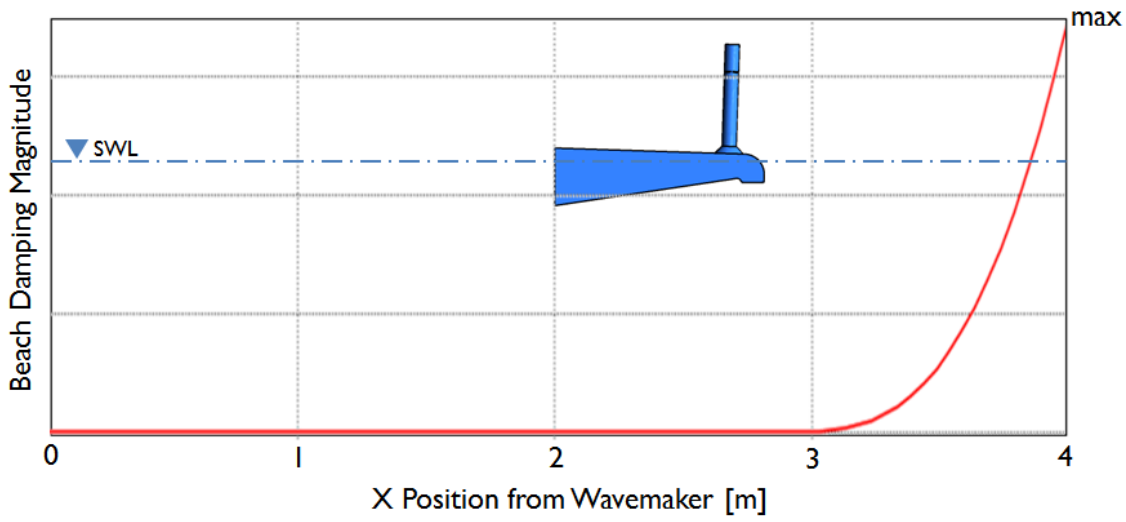

Figure 7.6, Magnitude of the momentum loss term for the numerical 'beach' applied over the last metre of the domain length.

7.8 Mesh and Time Step

The mesh and time step for this preliminary model were based upon the methodologies in the work by Westphalen *et al.* (2007) and Maguire and Ingram (2009), who had also used CFX to model water waves. An unstructured, quadrilateral and triangular mesh was used for the 'far field' of the fluid domain away from water free surface and model geometry. This was coarsened by an expansion factor of 1.2 away from the regions of mesh refinement. In order to better resolve the water free surface, a prism mesh with hexaheadral and quadrilateral elements was used. This was 'grown' from a surface that was at the still water level and the prism layers were extended to +/- 0.10 m from SWL. This was sufficient to capture the free surface elevation

of any of the wave conditions tested in the physical modelling in order that changes in mesh would not be required if larger waves were to be tested at a later date.

The coarsest mesh tested by Westphalen *et al.* (2007) had 3 elements per H whereas for the finest, this was increased to 6 elements per H. It was observed that at least 3 cells should span the wave height in order to resolve the free surface. Maguire and Ingram (2009) however, had a minimum of 8 cells per H in the coarsest mesh and used an aspect ratio of $1\Delta z : 2\Delta x$ in the prism region. The prism mesh used in this model comprised 15 element layers with a mesh size of Δx = 19 mm and Δz = 13 mm was used and is shown in more detail in Figure 7.7. There were 20 elements across the 0.4 m span of the domain, therefore the prism element Δy = 20 mm.

This aspect ratio meant that for the smallest wave height tested, 55mm, there were approximately 4 cells per H and 105 cells per L. It was acknowledged at the time that this was coarse and would likely not be suitable for use with smaller waves. Further work by Maguire (2011) that was published after this modelling had been completed, recommended that the free surface prism layer should have 200 cells per wavelength and 40 cells per wave height. This is far greater than was included for this model and so should be investigated in subsequent work.

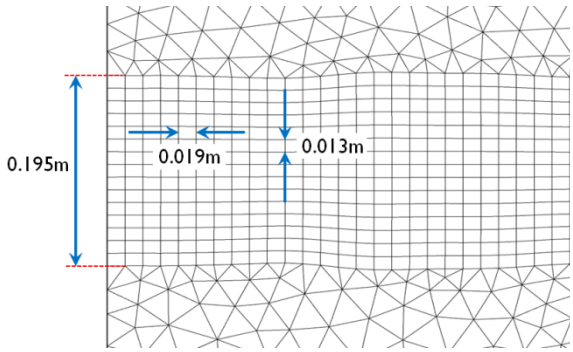

Figure 7.7, Detail of the free surface prism mesh.

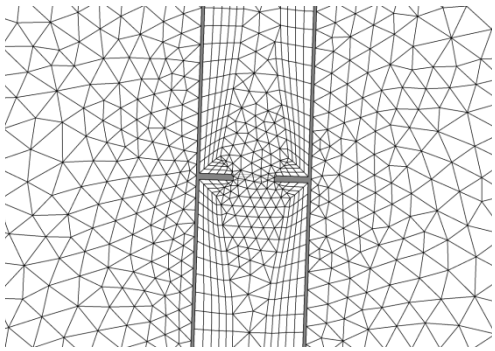

Figure 7.8, The mesh region around the orifice in the air exit tube.

A similar, but finer, prism layer expansion was also applied to the surfaces of the model geometry to provide a better refinement of the free surface and fluid interaction at the boundaries of the structure. The internal region within the duct was filled with an unstructured mesh with a maximum cell size of 10 mm. This was intended to suit any of the model geometries and prevent the need for complex meshing strategies. An example of the mesh surrounding the model geometry is given in Figure 7.9.

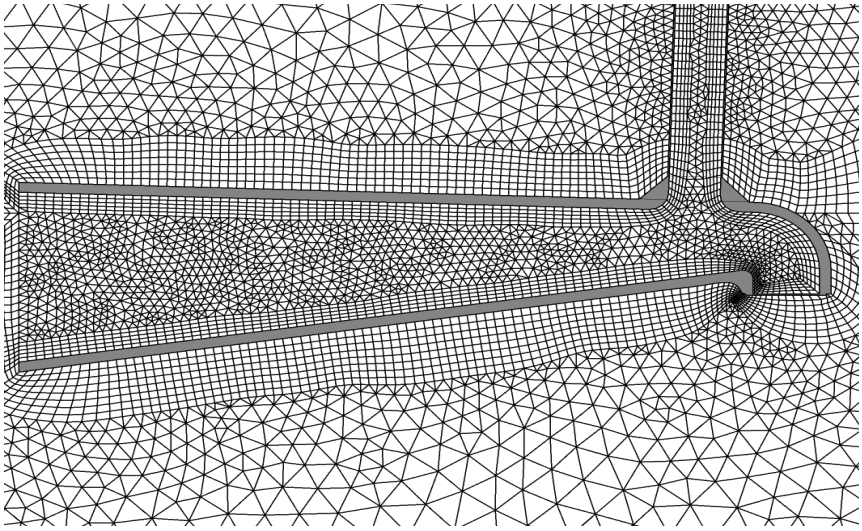

Figure 7.9, The mesh surrounding and within the geometry for the optimised model configuration.

The PTO in the CFD geometry was modelled by an orifice with the same dimensions as on the physical models, with a diameter of 20 mm. Similarly to the regions surrounding the model geometry, prism layers were included within the PTO tube for the exiting air and in the vicinity of the orifice plate. Mesh refinement was also included in the vicinity of the orifice with a maximum cell size set to 5mm. An example of the mesh region is shown in Figure 7.8.

Three different OWEL geometries were tested in the CFD model; the first was the baseline geometry that was reported in section 6.5.4, the second was the optimised geometry that featured a 7.5° base plate and parallel side walls, as detailed in section 6.6.7. The final geometry that was tested was a new geometry that had not been tested in the physical modelling investigations. This was the same as the optimised duct but had the baffle opening at the stern sealed off to prevent the inflow and outflow of water. This was intended to further investigate the observations made in section 6.5.4 that the water flow into and out of the duct at the stern was necessary for efficient operation and suggest whether this effect required additional testing. The mesh arrangements for the three different model configurations are shown in Figure 7.10 to Figure 7.12 and the summary statistics of the mesh are given in Table 16.

Table 16, A summary of the mesh statistics for the three model geometries.

Configuration	# Nodes	# Elements	# Tetrahedrons	# Prisms
Baseline	221,025	740,144	487,088	247,967
Optimised	278,784	978,719	681,337	290,678
Closed Baffle	253,696	832,375	534,407	292,943

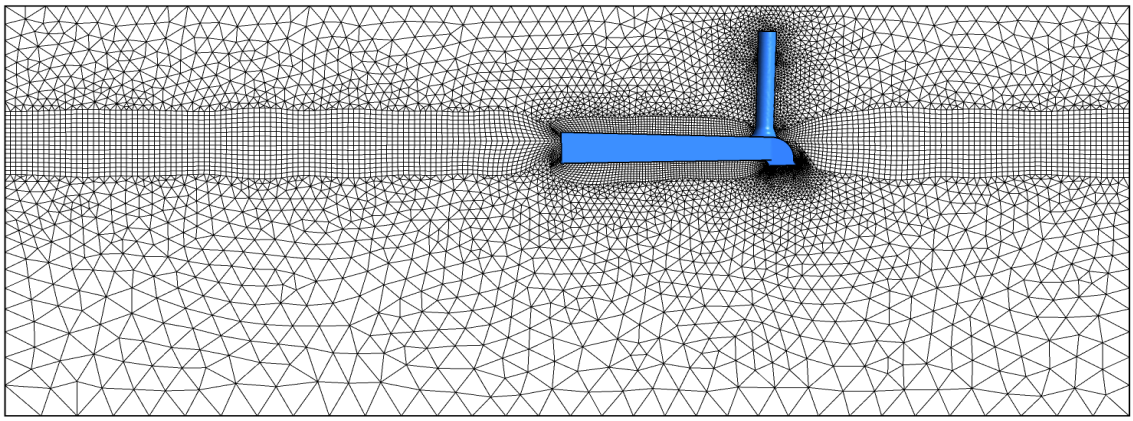

Figure 7.10, A slice of the mesh for baseline geometry taken down the centreline of the duct.

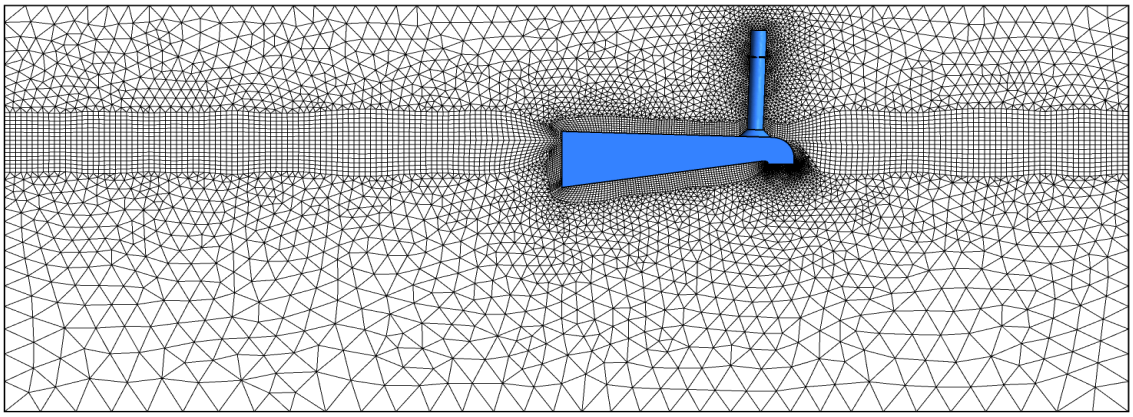

Figure 7.11, A slice of the mesh for new, optimised geometry taken down the centreline of the duct.

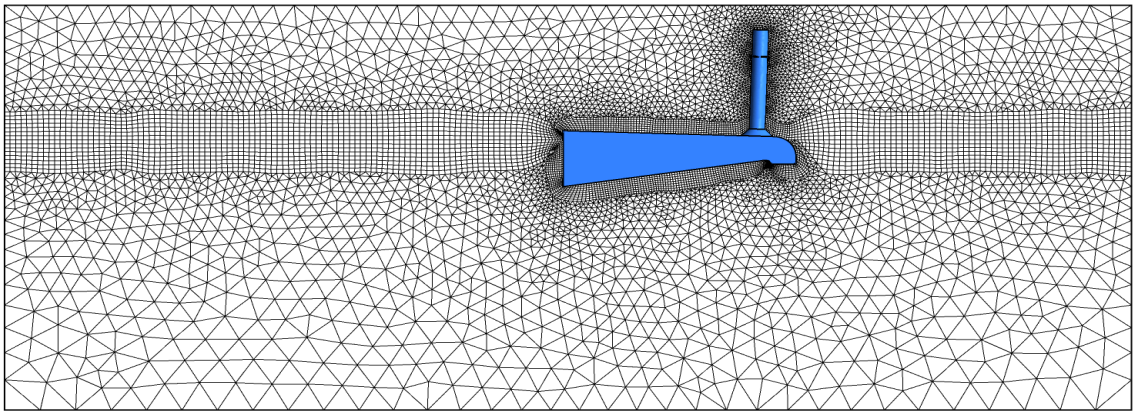

Figure 7.12, A slice of the mesh for closed baffle geometry taken down the centreline of the duct.

A constant time step of 0.01 s was used for all of the simulations run. Whilst no time step optimisation studies were carried out, this time step was estimated to be suitable to capture the majority of the flow effects, particularly those in the undisturbed wave field. Maguire and Ingram (2009) recommended that for a numerical wave tank, the Courant number, as defined for two dimensions in equation [30], should be between 1 and 2.

$$C = \frac{u\Delta t}{\Delta x} + \frac{w\Delta t}{\Delta z} \qquad [30]$$

Where C = Courant number, $u = x$ velocity [m.s^{-1}], Δt = time step [s], $w = z$ velocity [m.s^{-1}]. Maguire recommended that the wave phase speed (see equation [2], section 2.3.1) be used as the maximum u velocity rather than the maximum particle velocity. The longest period wave tested (T = 1.47 s) had a phase speed of 2.23 m.s^{-1} and a maximum particle velocity of 0.196 m.s^{-1}. Taking the phase speed as u, maximum particle velocity as w, Δt as 0.01 and mesh sizes as those in Figure 7.7, gives a maximum Courant number, in the undisturbed wave field, of ~1.32, which is within Maguire's suggested range.

Recommendations made by ANSYS were used for many of the solver control options such as a High Resolution advection scheme and Second Order Backward Euler transient scheme. A default value of 5 % turbulence intensity was used at the wave generating boundary. The standard k-ε turbulence model was used throughout the fluid domain of the model and was chosen due to its general applicability to a range of fluid dynamics problems. Furthermore, Marjani *et al.* (2006), Zullah *et al.* (2010) and Liu *et al.* (2011) used the k-ε model in their CFD simulations of OWCs.

The solutions were deemed to have converged once the RMS of all scaled residuals were less than 10^{-4} or after a maximum number of 10 coefficient iteration loops. By the time the simulation had progressed approximately half way through, these convergence criterion were being achieved with all RMS residuals being less than 10^{-4}, requiring 3 – 6 iterations per time step. The maximum residuals for mass and momentum typically peaked at approximately 0.01, with the V momentum having the greatest residual. This is likely to be a result of the vertical airflow through the orifice not being accurately solved.

All of the models were run to simulate a total of 15 seconds of real time which was sufficient for at least 8 wave periods to be generated and pass the duct. Results were output from the simulation at a frequency of 20 Hz. A typical run took between 53 and 60 hours to complete on 4 processors with a total of 1500 time steps. The range of solution times was due to the variations in the number of elements in each of the model configurations.

7.9 Results

To test the model, two wave test cases were run for three different duct geometries. The test runs were chosen so that physical modelling data was available for comparison and validation.

The air power developed was measured using the same methodology as described in section 3.6.1 and the pressure was measured either side of the orifice plate at each data output interval.

It was assumed that the C_D value of the orifice was the same for the CFD model as it was for the physical tests.

7.9.1 Waves

The properties of the two wave test cases that were trialled in the model are given in Table 17. These wave properties were used as input parameters to generate the wave profile and velocities used for the wave generation boundary of the domain.

Table 17, The input parameters of the two wave conditions run in each of the simulations for the three geometry configurations.

Test #	Period [s]	Height [mm]	Wavelength [m]	Wavelength / Duct Length
1	1.15	54.8	2.06	2.48
2	1.47	81.7	3.28	3.95

Westphalen and Maguire had both reported that wave height degradation in the CFX models was an issue as the amplitude was attenuated as the waves propagated along the domain. This effect was also observed in the results from these models and Figure 7.13 shows an example of the reduction. The data series "WP1" was monitored at a point 0.5 m downstream of the wave generation boundary. The second series, "WP3", was measured at a point 1.5 m beyond WP1 which was at the same x position as the duct entrance. The results for this wave case show a 15 % reduction in wave height after the wave had progressed by 0.75L. This meant that the actual wave height at the duct entrance had to be determined from the post processed data because the wave height, which was used as the input parameter, differed from the generated wave height. The wave height was therefore measured at WP3, adjacent to the duct entrance.

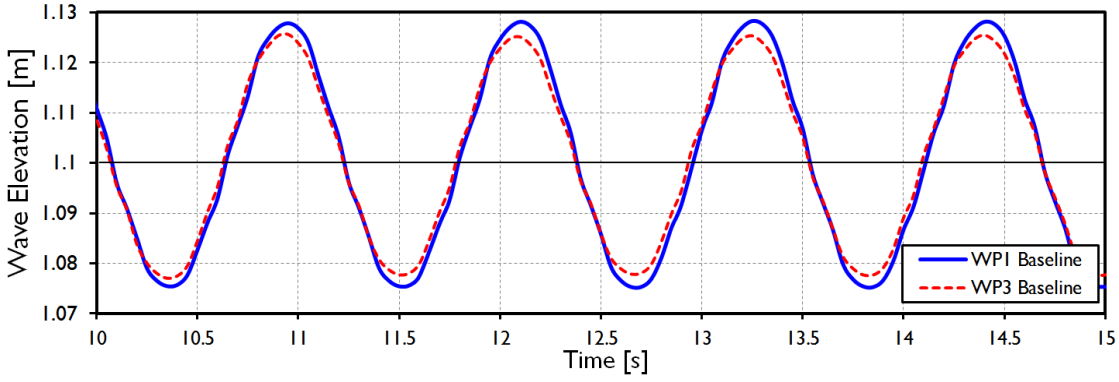

Figure 7.13, An example of the wave height attenuation after Wave #1 had propagated 1.5m along the domain.

7.9.2 Baseline Geometry

The measured wave height of wave #1 for the baseline geometry model run at the duct entrance was 50.4 mm and a comparison between the free surface elevation from the CFD and experimental models is given in Figure 7.14. This was a reasonable agreement however, the trough amplitude was less than the experimental observation meaning the CFD wave height was 4.6 mm smaller than intended.

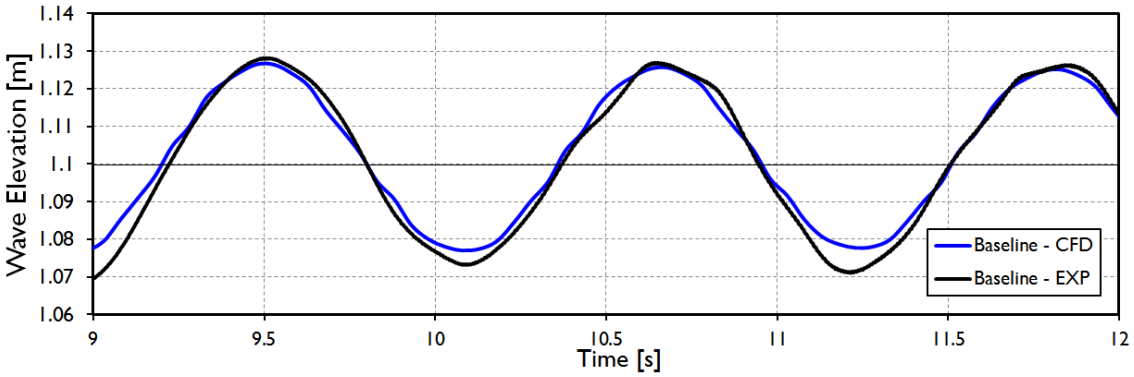

Figure 7.14, A comparison of the wave profiles from the CFD and experimental modelling, Wave #1.

The differential pressure drop across the orifice was modelled reasonably well as shown by the comparison between CFD and experimental data in Figure 7.15. Similar features are present in the two time series however, the CFD model generally over predicted the airflow.

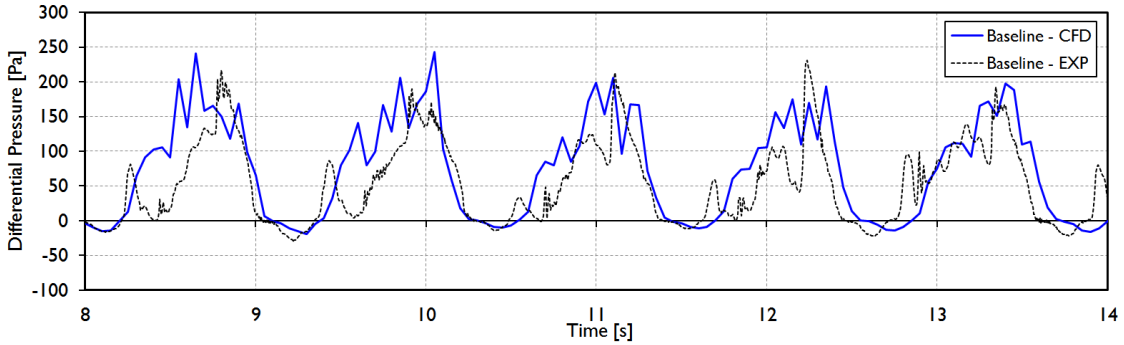

Figure 7.15, A comparison between the differential pressure drop across the orifice plate for the CFD and experimental models with the baseline geometry with Wave #1.

Unlike the case of Wave #1, the CFD model generated waves larger than the physical model for wave #2. Figure 7.16 shows a comparison of the two data sets with the average measured height at the duct entrance being 108.8 mm.

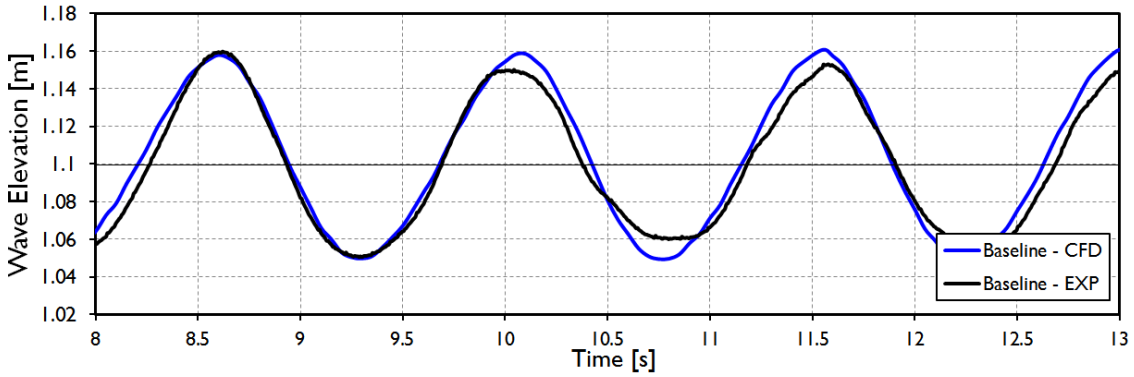

Figure 7.16, A comparison of the wave profiles from the CFD and experimental modelling, Wave #2.

The differential pressure across the orifice in the CFD model was far greater than the physical data, however, this was a result of the wave height being ~30 % larger. A comparison between the flow characteristics from the two models is provided in Figure 7.17.

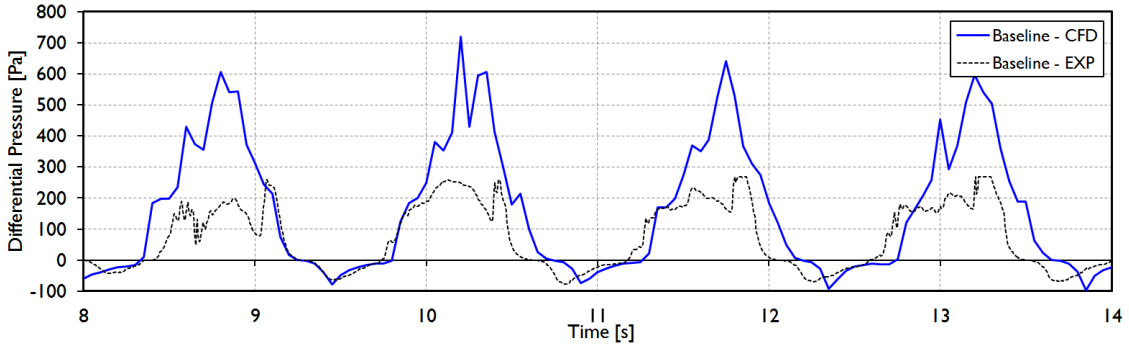

Figure 7.17, A comparison between the differential pressure drop across the orifice plate for the CFD and experimental models with the baseline geometry with Wave #2.

The average pressure drop, air flow rate and wave-to-pneumatic efficiency for the two wave cases from the CFD model are given in Table 18 with the equivalent efficiency values from the physical modelling for comparison. For these two examples the CFD model predicted the average performance of the baseline duct to be at least double that of the physical modelling results.

Table 18, A comparison of the measured performance of the baseline CFD model and the equivalent experimental efficiency.

Test #	Period [s]	Height [mm]		Mean dP [Pa]		Mean Q [m³/s]		Efficiency [%]	
		EXP	CFD	EXP	CFD	EXP	CFD	EXP	CFD
1	1.15	54.8	50.4	45.29	77.07	0.00137	0.00188	13.5	31.2
2	1.47	81.7	108.8	69.89	182.19	0.00166	0.00267	9.6	20.7

7.9.3 Optimised Geometry

In the model of the optimised geometry, wave #1 was similar to that of the physical modelling data, as shown in Figure 7.18, and the average height at the duct entrance was 56.2 mm which was only slightly greater than intended.

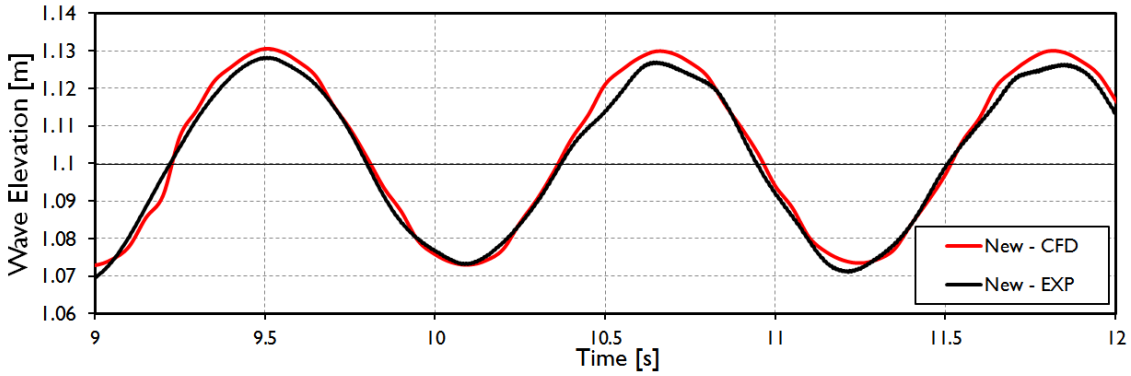

Figure 7.18, A comparison of the wave profiles for wave #1 from the CFD and physical experimental modelling.

The air flow through the orifice was also suitably modelled, with the CFD and physical results comparing well as Figure 7.19 shows. The peak differential pressures were similar however, the flow effects at the beginning of each wave cycle have not been captured by the model.

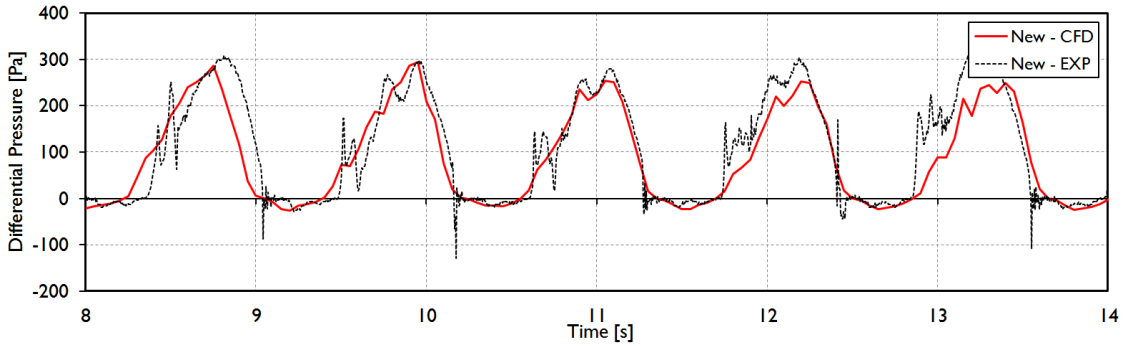

Figure 7.19, A comparison between the differential pressure drop across the orifice plate for the CFD and experimental models with the optimised geometry with Wave #1.

Similarly for the wave #2 conditions in the baseline geometry model, the wave height was far greater than expected for the optimised geometry. The average wave height at the duct entrance was 109.1 mm as can be seen in Figure 7.20.

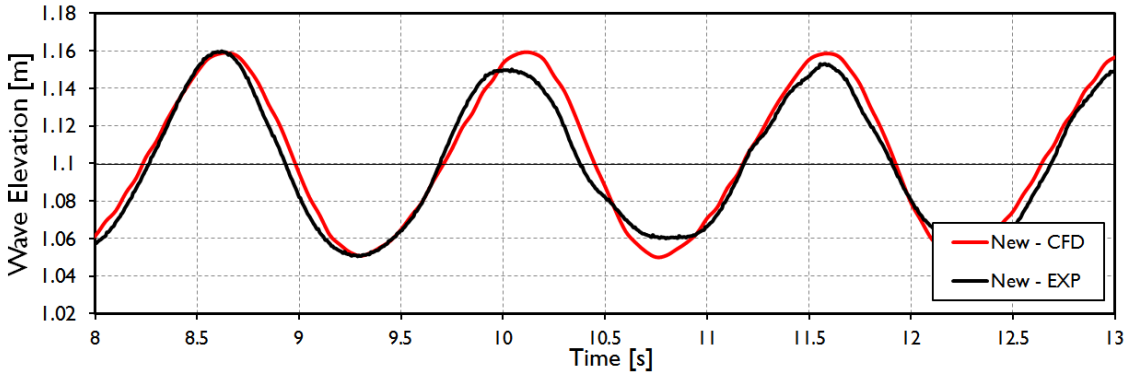

Figure 7.20, A comparison between the wave profiles at the duct entrance for wave #2 from the CFD and experimental modelling.

Comparing the differential pressure across the orifice for the CFD and physical models, in Figure 7.21, shows that the CFD model significantly over predicted the air flow. It is likely however, that this was partially due to the waves being higher in the CFD model than the physical model tests.

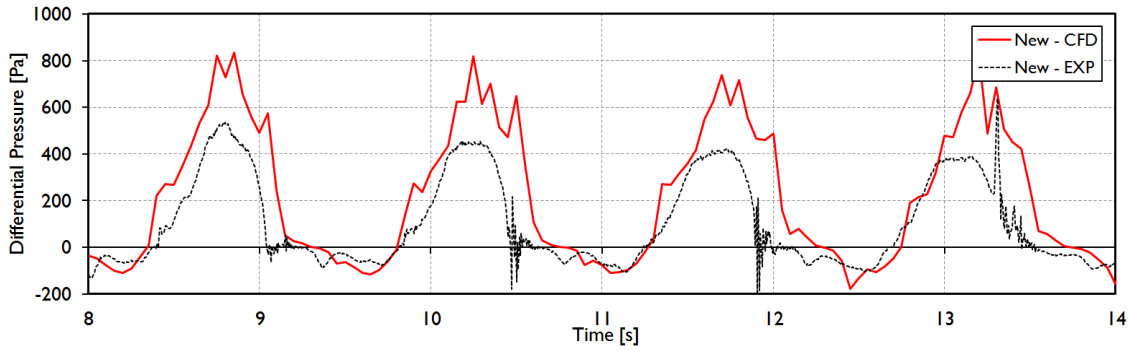

Figure 7.21, A comparison between the differential pressure drop across the orifice plate for the CFD and experimental models with the optimised geometry in wave #2.

The average pressure drop, air flow rate and wave-to-pneumatic efficiency for the two wave cases from the optimised geometry CFD model are given in Table 19 with the equivalent efficiency values from the physical modelling for comparison. Whilst the pressure differential for wave #1 appeared to be modelled reasonably well, the CFD model under predicted the conversion efficiency. For the second wave condition however, the CFD model over predicted the performance of the geometry.

Table 19, A comparison of the measured performance of the optimised geometry, CFD model and the equivalent experimental wave-to-pneumatic efficiency.

Test #	Period [s]	Height [mm]		Mean dP [Pa]		Mean Q [m³/s]		Efficiency [%]	
		EXP	CFD	EXP	CFD	EXP	CFD	EXP	CFD
1	1.15	54.8	56.2	113.06	98.78	0.0021	0.0020	51.4	38.1
2	1.47	81.7	109.1	125.33	255.47	0.0020	0.0032	23.9	33.7

7.9.4 Closed Baffle Geometry

Observations from the physical modelling, described in detail in section 6.5.4, postulated that the baffle water exit at the stern of the duct aided power capture through an OWC type effect caused by the difference in the locations of the internal and external wave crests. By sealing off the exit, CFD simulations were used to compare the flows of water and how this affected the device performance.

Figure 7.22 and Figure 7.23 provide comparisons between the CFD, with the closed baffle geometry, and the towing tank data for the wave profile measured at the duct entrance for wave #1 and #2. Similarly to the results from the two other CFD model configurations, wave #1 had an average wave height of 59.9 mm, similar to the expected height, whereas the average wave height of #2 was 111.9 mm which was much greater than the 82 mm input.

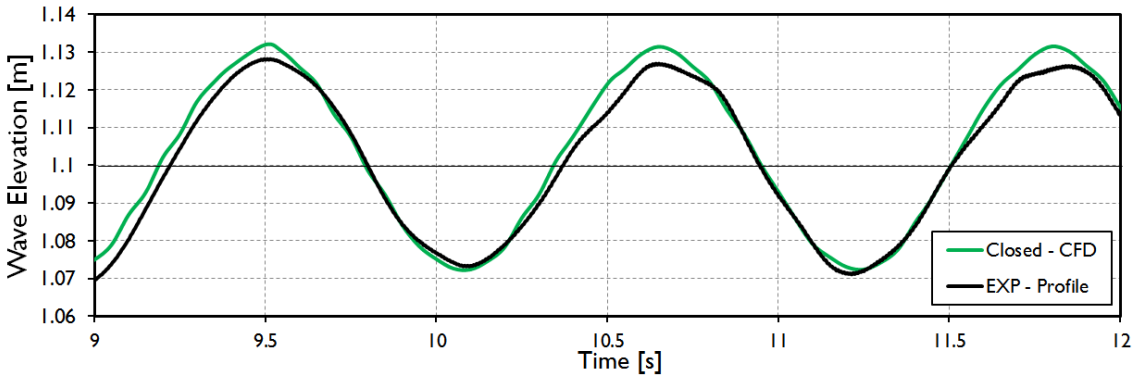

Figure 7.22, A comparison between the wave profiles from the CFD and experimental modelling for wave #1.

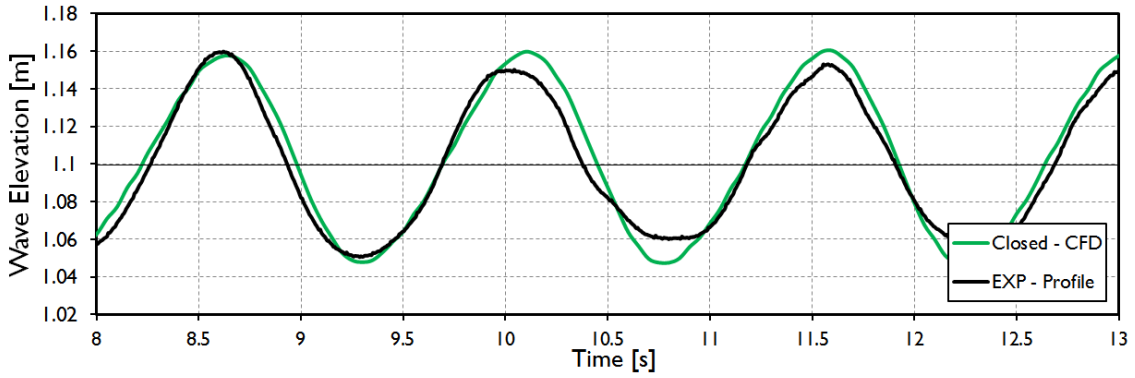

Figure 7.23, A comparison between the wave profiles from the CFD and experimental modelling for wave #2.

As this geometry had not been evaluated in the wave tank, there was no physical modelling data to compare the performance to. From the results in Table 20 however, it can be seen that for wave #1, the performance of the closed baffle duct was far lower than the other two geometries.

Whereas for wave #2, the performance of the optimised geometry was better than that of the closed baffle but the baseline duct had a lower average conversion efficiency.

Table 20, The measured performance of the closed baffle, CFD model.

Test #	Period [s]	Height [mm]	Mean dP [Pa]	Mean Q [m³/s]	Efficiency [%]
1	1.15	59.9	43.18	0.0014	9.6
2	1.47	111.9	232.82	0.0030	28.9

No strong conclusions can be drawn from the comparison of these two results with the other CFD results, however this does suggest that the baffle influences the energy conversion process. Further investigation is required to determine if this influence is detrimental or beneficial and for which wave conditions. This should be carried out by physical modelling experiments until the CFD model has been improved and validated to provide confidence in its results.

7.10 Discussion and Conclusions

The previous mathematical and CFD modelling carried out prior to this research commencing had few useful conclusions and is reported in Appendix A1.2. The work presented in this chapter was predominantly driven by ITP's desire to have a numerical model to inform the design of the large scale demonstrator.

The review of OWC numerical modelling techniques concluded that simple analytical models of mass-spring-damper systems could be roughly translated to model OWEL, however, in much the same way that potential flow models are not able to accurately model many of the flow effects occurring within the OWEL duct, they would therefore be of limited use. For performance to be assessed, it was deemed essential to capture the interaction between the water and air as the wave crest propagates along the duct. The review concluded that the only method capable of capturing all of the flow physics was CFD.

The CFD model developed for this research utilised some of the boundary conditions from the previous CFD work although some boundary conditions such as the Stokes' wave generation boundary were developed specifically for this model.

The reasonable comparison between the CFD simulation results and those from the physical modelling suggested that the parameters set on the CFD model were good for an initial model set up. This also demonstrated the suitability of CFD to model the conversion performance of a static duct.

The results are from the model are qualitative and demonstrate the key principles, which help to more closely investigate the characteristics of the conversion process. Further investigations would be required to demonstrate the quantitative reliability of the results. This would include investigations into issues such as grid and time independence and convergence; setting RMS and maximum residual tolerance levels; and altering the maximum number of iteration loops to achieve sufficient convergence.

The lack of grid and time step independence studies is likely to have meant that some spatial and temporal effects may not have been correctly captured. This includes short duration events such as high velocity flows caused by wave impacts, or small eddies and vortices that may have been formed but were too small to be captured by the size of the grid. It is likely however that, as the results compare relatively well to the physical experiments, the inclusion of these phenomena would not lead to any significant changes in the CFD results.

High Courant numbers were present in the regions of air within the domain, particularly around the orifice where air velocities frequently exceeded 10 m/s. This suggests therefore that the mesh refinement or length of time step was not adequate. This may be mitigated in future models by incorporating a porous loss region as a replacement for the orifice to simulate the same damping and resistance to the flow as the orifice. This would remove the requirement of a fine mesh to capture the high velocity, turbulent flow through the orifice.

Despite the discrepancies between the CFD and physical modelling data, these investigations proved the applicability of CFD to be suitable for modelling the performance of a static OWEL duct.

8 Implications for a Marine Demonstrator

8.1 Introduction

An objective of this work was to improve the hydraulic design and demonstrate the resulting increase in the commercial prospects and competitiveness of the device. Increases in the performance of OWEL can be seen through the progression of the physical modelling studies as learning and experimentation led to more beneficial designs. Whilst this shows comparative increases in the wave-to-pneumatic efficiency it does not present tangible figures to the device developer that indicate a greater overall performance. It is therefore necessary to show the gains in energy yield productivity that have been made as a result of this research. Furthermore, these figures can be used in comparisons with other devices to assess the competitiveness and therefore the likely viability of the device.

It is beyond the scope of this work to derive project specific metrics such as CAPEX, OPEX and LCOE values, discussed in section 3.2, as this would require significant further work to determine suitable costs for each aspect of the deployment. A more pertinent approach therefore would be to compare the annual predicted energy yield of a similar device in the same wave climate. This is with the assumption that the similar device has been deemed to have commercial viability by the technology developer.

The objective of this chapter is to consider the implications that the findings from the research have on the commercial prospects for the device. This begins with a discussion of the size of the device and therefore the implied scale of the laboratory physical modelling. By altering the duct length of the device it is expected that the performance can be ‘tuned’ to the design wave climate of the deployment site. This would therefore, maximise the annual energy yield and hence the revenue generated from sale of electricity. This discussion is followed by an analysis of the predicted energy yield of the large scale demonstrator at the Wave Hub site based upon the dimensions specified by ITP/OWEL and the performance derived from the physical modelling. Four different ‘performance maps’ were used in the analysis to estimate the productivity of the static and floating variants of the baseline and optimised geometries in order to demonstrate the performance gains made as a result of this research. This methodology was then applied to a larger variant of the OWEL geometry to predict the annual productivity if it were installed at the EMEC test site. This was compared with the performance of a similarly scaled OE Buoy also at EMEC to demonstrate the similarities in predicted energy yield.

8.2 Discussion on Scale

Prior to commencing this research, the device developer proposed that a full scale OWEL unit would likely be over 100 m in length and, if combined into a multi-unit platform, in excess of 100 m in width. It is likely that the cost of such a structure could far outweigh its abilities to deliver power and so would reduce its profitability. The full scale device dimensions were however, based upon results from the proof of concept physical modelling and so required further investigation.

All wavelength dependent wave energy converters should be designed to operate most efficiently in the wave climate they are intended to be deployed in. This implies that the parameter that tunes their performance to a particular wavelength should be optimised so that the peak performance of the WEC coincides with the conditions at which the maximum energy is available at the site. The length of the OWEL duct defines the wavelengths at which the peaks in conversion efficiency occur. In addition, this also modifies the motions of the device which further influences the power capture.

In the initial, 2D wave flume testing, three peaks in performance were identified, each occurring at a different wavelength. The most ideal of these occurred at a range of $L/L_D = 3.5 – 3.8$ which would result in a relatively small device for a typical design wavelength at an offshore site. This peak in performance however, was not observed in any of the subsequent testing with the different model geometries.

In the single duct, 3D physical modelling studies, the predominant regions of increased efficiency were observed at conditions centred around L/L_D ratios of 1, 1.2, 1.6 and 2.5. For floating conditions however, the peak at $L/L_D = 2.5$ did not occur due to the device motions having a detrimental effect on the conversion process. Figure 8.1 shows the required full scale duct length to shift the three main performance peaks to the desired design wave period specific to the deployment site. This shows that, had the $L/L_D = 2.5$ performance peak been achieved with a floating model, the full scale duct length would have been relatively short. It is likely however, that, unless further advances are made in order to achieve higher efficiencies at longer wavelengths, the required duct length of a full scale device is likely to be large. The design wave period for the Wave Hub site is approximately 9 seconds, as was shown in Figure 4.20, see section 4.5. This would therefore require a duct length of ~80 m in order to make the peak performance ($L/L_D = 1.6$) coincide with the maximum available energy at the site. Whilst this duct length will yield the greatest power generation per annum, a compromise will be required to ensure that the CAPEX of the structure is minimised whilst maximising the device output. It

should be noted that it has been assumed that the peak performance will occur at the same L/L_D ratios at large scale as they did in the small scale models.

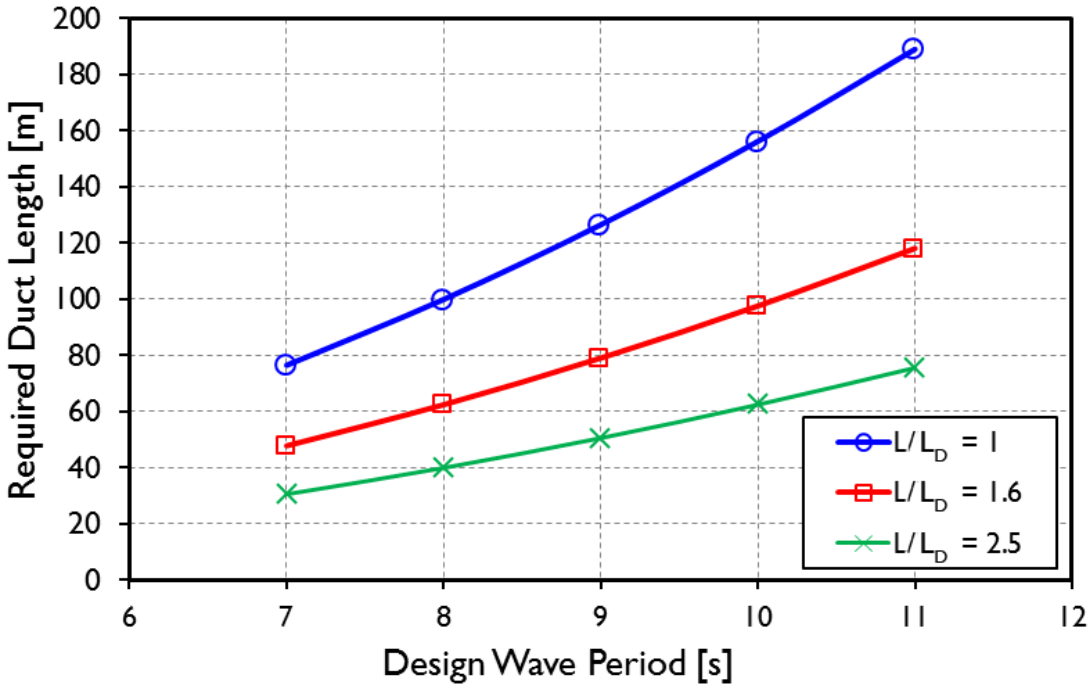

Figure 8.1, The full scale duct length required in order to locate each of the three performance peaks at the design wave period of the deployment site.

From the initial calculations and cost predictions by ITP, a device with a duct length of 42 m will have a structural weight of approximately 550 tonnes. For the marine demonstrator, this structure will be mostly constructed from steel and a total structural cost of £1m has been estimated. Increasing the duct length would significantly increase the structural weight and cost as the forces exerted on a structure do not scale linearly with length. A duct length of 42 m has been assumed by ITP to be the largest structure that can be accommodated with the proposed budget. This therefore, implies that the model scale of the wave basin and towing tank tests was 1:50. From Figure 8.1, a device with a duct length of 42 m would have a peak performance, for $L/L_D = 1.6$, in sea states of approximately 6.5 s. Whilst these sea states are some of the most commonly occurring, as is shown in Figure 8.4, they have a low annual energy yield and so the annual electricity generation for this device configuration would likely be lower than it was initially desired.

8.3 Productivity Analysis

8.3.1 Introduction

In order to predict the productivity of OWEL in a real sea a similar methodology to that in Lavelle and Kofoed (2011) was used. This was based upon the performance data derived from

the scale modelling and wave occurrence data for the wave sites of interest. The examples presented here are intended to demonstrate the gains in performance of a single duct machine that have been made as a direct result of this work. The predicted annual productivity of a full scale machine at the Wave Hub site, initially with the baseline geometry then the optimised geometry, in both static and floating configurations is presented.

Throughout this assessment, it has been assumed that the scale ratio between the physical model tested in the towing tank and the marine demonstrator for the Wave Hub site was 50.

8.3.2 Methodology

The annual energy productivity of a device is

$$E_{annual} = 24 \times 365 \times \sum_i \sum_j P_{OWEL\ i,j}\, F_{i,j} \quad [\mathbf{MWh/yr}] \qquad [31]$$

Where $P_{OWEL\ i,j}$ is the power matrix of the device that has been arranged into discrete 'bins', with *i* wave periods and *j* wave heights. $F_{i,j}$ is the frequency of occurrence of each combination of *i,j* sea state as a proportion of the year.

$P_{OWEL\ i,j}$ is determined by

$$P_{OWEL\ i,j} = width \times P_{wave\ i,j} \times \eta_{i,j} \qquad [\mathbf{MW}] \qquad [32]$$

Where *width* is the dimension of the duct entry width which, in the case of the full scale device, is 14 m. $P_{wave\ i,j}$ is the matrix containing the power available in the wave crest per unit length [MW/m] for each of the bins representing the *i* wave periods and *j* wave heights. This was determined using the relationship for wave power in an irregular sea state as provided in equation [10]. $\eta_{i,j}$ is the wave-to-wire efficiency of OWEL at each *i,j* sea state and was calculated from the efficiency contour plots that have been the predominant measure of performance throughout this work.

The associated wave periods and heights of the scatter of wave-to-pneumatic efficiency values were scaled by a factor of 50 and were combined with the occurrence scatter of the Wave Hub site. In some instances where the occurrence bins were outside of the range of the scaled efficiencies, the device efficiency was conservatively extrapolated in order to overlay the Wave Hub scatter. Then, for each sea state bin from the Wave Hub occurrence scatter, the predicted efficiency at each *i* period and *j* height was interpolated from the wave-to-pneumatic efficiency. This provided an estimate of the conversion efficiency of the device for each bin of the site data.

Assumptions were then made to generate the wave-to-wire efficiencies based upon the wave-to-pneumatic efficiencies, such that

$$\eta_{wave-to-wire} = \eta_{wave-to-pneu} \times \eta_{turbine} \times \eta_{generator} \times \eta_{electrical} \quad [33]$$

Where $\eta_{turbine}$ is the efficiency of the turbine PTO in converting the airflow to shaft work to be transmitted to the generator. $\eta_{generator}$ is the efficiency of the generator at converting the shaft power to electrical power and was estimated at a constant value of 0.95. $\eta_{electrical}$ is the efficiency of the electrical subsystems in converting the electrical power output from the generator into power suitable for distribution to the National Grid. This was estimated at 0.97.

$\eta_{turbine}$ was estimated to represent a constant value of pneumatic-to-shaft power efficiency. Whilst the efficiency of a turbine will vary depending on the sea state and resulting airflow, a lack of reliable data for a power curve meant that an approximation had to be made. The review of full scale power take off in Appendix A1.3 concluded that Dresser Rand's Hydro Air, impulse turbine would likely be the most suitable turbine for OWEL. Natanzi *et al.* (2011) reported that the peak efficiency of the current Hydro Air prototype turbine was estimated by CFD modelling to exceed 75 % with efficiencies over 60 % for much of the performance curve. Assuming a degree of learning through the development of the turbine and a performance increase due to the requirement of the turbine to operate only in uni-directional airflow, it was estimated that an optimistic turbine efficiency of 75 % could be achieved.

The review of the effects of air compressibility at small scale in section 3.5 concluded that reduced scale models would over predict the pneumatic power. As the towing tank model did not compensate for the effects of compressibility it was decided to include an additional loss into the turbine efficiency to compensate for the reduction in air power due to compressibility effects. Weber (2007) predicted that from the results of a 1:10 scale OWC model the equivalent full scale performance was over estimated by an average of approximately 10 %. Therefore, the assumed turbine efficiency was reduced so that $\eta_{turbine}$= 0.65. Whilst this loss may be greater when comparing 1:50 scale results to those of a 1:1 device, no data is available to suggest such values.

A further assumption of this methodology was that the performance of the small scale model in regular waves was deemed to be analogous to the performance in irregular waves. The comparisons made with the multi-duct model in chapter 5 between performance in regular and irregular waves suggest that this is a fair assumption, particularly with a static model. For a

floating model, the performance in irregular seas may even be increased over that in regular waves due to the modification of the floating dynamics, see section 5.9.2.

8.3.3 Wave Hub Climate

The Wave Hub occurrence scatter plot is upon data from the Met Office's UK Waters Model for grid point U04 (50.39°N 5.58°W), [Halcrow (2006)]. Whilst this data was from a numerical model, little continuous wave buoy data is available for the Wave Hub site [Smith *et al.* (2011)] and so the model data was deemed the most suitable source. The U04 data is plotted in Figure 8.2 with the occurrence scatter taken from four wave rider buoy deployments during 2005-2006 for comparison [Pitt (2006)]. The location of the four wave buoy measurements along with the U04 point are shown in relation to the Wave Hub site area in Figure 8.3.

The occurrence data from the UK Waters Model was taken and grouped into discrete bins of T_z and H_s. The zero crossing wave periods, T_z, were then converted into their respective energy periods, T_e, using the relationship from Pitt (2006);

$$T_e = 1.125T_z + 0.6478 \quad [\mathbf{s}] \qquad [34]$$

This relationship was determined by plotting the T_z data against a range of T_e values that were derived from the integration of the spectral ordinates from a range of sea states from the UKMO model.

The wave occurrence data were organised into the table shown in Figure 8.4 to provide the joint probability scatter plot for the site. The values of T_e and H_s are the median values of each bin and were then used in the calculation of the available wave power of each bin. This method has a number of limitations for assessing full scale sites; the distribution of occurrence within each bin is not represented and so the available power of a bin may be over or underestimated depending on the skew of the data. Furthermore, the spectral shapes and variations of the sea state associated with each data bin are not used for these calculations. This may be of particular importance when investigating sites with site specific spectral features such as bi-modal seas. This is a key trait of the Wave Hub spectra, particularly in low energy seas as these often comprise wind wave and swell components as shown in the work by Smith *et al.* (2012). Nevertheless, for the purposes of this initial productivity assessment, these simplifying assumptions are suitable but the results should be considered with this in mind.

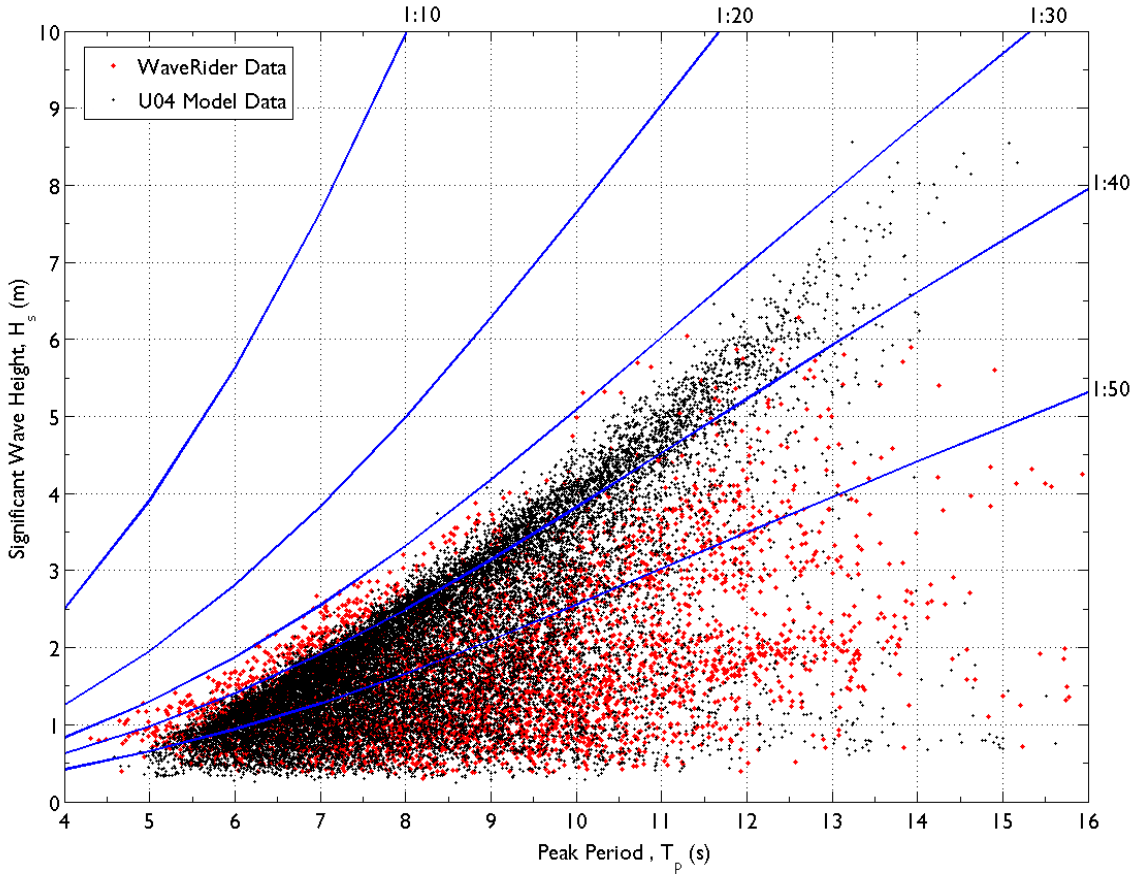

Figure 8.2, Comparison of the UKMO's U04 model data and the wave rider buoy data from the 2005-2006 deployments, including iso-lines of constant wave steepness.

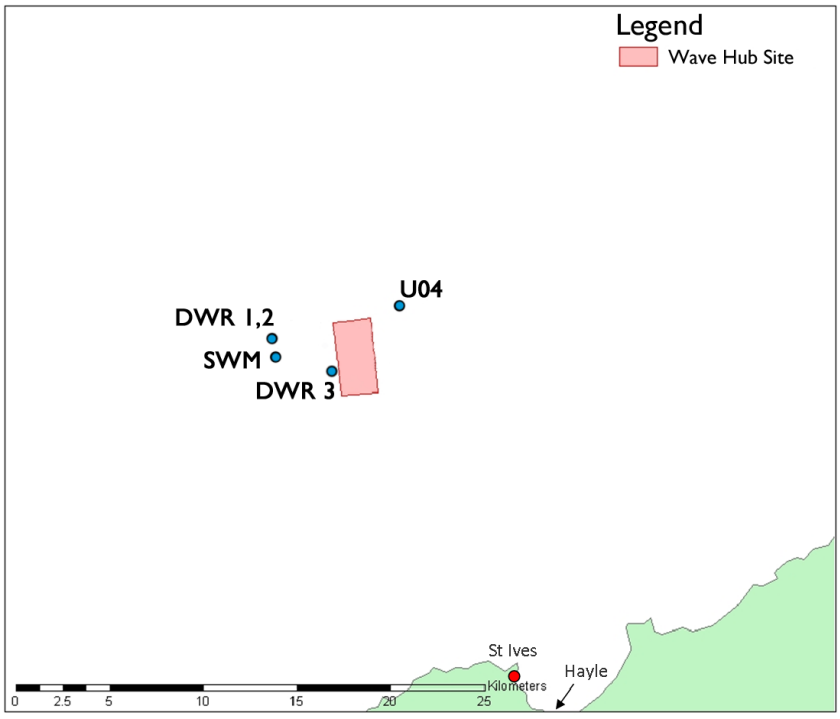

Figure 8.3, The locations of the U04 point, four wave buoy deployments and the Wave Hub site, modified from Smith *et al.* (2011).

Te (s)	4.59	5.71	6.84	7.96	9.09	10.21	11.34	12.46	13.59	14.71	15.84	Total
Hs (m)												
0.25	429	464	210	106	41	26	13	4				1293
0.75	1623	4403	1695	734	299	107	27	22	4	3		8917
1.25	242	6035	2615	1028	396	122	80	31	15	6	2	10572
1.75	20	1528	4929	937	306	140	54	18	8	3	1	7944
2.25		45	3748	1466	338	142	54	21	6	1		5821
2.75			669	3061	375	124	33	7	6	3		4278
3.25			36	2067	647	107	48	11	4			2920
3.75				527	1401	99	33	11	2			2073
4.25				62	1307	161	36	11				1577
4.75				7	549	604	19	6	3			1188
5.25					100	669	31	6	1			807
5.75					16	432	93	8				549
6.25					2	126	213	5				346
6.75						36	205	12	2			255
7.25						6	102	29	4			141
7.75					1		44	60	1			106
8.25							4	50	2			56
8.75							1	18	7			26
9.25							1	2	11			14
9.75									13			13
10.25								1	9			10
10.75									2	3		5
11.25									2	1		3
11.75										4		4
12.25												0
12.75											1	1
	2314	12475	13902	9995	5778	2901	1091	333	102	24	4	48919

Figure 8.4, Joint probability plot for the Wave Hub site with the respective T_e and H_s bins.

8.3.4 Results

Further assumptions were made by OWEL and ITP regarding operating conditions for electricity generation; it is not expected to deliver power in sea states with $H_s < 1$ m and so these sea states have not been included in the analysis. It is likely also that there will be no generation in sea states greater than $H_s > 7$ m, however this will be determined following structural load analysis, turbine capabilities and operational experience. Power generation for sea states with $H_s > 7$ m has been included in the productivity analysis, however this typically only accounts for < 10 % of the annual power.

The limitations of the wave tank in the physical investigations restricted the range of test wave conditions that could be generated. This meant that performance data was not available over the whole range of the scaled Wave Hub conditions and so some extrapolation beyond the bounds of the measured efficiency was necessary. The scatter plots in Figure 8.5 and Figure 8.6 show the wave conditions for the experimental data for the baseline and optimised model configurations overlaid onto the scaled Wave Hub climate. Four additional, extrapolated points

were required so that the experimental data encompassed the entire Wave Hub scatter. Whilst the inclusion of extrapolated data is not ideal, the limitations of the wave tank did not allow the testing to be extended to conditions to fully represent the scaled Wave Hub conditions. The efficiency values at each of these points were conservative estimates based upon the general performance of each configuration and the nearest conversion efficiencies. Table 21 provides a summary of the additional, estimated efficiency values included for extrapolation. Furthermore, the component of predicted energy generation from these more extreme bounds is low and therefore, any errors brought about by the inclusion of these extrapolated points are not likely to be significant.

Table 21, Four additional efficiency points required for extrapolation.

T [s]	H [mm]	Baseline Static [%]	Baseline Floating [%]	Optimal Static [%]	Optimal Floating [%]
1.5	20	2.0	1.0	15.0	2.0
2.3	20	2.0	1.0	5.0	1.0
1.6	190	1.0	1.0	1.0	1.0
2.1	260	0.1	1.0	0.1	0.1

The four plots in Figure 8.7 show the extrapolated efficiency contour plots for the two device geometries in static and floating configurations with the data points used to create them. The Wave Hub scatter points are overlaid onto these contour plots and the application of equation [32] at each of these points yields the average electrical power generated at each sea state.

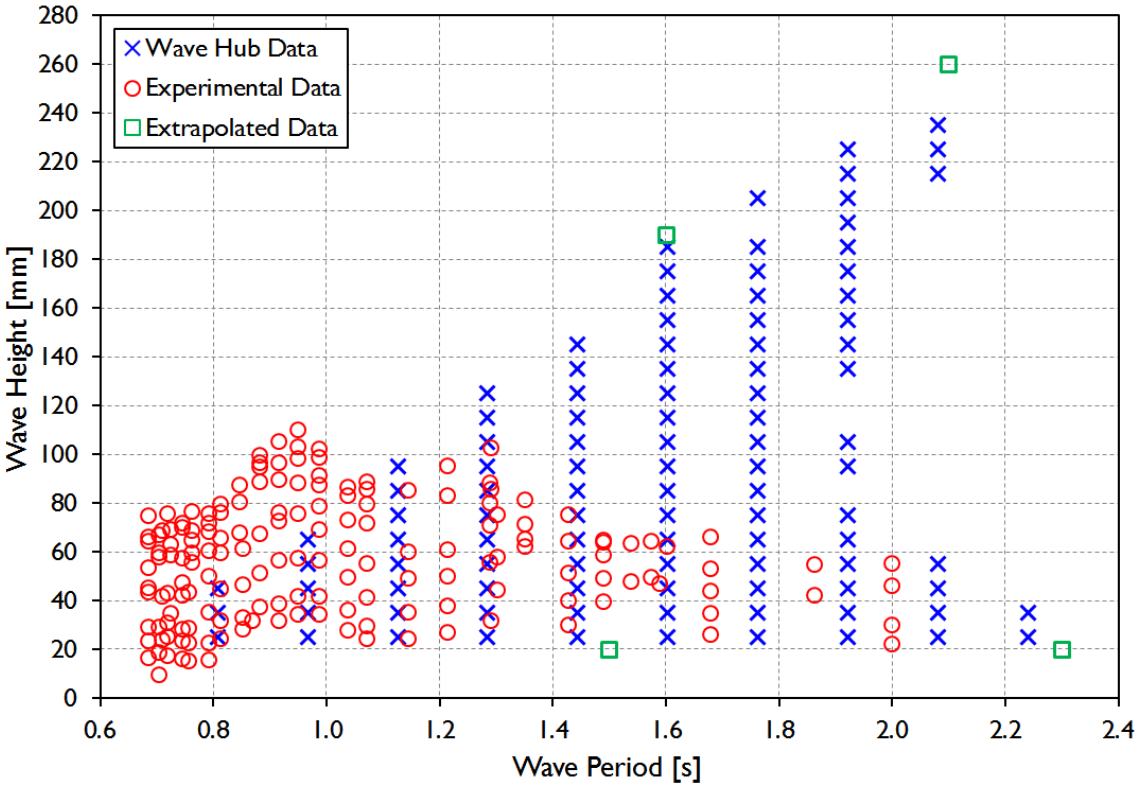

Figure 8.5, Additional extrapolated data points required for interpolation of Wave Hub data points, scaled at 1:50, onto the baseline experimental results.

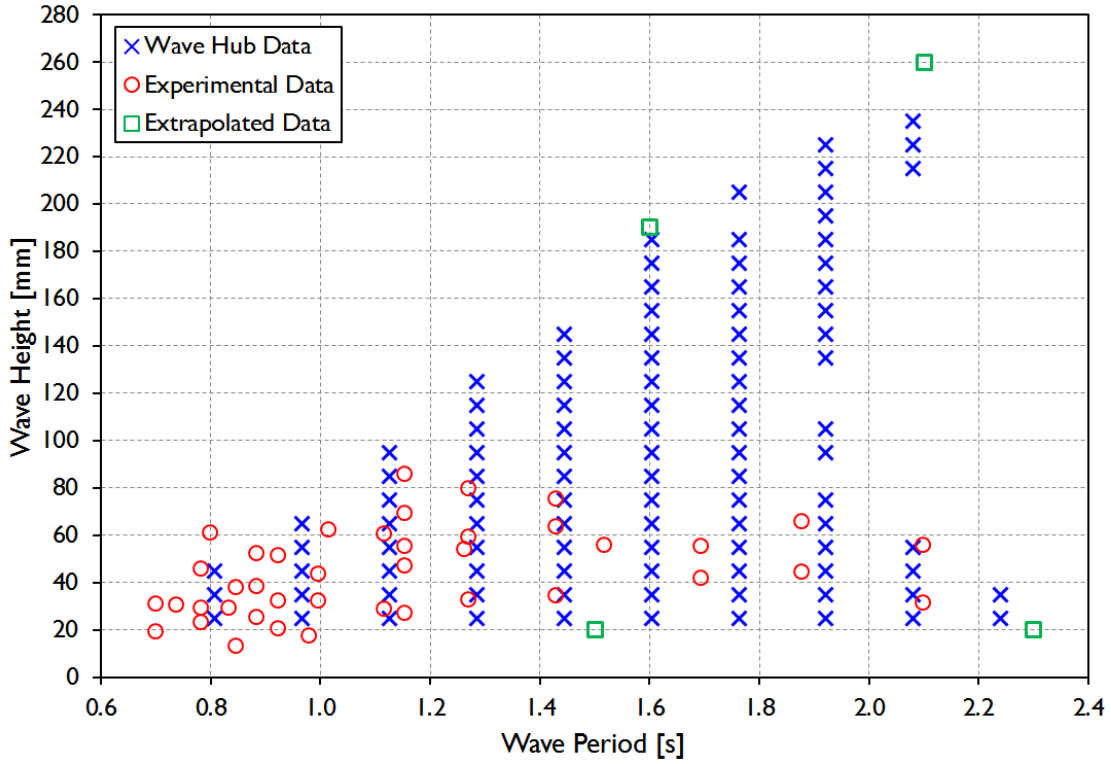

Figure 8.6, Additional extrapolated data points required for interpolation of Wave Hub data points, scaled at 1:50, onto the optimised model experimental results.

Figure 8.7 shows the extrapolated data points, Wave Hub records and experimental data points overlaid onto the resulting efficiency contour plots for the two geometry configurations in static and floating conditions. The plots show that the extrapolated points had little significant influence on the characteristics of the performance contour plots. In many instances, the inclusion of the additional manufactured data, led to conservative regions in the contour plots, as indicated by the white regions which are equivalent to zero efficiency.

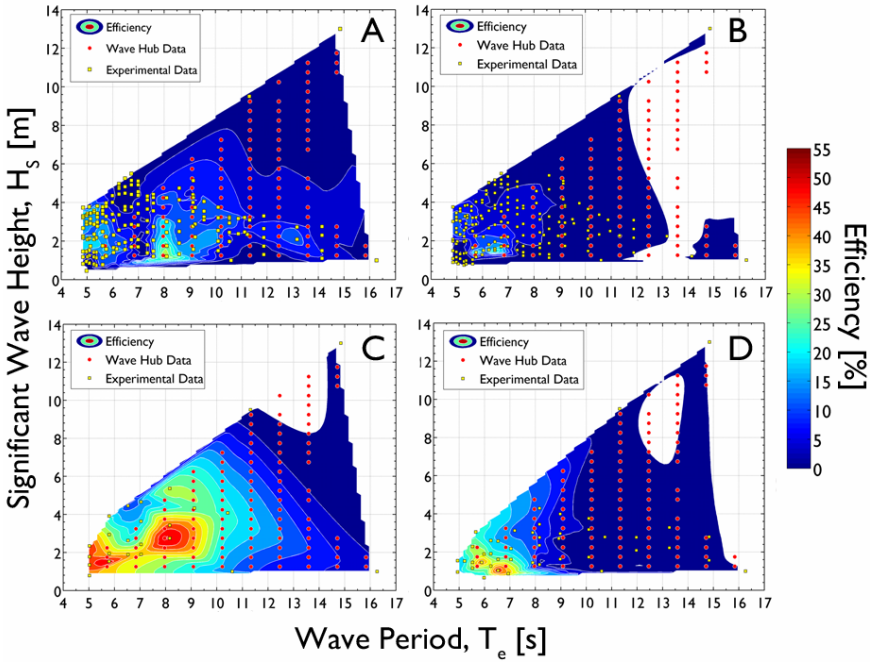

Figure 8.7, Efficiency contour plots for the two geometry configurations in both static and floating conditions with the experimental data and Wave Hub scatter overlaid.

The results presented in Figure 8.8 to Figure 8.11 are the predicted electrical energy for each of the four device configurations considered in this analysis. The annual energy generated at each sea state bin occurring at Wave Hub is shown in addition to the totals for each range of wave heights and periods. These plots show the poor energy productivity of the floating devices in sea states with $T_e > \sim 12$ s. The peak energy generation can be seen to shift depending on whether the device is static or floating. For these cases, the peak generating conditions reduce in wave period and height for the floating devices in comparison to those that are static.

The values in Table 22 summarise the predicted annual power and energy generation for the four cases at the Wave Hub site. This shows the performance gains made for a single duct device as a result of the physical modelling studies. The productivity of the static, optimised geometry was predicted to be 376.8 MWh greater than the initial, baseline configuration, which is the equivalent of a 198 % increase. Furthermore, the optimised floating device was estimated to exceed the annual generation of the baseline design by 85.4 MWh of electricity per annum, which would be a 124 % increase.

Te [s]	4.59	5.71	6.84	7.96	9.09	10.21	11.34	12.46	13.59	14.71	15.84	Total	
Hs [m]													
1.25	0.56	6.17	0.98	2.85	0.63	0.08	0.01	0.01	0.02	0.01	0.00	11.31	
1.75	0.09	3.28	2.73	4.49	1.06	0.28	0.04	0.04	0.02	0.00	0.00	12.05	
2.25		0.15	5.90	9.13	1.64	0.66	0.13	0.10	0.03	0.00		17.74	
2.75			1.66	27.13	2.44	0.97	0.15	0.05	0.03	0.01		32.43	
3.25			0.10	16.77	5.66	0.93	0.37	0.06	0.02			23.90	
3.75				4.30	13.96	1.12	0.25	0.07	0.01			19.71	
4.25				0.93	15.98	2.00	0.31	0.08				19.30	
4.75				0.08	7.20	8.99	0.18	0.05	0.03			16.53	
5.25					1.75	11.33	0.32	0.06	0.01			13.47	
5.75					0.29	8.00	1.03	0.09				9.41	
6.25						2.47	2.48	0.06				5.01	
6.75						0.72	2.48	0.16	0.03			3.39	
7.25					0.03	0.12	1.26	0.39	0.05			1.86	
7.75							0.54	0.80	0.01			1.36	
8.25							0.05	0.63	0.03			0.70	
8.75							0.01	0.20	0.10			0.31	
9.25							0.01	0.02	0.15			0.17	
9.75									0.16			0.16	
10.25								0.01	0.10			0.10	
10.75									0.02	0.04		0.06	
11.25									0.02	0.01		0.03	
11.75										0.04		0.04	
12.25												0.00	
												0.00	
Total	0.65	9.60	11.37	65.68	50.64	37.66	9.63	2.86	0.82	0.11	0.00	189.04	[MWh]

Figure 8.8, Annual energy generation for the static, baseline configuration.

Te [s]	4.59	5.71	6.84	7.96	9.09	10.21	11.34	12.46	13.59	14.71	15.84	Total	
Hs [m]													
1.25	0.42	5.26	1.60	0.06	0.04	0.00	0.00	0.00	0.00	0.00	0.00	7.38	
1.75	0.04	1.94	11.45	0.60	0.01	0.01	0.00	0.00	0.00	0.00	0.00	14.05	
2.25		0.09	10.02	2.58	0.16	0.03	0.01	0.00	0.00	0.00		12.89	
2.75			1.94	7.33	0.42	0.08	0.01	0.00	0.00	0.00		9.79	
3.25			0.09	6.00	1.11	0.10	0.03	0.00	0.00			7.33	
3.75				2.46	3.22	0.16	0.02	0.00	0.00			5.86	
4.25				0.37	3.67	0.28	0.03	0.00				4.34	
4.75				0.04	1.75	1.23	0.02	0.00	0.00			3.03	
5.25					0.36	1.57	0.03	0.00	0.00			1.96	
5.75					0.07	1.13	0.08	0.00				1.28	
6.25						0.36	0.17	0.00				0.53	
6.75						0.11	0.15	0.00	0.00			0.26	
7.25					0.01	0.02	0.07	0.00	0.00			0.09	
7.75							0.02	0.00	0.00			0.02	
8.25							0.00	0.00	0.00			0.00	
8.75							0.00	0.00	0.00			0.00	
9.25							0.00	0.00	0.00			0.00	
9.75									0.00			0.00	
10.25								0.00	0.00			0.00	
10.75									0.00	0.00		0.00	
11.25									0.00	0.00		0.00	
11.75										0.00		0.00	
12.25												0.00	
												0.00	
Total	0.46	7.29	25.11	19.44	10.81	5.07	0.65	0.00	0.00	0.00	0.00	68.83	[MWh]

Figure 8.9, Annual energy generation for the floating, baseline configuration.

Te [s]	4.59	5.71	6.84	7.96	9.09	10.21	11.34	12.46	13.59	14.71	15.84	Total	
Hs [m]													
1.25	0.47	16.71	6.95	2.69	0.96	0.26	0.13	0.04	0.02	0.01	0.00	28.25	
1.75	0.08	8.73	28.30	5.63	2.03	0.64	0.19	0.06	0.02	0.01	0.00	45.71	
2.25		0.35	31.32	19.83	4.51	1.18	0.37	0.13	0.03	0.00		57.73	
2.75			6.53	69.10	7.90	1.66	0.38	0.07	0.05	0.01		85.70	
3.25			0.41	59.02	18.80	2.11	0.83	0.16	0.04			81.37	
3.75				16.56	48.30	2.64	0.75	0.19	0.02			68.46	
4.25				1.68	43.65	5.30	1.00	0.22				51.85	
4.75				0.23	24.86	23.71	0.61	0.13	0.03			49.58	
5.25					5.35	30.03	1.11	0.14	0.01			36.64	
5.75					0.95	21.35	3.53	0.18				26.01	
6.25					0.13	6.62	8.22	0.10				15.06	
6.75						1.94	7.68	0.20	0.01			9.83	
7.25						0.32	3.51	0.39	0.02			4.24	
7.75							1.30	0.63	0.00			1.93	
8.25							0.09	0.32	0.00			0.41	
8.75							0.02	0.03	0.00			0.04	
9.25							0.01	0.00	0.00			0.01	
9.75									0.00			0.00	
10.25								0.00	0.00			0.00	
10.75									0.00	0.02		0.02	
11.25									0.00	0.01		0.01	
11.75										0.02		0.02	
12.25												0.00	
												0.00	
Total	0.55	25.80	73.51	174.75	157.43	97.76	29.72	2.99	0.26	0.08	0.00	562.85	[MWh]

Figure 8.10, Annual energy generation for the static, optimal configuration at Wave Hub.

Te [s]	4.59	5.71	6.84	7.96	9.09	10.21	11.34	12.46	13.59	14.71	15.84	Total	
Hs [m]													
1.25	0.46	13.84	7.89	0.91	0.12	0.03	0.00	0.00	0.00	0.00	0.00	23.24	
1.75	0.08	6.39	19.76	1.82	0.27	0.06	0.01	0.00	0.00	0.00	0.00	28.40	
2.25		0.29	18.57	5.26	0.29	0.12	0.03	0.01	0.00	0.00		24.57	
2.75			4.09	15.72	0.45	0.20	0.04	0.00	0.00	0.00		20.49	
3.25			0.31	13.91	2.32	0.28	0.08	0.01	0.00			16.91	
3.75				5.11	5.90	0.32	0.08	0.02	0.00			11.42	
4.25				0.88	7.36	0.66	0.10	0.02				9.02	
4.75				0.13	4.54	2.97	0.06	0.01	0.00			7.71	
5.25					1.28	3.82	0.11	0.01	0.00			5.23	
5.75					0.30	2.78	0.37	0.01				3.46	
6.25					0.04	0.91	0.88	0.01				1.83	
6.75						0.30	0.87	0.01	0.00			1.17	
7.25						0.07	0.44	0.00	0.00			0.51	
7.75							0.19	0.00	0.00			0.19	
8.25							0.02	0.00	0.00			0.02	
8.75							0.00	0.00	0.00			0.00	
9.25							0.01	0.00	0.00			0.01	
9.75									0.00			0.00	
10.25								0.00	0.00			0.00	
10.75									0.00	0.01		0.01	
11.25									0.00	0.00		0.00	
11.75										0.01		0.01	
12.25												0.00	
												0.00	
Total	0.54	20.52	50.61	43.74	22.86	12.50	3.28	0.11	0.02	0.02	0.00	154.20	[MWh]

Figure 8.11, Annual energy generation for the floating, optimal configuration at Wave Hub.

Table 22, A summary of the predicted average annual power output and energy yield for the four cases at the Wave Hub site.

Configuration	Average Annual Instantaneous Output [kW]	Average Annual Energy Output [MWh]
Baseline - Static	21.58	189.04
Baseline - Floating	7.88	68.83
Optimal - Static	64.26	562.85
Optimal - Floating	17.62	154.20

8.4 Comparison with OE Buoy

In order to make an approximate comparison with a similar wave energy converter, the data from the report by Lavelle and Kofoed (2011) was used. This estimated the full scale performance of OE Buoy at the EMEC test site based upon the performance results from the 1:4 scale testing. The report did not include the wave resource occurrence data for the EMEC site that was used in their calculations. A report by Nielsen and Pontes (2010) included an annual joint probability for the wave resource at the EMEC site, derived from a numerical wave model. This data was found to suggest that, in deep water, an annual average wave power of 22.3 kW/m was available at the site which is similar to the 21.8 kW/m stated by Babarit *et al.* (2012). The resource data used by Lavelle and Kofoed (2011) however, had an annual average power of 38.9 kW/m. The predicted energy output of OE Buoy is therefore higher than that of OWEL. A further limitation of the OE Buoy predictions was that the wave-to-wire efficiency had been extrapolated beyond the bounds of the experiments by assuming that it was constant for each 'bin' of wave period rather than the conservative method described in section 8.3.2. The extrapolation method used by Lavelle and Kofoed (2011) meant that the wave-to-wire efficiency was the same for all wave heights at each period, whereas it is likely that the performance would vary with the incident wave height.

By scaling the physical models of the OWEL duct by a factor of 1:58, the full scale duct length of OWEL increases to 48 m, which would be the same as a full scale OE Buoy. However, this would only result in a duct width of 16 m, which is 8 m narrower than OE Buoy. For the purposes of this calculation, it was assumed that increasing the duct width linearly increases the power entering the duct without altering the conversion performance. The duct entry width of OWEL was therefore assumed to equal that of the full scale OE Buoy at 24 m.

The same methodology as described in section 8.3.2 was used to estimate the annual electricity production of OWEL at the EMEC site, based on the small scale efficiency results from the towing tank testing. The results of this analysis are presented in Figure 8.12, which shows the annual energy contribution of each sea state to the total amount of electricity generated. It was predicted that an annual production of 300 MWh of electricity could be achieved, which implies an annual average wave-to-wire efficiency of ~6 %, for the average wave resource. This is approximately double the productivity in comparison to a device deployed at the Wave Hub site, despite the two wave climates having a similar wave energy resource and for only a slightly larger device. This highlights the importance of correctly sizing the dimensions of the device to match the wave resource so that the region of peak efficiency is better aligned with the peak energy available at the site.

Te [s]	4.2	5.4	6.6	7.8	9	10.2	11.4	12.6	13.8	15	16.2	17.4	Total	
Hs [m]														
0.25	0.00	0.00	0.00	0.00	0.00	0.00	0.00	0.00	0.00				0.00	
0.75	0.63	4.00	3.27	1.91	0.19	0.01	0.00	0.00	0.00				10.02	
1.25	0.34	6.51	13.18	6.91	0.38	0.10	0.02	0.00		0.00	0.00	0.00	27.44	
1.75	0.20	3.98	35.21	10.83	1.38	0.23	0.05	0.00			0.00		51.88	
2.25		1.22	30.32	18.33	2.80	0.26	0.10	0.02	0.00				53.06	
2.75		0.19	8.32	31.29	3.89	0.18	0.16	0.03	0.01	0.00		0.00	44.08	
3.25		0.05	1.27	24.62	10.19	0.35	0.22	0.04	0.01	0.01			36.75	
3.75			0.17	6.56	18.53	1.56	0.25	0.03	0.01	0.00			27.10	
4.25				0.71	15.24	2.54	0.33	0.11	0.03		0.01	0.01	18.98	
4.75				0.12	5.65	4.81	0.54	0.09	0.03	0.01			11.25	
5.25					0.70	5.35	0.85	0.14	0.01				7.06	
5.75						2.33	1.90	0.04	0.00	0.01			4.28	
6.25				0.05	0.08	0.58	2.10	0.09	0.01				2.91	
6.75					0.09	0.07	1.60	0.58	0.01				2.34	
7.25							0.88	0.78		0.00			1.67	
7.75							0.48	0.69	0.00	0.00			1.18	
8.25							0.12	0.16	0.01				0.30	
8.75								0.11	0.00				0.11	
9.25								0.01	0.00	0.00			0.01	
9.75									0.00	0.00			0.00	
10.25									0.00	0.00			0.00	
10.75										0.00			0.00	
11.25										0.00			0.00	
													0.00	
Total	1.16	15.95	91.72	101.33	59.12	18.37	9.63	2.94	0.14	0.04	0.01	0.01	300.43	[MWh]

Figure 8.12, Estimated annual energy yield of OWEL Scaled at 1:58 with a duct width of 24 m at EMEC.

The estimated productivity for OE Buoy at the EMEC site is 423.7 MWh/annum, [Lavelle and Kofoed (2011)]. This is ~40 % greater than that predicted for OWEL, as summarised in Table 23. It should be reiterated however, that these predictions were made using two different wave resource data sets, with one being an average of 75 % more energetic than the other. These values are intended to demonstrate the similarities in energy yield between the two devices rather than being a direct comparison. Comparing the figures in Table 23, it can be postulated

that productivity analysis for OWEL, in the same wave resource as the OE Buoy analysis, would yield a similar annual electricity generation.

Table 23, Comparison of the predicted energy yield from a full scale OWEL and OE Buoy at the EMEC test site.

Device	Annual Average, Available Wave Power [kW/m]	Average Annual Power Generation [MWh]
OE Buoy	38.9	423.7
OWEL	22.3	300.4

Despite these two predicted annual power generation values being comparable, they are low when considering that the steel structures would be 48 m long by 24 m wide. In comparison, a study by Dalton and Lewis (2011) predicted from the performance of a 30th scale, floating OWC, that a full scale device deployed off the Irish coast in an average annual wave climate of 50 kW/m, would generate approximately 1,200 MWh/yr. Whilst this analysis was for an idealised device at a different site to the other two scenarios, it is significantly greater than the estimations made for OWEL or OE Buoy. A study, by Babarit *et al.* (2012), created a simple wave-to-wire model of a number of generic WECs, including a floating OWC. This analysis predicted that the absorbed energy of an OWC deployed at EMEC, in a wave climate of 21.8 kW/m, would be approximately 2,275 MWh/yr, (+/- 569 MWh). This is even higher than the estimate by Dalton and Lewis (2011) but has much uncertainty surrounding the idealised numerical models and assumptions made. Nevertheless, it also suggests that the predicted electrical generation of 300 – 400 MWh/yr is very low. The productivity estimations for these demonstration devices are likely to be far lower than the output that can be expected from a commercial machine. Continued development of these devices will be required to increase their power generation capabilities such that they are able to deliver electricity at a utility scale.

8.5 Discussion

This chapter was intended to quantify the gains in the performance of the device that have resulted from the conclusions of this research and to demonstrate the commercial competitiveness of the technology.

Designing a device to generate the maximum power over the course of a year requires the performance peak efficiency to coincide with the available peak energy of a wave climate. Performance peaks occurring at larger L/L_D ratios result in shorter design duct lengths and therefore, the device costs are likely to be lower.

For a floating OWEL device, it is unlikely that the performance will feature a peak at $L/L_D = 2.5$ unless the vessel motions of future devices can be altered to prevent the motions from being detrimental to the performance at these wavelength ratios. For this reason, peak performance occurs at lower L/L_D ratios. Therefore, for a design wave period of 9 seconds as is typical for Atlantic sites such as Wave Hub, a duct length of approximately 80 m would be required for the performance peak at $L/L_D = 1.6$ to coincide with the peak energy available. This would increase further to ~125 m if the performance peak occurred at $L/L_D = 1.0$.

Whilst the coincidence of the peak device performance and maximum annual available energy will yield the greatest annual energy yield, the resulting duct length may be detrimental to the economics of the device. To ensure the lowest cost of energy therefore, the design duct length for a particular site will need to be optimised to maximise the energy yield and minimise the cost implications of a longer duct.

In order to quantify the performance improvements that have been made as a result of this research, productivity predictions were made for the annual electricity generation of different device configurations at the Wave Hub site. The productivity of the static, optimised geometry was predicted to be 376.8 MWh greater than the initial, baseline configuration, which is the equivalent of a 198 % increase. Furthermore, the optimised floating device was estimated to exceed the annual generation of the baseline design by 85.4 MWh of electricity per annum, which would be a 124 % increase.

Following a similar analysis, the performance of a larger device was estimated for the EMEC test site, wave climate. This was then compared with the estimations made for the OE Buoy device at the same site. Comparing the annual productivity estimations for these two devices with the theoretical predictions made for floating OWC devices suggested that the output of both OWEL and OE Buoy is relatively low. It was noted that these values were for demonstration devices and that their output is likely to be less than that of the equivalent commercialised technology.

9 Conclusions and Future Work

The work undertaken during the course of this research has contributed to the knowledge of the OWEL wave energy converter and increased the fundamental understanding of the conversion process. Through a series of extensive physical modelling studies, the performance characteristics were determined and modifications to the design were made to evaluate their effect on the device efficiency. As a result, the hydrodynamic design of the device has been significantly improved, which has led to a 124 % increase in the predicted productivity of a full scale unit and has estimated a competitive level of power generation.

9.1 Conclusions

9.1.1 Background Review

Assessment of the previous OWEL development work, encompassing both small and intermediate scale physical modelling as well as theoretical and CFD modelling, showed that few conclusions could be drawn and there was a significant lack of knowledge despite the extensive amount of work undertaken.

A review of the wave energy industry identified 10 different WEC technologies that were perceived as being developed in direct competition with OWEL. Each was found to have both favourable aspects and design weaknesses meaning that no device was perceived to be superior.

A literature review of the physical modelling and development OWCs provided background information from which testing methodologies could be gleaned and lessons learned from the findings of previous research due to the synergies between the two devices.

9.1.2 Initial Physical Modelling

The preliminary investigations were intended to re-evaluate the findings from the previous development work; determine the performance characteristics; investigate an alternative PTO simulator; and to observe the conversion process.

Wave-to-pneumatic efficiency peaks exceeding 40 % were found to occur at defined ranges of wavelength/duct length, L/L_D, ratio: predominantly 1.0 – 1.5 and 3.5 – 3.8., with a third, smaller peak at $L/L_D = 2.5$.

An orifice PTO simulator was found to be a suitable alternative to the previously proposed approach. The performance was found to be sensitive to the damping applied by the orifice.

Observation of the conversion process within the duct led to suggestions for design modifications to improve the performance. As a result, the performance was found to be dependent on the internal wave reflections, standing waves, and that by trimming the duct bow upwards, with the stern at SWL the characteristics of the conversion performance were improved.

9.1.3 Multi-Duct Platform

These investigations suggested that a floating, multi-duct platform could be a future configuration of OWEL however, the economics of such a device would first have to be considered.

Performance of the static model in irregular seas was comparable to that in regular waves however, in both cases, the performance was lower than that of the previous 2D model.

The original naval architecture design was found to be inadequate as it resulted in poor performance due to it lacking floating stability. A model with a redesigned buoyancy and ballast distribution and with the addition of motion drag plates, resulted in better performance but floating performance was still lower than was anticipated. Performance of the floating model improved when tested in irregular seas as the random nature of the water surface acted to reduce the effective motions of the device.

The poor performance of the floating model was attributed to the static peak in performance occurring at a wave period at which the pitch and surge motion response of the model was also at its greatest.

The large reduction in performance between the static and floating devices highlighted the need to investigate the naval architecture design to prevent the motions from adversely affecting the performance. Furthermore, the many variables and complexity of the multi-duct model did not aid the experimental work. It was therefore challenging to isolate the effects from the caused by the different model parameters in order to study individual characteristics. Nevertheless, the results from the testing comprised a significant proportion of the SWRDA funded project and were successfully used to show the potential of the device and obtain further funding to continue the technology development.

9.1.4 Single Duct Unit

Three phases of physical modelling were carried out to investigate the behaviour of a single duct configuration of OWEL in order to inform the design of the large scale marine demonstrator being developed in a TSB funded project that ran in parallel to this research.

Software was developed to drive the wave paddles and acquire the sensor data. Time was also spent calibrating the waves in the tank, developing the experimental method and finding the limitations of the facility.

The first phase investigated a geometry that was a single duct taken directly from the multi-duct platform model and was considered the baseline design for these experiments. The performance of the static, model was comparable to that of the multi-duct model. Observation of the internal wave crests aided development of the simple theory of operation and showed a difference in position of the internal and external wave crests. The initial naval architecture design for the single duct was found to be unsuitable and was redesigned to be more stable, resulting in increased performance.

The second phase was used to study how changes in duct geometry influenced power capture. Performance was found to be sensitive to the floor and side wall angles. Parallel walls of the duct increased the conversion efficiency and increasing the floor angle to capture a greater depth of the water column also increased the performance.

The final phase of testing investigated the effect of the buoyancy distribution and device trim on the performance of the improved geometry design. Buoyancy distributions concentrated towards the bow of the model brought forward the longitudinal centre of floatation and were shown to increase the peak conversion efficiencies. It was found that comparisons between static and floating models should be treated with caution, as the floating dynamics significantly influence the performance magnitudes and the position of the peak performance. The coinciding periods of peak performance of a static model and the period of peak pitch and heave response of the floating model was attributed to the reduction in performance between the static and floating models. Setting the duct trim to be lower for longer wave periods and higher for shorter wave periods resulted in the highest efficiencies for the floating configuration. This suggested that active trim and ballast control would be beneficial for a full scale device.

The testing increased the performance of the floating model in comparison to that of the initial, baseline design. This demonstrated the ability of the device to be able to operate efficiently as a single, floating unit albeit with reduced efficiencies in comparison to the static configuration. The buoyancy arrangement adopted for the full scale demonstrator has been based upon the most beneficial design tested and a variable ballast system incorporated to allow for changes in trim to benefit the power capture.

9.1.5 Theoretical Modelling Approaches

Methods that could be used to develop a theoretical, performance model of OWEL were investigated with the aim that a model would allow further design optimisation studies to be carried out following the physical modelling. A review of methodologies applied to model OWC devices discussed the three principal approaches; analytical models, potential flow and CFD. The use of CFD was concluded to be the most useful of the various approaches as more complex flow physics could be modelled and with the potential for floating motions to be included in future studies.

The CFD model, developed as an initial application of the method, was shown to be able to model a static configuration of the single duct geometry and the agreement between the theoretical and empirical results was reasonable. With further development and improvement of the model it is likely that the agreement would be improved. This initial methodology was subsequently used by a TSB project partner in the development of a 3 DoF, CFD model simulating the floating dynamics and performance of the device.

9.1.6 Implications for a Marine Demonstrator

The experiments carried out with the single duct model, in particular, were conducted to inform the design of a large scale, marine demonstrator that OWEL intend to deploy at Wave Hub. The results of these investigations have led to the development of a device that is predicted to perform significantly better than the original, baseline design.

To match the peak performance of the device with the design wave conditions for Wave Hub, it was predicted that a duct length of approximately 80 m would be required. Through productivity analysis of four different full scale device configurations at the Wave Hub site, it was shown that:

- For a static device, the optimised, single duct geometry, with parallel side walls and 7.5° floor angle, was predicted to generate 563 MWh/annum; a 198 % increase over the baseline equivalent device.
- For a floating device, the optimised geometry with a buoyancy distribution concentrated towards the bow and a variable trim strategy, was predicted to generate 154 MWh/annum; a 124 % increase over the baseline floating device.

These conclusions demonstrate the gains in energy generation that have been a direct result of this work. Through the extensive physical modelling, the commercial prospects of the technology have been improved.

A comparative study between results from the annual power generation predictions of the OE Buoy WEC and a full scale OWEL device deployed at the EMEC test site, predicted that a full scale device could be expected to deliver a competitive level of energy.

9.1.7 The Commercial Advancement of OWEL

The initial physical modelling and multi-duct testing formed the majority of the work carried out in the SWRDA funded project. The objectives within both were successfully met and their conclusions significantly contributed to the successful completion of the project. The learning from these investigations and the outcomes of the SWRDA project directly led to the award of the funding for the TSB project which allowed the development of OWEL to continue.

Physical modelling in the towing tank with the single duct was essential for the TSB project to progress. Laboratory studies had not been included as a work package within the project and, in hindsight, without it the design work being carried out would have been largely based upon numerical modelling results and would therefore have incurred large safety factors.

The development of the initial CFD model allowed the numerical modelling work package within the TSB project to be commenced with a proposed methodology. This was used directly in the development of a more advanced CFD model with 3 DoF device motions. This model was subsequently used to predict motions, performance and water pressures for the large scale marine demonstrator.

The outcomes of this work have therefore been central in the progression of the OWEL development and have considerably aided its advancement towards being a commercial technology.

9.2 Further Investigations

9.2.1 Planned Work

The work suggested in this section has been planned by ITP and OWEL to be undertaken during the next stages of development of the device. These investigations are considered essential to continue the design of the marine demonstrator and advance the TSB project.

The single duct with the optimised geometry and naval architecture design should be further tested but in an ocean wave basin to determine the behaviour in realistic, irregular sea states.

This would allow additional productivity assessments to be carried out to provide better predictions of the energy yield in a marine environment. Furthermore, this would demonstrate the changes to the performance and motions of the single duct when subjected to excitement from multiple wave periods within a sea state.

Future experimental modelling efforts should continue to investigate the effect of motions and in particular, ways in which to modify the device to benefit the power capture in longer period wave conditions where $L/L_D > 2.5$. This would significantly improve the commercial potential of the device by delivering more power with the possibility of reducing the duct length and therefore, the cost of the structure.

9.2.2 Recommended Work

The following topics of investigation are suggested by the author and have been conceived based upon the conclusions and observations made in this work.

Specific investigations into the transition from the duct into the power take-off tube will be necessary. It was observed in the physical modelling that this is a critical region which is required to pass large air flow rates from the duct to the turbine whilst minimising losses and maintaining a suitable constriction in cross sectional area.

Consideration should be given to the issue of water exiting upwards through the PTO ducting and into the turbine. Typically, turbines are able to deal with moderate amounts of spray but not large volumes of water. This however, cannot be investigated in small models due to the effects of scale and so an alternative modelling approach, such as CFD, should be used.

The CFD modelling and observations in the laboratory experiments suggested that the baffle opening at the stern of the duct has an effect on the energy conversion process. Additional investigations to examine this effect would be of interest, particularly if the baffle is beneficial to the performance.

Further development of a rigid body, CFD model based upon the initial work presented here. This is important as the static device characteristics are very different to those of a device with motions.
If funding could be obtained, the ideal and logical progression from these small scale model tests would be to advance to the testing of another intermediate scale device either at a deep

water ocean basin or at a marine test site with scaled conditions. This would offer a number of advantages over laboratory scale investigations, particularly to reduce scale effects, incorporate a more realistic PTO, test control methodologies and to help validate the predictions made from the model testing. This would provide data to determine the scalability of the device and whether performance estimations can be made from the small scale data.

10 References

AGGIDIS, G. A. & MINGHAM, C. (2009). A Joint Numerical and Experimental Study of a Surging Point Absorbing Wave Energy Converter (WRASPA). *Joule Centre Research Grant Joint Final Report - JIRP306/02.*

AIRY, G. B. (1845). On Tides and Waves. *Encyclopedia Metropolitan.* London.

ALCORN, R., HUNTER, S., SIGNORELLI, C., OBEYESEKERA, R., FINNIGAN, T. & DENNISS, T. (2005). Results of the Testing of the Energetech Wave Energy Plant at Port Kembla on October 26, 2005.

ALVES, M. (2005). Analysis of the Diffraction Response in OWC Power Plants. *Wavetrain Deliverable 11: 2D Viscous OWC Modelling.*

ANAND, S., JAYASHANKAR, V., NAGATA, S., TOYOTA, K., M.TAKAO & SETOGUCHI, T. (2007a). Turbines for Wave Energy Plants. *8th International Symposium on Experimental and Computational Aerothermodynamics of Internal Flows.* Lyon, France.

ANAND, S., JAYASHANKAR, V., NAGATA, S., TOYOTA, K., TAKAO, M. & SETOGUCHI, T. (2007b). Performance estimation of bi-directional turbines in wave energy plants. *Journal of Thermal Science,* 16**,** 346-352.

ANDERSON, J. (1995). *Computational Fluid Dyanmics*, McGraw-Hill.

ANSYS (2010). *ANSYS® CFX Version 13.0 Documentation*.

AWS OCEAN ENERGY. (2012). *Company Webpage* [Online]. Available: http://www.awsocean.com [Accessed 15th August 2012].

BABARIT, A., HALS, J., MULIAWAN, M. J., KURNIAWAN, A., MOAN, T. & KROKSTAD, J. (2012). Numerical benchmarking study of a selection of wave energy converters. *Renewable Energy,* 41**,** 44-63.

BAGHAEI, A. (2010). The Technology and the Maui Wave Energy Project. *Asia Pacific Clean Energy Summit.* Honolulu, Hawaii.

BAGHAEI, A. (2012). The World's First 1MW Wave Energy Converter. *4th International Conference on Ocean Energy.* Dublin, Ireland.

BEATTIE, W. C. & RAGHUNATHAN, S. (1993). A novel contra rotating Wells turbine. *European Wave Energy Symposium.* Edinburgh, UK.

BHINDER, M. A., MINGHAM, C. G., CAUSON, D. M., RAHMATI, M. T., AGGIDIS, G. A. & CHAPLIN, R. V. (2009). Numerical and experimental study of a point absorbing wave energy converter in regular waves. *Clean Electrical Power, 2009 International Conference on.*

BJERKE, I. K., SJOLTE, J., HJETLAND, E. & TJENSVOLL, G. (2011). Experiences from Field Testing with the BOLT Wave Energy Converter. *9th European Wave and Tidal Energy Conference.* Southampton, UK.

BOCCOTTI, P. (2007). Caisson Breakwaters Embodying an OWC with a Small Opening - Part I: Theory. *Ocean Engineering,* 34**,** 806-819.

BOCCOTTI, P., FILIANOTI, P., FIAMMA, V. & ARENA, F. (2007). Caisson Breakwaters Embodying an OWC with a Small Opening - Part II: A Small-Scale Field Experiment. *Ocean Engineering,* 34**,** 820-841.

BRENDMO, A., FALNES, J. & LILLEBEKKEN, P. M. (1996). Linear Modelling of Oscillating Water Columns Including Viscous Loss. *Applied Ocean Research,* 18**,** 65-75.

BRETSCHNEIDER, C. L. (1959). Wave Variability and Wave Spectra for Wind-Generated Gravity Waves. *Technical Memorandum No. 118.* US Army Corps of Engineers.

BRITISH STANDARDS INSTITUTION (2003). Orifice plates. *Measurement of fluid flow by means of pressure differential devices inserted in circular cross-section conduits running full. BS EN ISO 5167-2:2003.* Milton Keynes: BSI.

BRITO-MELO, A., HOFMANN, T., SARMENTO, A. J. N. A., CLEMENT, A. H. & DELHOMMEAU, G. (2000). Numerical modelling of OWC-shoreline devices including the effect of surrounding coastline and non-flat bottom. *10th International Offshore and Polar Eng Conference.*

BWEA (2009). Powering a Green Economy: Wind, wave and tidal's contribution to Britain's industrial future. *British Wind Energy Association.*

CAMPOREALE, S. M., FILIANOTI, P. & TORRESI, M. (2011). Performance of a Wells Turbine in an OWC Device in Comparison to Laboratory Tests *9th European Wave and Tidal Energy Conference.* Southampton, UK.

CARBON TRUST (2003). Construction of an Offshore Wave Energy Converter. Carbon Trust Grant #2003-3-122.

CARBON TRUST (2011). Accelerating Marine Energy.

CASTRO, F., MARJANI, A. E., RODRIGUEZ, M. A. & PARRA, T. (2007). Viscous flow analysis in a radial impulse turbine for OWC wave energy systems. *7th European Wave and Tidal Energy Conference.* Porto, Portugal.

CHAKRABARTI, S. K. (1994). *Offshore Structure Modeling,* Advanced Series on Ocean Engineering - Vol. 9, World Scientific.

CHAPLIN, J. R., HELLER, V., FARLEY, F. J. M., HEARN, G. E. & RAINEY, R. C. T. (2012). Laboratory testing the Anaconda. *Philosophical Transactions of the Royal Society A: Mathematical, Physical and Engineering Sciences,* 370**,** 403-424.

CHARLIER, R. H. & JUSTUS, J. R. (1993). *Ocean Energies: Environmental, Economic and Technological Aspects of Alternative Power Sources* Elsevier.

CORES (2012). Components for Ocean Renewable Energy Systems (CORES) Final Summary Report *EU FP7 - 213633.*

CRUZ, J. (2008). *Ocean Wave Energy - Current Status and Future Perspectives*, Springer.

CURRAN, R., STEWART, P., T., WHITTAKER & T., T. J. (1997). Design synthesis of oscillating water column wave energy converters : performance matching. 211.

CURRAN, R. (2002). Productivity of Ocean-Wave-Energy Converters: Turbine Design. *Journal of Energy Engineering,* 128**,** 13-31.

CURRAN, R. & FOLLEY, M. (2008). Power Take-Off Systems - Air Turbine Design for OWCs. *In:* CRUZ, J. (ed.) *Ocean Wave Energy - Current Status and Future Prepectives.* Springer.

CURRAN, R. & GATO, L. M. C. (1997). The energy conversion performance of several types of Wells turbine designs. *Proceedings of the Institution of Mechanical Engineers, Part A: Journal of Power and Energy,* 211**,** 133-145.

CURRAN, R., RAGHUNATHAN, S., STEWART, T. P. & WHITTAKER, T. J. T. (1995). Matching a Wells Turbine to the Islay Oscillating Water Column Wave Power Converter. *14th Conference on Ocean, Offshore and Arctic Engineering.* Copenhagen, Denmark.

CURRAN, R., WHITTAKER, T. J. T. & STEWART, T. P. (1998). Aerodynamic conversion of ocean power from wave to wire. *Energy Conversion and Management,* 39**,** 1919-1929.

DALTON, G. J. & LEWIS, T. (2011). Performance and economic feasibility analysis of 5 wave energy devices off the west coast of Ireland. *9th European Wave and Tidal Energy Conference.* Southampton, UK.

DECC (2011a). Consultation on proposals for the levels of banded support under the Renewables Obligation for the period 2013-17 and the Renewables Obligation Order 2012. *Department of Energy and Climate Change.*

DECC (2011b). Digest of United Kingdom energy statistics (DUKES) - Electricity. Department of Energy and Climate Change, London.

DECC. (2012). *South West Makes a Splash as First Marine Energy Park* [Online]. Available: http://www.decc.gov.uk/en/content/cms/news/pn12_003/pn12_003.aspx [Accessed 4th March 2012].

DELAURÉ, Y. M. C. & LEWIS, A. (2003). 3D hydrodynamic modelling of fixed oscillating water column wave power plant by a boundary element methods. *Ocean Engineering,* 30**,** 309-330.

DTI (2000). New and Renewable Energy: Prospects in the UK for the 21st Century: Supporting Analysis. *ETSU R-122 (Energy Technology Support Unit).*

DTI (2007). *Meeting the Energy Challenge - A White Paper on Energy,* Department of Trade and Industry, London.

DUCKERS, L., MINNS, N., ROBERT, H. & WATSONSIMON (2008). A Novel, Compact Wave Energy Converter. *10th World Renewable Energy Congress.* Glasgow, Scotland.

ECCC (2012). The Future of Marine Renwables in the UK. *House of Commons, Energy and Climate Change Committee.*

EVANS, D. V. (1978). The Oscillating Water Column Wave-energy Device. *IMA J Appl Math,* 22**,** 423-433.

EVANS, D. V. (1982). Wave-power absorption by systems of oscillating surface pressure distributions. *Journal of Fluid Mechanics Digital Archive,* 114**,** 481-499.

EVANS, D. V. & PORTER, R. (1997). Efficient Calculation of Hydrodynamic Properties of OWC-Type Devices. *Journal of Offshore Mechanics and Arctic Engineering,* 119**,** 210-218.

FALCÃO, A. F. D. O. (2010). Wave energy utilization: A review of the technologies. *Renewable and Sustainable Energy Reviews,* 14**,** 899-918.

FALCÃO, A. F. D. O. & JUSTINO, P. A. P. (1999). OWC wave energy devices with air flow control. *Ocean Engineering,* 26**,** 1275-1295.

FALCÃO, A. F. O., GATO, L. M. C. & NUNES, E. P. A. S. (2011). A New Radial Self-rectifying Air Turbine for Use in OWC Wave Energy Converters *9th European Wave and Tidal Energy Conference.* Southampton, UK.

FALNES, J. (1992). Review of wave energy research in Norway. *Workshop on Wave Energy R&D.* European Commission, Rep. EUR 15079, Cork, Ireland.

FALNES, J. (2002). *Ocean Waves and Oscillating Systems*, Cambridge University Press.

FALNES, J. & HALS, J. (2012). Heaving buoys, point absorbers and arrays. *Philosophical Transactions of the Royal Society A: Mathematical, Physical and Engineering Sciences,* 370**,** 246-277.

FALNES, J. & MCIVER, P. (1985). Surface wave interactions with systems of oscillating bodies and pressure distributions. *Applied Ocean Research,* 7**,** 225-234.

FENTON, J. D. (1985). A Fifth-Order Stokes Theory for Steady Waves. *Journal of Waterway, Port, Coastal and Ocean Engineering,* 111**,** 216-234.

FINNEGAN, T. & AULD, D. (2003). Model Testing of a Variable-Pitch Aerodynamic Turbine *13th International Offshore and Polar Engineering Conference.* Honolulu, USA.

FOLLEY, M., CURRAN, R. & WHITTAKER, T. (2006). Comparison of LIMPET contra-rotating wells turbine with theoretical and model test predictions. *Ocean Engineering,* 33**,** 1056-1069.

FOLLEY, M. & WHITTAKER, T. (2005). The Effect of Plenum Chamber Volume and Air Turbine Hysteresis on the Optimal Performance of Oscillating Water Columns. *ASME Conference Proceedings,* 2005**,** 493-498.

FOLLEY, M. & WHITTAKER, T. J. (2002). Identification of non-linear flow characteristics of the LIMPET shoreline OWC *Twelfth International Offshore and Polar Engineering Conference.* Kitakyushu, Japan.

FOLLEY, M. & WHITTAKER, T. J. T. (2009). Analysis of the nearshore wave energy resource. *Renewable Energy,* 34**,** 1709-1715.

FOLLEY, M., WHITTAKER, T. W. T. & HOFF, J. V. T. (2007). The design of small seabed-mounted bottom-hinged wave energy converters *7th European Wave and Tidal Conference.* Oporto, Portugal.

FORESTIER, J. M., HOLMES, B., BARRETT, S. & LEWIS, A. W. (2007). Value and Validation of Small Scale Physical Model Tests of Floating Wave Energy Converters. *7th European Wave and Tidal Energy Conference.* Porto, Portugal.

FRYER, D. K. & THOMAS, M. W. S. (1975). A linear twin wire probe for measuring water waves. *Journal of Physics E: Scientific Instruments,* 8**,** 405-408.
GAJAN, P., MOTTRAM, R. C., HEBRARD, P., ANDRIAMIHAFY, H. & PLATET, B. (1992). The influence of pulsating flows on orifice plate flowmeters. *Flow Measurement and Instrumentation,* 3**,** 118-129.
GAREEV, A. (2011). *Analysis of Variable Pitch Air Turbines for Oscillating Water Column (OWC) Wave Energy Converters.* Doctor of Philosophy, University of Wollongong - Available Online: http://ro.uow.edu.au/theses/3418.
GATO, L. M. C. & DE O. FALCÃO, A. F. (1988). Aerodynamics of the Wells Turbine. *International Journal of Mechanical Sciences,* 30**,** 383-395.
GERVELAS, R., TRARIEUX, F. & PATEL, M. (2011). A time-domain simulator for an oscillating water column in irregular waves at model scale. *Ocean Engineering,* 38**,** 1007-1013.
GILLOTEAUX, J.-C., BABARIT, A., DUCROZET, G., DURAND, M. & CLÉMENT, A. H. (2007). Non-Linear model to simulate large amplitude motions: application to wave energy conversion. *22nd International Workshop on Water Waves & Floating Bodies.* Plitvice, Croatia.
GUNN, K. & STOCK-WILLIAMS, C. (2012). Quantifying the global wave power resource. *Renewable Energy,* 44**,** 296-304.
HALCROW (2006). Wave Hub Development and Design Phase Coastal Processes Study. *Report for the South West of England Development Agency.*
HALS, J. (2010). Small-body approximation and Morison's equation. *Presentation from Wavetrain2 course.* Centre for Ships and Ocean Structures (CeSOS), NTNU, Trondheim, Norway.
HARTIGAN, P. (2012). *The Wavebob Device* [Online]. STANDPOINT FP7 EU Project. Available: http://www.fp7-standpoint.eu/index.php/en/wave-energy/wavebob-device [Accessed 15th August 2012].
HASSELMAN, K., BARNETT, T. P., BOUWS, E., CARLSON, D. E. & HASSELMANN, P. (1973). Measurements of wind-wave growth and swell decay during the Joint North Sea Wave Project (JONSWAP). *Deutsche Hydrographische Zeitschrift,* 8.
HEATH, T. V. (2007). The Development of a Turbo-Generation System for Application in OWC Breakwaters *7th European Wave and Tidal Energy Conference.* Porto, Portugal.
HEATH, T. V. (2012). A review of oscillating water columns. *Philosophical Transactions of the Royal Society A: Mathematical, Physical and Engineering Sciences,* 370**,** 235-245.
HELLER, V. (2011). Scale Effects in Physical Hydraulic Engineering Models. *Journal of Hydraulic Research,* 49**,** 293-306.
HERRING, S. (2007). *Design & Evaluation of Turbines for Use in OWC Power Plants.* PhD Thesis, Cranfield University.
HJETLAND, E., TJENSVOLL, G., BJERKE, I. K., SJOLTE, J. & KOEFOED, A. (2011). A brief introduction to the BOLT-2-WAVEHUB project. *9th European Wave and Tidal Energy Conference.* Southampton, UK.
HM GOVERNMENT (2009). The UK Renewable Energy Strategy, Department for Energy and Climate Change - Cm 7686
HOLMES, B. (2009). Tank Testing of Wave Energy Conversion Systems. *Report for European Marine Energy Centre (EMEC).* Orkney, UK.
HOLMES, B. & NIELSEN, K. (2010). Report T02-2.1 Guidelines for the Development & Testing of Wave Energy Systems. *OES-IA Annex II Task 2.1.*
HORKO, M. (2007). *CFD Optimisation of an Oscillating Water Column Energy Converter.* MSc, University of Western Australia.
HUNTER, S. (2011). Oceanlinx update and the future commercialisation of emerging marine renewable technology. *All Energy Australia.* Melbourne, Australia.
IEA-OES (2003). Implementing Agreement on Ocean Energy Systems - Annex II Report. International Energy Association,.
IEA (2011). *Key World Energy Statistics,* International Energy Agency, Paris.

IMAI, Y., TOYOTA, K., NAGATA, S., SETOGUCHI, T. & TAKAO, M. (2011). An Experimental Study on Generating Efficiency of a Wave Energy Converter "Backward Bent Duct Buoy". *9th European Wave and Tidal Energy Conference.* Southampton, UK.

JAYASHANKAR, V., ANAND, S., GEETHA, T., SANTHAKUMAR, S., JAGADEESH KUMAR, V., RAVINDRAN, M., SETOGUCHI, T., TAKAO, M., TOYOTA, K. & NAGATA, S. (2009a). A twin unidirectional impulse turbine topology for OWC based wave energy plants. *Renewable Energy,* 34**,** 692-698.

JAYASHANKAR, V., SIVASHANKAR, P. & VINATHA, U. (2009b). Measurements for proof of concept validation of a twin unidirectional turbine wave energy plant. *I2MTC - Instrumentation and Measurement Technology Conference.* Singapore.

JOHANNING, L., SMITH, G. & WOLFRAM, J. (2006). Mooring design approach for wave energy converters. *Proceedings of the Institution of Mechanical Engineers, Part M: Journal of Engineering for the Maritime Environment,* 220**,** 159-174.

JOHNSON, F., CHUDLEY, J. & DAI, Y. M. (2003). Prolongation of the Deployment and Monitoring of a Multiple Oscillating Water Column Wave Energy Converter. *The University of Plymouth for DTI Project URN 03/634.*

JORDAN, P. (2008). PowerBuoy Deployments (Present and Future). *All-Energy Conference and Exhibition.* Aberdeen, Scotland.

JOSSET, C., BABARIT, A. & CLÉMENT, A. H. (2007). A wave-to-wire model of the SEAREV wave energy converter. *Proceedings of the Institution of Mechanical Engineers, Part M: Journal of Engineering for the Maritime Environment,* 221**,** 81-93.

JOSSET, C. & CLÉMENT, A. H. (2007). A time-domain numerical simulator for oscillating water column wave power plants. *Renewable Energy,* 32**,** 1379-1402.

KALLESØE, B. S., DIXEN, F. H., HANSEN, H. F. & KØHLER, A. (2009). Prototype test and modeling of a combined wave and wind energy conversion system. *8th European Wave and Tidal Energy Conference.* Uppsala, Sweden.

KANEKO, K., SETOGUCHI, T. & RAGHUNATHAN, S. (1992). Self-Rectifying Turbines for Wave Energy Conversion. *International Journal of Offshore and Polar Engineering,* 2.

KEMP, J., DERRICK, A., O'NIANS, J. & UPADHYAY, D. (2005). The OWEL Wave Energy Converter as a Platform for Combined Wave and Wind Power Generation. *6th European Wave and Tidal Energy Conference.* Glasgow, UK.

KIM, T.-H., TAKAO, M., SETOGUCHI, T., KANEKO, K. & INOUE, M. (2001). Performance comparison of turbines for wave power conversion. *International Journal of Thermal Sciences,* 40**,** 681-689.

KNOTT, G. F. & FLOWER, J. O. (1980). Measurement of energy losses in oscillatory flow through a pipe exit. *Applied Ocean Research,* 2**,** 155-164.

KNOTT, G. F. & MACKLEY, M. R. (1980). On Eddy Motions near Plates and Ducts, Induced by Water Waves and Periodic Flows. *Philosophical Transactions of the Royal Society of London. Series A, Mathematical and Physical Sciences,* 294**,** 599-623.

KOFOED, J. P., FRIGAARD, P., FRIIS-MADSEN, E. & SØRENSEN, H. C. (2006). Prototype testing of the wave energy converter wave dragon. *Renewable Energy,* 31**,** 181-189.

KOOLA, P. M., RAVINDRAN, M. & NARAYANA, P. A. A. (1995). Model Studies of Oscillating Water Column Wave-Energy Device. *Journal of Energy Engineering,* 121**,** 14-27.

KROHN, D., MATTHEWS, S., ADAMS, J. & VALPY, B. (2012). Marine Energy in the UK - State of the Industry Report 2012. Renewable UK.

KURNIAWAN, A., HALS, J. & MOAN, T. (2011). Modelling and Simulation of a Floating Oscillating Water Column. *30th International Conference on Ocean, Offshore and Arctic Engineering.* Rotterdam, Netherlands.

LAVELLE, J. & KOFOED, J. P. (2011). Power Production Analysis of the OE Buoy WEC for the CORES Project. *CORES EU Project, DCE Technical Report No. 119.*

LEE, C.-H., NEWMAN, J. N. & NIELSEN, F. (1996). Wave Interactions with Oscillating Water Column. *6th International Offshore Polar Engineering Conference* Los Angeles, USA.

LIU, Z., HYUN, B.-S. & HONG, K. (2011). Numerical study of air chamber for oscillating water column wave energy convertor. *China Ocean Engineering,* 25**,** 169-178.

LIU, Z., HYUN, B.-S., JIN, J., CHOI, Y., SHI, H. & ZHANG, Q. (2010a). A wave focusing device for OWC wave energy convertor. *OCEANS 2010 IEEE - Sydney.*

LIU, Z., HYUN, B.-S., SHI, H. & HONG, K. (2010b). Practical Simulation of Oscillating Water Column Chamber for Wave Energy Conversion. *International Journal of Green Energy,* 7**,** 337-346.

LOCKETT, F. P. (1985). Power take-off and output from the Sea-Lanchester Clam wave energy device. *Offshore and Coastal Modelling.* Washington, DC: AGU.

LONGUET-HIGGINS, M. S., CARTWRIGHT, D. E. & SMITH, N. D. (1963). Observations of the Directional Spectrum of Sea Waves Using the Motions of a Floating Buoy. *Ocean Wave Spectra.* Prentice-Hall.

LUCAS, J., CRUZ, J., SALTER, S., TAYLOR, J. & BRYDEN, I. (2007). Update on the modelling of a 1:33 scale model of a modified Edinburgh duck WEC. *7th European Wave and Tidal Energy Conference.* Porto, Portugal.

LUCAS, J., SALTER, S. H., CRUZ, J. A. & TAYLOR, J. (2009). Performance optimisation of a modified Duck through optimal mass distribution. *8th European Wave and Tidal Energy Conference.* Uppsala, Sweden.

LUCAS, J. A. A. (2011). *The Dynamics of a Horizontal Cylinder Oscillating as a Wave Energy Converter About an Off-Centred Axis.* PhD, University of Edinburgh.

MAEDA, H., KINOSHITA, T., MASUDA, K. & KATO, W. (1985). Fundamental Research on Oscillating Water Column Wave Power Absorbers. *Journal of Energy Resources Technology,* 107**,** 81-86.

MAEDA, H., SANTHAKUMAR, S., SETOGUCHI, T., TAKAO, M., KINOUE, Y. & KANEKO, K. (1999). Performance of an impulse turbine with fixed guide vanes for wave power conversion. *Renewable Energy,* 17**,** 533-547.

MAEDA, H., SETOGUCHI, T., TAKAO, M., SAKURADA, K., KIM, T.-H. & KANEKO, K. (2001). Comparative Study of Turbines for Wave Energy Conversion. *Journal of Thermal Science,* 10**,** 26-31.

MAGUIRE, A. E. (2011). *Geometric design considerations and control methodologies for absorbing wavemakers.* PhD thesis, University of Edinburgh.

MAGUIRE, A. E. & INGRAM, D. M. (2009). Hydrodynamics and absorption efficiencies of wavemakers. *8th European Wave and Tidal Energy Conference.* Uppsala, Sweden.

MARJANI, A. E., CASTRO, F., BAHAJI, M. & FILALI, B. (2006). 3D Unsteady Flow Simulation in an OWC Wave Converter Plant. *International Conference on Renewable Energies and Power Quality (ICREPQ '06).* Palma de Mallorca.

MARJANI, A. E., CASTRO RUIZ, F., RODRIGUEZ, M. A. & PARRA SANTOS, M. T. (2008). Numerical modelling in wave energy conversion systems. *Energy,* 33**,** 1246-1253.

MARTINS, E., RAMOS, F. S., CARRILHO, L., JUSTINO, P., GATO, L., TRIGO, L. & NEUMANN, F. (2005). CEODOURO PROJECT: OVERALL DESIGN OF AN OWC : IN THE NEW OPORTO BREAKWATER. *6th European Wave and Tidal Energy Conference* Glasgow, UK.

MASUDA, Y. (1971). Wave-activated generator. *Int. Coll. on the Expositions of the Oceans (Trans.).* Bordeaux, France.

MASUDA, Y. (1991). Improvement of Economy of Wave Power Generation by Backward Bent Duct Buoy. *OCEANS '91. 'Ocean Technologies and Opportunities in the Pacific for the 90's'. Proceedings.*

MASUDA, Y., KUBOKI, T., THAKKER, A., LEWIS, T., LIANG, X. & SUN, P. (2002). Prospect of Economical Wave Power Electric Generator by the Terminator Backward

Bent Duct Buoy (BBDB). *Twelfth International Offshore and Polar Engineering Conference.* Kitakyushu, Japan.
MASUDA, Y., YAMAZAKI, T., OUTA, Y. & MCCORMICK, M. (1987). Study of Backward Bent Duct Buoy. *OCEANS '87.* Halifax, Canada.
MASUDA, Y., YAMAZAKI, T., OUTA, Y. & MCCORMICK, M. E. (1988). The Backward Bent Duct Buoy - An Improved Floating Type Wave Power Device. *OCEANS '88. 'A Partnership of Marine Interests'. Proceedings.*
MCCORMICK, M. E. (1974a). Analysis of a Wave Energy Conversion Buoy. *Journal of Hydronautics,* 8**,** 77-82.
MCCORMICK, M. E. (1974b). A Parametric study of a Wave-Energy Conversion Buoy. *Offshore Technology Conference.* Houston, Texas.
MCCORMICK, M. E. (1976). A modified linear analysis of a wave-energy conversion buoy. *Ocean Engineering,* 3**,** 133-144.
MCCORMICK, M. E., CARSON, B. & RAU, D. (1975). An Experimental Study of a Wave-Energy Conversion Buoy. *Marine Technology Society,* 9**,** 39-42.
MCCORMICK, M. E. & SHEEHAN, W. E. (1992). Positive Drift of Backward-Bent Duct Barge. *Journal of Waterway, Port, Coastal, and Ocean Engineering,* 118**,** 106-111.
MICHEL, W. H. (1999). Sea Spectra Revisited. *Marine Technology,* 36**,** 211-227.
MORRISON, G. L., HALL, K. R., HOLSTE, J. C., MACEK, M. L., IHFE, L. M., DEOTTE JR, R. E. & TERRACINA, D. P. (1994). Comparison of orifice and slotted plate flowmeters. *Flow Measurement and Instrumentation,* 5**,** 71-77.
MORRISON, I. G. (1995). *The Hydrodynamic Performance of an Oscillating Water Column Wave Energy Converter.* PhD, University of Edinburgh.
MORRISON, I. G. & GREATED, C. A. (1992). Oscillating Water Column Modelling. *23rd Conference on Coastal Engineering.* Venice, Italy.
MÜLLER, G. & J.T. WHITTAKER, T. (1995). Visualisation of flow conditions inside a shoreline wave power-station. *Ocean Engineering,* 22**,** 629-641.
MYERS, L. E., BAHAJ, A. S., RETZLER, C., PIZER, D., GARDNER, F., BITTENCOURT, C. & FLINN, J. (2010). EquiMar Deliverable D5.2 - Device Classification Template *Equitable Testing and Evaluation of Marine Energy Extraction Devices in terms of Performance, Cost and Environmental Impact - 213380.* EQUIMAR.
NAREC (2005). Test Results Offshore Wave Energy Limited #DO1-0004-R7, National Renewable Energy Centre.
NATANZI, S., TEIXEIRA, J. A. & LAIRD, G. (2011). A Novel High-Efficiency Impulse Turbine for Use in Oscillating Water Column Devices. *9th European Wave and Tidal Energy Conference.* Southampton, UK.
NEWMAN, J. N. (1992). Panel methods in marine hydrodynamics. *11th Australasian Fluid Mechanics Conference.* Hobart, Tasmania.
NWOGU, O. G. & DEMIRBILEK, Z. (2001). BOUSS - 2D: A Boussinesq Wave Model for Coastal Regions and Harbors. *Technical Report ERDC/CHL TR-01-25, U.S.* . Army Engineer Research and Development Center, Vicksburg, MS.
O'BOYLE, M. L., ELSAESSER, B., WHITTAKER, T. & FOLLEY, M. (2011). Assessment of Wave Basin Homogeneity for Wave Energy Converter Array Studies. *9th European Wave and Tidal Energy Conference.* Southampton, UK.
O'SULLIVAN, D., GRIFFITHS, J., EGAN, M. G. & LEWIS, A. W. (2010). Development of an Electrical Power Take Off System for a Sea-Test Scaled Offshore Wave Energy Device. *Renewable Energy,* 36**,** 1236-1244.
OWEL (2005). Initial Development Phase Project Report, Offshore Wave Energy Limited.
PAIXÃO CONDE, J. M. & GATO, L. M. C. (2008). Numerical study of the air-flow in an oscillating water column wave energy converter. *Renewable Energy,* 33**,** 2637-2644.
PALME, A. (1920). Wave Motion Turbine. *Power,* 52**,** 200-201.
PAYNE, G. (2008). Guidance for the Experimental Tank Testing of Wave Energy Converters. *SuperGen Marine Report.*
PEGRUM, M. (2001). Tank Testing of a Wave Energy Converter. QinetiQ.

PIERSON, W. J., JR. & MOSKOWITZ, L. (1964). A Proposed Spectral Form for Fully Developed Wind Seas Based on the Similarity Theory of S. A. Kitaigorodskii. *J. Geophys. Res.,* 69**,** 5181-5190.

PITT, E. G. (2006). The wave power climate at the Wave Hub site - Applied Wave Research. SWERDA.

PONTES, M. T., CÂNDIDO, J., HENRIQUES, J. C. C. & JUSTINO, P. (2005). Optimizing OWC Sitting in the Nearshore. *6th European Wave and Tidal Energy Conference.* Glasgow, UK.

PRADO, D., GARDNER, DAMEN & POLINDER (2006). Modelling and test results of the Archimedes wave swing. *Proceedings of the I MECH E Part A Journal of Power and Energy,* 220**,** 855-868.

PRASAD, D., KEDARNATH, S., BIREN, P., PURNIMA, J. & JAYASHANKAR, V. (2011). Performance analysis of a floating power plant with a unidirectional turbine based power module. *World Renewable Energy Congress.* Linköping, Sweden.

RABINOVICH, A. B. (2009). Seiches and Harbor Oscillations. *In:* KIM, Y. C. (ed.) *Handbook of Coastal and Ocean Engineering.* Singapore: World Scientific Publishing.

RAGHUNATHAN, S. (1995a). *A methodology for Wells turbine design for wave energy conversion,* Bury St Edmunds, ROYAUME-UNI, Professionnal Engineering Publishing.

RAGHUNATHAN, S. (1995b). The wells air turbine for wave energy conversion. *Progress in Aerospace Sciences,* 31**,** 335-386.

RAGHUNATHAN, S., CURRAN, R. & WHITTAKER, T. J. T. (1995). Performance of the Islay Wells Air Turbine. *Institution of Mechanical Engineers - Part A: Journal of Power and Energy***,** 55-62.

RAGHUNATHAN, S. & TAN, C. P. (1982). Performance of the Wells turbine at starting. *Journal of Energy,* 6**,** 430-431.

RAWSON, K. J. & TUPPER, E. C. (1994). *Basic Ship Theory*, Longman Scientific & Technical

READER-HARRIS, M. J. & SATTARY, J. A. (1990). The orifice plate discharge coefficient equation. *Flow Measurement and Instrumentation,* 1**,** 67-76.

RENEWABLEUK (2011a). State of the Industry Report - Onshore and Offshore Wind: A Progress Update.

RENEWABLEUK (2011b). Wave and Tidal in the UK - A State of the Industry Report.

SALTER, S. H. (1974). Wave power. *Nature,* 249**,** 720-724.

SARMENTO, A. (2010). State of the Art Report WP1 - Numerical Modelling of Wave Energy Converters. *Deliverable Report of Wavetrain 2, FP7 ITN 215414.* Ecole Centrale de Nantes.

SARMENTO, A. J. N. A. (1992). Wave flume experiments on two-dimensional oscillating water column wave energy devices. *Experiments in Fluids,* 12**,** 286-292.

SARMENTO, A. J. N. A. (1993). Model-Test Optimization of an OWC Wave Power Plant. *International Journal of Offshore and Polar Engineering,* 3.

SARMENTO, A. J. N. A. & FALCÃO, A. F. D. O. (1985). Wave generation by an oscillating surface-pressure and its application in wave-energy extraction. *Journal of Fluid Mechanics,* 150**,** 467-485.

SCUOTTO, M. & FALCÃO, A. F. D. O. (2005). Wells and Impulse Turbines in an OWC Wave Power Plant: A Comparison. *6th European Wave and Tidal Energy Conference.* Glasgow, UK.

ŞENTÜRK, U. & ÖZDAMAR, A. (2011). Modelling the Interaction between Water Waves and the Oscillating Water Column Wave Energy Device. *MATHEMATICAL & COMPUTATIONAL APPLICATIONS,* Vol. 16, No. 3**,** pp. 630-640.

SETOGUCHI, T., RAGHUNATHAN, S., TAKAO, M. & KANEKO, K. (1997). Air-Turbine with Self-Pitch-Controlled Blades for Wave Energy Conversion (Estimation of Performances in Periodically Oscillating Flow). *International Journal of Rotating Machinery,* 3**,** 233-238.

SETOGUCHI, T., SANTHAKUMAR, S., MAEDA, H., TAKAO, M. & KANEKO, K. (2001). A review of impulse turbines for wave energy conversion. *Renewable Energy,* 23**,** 261-292.

SETOGUCHI, T. & TAKAO, M. (2006). Current status of self rectifying air turbines for wave energy conversion. *Energy Conversion and Management,* 47**,** 2382-2396.

SEYMOUR, R. J. (1992). *Ocean Energy Recovery: The State of the Art*, Amer Society of Civil Engineers

SHENG, W., LEWIS, T., ALCORN, R., JOHANING, L. & KIRRANE, P. (2010). Experimental Investigation of Hydrodynamic Characteristics of a Moored Floating WEC. *3rd International Conference on Ocean Energy.* Bilbao, Spain.

SMITH, H. C. M., HAVERSON, D., SMITH, G. H., CORNISH, C. S. & BALDOCK, D. (2011). Assessment of the Wave and Current Resource at the Wave Hub Site. *PRIMaRE Report for Wave Hub, UK*.

SMITH, H. C. M., PEARCE, C. & MILLAR, D. L. (2012). Further analysis of change in nearshore wave climate due to an offshore wave farm: An enhanced case study for the Wave Hub site. *Renewable Energy,* 40**,** 51-64.

SØRENSEN, H. C. & FRIIS-MADSEN, E. (2010). Wave Dragon from Demonstration to Market. *3rd International Conference on Ocean Energy.* Bilbao, Spain.

SORENSEN, R. M. (2006). *Basic Coastal Engineering*, Springer.

SPENCER, E. A. (1982). Progress on international standardization of orifice plates for flow measurement. *International Journal of Heat and Fluid Flow,* 3**,** 59-66.

STANSELL, P. & PIZER, D. J. (2012). Maximum wave-power absorption by attenuating line absorbers under volume constraints. *Applied Ocean Research - In Press,* arXiv:1112.3494v4 [physics.flu-dyn].

STEER, A. P. (2002). Theoretical Analysis of a Wave Energy Converter. QinetiQ.

STERN, N. (2006). *The Economics of Climate Change: The Stern Review*, {Cambridge University Press}.

STIVEN, T. (2012). OPT Technology Update – the drive for scale, efficiency, reliability and lower cost. *Ocean Energy Conference.* Brussels, Belgium.

STREET, K. (2009). Orecon's 1.5MW MRC– a wave energy device for a 25 year commercial life. *WavEC Seminar.* Lisbon, Portugal.

SUZUKI, M., KUBOKI, T., NAGATA, S. & SETOGUCHI, T. (2011). Numerical Investigation of 2D Optimal Profile of Backward-Bent Duct Type Wave Energy Converter. *Journal of Offshore Mechanics and Arctic Engineering,* 133**,** 041602-8.

SUZUKI, M., TAKAO, M., S.NAGATA, SETOGUCHI, T. & ARAKAWA, C. (2010). Performance Prediction of OWC Type Floating Wave Power Generation Installing Impulse Turbine *3rd International Conference on Ocean Energy.* Bilbao, Spain.

SZUMKO, S. (1989). Mechanical Model for Oscillating Water Column with Compressibility. *Journal of Engineering Mechanics,* 115**,** 1851-1866.

TAKAO, M. & SETOGUCHI, T. (2012). Air Turbines for Wave Energy Conversion. *International Journal of Rotating Machinery,* 2012**,** 10.

TAKAO, M., SETOGUCHI, T., KANEKO, K. & INOUE, M. (1997). Air Turbine with Self-Pitch Controlled Blades for Wave Energy Conversion. *International Journal of Offshore and Polar Engineering,* 7.

TAYLOR, J. R. M. & CALDWELL, N. J. (1998). Design and Construction of the Variable-Pitch Air Turbine for the Azores Wave Energy Plant. *3rd European Wave Power Conference.* Patras, Greece.

TEASE, W. K. (2003). Dynamic Response of a Variable Pitch Wells Turbine *5th European Wave Energy Conference.* Cork, Ireland.

TEASE, W. K., LEES, J. & HALL, A. (2007). Advances in Oscillating Water Column Air Turbine Development. *7th European Wave Energy Conference.* Porto, Portugal.

TEDD, J., KOFOED, J. P., JASINSKI, M., MORRIS, A., E. FRIIS-MADSEN, WISNIEWSKI, R. & BENDTSEN, J. D. (2007). Advanced Control Techniques for WEC Wave Dragon. *7th European Wave and Tidal Energy Conference.* Porto.

THAKKER, A., FRAWLEY, P., KHALEEQ, H. B. & BAJEET, E. S. (2001). Comparison of 0.6m Impulse and Wells Turbines for Wave Energy Conversion Under Similar Conditions *Eleventh lnternational Offshore and Polar Engineering Conference* Stavanger, Norway.

THAKKER, A. & HOURIGAN, F. (2004). Modeling and scaling of the impulse turbine for wave power applications. *Renewable Energy,* 29**,** 305-317.

THAKKER, A., JARVIS, J. & SAHED, A. (2009). Design charts for impulse turbine wave energy extraction using experimental data. *Renewable Energy,* 34**,** 2264-2270.

THOMAS, G. (2008). The Theory Behind the Conversion of Ocean Wave Energy: a Review. *In:* CRUZ, J. (ed.) *OceanWave Energy - Current Status and Future Prepectives.* Springer.

THORPE, T. (1999). A Brief Review of Wave Energy, ETSU Report R-120 for the UK Department of Trade and Industry. (Energy Technology Support Unit).

TORRE-ENCISO, Y., ORTUBIA, I., AGUILETA, L. I. L. D. & MARQUÉS, J. (2009). Mutriku Wave Power Plant: from the thinking out to the reality. *8th European Wave and Tidal Energy Conference.* Uppsala, Sweden.

VENUGOPAL, V., DAVEY, T., SMITH, H., SMITH, G., CAVALERI, L., PREVOSTO, M., GIRARD, F., LAWRENCE, J. & HOLMES, B. (2011). Resource Assessment - Wave Resource Characterisation and Site Assessment. *In:* INGRAM, D., SMITH, G., BITTENCOURT-FERREIRA, C. & SMITH, H. (eds.) *Protocols for the Equitable Assessment of Marine Energy Converters - EquiMar Deliverable Report.*

WASHIO, Y., OSAWA, H. & OGATA, T. (2001). The Open Sea Tests of The Offshore Floating Type Wave Power Device "Mighty Whale" - Characteristics of Wave Energy Absoption and Power Generation.

WAVEGEN (2002). Research into the Further Development of the Limpet Shoreline Wave Energy Plant - Final Report. *Report for DTI Sustainable Energy Programme, ETSU V/06/00183/REP.*

WAVEGEN (2003). Research into the Further Development of the Limpet Shoreline Wave Energy Plant - Supplement to the Final Report. *Report for DTI Sustainable Energy Programme, ETSU V/06/00183/REP.*

WAVEPLAM (2009). State of the Art Analysis - A Cautiously Optimistic Review of the Technical Status of Wave Energy Technology. *Waveplam project - funded under the Intelligent Energy Europe Programme, EIE/07/038/SI2.466832*

WEBER, J. (2007). Representation of non-linear aero-thermodynamic effects during small scale physical modeling of OWC wave energy converters. *Proceedings of the 7th European Wave and Tidal Energy Conference.* Porto, Portugal.

WESTPHALEN, J., GREAVES, D. M. & WILLIAMS, C. J. K. (2007). Comparison of Free Surface Wave Simulations using STAR CCM+ and CFX. *10th Numerical Towing Tank Symposium.* Hamburg, Germany.

WHITE, P. R. S. (1991). A phenomenological design tool for Wells turbines. *Seminar on wave energy - Institute of Mechanical Engineers.* London, UK.

WHITTAKER, T., COLLIER, D., FOLLEY, M., OSTERRIED, M., HENRY, A. & CROWLEY, M. (2007). The development of Oyster - A shallow water surging wave energy converter *7th European Wave and Tidal Energy Conference.* Porto, Portugal.

WHITTAKER, T. J. T. (1993). The development of shoreline wavepower in the UK. *Renewable Energy - Clean Power 2001, 1993., International Conference on.*

WHITTAKER, T. J. T. (1997). Learning Form The Islay Wave Power Plant. *IEE Colloquium on Wave Power: An Engineering and Commercial Perspective (Digest No: 1997/098).* London, UK.

WHITTAKER, T. J. T., BEATTIE, W., FOLLEY, M., BOAKE, C., WRIGHT, A. & OSTERRIED, M. (2004). The Limpet Wave Power Project – The First Years Of Operation. *Scottish Hydraulics Study Group - Seminar on the Hydraulic Aspects of Renewable Energy.*

WHITTAKER, T. J. T., BEATTIE, W., RAGHUNATHAN, S., THOMPSON, A., STEWART, T. & CURRAN, R. (1997). The Islay Wave Power Project: An Engieering Perspective. *Proceedings of the ICE - Water Maritime and Energy,* 124**,** 189 -201.

WHITTAKER, T. J. T., LONG, A. E., THOMPSON, A. & MCILWAINE, S. J. (1991). Islay Gulley Shoreline Wave Energy Device Phase 2 Device Construction and Pneumatic Power Monitoring,. *Report No. T-WV-1680. Energy Technology Support Unit Harwell.*

WILSON, B. (1972). Seiches. *In:* CHOW, V. T. (ed.) *Advances in Hydrosciences.*

WINTER, A. J. B. (1980). The UK wave energy resource. *Nature,* 287**,** 826-828.

YEMM, R. (2008). Pelamis. *In:* CRUZ, J. A. (ed.) *Ocean Wave Energy - Current Status and Future Perspectives.* Springer.

YEMM, R., PIZER, D., RETZLER, C. & HENDERSON, R. (2012). Pelamis: experience from concept to connection. *Philosophical Transactions of the Royal Society A: Mathematical, Physical and Engineering Sciences,* 370**,** 365-380.

YOON, J. Y., SUNG, N. W. & LEE, C. H. (2009). Effect of distance between 90° elbow close to upstream of orifice plate and the orifice plate on discharge coefficient. *Proceedings of the Institution of Mechanical Engineers, Part E: Journal of Process Mechanical Engineering,* 223**,** 97-100.

YOU, Y., SHENG, S., WU, B. & HE, Y. (2012). Wave energy technology in China. *Philosophical Transactions of the Royal Society A: Mathematical, Physical and Engineering Sciences,* 370**,** 472-480.

ZHANG, Y., ZOU, Q.-P. & GREAVES, D. (2012). Air-water two-phase flow modelling of hydrodynamic performance of an oscillating water column device. *Renewable Energy,* 41**,** 159-170.

ZULLAH, M., PRASAD, D., AHMED, M. & LEE, Y.-H. (2010). Performance analysis of a wave energy converter using numerical simulation technique. *SCIENCE CHINA Technological Sciences,* 53**,** 13-18.

11 Published Papers

Parts of this work have been presented at international conferences and published in a journal. The references for the four conference papers the journal paper are provided below.

LEYBOURNE, M., BATTEN, W. M. J., BAHAJ, A. S., O'NIANS, J. & TRAYLOR, H. (2008). Preliminary findings from a laboratory scale model of a ducted wave energy converter, 10th World Renewable Energy Congress, Glasgow, UK.

LEYBOURNE, M., BATTEN, W. M. J., BAHAJ, A. S., O'NIANS, J. & MINNS, N. (2009) A Parametric Experimental Study of the 2D Performance of a Ducted Wave Energy Converter. 8th European Wave and Tidal Energy Conference, Uppsala, Sweden.

LEYBOURNE, M., BATTEN, W. M. J., BAHAJ, A. S., MINNS, N. & O'NIANS, J. (2010). Experimental and Computational Modelling of the OWEL Wave Energy Converter. 3rd International Conference on Ocean Energy, Bilbao, Spain.

LEYBOURNE, M., BATTEN, W. M. J., BAHAJ, A. S., MINNS, N. & O'NIANS, J. (2011). Preliminary design of the OWEL wave energy converter commercial demonstrator. World Renewable Energy Congress, Linköping, Sweden.

LEYBOURNE, M., BATTEN, W. M. J., BAHAJ, A. S., MINNS, N. & O'NIANS, J. (2012) Preliminary Design of the OWEL Wave Energy Converter Pre-Commercial Demonstrator. Renewable Energy, Available online 13 September 2012, ISSN 0960-1481, 10.1016/j.renene.2012.08.019.

Appendices

A1 Review of OWEL Development Work

A1.1 Proof of Concept Physical Modelling

The initial experimental studies of the device were funded by a DTI Smart grant and were conducted by QinetiQ under contract from OWEL to test a "1:100" scale model. Experiments were carried out in a towing tank at the Southampton Solent University with regular waves, detailed in Table 24, for both floating and static models in various geometrical configurations. The dimensions of the tank are 60 m x 3.7 m x 1.8 m deep and so were well suited for 1:100, deep water conditions however, reflections owing to the relatively narrow separation between the model and tank walls would have influenced the tests. The internal duct length of the model was 1.57 m, a beam of 0.61 m and draught of 0.39 m at the duct entrance.

The objectives of this first phase of physical investigations were to;

- prove the operating concept of the device
- test the sensitivity of performance to geometric configurations
- to provide results to validate a theoretical model.

The waves chosen for the testing were based on the assumption that the model was of 1:100 scale as, at the time, the belief was the full scale device would be approximately 150 m long, although there was no data to back this up. These conditions therefore represented waves of 7.5, 8.5 and 10 seconds in period and ranging from 4 – 8 m in height. Currently, the duct length of the full scale OWEL demonstrator is proposed to be approximately 42m long making this particular model ~1:27 scale. This implies that the scaled size of the wave conditions were too small for the actual size of the duct tested. In hindsight, it would have been more appropriate to test fewer configurations, over a wider range of wave conditions in order to prove the concept and study the performance characteristics.

Table 24, The eight wave conditions used throughout the testing.

#	Wave Period [s]	Wave Height [mm]	Wavelength/Duct Length
1	0.75	40	0.56
2	0.75	60	0.56

3	0.85	40	0.72
4	0.85	60	0.72
5	0.85	80	0.72
6	1.00	40	0.99
7	1.00	60	0.99
8	1.00	80	0.99

It was originally conceived that the incident wave would compress the air trapped ahead of the crest within the duct before a non-return valve opened and allowed the compressed air to exit. The pressurised air would then pass into a pressure vessel acting as an accumulator and energy storage so that the air it contained could be released at a steady rate through an air turbine PTO. This system was simulated on this small scale model and the pressure accumulation vessel, with a volume of 0.023 m^3, can be seen mounted on top of the duct in Figure 3.10. Whilst in principle this seems like a reasonable method, the practicalities of applying it in small scale testing are challenging. This was demonstrated in these tests as the non-return valve and pressure vessel brought about the most sources of errors and uncertainty. The non-return valve had an opening pressure of 500 Pa. This was sufficient for the first few waves of each run however, once the pressure inside the vessel had risen above 500 Pa, the pressure generated in the duct was too low to open the valve. In addition, after each run, the pressure vessel was depressurised by opening a tap and it was thought that inconsistent sealing of the tap caused a leak from the reservoir, resulting in further losses and uncertainty.

The performance of the model was measured in two ways; the peaks of the air pressure before the non-return valve were taken and averaged to give a mean peak P1 value and this was compared with the mean of the "steady state" pressure of the air accumulator, P2. The steady state pressure was deemed as an average of the pressure within the accumulator between 2/3rds of the way through the test and the end of the run. In many cases where only the first few waves delivered air to the accumulator, the mean peak, P1 pressure was very similar to that of the P2 steady state. The issues with the non-return valve hindered the drawing of any firm conclusions. The reservoir pressure did not rise as expected because of this and so only pressures developed within the duct were suitable indicators of performance. It is also likely that the bulky pressure reservoir would have affected the motions of the duct when floating, as this would have raised the position of the Centre of Gravity (CoG), therefore reducing the stability.

Perhaps though, the greatest affect this PTO method would have had on the conversion performance was the damping and resistance it applied to the air and progressing wave. OWCs are sensitive to the damping from the PTO, as discussed in section 3.4.2, and it has since been shown in section 0 that OWEL behaves similarly. The non-return valve did not open until a pressure differential of 500 Pa had been achieved between the duct and the accumulator. This therefore, would have effectively applied a very high level of damping, due to the work done on the compression of the air pocket as the wave advanced. It is likely that in some cases, the pressure within the duct would have broken the seal between the wave crest and the duct roof, causing the trapped air to be lost out of the duct entrance. This is another uncertainty from the testing and not enough data exists to investigate these theories further.

During the testing the model was modified to examine the effect of geometry on the device's performance. The ramp and side wall angle were altered, baffle modified and freeboard depth changed. This concluded the following:

- Sidewall angle had some effect on the pressure within the duct but was not significant.
- Horizontal duct floor produced largest pressures with long waves.
- Steepest floor produced largest pressure with short waves.
- Removal of the floor significantly reduced the generated pressures as the internal wave maintained deep water conditions and so did not increase in height.

Two sets of tests with 8 waves were run with the model free floating but loosely tethered to a gantry over the tank. The two runs differed in that, in the initial set, the model had a freeboard of 100 mm whereas this was reduced to 50 mm in the second test. A set of accelerometers measured the magnitude of the motions in 6 DoF. As would be expected from uni-directional, regular waves, the duct roll angles were low and for the majority of tests was less than 0.5°. Despite the loose lines not offering the restoring force of a mooring system, the pitch magnitude was relatively low. The greatest angle recorded was 2.3° with wave #5, the steepest wave in the tests. It is likely that the short wavelength waves kept the pitch excursions to a minimum. It has been seen in recent physical modelling, section 6.5.7, that pitch is small for low ratios of wavelength to duct length. The results indicated that the pressures generated in the free floating model were comparable to those from the static with only a slight reduction in some cases. Whilst this may have been the case for the peak air pressures evolved within the duct, it is likely that the resulting flow rates that would have been lower although no data was presented to show this.

The optimum configuration that performed well across the range of waves, with generally the highest pressures, was a static model with a 50 mm freeboard. A summary of the input waves

and mean peak pressures evolved within the duct is given in Table 25. However, without knowing time series data for these cases it is not possible to draw any accurate conclusions or calculate the energy converted. The pressures recorded here may be as a result of a short peak pressure event in each wave cycle. In comparison to the results from the initial 2D testing in section 4.7.8, the mean peak pressures are greater due to the larger geometry and much higher resistance to flow provided by the non-return valve in comparison to an orifice.

Table 25, Summary of wave conditions and pressures for the best static configuration.

Wave Test #	T [s]	Nominal H [mm]	Actual H [mm]	Mean P1 peaks [Pa]
1	0.75	40	43.53	419.9
2	0.75	60	66.44	849.8
2	0.75	60	67.13	662.3
3	0.85	40	44.63	497.1
4	0.85	60	65.18	1089.2
5	0.85	80	96.53	1209.5
6	1.00	40	39.33	533.6
7	1.00	60	62.19	897.6
8	1.00	80	84.75	1049.8

The results from the tests concluded that, rather intuitively for WECs, the geometry of the duct should be tuned to the wave conditions of the typical wave environment at a site. The tests showed the importance of setting a suitable freeboard to ensure wave crests make a seal within the duct. Setting this too small ensures a seal but this also reduces the capture volume of air ahead of the wave. This suggests that an optimum freeboard level was achievable to strike a balance between sealing performance and maximum air flow. This was investigated in the initial 2D testing and an alternative model configuration was conceived to reduce the sensitivity of performance due to freeboard.

As a result of an unsuitable model scale PTO, limited wave test conditions and a lack of data from the tests, little can be concluded from the available report and these physical investigations. The results from these tests were used to calibrate a theoretical model which was developed in parallel with the physical modelling.

A1.2 Proof of Concept Theoretical Modelling

A mathematical model of the performance of OWEL was prepared and run by QinetiQ in 2001 and was reported by Steer (2002). The model was written using the mathematical software, 'Maple™' prior to the commencement of the 1:100 hydrodynamic tests and then modified afterwards to incorporate the learning achieved throughout the study. The objectives of the theoretical modelling were to provide a model of a static device that was calibrated to the results from the physical testing and that could be scaled up to provide a full scale, power output prediction.

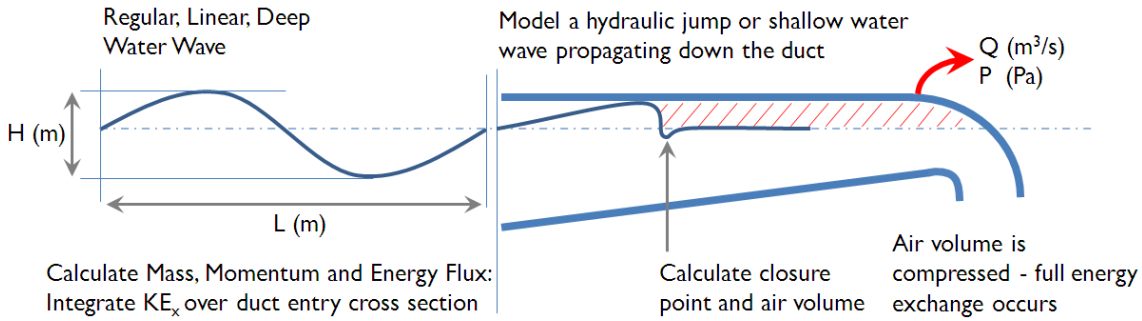

Figure 11.1, Schematic of the processes in the initial theoretical model.

The conversion process was subdivided into several phases, each described using a simplified physical model. The simplifications were necessary to avoid complications arising from non-linearities. Figure 11.1 shows a schematic of the breakdown of the processes modelled and the calculations made. A regular, sinusoidal wave was initially specified with a height and wavelength. The horizontal kinetic energy of the wave was integrated over the capture depth of the duct entrance and multiplied by the beam to provide an energy flux into the duct. In addition, the mass and momentum fluxes from the wave were also calculated. Within the duct the wave was modelled either as a hydraulic jump or a smooth, shallow water wave if its strength was calculated to be insufficient to generate a hydraulic jump. The point of sealing, or closure point, was calculated at the point where the cross section of water behind the hydraulic jump equalled the duct cross section. From that point the volume of trapped air ahead of the closure point was determined. Assuming an isothermal, ideal process the wave front does work on the air volume as it propagates, compressing the air. Compression continues until the non-return valve opening pressure is achieved, at which point the pressure and volume flow rate of the air into the accumulator were calculated. In the revision of the model following the physical tests, the hydraulic jump model was abandoned and instead the internal wave was assumed to be a deep water wave with a modified wave amplitude.

The simplifications in the model neglected a number of loss mechanisms which were deemed too small or impractical to calculate and included;

- transients from the formation of the water surge within the duct
- viscous propagation losses of the wave front
- increasing gravitational potential energy as the wave moves up the ramp
- flow losses in the airways
- leakage losses from a physical device

However, perhaps the greatest simplification made was to assume that the internal wave transmits all of its energy into the air being compressed. This would mean that no remnant kinetic energy would be present in the water after the air is compressed. It was observed in the initial 2D tests (see chapter 4) that actually a large proportion of remnant wave energy exists within the water after compressing the air. Therefore, an energy dispersing baffle is required for efficient operation. By neglecting this energy loss, any results would have certainly over estimated conversion performance and air pressures developed.

In comparison to the experimental results, the model predicted pressures between 10 % and 100 % greater than those measured. The wide range of deviation can be attributed to the simplicity of the model and the amount of loss mechanisms neglected. The trapped volume of air calculated was also over estimated and so a calibration factor was applied to this based on the physical results. The parameters of the model were then scaled up by a factor of 100 as this was also assumed to be a 1:100 scale representation. This was then tested with a wave with a height of 6 m and length of 100 m equating to a period of approximately 8 seconds. Whereas, the model had predicted a small scale efficiency of ~45 % for the scaled version of this wave, at full scale it predicted a conversion efficiency of ~17 %. Efficiency was defined as the ratio of average power delivered to the reservoir to the incident wave power. Differences in performance can be attributed to assumptions made on the removal of air from the accumulator by a turbine and that the accumulator volume was scaled cubically. It was concluded that an optimum accumulator volume was required to reduce losses from the compression within the duct to expansion into the oversized accumulator.

The results from the theoretical investigation are limited and had few conclusions. It was however recommended that;

- the device be operated with a large draught to capture maximum wave energy
- in-depth investigations be carried out into the flow processes involved in wave sealing
- a general improved knowledge be gained before conducting larger scale testing.

Despite these recommendations being made by both components of this phase of testing, no additional investigations were made before proceeding to the much larger scale device a few years later. A successful application by OWEL for funding from the Carbon Trust was based upon the results of this initial proof of concept study. It would seem therefore, that this preliminary work proved the concept and demonstrated OWEL's potential as a full scale WEC.

A1.3 Intermediate Scale Testing

Following on from the early investigations, a test programme comprising studies of a series of "1:10" scale models was conducted by the National Renewable Energy Centre, Narec [NaREC (2005)], under the supervision of OWEL funded by the Carbon Trust, grant #2003-3-122 [Carbon Trust (2003)]. Three individual devices, with dimensions summarised in Figure 11.2, were constructed from sheet steel with a supporting, structural frame and in total, weighed approximately 4 tonnes. With modifications to one of the devices, a total of five different model geometrical configurations were tested with 9 regular wave conditions as summarised in Table 26. The geometries and test conditions were intended to represent 1:10 scale as, at the time, it was anticipated that the full scale device would likely be ~150 m in length. In each case the models were rigidly fixed within the wave tank on top of a steel, shipping container and the freeboard set at 0.15 m. These tests were very similar in terms of objectives, to the 1:100 study;

- Compare scaled up performance with the previous '1:100' results.
- Geometric optimisation of side wall angle, floor angle, baffle and a remedial modification to the duct entrance.
- Provide data to calibrate and validate theoretical model, see section 3.3.4.

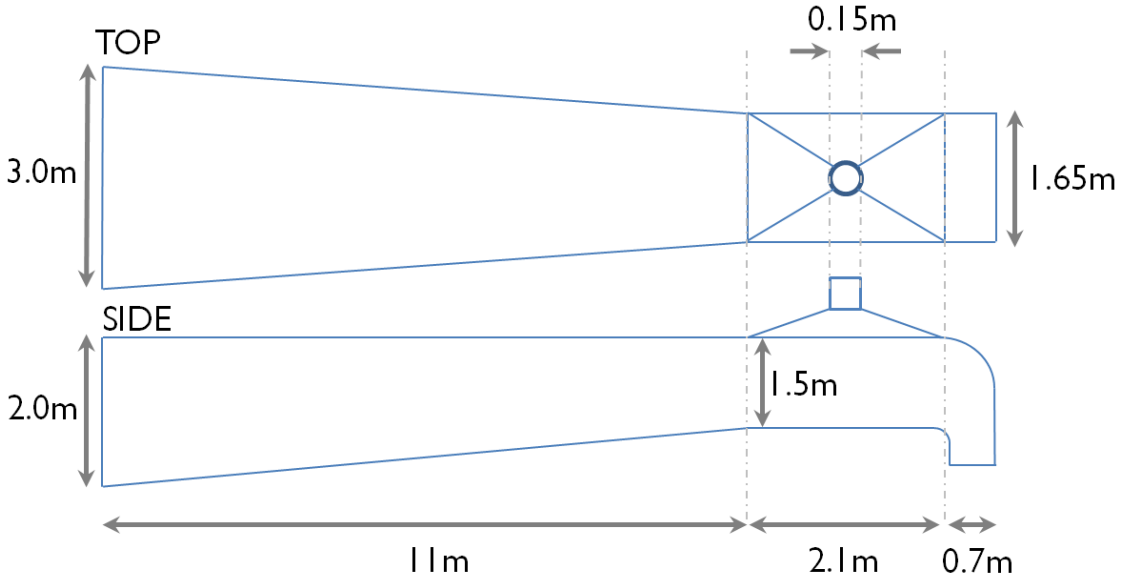

Figure 11.2, Sketch of the 1:10 device showing the relevant dimensions.

Although the number of test conditions remained the same as the initial testing, the range of wavelength to duct length ratios increased. For ease of results comparison, it would perhaps have been more convenient to test the same conditions as the 1:100 tests but appropriately scaled to this model. With the scale of 1:10, these test conditions were intended to replicate waves with periods of T = 6.6 s – 12.0 s and heights of H = 2 m – 4 m. These scale to be smaller in height than those from the 1:100 tests but in a similar range of periods. As previously mentioned in the discussion of the scale for the 1:100 model, the current full scale device has a duct length of ~42 m. This would therefore imply that these tests were at a scale of 1:3.

Table 26, Summary of the test conditions for the intermediate scale physical modelling.

#	Wave Period [s]	Wave Height [m]	Wavelength/Duct Length
1	2.1	0.2	0.50
2	2.1	0.3	0.50
3	2.1	0.4	0.50
4	3.0	0.2	1.00
5	3.0	0.3	1.00
6	3.0	0.4	1.00
7	3.8	0.2	1.60
8	3.8	0.3	1.60
9	3.8	0.4	1.60

The PTO was the same design as that used in the 1:100 tests, including a large non-return valve and pressure reservoir. It was found during testing that the valve had an opening pressure of ~600 Pa which was of a similar magnitude to the typical pressures generated within the duct. The compressed air was allowed to pass through the valve along 10 m of flexible pipe to a large accumulator with a volume of ~2.7 m^3. For the majority of tests, the vessel was sealed and pressure was allowed to build up, however, it did feature an exit pipe which allowed air to be released through an orifice used to determine the flow rate.

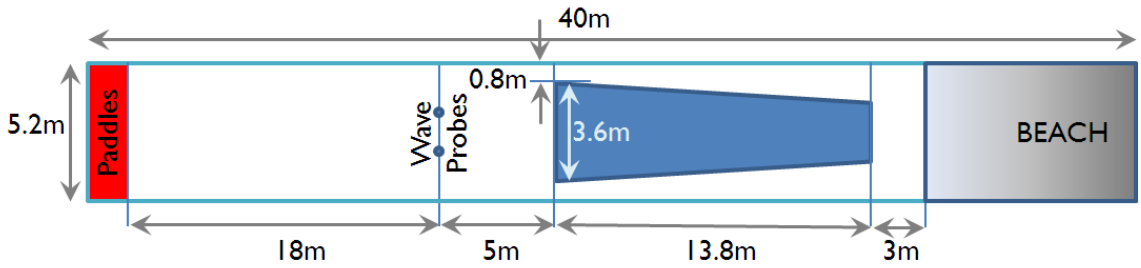

Figure 11.3, A schematic of the experimental set up within the facility.

Pressure, temperature and wave data were recorded for each run at a sample rate of 10Hz. As with the previous tests, the performance of each configuration was determined by comparison of the mean of the peaks of the pressure, upstream of the non-return valve, p_1. For waves 1 – 3, the mean peak pressures were around 1,200 Pa across all of the configurations, this rose to ~2,000 Pa for waves 4 – 6 and in excess of 3,000 Pa for waves 7 – 9. The initial analysis only commented on the trends in mean peak pressures for the different configurations in each wave condition. From this, the report concluded that the trends in pressure were not dependent on the floor or sidewall angle of the duct – the same conclusion as was reached in the previous investigation. The changes in floor angle were as a result of rotations about the duct entrance and so steepening it did not capture any additional depth of the water column. Further conclusions were that peak pressures were developed in the longer wavelength waves and when wave amplitudes substantially exceeded the WEC freeboard with a ratio of freeboard to amplitude of around 0.6. This however, this is not unexpected as these wave conditions were the most energetic in the tests and would likely have imparted the greatest pressures.

The results were reanalysed in a subsequent study and an alternative method for determining performance was introduced after external consultancy with QinetiQ. The graph in Figure 11.4 is a time history of air pressure within the duct (p_1) and pressure within the accumulator (p_2) for wave #9 (T = 3.8 s, H = 0.4 m). This shows the typical behaviour of the pressures at the start of a test. The fluctuation of p_1 was similar for each wave whereas the step increases in p_2 were large to begin but as the pressure within the accumulator increased the change in pressure due to air delivered by each cycle reduced. This power measuring approach considered the energy passing into the pressure vessel and based on the relationship that power is the product of mass flow rate and work done on the fluid.

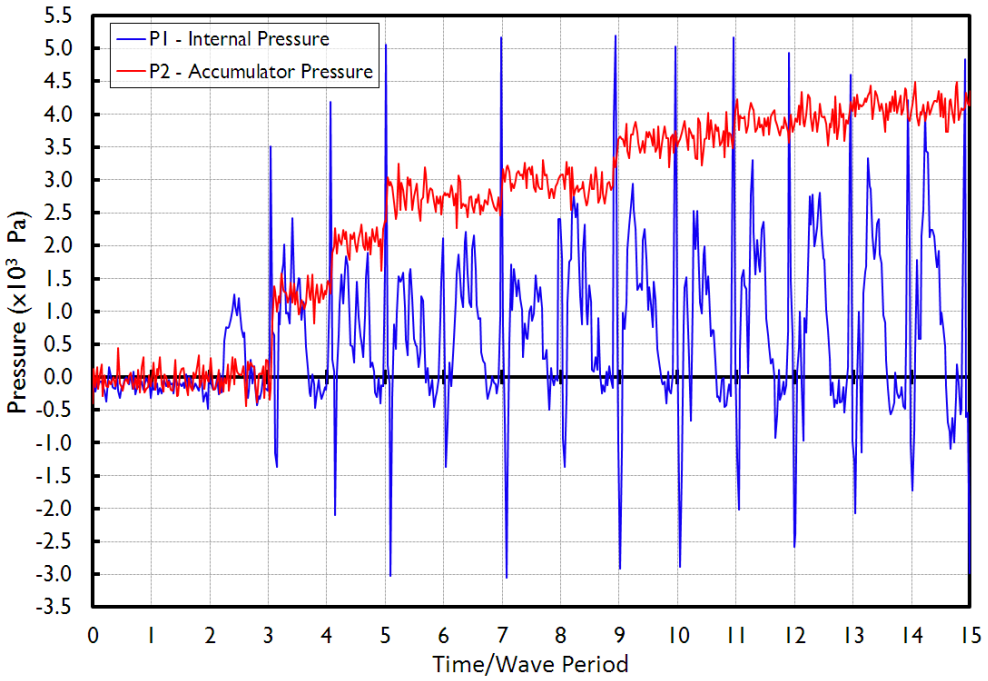

Figure 11.4, An example time history of internal (p_1) and air accumulator pressures (p_2).

With the first cycle as an example, the change in air mass within the accumulator is defined as;

$$dm = \frac{dp.V}{RT} \quad [\mathbf{kg}] \qquad [35]$$

With dp = 1,250 Pa, V = 2.96 m^3, R = 278 J/kgK, T = 288 K, the change in mass was ~0.046 kg. Taking the mean over the wave period yields the mass flow rate = 0.0121 kg/s. The work done on the fluid is

$$w = RT.ln\left(\frac{p_2}{p_0}\right) \quad [\mathbf{J/kg}] \qquad [36]$$

Where p_2/p_0 is the ratio of the pressure increase within the volume. In this instance the ratio was 1.0124 and so the work done was 1018 J/kg. The average power delivered to the accumulator over the wave cycle was therefore, 12.3 W. The power entering the duct from wave #9 was 1,790 W, so the resulting wave to pneumatic efficiency from the first cycle was less than 0.7 %.

Efficiencies in the reports available were all calculated from averages of the peaks of p_1 and p_2. These therefore assumed that the peaks were achieved within one wave cycle and not an incremental stepping function over a number of wave cycles. Typically though, most conversion efficiencies presented were less than 30 %. A summary of the mean pressures, powers and conversion efficiencies measured for a particular configuration over the nine wave conditions is presented for reference in Table 27.

Table 27, An example summary of the performance results for a device configuration.

Test #	Input Height [m]	Period [s]	Actual Height [m]	Mean Peak p_1 [Pa]	Mean p_2 Increment [Pa]	Air Power [W]	Wave Power [W]	Efficiency [%]
1	0.2	2.1	0.24	250	-100	0	345	0
2	0.2	3	0.27	930	20	0	627	0
3	0.2	3.8	0.36	1450	620	21	1407	1
4	0.3	2.1	0.36	850	260	0	783	0
5	0.3	3	0.43	2020	1840	202	1587	13
6	0.3	3.8	0.53	3600	4050	242	3237	7
7	0.4	2.1	0.47	1500	860	116	1326	9
8	0.4	3	0.6	2640	2340	1016	3048	33
9	0.4	3.8	0.64	5770	6630	1618	5556	29

A unexpected point to note is that the device tested in these 1:10 investigations was not a factor of 10 times greater than the 1:100 model and as mentioned, nor were the wave conditions. This therefore made comparisons between the two sets of tests problematic. The closest condition that follows Froude similitude is that of wave #6 from both tests, although the 1:10 scaled period should have been larger than the 3 seconds used. In the 1:100 tests, the mean peak internal pressure for wave #6 was 533.6 Pa whereas for the 1:10 tests this was ~2,200 Pa.

Perhaps the most significant issue encountered in the testing was the limited width of the wave tank with respect to the dimensions of the model. As shown in Figure 11.3, the Narec wave flume is 5.2 m wide and so the 3.6 m wide model presented a blockage of nearly 70 % in the tank. It was stated in the test report that a high level of wave reflections was observed and this limited the quality of waves and the length of run time possible. Quite simply, the device was too large for the facility.

Leakage within the PTO system added uncertainty to the data as it meant that the accumulated pressure within the reservoir decreased slowly in between waves as air escaped. This was also an issue that was encountered in the 1:100 tests and hindered the calculation of reliable power estimates. In some instances the seal between the wave crest and duct roof failed due to increasing pressure ahead of the wave front. This phenomenon was termed ‘blowblack’ because of the exiting air passing out of the duct entrance and was a result of high resistance applied by

the PTO. A lip was installed on the roof of the duct entrance to try to alleviate this but was not successful. Once again, the complex power take off system resulted in uncertainty, losses and uncertain relationship from the results.

In summary, the results from this testing programme provided little reliable evidence to demonstrate the performance of OWEL and examine the relationships of the parameters that were studied. Whilst some conclusions were given based upon the magnitude of the peak pressures within the duct, the validity of the arguments is questionable. Issues experienced during testing such as the excessive applied PTO damping, high blockage and wave reflections are the primary basis for the lack of confidence in the data. It seems that, as the budget was available, a decision was made to construct the largest model possible and test it to demonstrate the performance at a scale closer to that of a full size demonstrator. Whilst it is beneficial to examine the effects of scale before progressing to full scale, little thought appears to have been given to the practicalities this scale of testing. Geometric optimisation of any WEC should be carried out either at small scale or in numerical models. Conducting these investigations with a 4 tonne model, taking a week to set up and run nine test conditions was not a productive use of time, money or resources. Further to this, no irregular wave spectra were run and floating performance was not evaluated meaning that realistic scenarios were not investigated.

A1.4 Initial CFD Modelling

A second aspect of the Carbon Trust funded project was a theoretical study of the 1:10 scale device which was commenced prior to the physical modelling. The commercial Computational Fluid Dynamics (CFD) solver ANSYS® CFX 5™ was used in the multiphase, transient simulations. The objectives of the CFD modelling were to:

- Initially model a simplified 2D, 1:100 model.
- Validate a 3D, 1:100 model using the results from the 1:100 physical testing results.
- Create a 1:10, 3D model of the device using the validated methodology.
- Run experiments with the model to optimise the geometry, prior to physical modelling.

The model only incorporated the geometry of the duct and not the fluid domain of the wave tank. The internal domain of the solid geometry was meshed with unstructured, tetrahedral elements. A time step size equating to $1/100^{th}$ of the wave period was used for each simulation. The boundary conditions were developed in the simplified model; walls were non-slip, the baffle water exit was specified as an opening with a hydrostatic pressure determined by the water depth, the air outlet was controlled by a step function that allowed flow out of the domain

if the average pressure across the boundary was greater than the non-return valve opening pressure from the physical tests. The duct entrance boundary was used to generate regular waves that propagated into the duct. The free surface elevation, horizontal and vertical water velocities were all specified using the Airy wave equations, although an error in this has subsequently been discovered that meant at $t = 0$, the wave was $\pi/4$ through its cycle. Nevertheless, the work concluded that the boundary conditions sufficiently modelled the processes required.

The purpose of these initial simple models was to formulate and test the initial and boundary conditions, with the advantage of having experimental data, before moving to a larger simulation. The 1:100 tests were simplified to be modelled by a representative 2D model. Once the 2D boundary conditions were sufficiently developed and the model was operating as required, the 2D model methodology was applied to a 3D geometry of the 1:100 duct. For this and the subsequent 3D models, a symmetry plane, running along the longitudinal axis, was used to reduce the domain size and computational requirement. Results from a validation case for both the CFD and physical, 2D and 3D models are given in Table 28. Whilst these pressures are of similar orders of magnitude, they do not compare particularly well and it may have been useful to modify the model to improve the agreement. It is also uncertain whether more than one validation case was used to compare CFD and physical experiments.

Table 28, A summary of the results for the validation cases of the 2D and 3D models.

2D/3D Model	Parameter	Physical Modelling Pressure [Pa]	CFD Modelling Pressure [Pa]
2D	Peak Pressure	122.3	139.6
2D	Mean of Peak Pressures	78.8	42.3
3D	Peak Pressure	133.42	224.97
3D	Mean of Peak Pressures	125.26	152.38

The modelling methodology was applied to a 3D, 1:10 scale geometry which was meshed in a similar manner to the 1:100 geometry and typically comprised ~1 million elements. Simulations were run to evaluate various design features of the device such as duct length and the shape and position of the outlet. The results were post-processed to calculate the developed pressures at the outlet therefore giving an indicator of performance. Contour and vector plots such as that in Figure 11.5 were also used to show the air-water volume fraction and water velocities during testing. The model geometry was then altered in response to results and findings from the CFD

testing. The optimised geometry was used as the design basis for the structural design of the 1:10 device constructed for the physical modelling, however, no results or evidence of this optimisation procedure are given.

Figure 11.5, An example of a 1:10 scale CFD simulation showing the water volume fraction of a wave propagating along the duct.

The limited computing resource available to the project would likely have hindered the ability to generate accurate solutions with the necessary temporal and spatial resolution. It can be seen, for example, in Figure 11.5 that the water volume fraction around the free surface has poor resolution and lacks definition between the two fluid phases. This suggests that the mesh at the free surface was not fine enough to accurately model the fluid in the upper section of the duct. It is important that the mesh is refined around the free surface to properly capture the fluid interface and model the sealing characteristics of the wave crest with the duct roof as this is the key event in the conversion cycle. Another limitation of the models is that the wave input condition was specified at the duct entrance rather than in a length of domain representing the wave tank. This would have not correctly represented the actual wave entering the duct, particularly in the case where the amplitude exceeded the entry freeboard.

Limited information exists regarding the CFD testing work package of the project, whether in reports or stored computational data. It is therefore challenging to draw any firm conclusions from it or learn lessons from the methodology. The progression of developing the model from a simplified, small, 2D problem to a large 3D model with the added complexities was a sensible approach to take. It allowed the rapid development and fine tuning of the boundary and initial conditions with a small model that could be run relatively quickly.

A2 Additional Background Information

A2.1 Scale Laws

When testing any scaled models, it is important to consider the physical processes that are occurring and their relative consequence to each other. Not all physical processes can be governed by the same scaling law and so the dominant processes within the model should be compared and the appropriate scaling law adopted. It is for this reason that a scaled model will never fully represent the prototype behaviour. These differences between scale and prototype are known as scale effects and the best way to mitigate these effects is to construct a model as close to prototype size as possible. However, this is seldom practical and so a trade-off between accuracy and scale of the model has to be found. Typically the scale of the model is chosen to match the conditions that the testing facilities can provide. It is often convenient to state the scale of the model in the ratio format "1:X", where X is the scale factor.

In order for a model to best represent the prototype, full scale situation, three types of similarity must be considered.

- Geometric Similarity – The shape and lengths of the model must resemble that of the prototype, where all lengths are scaled with a scale factor of 1:X.
- Kinematic Similarity – Motions of the model should be similar to those of the prototype so that velocities and directions of movement are scaled correctly.
- Dynamic Similarity – The similarity of forces, so that model forces are scaled to represent the magnitude of the prototype forces.

For engineering scenarios such as the modelling of wave energy converters, it is important to ensure that the dominant forces are correctly represented even if this is at the expense of smaller forces with lesser influence. In the case of hydraulic models with a free surface and gravity waves, gravitational forces dominate the physical processes. In these instances Froude scaling is the most applicable law of similitude as it can be generally assumed that viscous, surface tension and compressive forces are negligible in comparison.

A2.1.1 Froude Scaling

The Froude number, *Fr*, determines the relative importance of inertial forces acting on a fluid to the gravitational force due to its weight. It is defined as the square root of the ratio of inertial forces to gravitational forces;

$$\text{Froude Number, } Fr = \sqrt{\frac{\text{inertial force}}{\text{gravity force}}} = \sqrt{\frac{\rho L^2 u^2}{\rho L^3 g}} = \frac{u}{\sqrt{gl}} \qquad [37]$$

u = characteristic velocity g = acceleration due to gravity L = characteristic length

To comply with Froude similitude, the Froude number of the model, Fr_m, and prototype, Fr_p, must be the same, therefore

$$Fr_m = \frac{u_m}{\sqrt{gl_m}} = \frac{u_p}{\sqrt{gl_p}} = Fr_p \qquad [38]$$

A2.1.2 Reynolds Scaling

The Reynolds number of the model becomes the most important parameter when viscous forces are dominant. In a similar way to the Froude number, the Reynolds number demonstrates the relative importance of the inertial forces acting on the fluid to the viscous forces. i.e.

$$\text{Reynolds Number, } \mathrm{Re} = \frac{\text{inertial force}}{\text{viscous force}} = \frac{\rho L^2 u^2}{\mu u L} = \frac{\rho u L}{\mu} = \frac{uL}{\upsilon} \qquad [39]$$

Where, ρ = density, u = velocity, L = length, μ = dynamic viscosity and υ = kinematic viscosity. As with Froude similitude, the Reynolds number at model scale Re_m, must equal the full scale, prototype Reynolds number, Re_p, such that

$$\mathrm{Re}_m = \frac{\rho_m u_m L_m}{\mu_m} = \frac{\rho_p u_p L_p}{\mu_p} = \mathrm{Re}_p \qquad [40]$$

In wave energy applications Reynolds similitude is not often used as it is generally more applicable to gas flows or very small scale experiments where viscous forces dominate.

The geometric, kinematic and dynamic scale factors for both Froude and Reynolds similitude are summarised in Table A1.1.

Table A2.1, Similitude scaling ratios modified from Holmes (2009).

Characteristic	Dimension	Froude	Reynolds
Geometric			
Length	[L]	X	X
Area	[L^2]	X^2	X^2
Volume	[L^3]	X^3	X^3
Rotation	[L^0]	—	—
Kinematic			
Time	[T]	√X	X^2

Velocity	$[LT^{-1}]$	$\sqrt{X}$	X^{-1}
Acceleration	$[LT^{-2}]$	—	X^{-3}
Volume Flow	$[L^3T^{-1}]$	$X^{2.5}$	X
Dynamic			
Mass	[M]	X^3	X^3
Force	$[MLT^{-2}]$	X^3	—
Pressure	$[ML^{-1}T^{-2}]$	X	X^{-2}
Power	$[ML^2T^{-3}]$	$X^{3.5}$	X^{-1}

A2.2 Naval Architecture Theory

Prior to this research work commencing, the design realities of a floating, ocean deployed OWEL WEC had not been considered in any detail. The characteristics of the vessel's dynamics and their effect upon power capture were unknown and so investigative work was required to fill the gaps in the knowledge.

Throughout the physical modelling chapters, regular reference is made to a number of standard terms from naval architecture theory as buoyancy and ballast configurations are tested to understand the free floating motions of the various models. This section provides a brief overview of the main principles associated with the design of floating structures in order to provide a reference and point of context for the reader. Further information and introduction to these concepts is provided in most ship science text books such as Rawson and Tupper (1994).

A2.2.1 Terminology

Historically, mariners have coined numerous nautical terms that are universal when describing the parts and locations on ocean going vessels. The most commonly used terminology such as the front; *bow*, rear; *stern*, left side; *port* and right side; *starboard*, of a vessel are given in Figure A11.6. In order to maintain continuity with regular nautical conventions, these terms are used throughout this work and are often used when describing distributions or locations of ballast and buoyancy for example.

A free floating body is able to move in six degrees of freedom; three rotations and three translations, about or along the *x*, *y* and *z* axes. The motions associated to these degrees of freedom also have nautical terms and these are given, along with the direction of positive value, in Figure A11.7.

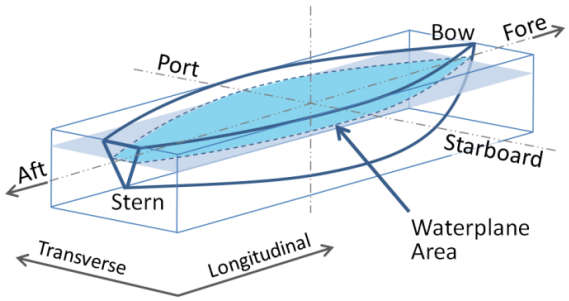

Figure A11.6, Nautical conventions for describing locations and directions on a vessel.

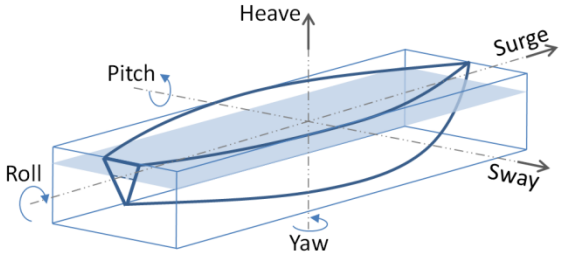

Figure A11.7, The six degrees of freedom for ship motion, indicating their positive directions.

A2.2.2 Floatation and Trim

Buoyancy was first documented in Archimedes' principle which states that "*Any floating object displaces its own weight of fluid"* and further to this; "*Any object, wholly or partially immersed in a fluid, is buoyed up by a force equal to the weight of the fluid displaced by the object"*. In other words, the hydrostatic pressure causing the upward, buoyant force is opposed by the weight of the object and, if in equilibrium, these forces will be equal and opposite. The weight can be considered to act from a single point known as the Centre of Gravity (CoG). Similarly the buoyancy can also be said to act vertically upwards from the Centre of Buoyancy (CoB) which is defined as the geometrical centre of the underwater volume. The waterline is the position at which the water free surface resides when the body is floating; taking a cross sectional slice through the body at the waterline provides the waterplane area. The draught and freeboard are the distances from the waterline to the lowest part of the vessel's hull and upper-deck respectively. A difference in the draught between the bow and stern is the trim. Any watertight volume of the body above the waterline is called 'Reserve Buoyancy' and only contributes to the buoyant force when the body is displaced so that a part of the reserve buoyancy is submerged below the waterline. It is a measure of a vessel's survivability and ability to withstand sinking but is also important when determining the stability, a concept which is subsequently discussed further. These concepts and terminology relating to a floating body are summarised in the schematic in Figure A11.8.

A2.2.3 Stability

Stability is a measure of effectiveness of a body to return to its original state after a small disturbance. In the case of WECs, it is typical to consider the disturbance due to a wave loading as this is the most common loading the vessel is likely to experience. A WEC such as OWEL

that is not reliant on motions for power capture should be designed to provide the right amount of stability; too much will result in high restoring forces requiring a stronger and more costly structure; too little could result in the vessel being inundated and possibly capsizing or sinking.

The Metacentre (M) is the intersection of the vertical lines through the centres of buoyancy in the initial and slightly inclined positions. The distance between the CoG and the Metacentre is the Metacentric Height (GM) and is a primary measure of stability of a vessel. The CoG must be below the Metacentre for the vessel to be stable and so have a positive GM.

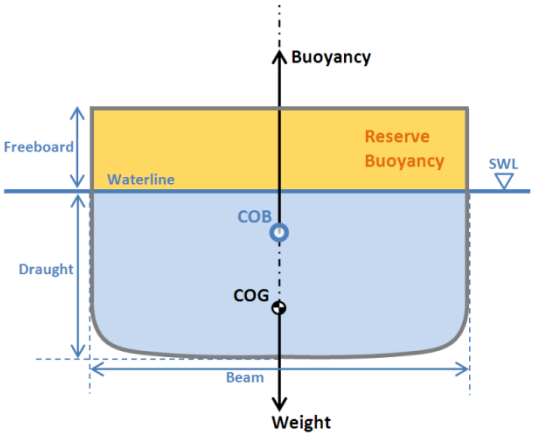

Figure A11.8, Terminology associated with a floating body.

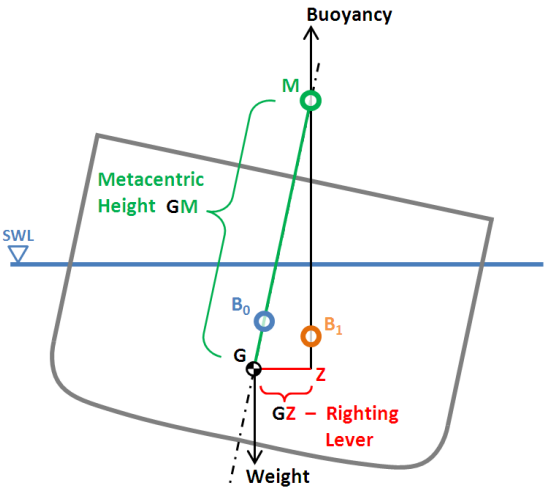

Figure A11.9, A diagram showing the effects on a vessel due to a slight inclination from rest.

The diagram in Figure A11.9 summarises the aforementioned definitions relating to the stability of a vessel and demonstrates the consequences when a body is displaced from rest. The cross section of the hull of a ship, shown in Figure A11.9, has a Centre of Buoyancy (CoB) at B_0 when at rest, however, when the hull is inclined, the CoB moves to B_1. In this instance, the CoG and CoB are acting vertically but at different points transversely and so a moment occurs between the two forces with a lever of length GZ. This moment and lever due to the forces, rights the hull and returns it to its original position at rest. The rate at which this restoring action occurs determines the stability of the vessel and is dependent on how the CoB moves when the vessel is displaced.

The best way to increase transverse stability is to reduce the height of the centre of gravity above the keel. Otherwise, the most effective method is through a change in hull form is to increase the beam with the expense of reducing the draught, as this will increase GZ.

For the specific case of the OWEL WEC, the pitching characteristics of the device are one of the more significant degrees of freedom and are strongly coupled to power capture. A vessel pitches about its Longitudinal Centre of Floatation (LCF) which is defined as the geometrical centre of the waterplane area. Altering the buoyancy distribution forward and aft will therefore change the position of the LCF and the magnitude of excursion at the bow and stern due to pitch. It is also important to consider the effect of the internal free surface on the stability of the OWEL duct. Stability is essentially a problem of balance and with a moving fluid inside a body, the balance is constantly altering. Oil and LNG tankers for example contain large tanks filled with a fluid. The movement of the fluid within these tanks, known as sloshing, can have severe detrimental effects on the stability and motions of the vessel due to the rapidly shifting mass distribution.

A2.2.4 Seakeeping

The term seakeeping is typically used to describe the ability of a vessel to carry out its role or duty for any given sea condition. In our specific example of a WEC, this term is mostly directed towards the characteristics of motions and how the device behaves in ocean waves. The seakeeping of a WEC should be such that power capture is maximised; this can be done by careful design of the ballast and buoyancy distributions.

The buoyancy distribution will not only define the location of the LCF but also the magnitude of the buoyant force at any given position on the hull when encountering a wave. The mass distribution, a combination of the structural and ballast weight, provides resistance to an acceleration arising from the motion of a vessel. Another method for altering the motion characteristics of a body is by the inclusion of damping plates. These simple additions provide a drag force when moved through the water in certain directions, further reducing the magnitude of the motions where necessary.

It is usual to express the motions of a body due to a given input force as a Response Amplitude Operator (RAO). This is simply the amplitude of the output response divided by the amplitude of input excitation. For WECs it is useful to express the movement of the hull as a function of the wave height. Figure A11.10 shows three typical curves that show how the pitch, heave and roll RAOs of a vessel change with wave period. These RAO curves are representative and show general trends. It is often the case that the response for a given wave amplitude will not be a linear relationship and so, particularly in higher waves, the motion RAO could be different to that for smaller waves with the same period.

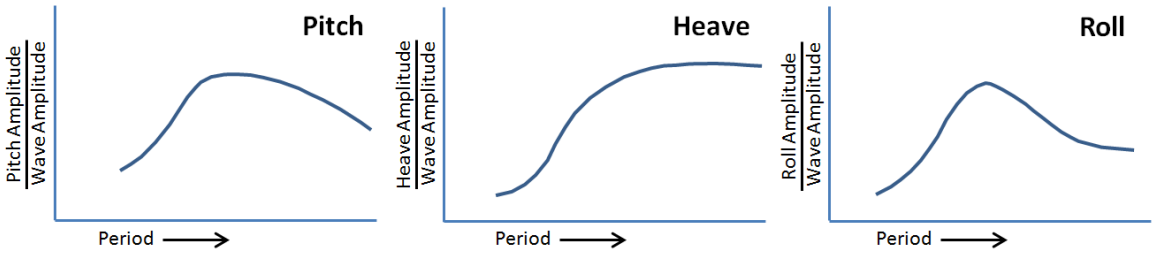

Figure A11.10, The shape of typical RAO graphs for a vessel in pitch, heave and roll.

For a freely floating vessel, motions in pitch, heave and roll are oscillatory and are opposed by the buoyant forces arising through the change in the position of the body. Yaw, surge and sway however, are not oscillatory and do not restore to an initial position. The inclusion of a mooring system alters these motions as movement in any degree of freedom is opposed by the moorings and so the body will tend to restore to an initial static equilibrium.

Moorings are commonly comprised of a series of chains, lines and anchors. There are many forms and arrangements of these, each with their own merits, characteristics and costs. Their function however, for whichever arrangement used, is universal; to provide station keeping for the vessel. This means to maintain the position of the floating object and prevent it from moving outside of the desired design range. In extreme storm conditions, this is a vital role as it prevents the vessel from being washed away by the wind and waves. A secondary function, which is more applicable to WECs than ships, is to provide additional forces when the vessel is disturbed. A mooring chain is usually many times longer than the water depth so that the majority of its length resides on the seabed in between the vessel and the anchor. This reduces the risk of snatch loads, where the chain becomes taught and full force is applied directly to the anchor, and also means that the greater the vessel moves, the greater the mooring force becomes as more chain is picked up off the sea bed. Similarly to the methods discussed previously, the design of the mooring system can be altered to meet the seakeeping requirements.

A2.3 Review of Full Scale Power Take-Off

A turbine for any wave energy converter using air as the working fluid should be designed to provide optimal system damping whilst simultaneously converting the flow efficiently into rotational shaft work over the design range of operational air flow rates. Through the historic development of OWCs a number of suitable turbine technologies have been researched and implemented both at scale under idealised conditions and in prototype deployments. Extensive literature reviews of air turbines for WECs can be found in [Takao and Setoguchi (2012), Gareev (2011), Curran and Folley (2008), Herring (2007), Anand *et al.* (2007a), Maeda *et al.*

(2001)] and provide full accounts of the experimental, comparative studies conducted on the various types of turbine for use in OWCs.

This overview introduces the types of turbines typically used in OWC applications and is not intended to be a comprehensive review of turbine design but rather to discuss the merits and disadvantages of the various turbines suitable for pneumatic power conversion in WECs. Focus is given to the two principal variants that have been extensively researched; the Wells turbine and the impulse turbine. The operating principle for each is described and comment is made on their application to OWCs in terms of efficiency, damping and key turbine design parameters. The choice of possible air turbine for OWEL is considered along with its requirements to provide an effective method of power take off. The choice of turbine type for the full scale device will determine the damping characteristics applied to air flow through the PTO and so the implications of this on the scale model testing are discussed in reference to 3.6. As concluded by many previous OWC developments [Thakker and Hourigan (2004), Wavegen (2002), Curran *et al.* (1995)] it is helpful to know the typical full scale PTO characteristics when carrying out small scale modelling so that the turbine can eventually be better matched to the requirements of the device.

A2.3.1 Wells Turbine

The classic power take off choice for an OWC is the Wells turbine and was developed by Dr. A.A. Wells in 1976 at Queen's University Belfast. This is a self-rectifying, reaction turbine that is designed for operation in bi-directional flows, [Gato and de O. Falcão (1988)]. Typically, symmetric NACA 00XX, un-cambered and un-tapered blades rotate in a continuous direction in a plane that is 90° to the incident air flow. Characteristically, the turbine exhibits a linear relationship between flow rate and induced pressure drop meaning that it provides a constant amount of damping. The combination of the axial air velocity, V_A and blade rotational velocity, U, determine the angle of incidence, α at which the flow approaches the blade, this is summarised by the velocity triangle in Figure A11.11. The rotational component of lift force, F_θ, generates the torque on the turbine shaft to turn the generator.

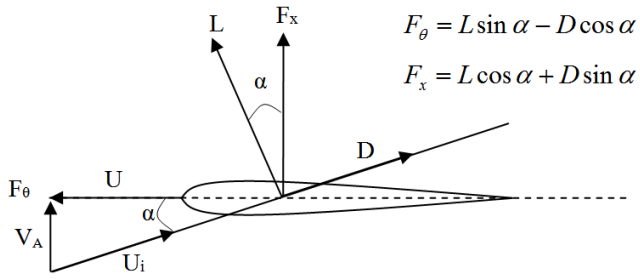

Figure A11.11, Velocity and force vectors associated with a Wells turbine blade.

Whilst the inherent simplicity of the Wells turbine being self-rectifying without the need for complex geometry is advantageous, it is typically characterised by a relatively modest conversion efficiency and a narrow bandwidth of performance. The range of flow conditions over which this type of turbine operates efficiently is governed by two key loss mechanisms; at high flow rates, produced by large water column displacement, the angle of attack increases which can lead to stall whereas in low flow, the drag from the blades exceeds the lift generated. Reduction of these losses necessitates the use of a variable geometry turbine or variable rotational speed. It should be noted that, from the velocity triangle in Figure A11.11, the blade velocity has to be large in comparison to the axial flow velocity in order to keep the angle of incidence small as typical $\alpha_{stall} \approx 18°$. In the case of OWCs and OWEL, large volumes of air with low velocity are forced into a small cross section turbine which can lead to large axial flow velocities, exacerbating the need for large blade velocity, [Paixão Conde and Gato (2008)]. The high rate of rotation, typically between 1000-1500 RPM, leads to large forces being applied to the blades and hub of the turbine as well as increased noise levels which have caused particular issues at the LIMPET and Mutriku plants [Whittaker *et al.* (2004), Tease *et al.* (2007)]. The turbine tip speed, and so the angle of incidence, is limited by local compressibility effects as the Mach number approaches sonic conditions and drag increases. For a turbine rotating at a constant speed, the angle of incidence at the hub is always greater than at the blade tip. This can be overcome by adding a component of twist to the blade geometry however, this is not possible for bi-directional turbines which require symmetric turbine performance. In order to reduce stall in high flow rates, blow off valves can be incorporated to allow air to escape prior to the turbine, thus reducing flow rate through the PTO, axial velocity and therefore the angle of attack. The loss of energy from the system through the opening of the valve is intended to be countered by an increase in turbine efficiency such that there is an overall gain in performance [Falcão and Justino (1999), Wavegen (2002)].

The airflow passage from the large cross sectional waterplane area of the device to the comparatively narrow ducting of the turbine should made as smooth as possible in order to

reduce separation, pressure losses and ensure a relatively uniform flow distribution to the turbine, [Folley *et al.* (2006), Paixão Conde and Gato (2008)].

The aerodynamic conversion efficiency of a turbine is the ratio of power due to torque from the blades, to the available air power across it and can be defined as

$$\eta_{aerodynamic} = \frac{T\omega}{\Delta p\, Q} \qquad [41]$$

Where T = torque, ω = angular velocity of turbine, Δp = pressure drop, Q = volumetric flow rate.

In the case of a Wells turbine, the torque is typically low whereas the angular velocity is high. The pressure drop and flow rates are determined by the damping requirements of the collector. The oscillatory nature of the flow in OWCs leads to a varying torque and power generated. This can be smoothed by including a high inertia flywheel as was the case with both the LIMPET and Islay OWCs, however, this incurs a significant amount of "windage" as energy is absorbed by the flywheel [Whittaker *et al.* (1997), Wavegen (2002)]. In order to be self-starting, Wells turbines are required to have low values of hub to tip ratio and high solidity as first investigated by Raghunathan and Tan (1982). This is a trait that is not beneficial for optimum turbine performance and so Wells turbines, typically, have poor self-starting characteristics and a trade-off between starting and performance found Raghunathan (1995b). A number of authors such as Curran *et al.* (1997), Raghunathan (1995a) White (1991) have presented various design methodologies to determine the key design parameters and suitable ranges for their optimum values.

Numerous numerical and physical studies have been conducted into the various configurations and optimisation of the design parameters of Wells turbines in order to overcome some of their limitations. These advanced design configurations have covered a variety of modifications to the baseline, monoplane design and have included the addition of a second rotor, turbines with guide vanes and turbines with self-pitching and controlled pitch blades.

Swirl losses incurred at the air exit of a Wells turbine were observed to be approximately 20% of the pneumatic energy available to the turbine in the Islay OWC [Whittaker *et al.* (1997)]. The rotor of the turbine imparts a swirl component to the airflow through the viscous interaction between the rotating blade surface and the axial airflow. Experiments with inlet and outlet, fixed guide vanes were conducted to optimally direct the airflow onto and off the blades and as an attempt to minimise swirl losses [Curran (2002)]. Investigations by Curran and Gato (1997) compared the performance of a monoplane configuration with and without guide vanes and

observed an increase in peak efficiency of at least 10% and an extension of the turbine's damping properties further into the stall region. This approach however, is typically intended to maximise the turbine efficiency over a specific flow range with the sacrifice of performance at the extreme air flows. The results from Curran and Gato (1997) showed that, whilst the performance was improved over a range of flow rates, the turbine stalled earlier, resulting in poorer efficiency.

A biplane design, comprising two lower solidity rotors, allows for a greater pressure drop for the case of higher power OWCs and can slightly increase the performance albeit limited by the increased swirl losses in the outflow [Curran and Gato (1997), Kaneko *et al.* (1992)]. Raghunathan *et al.* (1995) found that the stall of the biplane configuration could be delayed to a higher flow rate than a monoplane design but the overall peak efficiency was reduced and the pressure drop was considerably higher.

It was proposed by Beattie and Raghunathan (1993) that a biplane design with a contra-rotating rotor could be used as an alternative to guide vanes in order to recover the swirl energy imparted by the upstream rotor. Constant flow, quasi-static tests by Curran and Gato (1997) suggested that the performance of the contra-rotating configuration had a similar operational range and peak efficiency but with a much higher damping ratio in comparison with the monoplane turbine with guide vanes. Conclusions drawn from experiments and theoretical models by [Thomas (2008)] showed that a contra-rotating Wells turbine was aerodynamically more efficient than a biplane Wells turbine. Further to this, Curran (2002) suggested that the favourable interaction between the rotors at stall led to a more gradual reduction in efficiency in comparison to a monoplane design. It was also found that increasing the solidity of the counter rotating design led to a reduction in efficiency. However, when a turbine with this configuration was deployed on the LIMPET OWC device it was found that, in comparison to the small scale constant flow modelling, the performance was significantly reduced, [Folley *et al.* (2006)]. The early onset of stall observed on the LIMPET turbine led to a reduction in peak efficiency of approximately 52% and additionally a reduction in the effective performance bandwidth.

In contradiction to the previous findings, Folley concluded that the contra-rotating Wells turbine has a lower efficiency than a biplane or monoplane Wells turbine with guide vanes. The requirement for an additional generator or gearbox means that the contra-rotating design is also far more mechanically complex than the other types of turbine design. It was recommended that unless the performance of the turbine could be significantly improved, it would not be favourable to use one in comparison to the more traditional configurations.

The limited range of flow conditions over which fixed pitch Wells turbines are efficient can be extended by the modification of the blade angle of incidence. Turbines with variable pitch angle blades improve on the performance of turbines with fixed geometries and allow independent control of the pressure drop and flow rate and so too the pneumatic damping of the turbine. The angle of incidence can be reduced as the flow rate increases to maintain torque levels and prevent the onset of stall. Curran (2002) found that the peak efficiency of the turbine could be extended and maintained to flow rates up to three times greater than the point of stall for the more conventional designs. A passive or active approach to varying the pitch can be taken; either the blades can rotate by themselves due to an aerodynamically induced moment about a pivot or be actively actuated by a control system.

Takao *et al.* (1997) and Setoguchi *et al.* (1997) showed that Wells turbines with self-pitch controlled blades offered higher performance over conventional fixed pitch designs, with improved starting characteristics and a reduction in rotational speed necessary to maintain the effective angle of incidence. The performance of this passive design however, has not been verified in any deployed OWC plants.

An active approach to controlling the pitch of the rotating turbine blades allows for much more precise optimisation of the performance however, the inclusion of multiple moving parts and bearings adds a level of complexity to the turbine along with significant associated maintenance issues, [Tease (2003)]. A variable pitch Wells turbine with a rotor comprising 15 blades which could be pitched up to ±40°, was installed on the Pico OWC, [Taylor and Caldwell (1998)]. Experimental studies by Raghunathan (1995b), Curran (2002) and Tease (2003) showed that the operational flow envelope of a Wells turbine could be extended far beyond that of the typical point of stall of a fixed pitch device, with peak efficiencies, exceeding 70%, being maintained for much of the flow regime. Tease reported that peak blade pitch rates of 32°/s were required to maintain the conversion efficiency. An additional factor is that increasing the pitch angle reduces the solidity of the rotor and so requires a greater pitch angle to counter act the increased flow rate, this consequently leads to reduced damping from the turbine, [Curran and Folley (2008)]. Whilst this type of turbine may provide the highest performance and controllable characteristics in comparison to fixed geometry designs, the costs resulting from the increase complexity, maintenance, actuation system and control algorithm are likely to outweigh the benefits of increased productivity. It is likely that for these reasons, Wavegen, who supply the only commercially available Wells turbine, have opted for a fixed pitch, biplane design for their commercial product, [Tease *et al.* (2007), Torre-Enciso *et al.* (2009)].

The Dennis-Auld turbine was developed as an alternative to the variable pitch Wells turbine by the Australian company called Oceanlinx. In comparison to a standard Wells turbine, the Dennis-Auld is designed to operate under higher air flows and with a lower rotational speed (~500RPM), with the intention of generating higher torque, [Gareev (2011)]. Unlike the NACA 00XX series Wells turbine blades, the blades are symmetric about their mid chord allowing it to accept flow from either direction. The profile was designed by merging two front halves of a NACA 65-418 type blade. The blades rotate about their mid chord point to optimise the effective angle of incidence to the air flow. As the flow switches direction, the blades rapidly flip through a large angle in preparation for the air flow from the opposite direction. Initial small scale testing by Finnegan and Auld (2003) recorded peak efficiencies of up to 60% with the blades fixed at different angles of attack. The turbine was deployed on the first large scale Oceanlinx OWC [Alcorn *et al.* (2005)] and the peak turbine efficiency exceeded 60% for a narrow range of flow conditions but generally exceeded 40% for the majority of the flow conditions tested, [Gareev (2011)]. A disadvantage of the design is the large and rapid rotation that is required for the blade to undergo. This presents challenges to design a reliable and low maintenance engineering solution however, the lower rotational velocities mean that this is less of a technical barrier than for variable pitch Wells turbine designs.

In summary, the typical advantages associated with Wells turbines, are their technical simplicity, reliability and design robustness. Whereas many issues are inherent in the design, such as; low off design performance, poor self-starting characteristics, narrow operating bandwidth, high rotational speed and high noise.

A2.3.2 Impulse Turbines

Impulse turbines are most commonly found in applications to extract power from uni-directional, high pressure steam. The principle of operation is very different to the reaction type Wells and the rotor comprises a far greater number of blades.

The blades of an impulse turbine are not an aerofoil shape but instead more like a crescent which are intended to change the direction of the airflow and impart an impulsive change in momentum from it. The schematic in Figure A11.12 shows typical blade profiles, guide vanes and the velocity vector triangles for a simple impulse turbine. Guide vanes are required to accelerate the axial flow, thus inducing a pressure drop, and direct the air onto the blades at a suitable angle. For OWC applications with bi-directional flow, these guide vanes have the same

profile as their roles are reversed every half a cycle. The direction of the flow is further modified as it interacts with the blade profile and imparts energy to the blade with a resultant force causing a rotation of the rotor. The flow velocity decreases across the rotor as kinetic energy is transferred, however the pressure remains constant. As the velocity vectors in Figure A11.12 show, the air leaves the trailing edge of the rotor blades almost axially meaning that the angle of incidence with the outlet guide vanes for a fixed geometry turbine is large. This can result in separation and pressure losses on the downstream guide vanes and is therefore one of the limiting factors in bi-directional impulse turbine design.

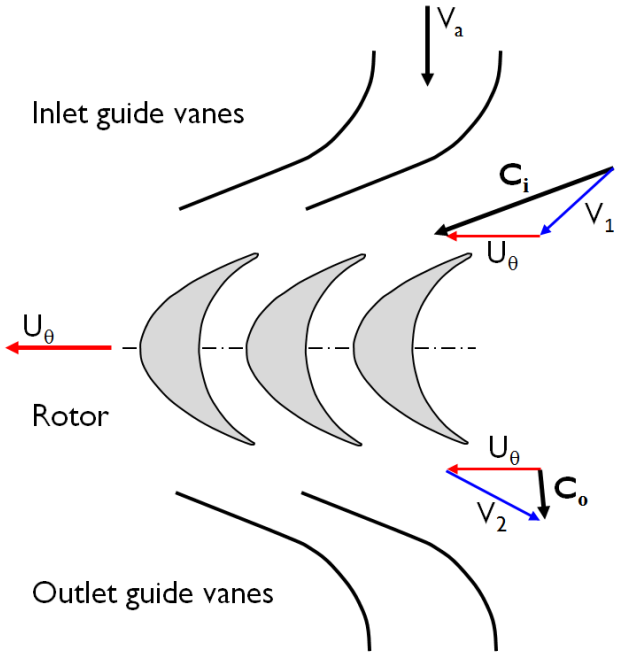

Figure A11.12, Schematic of an impulse turbine with velocity vector triangles modified from Herring (2007).

Impulse turbines have been extensively studied by Maeda *et al.* (1999), Setoguchi *et al.* (2001) and Thakker and Hourigan (2004) with various guide vane arrangements in order to rectify the flow of an OWC and provide an alternative to the Wells turbine. These focused on the performance comparison between fixed, self-pitching and linked guide vane configurations. Fixed guide vanes, as in Figure A11.12, provide a simple solution to direct the flow onto the rotor however, their downstream losses were found to be limiting to performance. By providing a pivot at the point on each vane closest to the rotor, the aerodynamic forces applied to the blades alter their angle of orientation to the flow and reduce the angle of incidence and so the associated losses. It was found however, that the downstream vanes did not always achieve the correct orientation and so a self-pitching, linked guide vane design was tested. In this configuration, each pair of up and downstream guide vanes were mechanically linked so that the aerodynamic moment applied on the upstream vane resulted in a reciprocal motion of the downstream vane via the link. Setoguchi *et al.* (2001) found that this linked configuration

outperformed the independent self-pitching guide vane turbine, which in turn performed better than the fixed guide vane design. In addition to the work by Thakker *et al.* (2009) provided a series of design charts, based on experimental and numerical modelling, to estimate suitable parameters to specify the full scale design of an impulse turbine for a given range of flow conditions and power rating.

The motivation for the development of Impulse turbines for OWC applications was to overcome some of the aforementioned, inherent disadvantages of the Wells turbine and so to provide a better suited and more efficient PTO. The blades of an impulse turbine cannot stall and so can maintain a high efficiency over a much wider range of flows than a Wells turbine. Their peak efficiency occurs at a larger optimum flow coefficient meaning that an impulse turbine, in comparison to a similarly rated Wells, is smaller and operates at a lower rotational velocity, typically 200 – 700 RPM [Thakker and Hourigan (2004)]; windage losses and acoustic emissions are therefore reduced. Additionally, the reduced diameter and lower rotational speed of an impulse turbine means that supersonic shock losses at the tips can be avoided as this is a critical design parameter for Wells turbines. The larger torque coefficient of an impulse turbine means that they are able to self-start and can accelerate faster than a Wells turbine, [Maeda *et al.* (2001)]. With reference to the definition of turbine aerodynamic efficiency in [41] this increased torque is counteracted by the reduction angular velocity of the rotor. These advantages are not only an attractive for OWC but also for OWEL as it is likely that the device will generate moderate pressure, pulses of air which will have a high peak pressure with subsequent flow being at a lower but steady pressure. Therefore, a wide range of flow coefficient will be experienced during one wave cycle and a turbine that can react quickly with high performance over a wide range of axial air velocities, will be most beneficial as the PTO for the device.

A disadvantage of the impulse turbine is that, due to its lower rotational speed, the potential for energy storage in a flywheel connected to the turbine shaft is reduced. An additional feature is that the relationship between the pressure drop and flow rate is non-linear unlike the linear trend of Wells turbines. Curran and Folley (2008) suggest that it is unclear whether, in realistic conditions, the linear pressure – flow relationship of a Wells turbine is more beneficial than that of the trend exhibited by an impulse turbine. In many of the comparative studies, the aerodynamic performance at steady state conditions are presented meaning that the relationship between the different PTO types and the wave energy collector is not examined. Therefore, whilst impulse turbines offer many advantages over Wells turbines, their damping characteristics applied to an OWC collector may be detrimental to the conversion performance. The non-linear relationship could mean that at low flow rates the device is under-damped and

conversely, over-damped at high flow. This is a conclusion that was drawn from the preliminary testing of the Islay OWC whereby the device was initially damped by an orifice before a Wells turbine was installed [Whittaker *et al.* (1991)]. Despite this, as mentioned previously in section 3.6.1 the non-linear damping may have little effect on the overall productivity of the OWC. At full scale however, limited published data exists to demonstrate the superior power generation of either turbine on the same plant.

In a fundamental steady state, laboratory comparison study by Kim *et al.* (2001), various Wells and impulse turbine configurations were tested to determine their relative aerodynamic merits. The experiments examined two types of impulse turbines (self-pitching guide vanes and fixed guide vanes) and three types of Wells turbines (fixed guide vanes, self-pitching blades and a biplane configuration with guide vanes). The results of these comparisons are shown in Figure A11.13 and demonstrate the key characteristic differences between the two types of turbine: The Wells turbines perform well at lower flow coefficients however, as their blades stall, their efficiency drops as quickly as it rose. The two impulse turbine types are characterised by a much broader operating range, typically at higher flow coefficients. These experiments were conducted at model scale with Reynolds numbers of between $0.4 \times 10^5 - 2 \times 10^5$, implying that scale effects would have affected the results, [Herring (2007)]. It is likely that, whilst the peak magnitudes may not be correct, the general trends are indicative and corroborate with observations made in similar work by Anand *et al.* (2007a) and Scuotto and Falcão (2005). On the contrary the small scale, laboratory comparison of a Wells and Impulse turbine by Thakker *et al.* (2001) concluded that the Wells turbine had a higher peak efficiency than the Impulse turbine. However, in agreement with Kim's results, the Impulse turbine performed more favourably over a wider range of flow coefficients due to the much lower speed of rotation and lack of stall. It was observed that the impulse turbine rotated at 350 RPM compared to the much faster 1700 RPM of the Wells and that the higher rotational speeds of the Wells were better suited to matching the requirements of a generator. The high performance of the Wells turbine suggested that it would be more appropriate for low energy applications whilst the impulse turbine would be better in high flow rate conditions. The Reynolds number was of the same order as that in the experiments by Kim *et al.* (2001), meaning that the Wells turbine would have been more prone to stall than a full scale system, implying difficulties in comparing prototype scaled devices. An overview of the peak efficiencies in steady and irregular air flows for a number of the different Wells and impulse turbine configurations is presented in Table A29. This is taken from the review by Setoguchi and Takao (2006) and is intended as a comparative summary to highlight the typical differences in performance between the leading turbine designs.

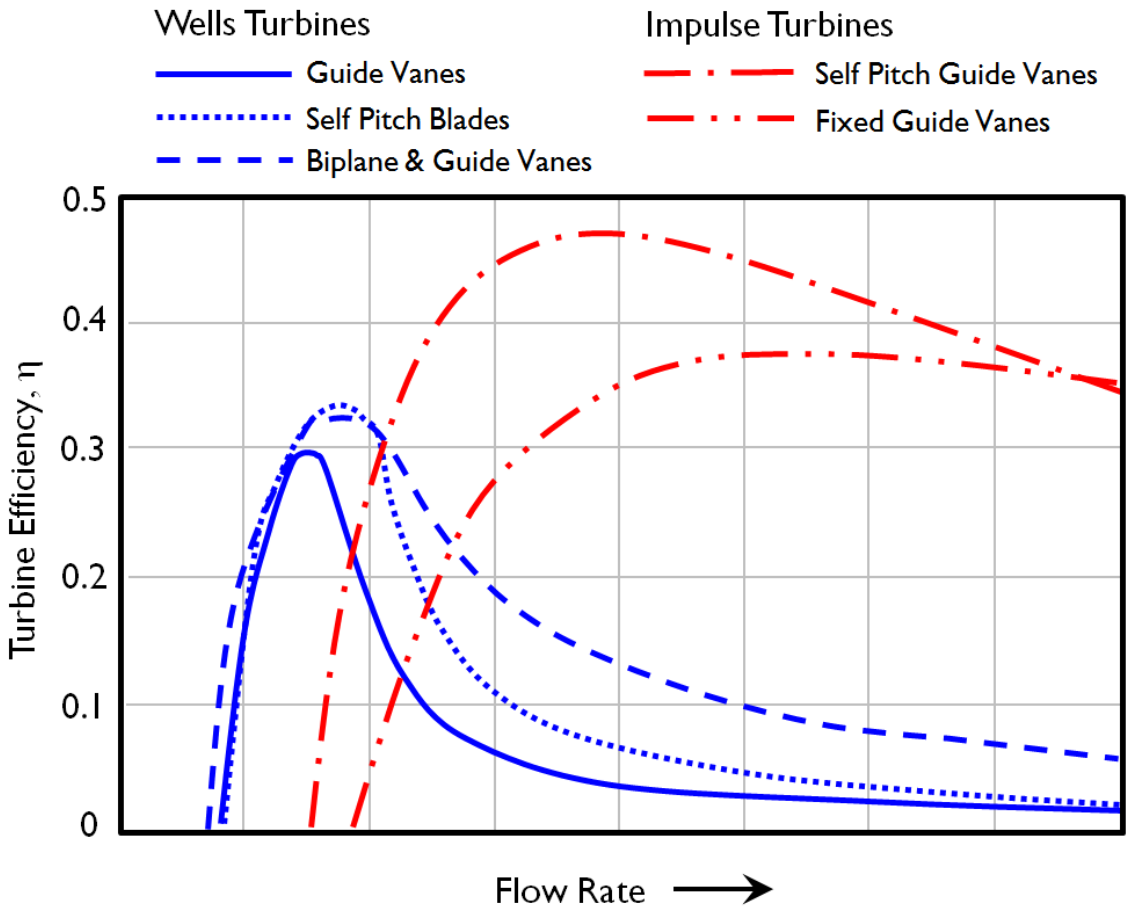

Figure A11.13, Comparison between the typical performance of various Wells and Impulse turbine types, modified from Kim *et al.* (2001).

The results of the laboratory scale, steady state comparative experiments were generally echoed by the conclusions of the subsequent numerical models intending to simulate full scale Wells and Impulse turbines on real OWC plants. A numerical model by Scuotto and Falcão (2005) was developed from data gathered from the Pico OWC plant and was used to make productivity comparisons between Wells and impulse turbines on the static device. The results showed that the Wells turbine was expected to generate more power annually but required a turbine with a diameter far greater than the impulse turbine. The study also indicated that, when the wave climate became more energetic, the impulse turbine was able to perform better and so had a greater increase in production in comparison to the Wells. Similarly, Anand *et al.* (2007b) developed a Simulink™ model to compare three different turbines installed on the fixed OWC at Vizhinjam in India. These were a 2 m diameter Wells turbine, 2 m Impulse and a 1.2 m impulse. The results showed that, whilst the peak efficiencies of the two similar turbines were comparable (~35%), the impulse turbine performed better over a wider range of sea states and in fact maintained the peak efficiency far beyond the point at which the Wells turbine had stalled.

Whilst laboratory results and the intuitive advantages indicate the benefits of impulse turbines over Wells, very few full scale impulse turbines have been deployed and in even fewer instances have the two been compared.

Table A29, A comparison of the peak efficiencies of various turbine types in steady and irregular air flow, from Setoguchi and Takao (2006).

Turbine Type	Peak Efficiency Steady Flow	Peak Efficiency Irregular Flow
Wells – Fixed Guide Vanes	0.492	0.30
Wells – Self Pitch Blades	0.496	0.44
Biplane Wells – Guide Vanes	0.534	0.34
Impulse – Fixed Guide Vanes	0.390	0.37
Impulse – Self Pitching Vanes	0.564	0.47

A 1 m diameter, self-pitching, linked guide vane impulse turbine, was installed on the Indian OWC at Vizhinjam as a replacement for the original Wells turbine. It was reported by Thakker and Hourigan (2004) that the impulse turbine performed better than the Wells however, maintenance and operational issues due to the large number of moving parts were encountered. After realising the limitations of the complex mechanical design, a fixed guide vane Impulse turbine was chosen to replace the self-pitching machine. This was found to have a poorer performance than the pitching guide vane turbine but still outperformed the original Wells.

A similar linked guide vane design was employed by the recent CORES project, however, all of the vanes were hydraulically actuated at the same instant. This turbine was installed on the ¼ scale OE Buoy in Galway Bay and replaced the previous Wells turbine. [CORES (2012)]. Little comparison was made between the Wells and impulse turbines other than that their peak efficiencies were similar at up to 65%. It was reported that the turbine required frequent maintenance and that the hydraulic actuation system consumed 2.2 kW of the PTO's 11 kW rated power.

In addition to the traditional axial, self-rectified impulse turbine, a number of other design configurations have been conceived and tested. These include radial turbines, [Castro *et al.* (2007) Falcão *et al.* (2011)] and a combination of uni-directional impulse turbines on a common shaft, [Jayashankar *et al.* (2009a) Prasad *et al.* (2011)]. Despite their design merits and possible advantages they are currently in a very early stage of research and so are not included in this discussion.

A further recent design evolution of the axial impulse turbine was the Hydro Air, Variable Radius Turbine in development by the commercial turbomachinery company, Dresser Rand. A review of turbines suitable for OWC applications by Herring (2007) suggested that there was more potential to increase the peak performance and bandwidth of an impulse turbine than a Wells turbine. Air enters the turbine at relatively low velocity and the inlet guide vanes impart swirl to the flow. The air accelerates through the reducing cross section duct, shaped like an hour-glass, and drives the rotor which is located at the narrowest point of the ducting. The air then decelerates through the expanding outlet ducting and is redirected by the outlet guide vanes. As the change in flow direction by the guide vanes occurs at a comparatively low air speed, the separation losses at the guide vanes are significantly reduced. Initial, small scale physical and CFD modelling resulted in peak aerodynamic efficiencies of up to 55% whilst a full scale CFD model predicted efficiencies exceeding 75%, [Natanzi *et al.* (2011)]. It was concluded that this performance increase was a step change in impulse turbine efficiency.